THE UNIVERSITY *of* EDINBURGH

Underground Study at LUNA of Proton-Induced Reactions on ^{6}Li at Astrophysical Energies

Thomas William Chillery

Doctor of Philosophy
The University of Edinburgh
July 2020

Abstract

Big Bang Nucleosynthesis (BBN) theory coupled with Cosmic Microwave Background measurements provide predictions on the modern day abundances of low mass isotopes, which are then compared to observations from stellar environments. Specifically ^{6,7}Li isotopic abundances are determined from spectral analysis of radiation emitted from the outer atmospheres of low mass pre-main sequence (PMS) stars. Current literature reports measured abundance of ^{6}Li is 1000 times higher than predicted. Two reactions which destroy ^{6}Li: ^{6}Li(p,α)^{3}He and ^{6}Li(p,γ)^{7}Be, have an impact on the predicted ^{6}Li abundances. A previous study measured the ^{6}Li(p,γ)^{7}Be reaction at relevant energies and proposed a new resonance which may affect the ^{6}Li abundances predicted from BBN. Until now the existence of this resonance has yet to be confirmed by an independent measurement.

This thesis work reports an experimental campaign aimed to measure both proton-induced destructive reactions on ^{6}Li across astrophysically relevant energies. These reactions were measured concurrently at the Laboratory for Underground Nuclear Astrophysics (LUNA) located under the Gran Sasso mountain in Italy, which benefits from a reduced natural background ($10^4 - 10^5$ reduced gamma-ray flux) compared to surface laboratories. A proton beam was accelerated at energies $E_{\mathrm{p}} = 80 - 395$ keV onto ^{6}Li-enriched solid targets nominally composed of Li_2O or Li_2WO_4 and evaporated on a tantalum backing. The charged particles and gamma rays were simultaneously detected using a Silicon and a High Purity Germanium detector, respectively.

The experimental yields were calculated from the data and deconvolved using a median energy approach to determine astrophysical S-factors for both ^{6}Li destruction reactions. Due to incomplete knowledge of the target stoichiometries during beam bombardment, the present S-factors were normalised to previously reported ^{6}Li(p,α)^{3}He reaction S-factors. Results from this work do not confirm

the existence of the proposed resonance in ^{6}Li(p,γ)^{7}Be. Present thermonuclear reaction rates are calculated to the highest precision to date and the astrophysical implications discussed. Comparisons to previous literature are presented.

Lay Summary

Our known Universe started with the Big Bang. For the first three minutes, everything was a hot and dense soup (plasma) of elementary particles, neutrons, and hydrogen (protons). This high temperature of approximately 2 billion degrees caused the Universe to rapidly expand and cool down. Below 1 billion degrees, the protons and neutrons began fusing to form light elements of deuterium, helium, and lithium. Deuterium is an example of an isotope of hydrogen, which has the same number of protons but a different number of neutrons. The process of combining lighter elements into heavier elements is called nucleosynthesis. As the Universe continued to expand, it cooled down enough to allow clouds of hydrogen and helium to clump together. As a result of their gravitational pull, these clouds collapsed into each other increasing the pressure and temperature at the centre of the gas. After about 10 million years the core ignited and began synthesising heavier elements, this is how the first stars were formed. The amount of a given element produced in the Big Bang is called its primordial abundance, and the amount made in a given star is called its stellar abundance.

Astronomers use Earthbound and space-based observatories to measure radiation emitted from these stars, allowing them to find out the elemental abundance of these astrophysical bodies. These abundances are governed by the nuclear physics processes occurring in the production/destruction sites. By comparing abundances from observations with the outputs of theoretical models, we can grasp the fundamental workings of these furnaces in the sky. Going further the observed stellar abundances for light (low mass) stars can be compared with primordial abundances from models of the Big Bang, allowing us to test our knowledge of the origin of all life and matter on Earth and beyond. At present, thanks to ever-increasing precision from observatories, the observed primordial abundances are in excellent agreement with predictions from Big Bang models for almost all isotopes, the exceptions being lithium-7 and lithium-6. Predicted

lithium-7 abundances are three times too high, and lithium-6 abundances are 1000 times too low to explain observations. These are referred to as the first and second lithium problems, respectively. The present work involved measuring nuclear reactions of protons interacting with lithium-6 and determine destruction probabilities of lithium-6 in the Big Bang and stellar environments.

Although the temperatures encountered in primordial nucleosynthesis are 1 billion degrees and give the protons lots of energy, the destruction probability of lithium-6 is still low enough to present a challenge for measurements in a laboratory. If an experiment was performed on the Earth's surface, the signal from lithium-6 destruction might be hidden by background radiation from cosmic events. For our experiment, the background radiation was reduced by measuring the reactions underground at the Laboratory for Underground Nuclear Astrophysics located under the Gran Sasso mountain in Italy. The mountain provides 1400 m of rock shielding, significantly reducing background levels and allowing us to successfully measure the reactions. Our result reduces the uncertainty of the lithium-6 destruction probability in the Big Bang, however, the lithium problems remain unsolved. This suggests further studies are required not necessarily in Nuclear Physics but perhaps in the fields of Cosmology or Particle Physics.

Declaration

I declare that this thesis was composed by myself, that the work contained herein is my own except where explicitly stated otherwise in the text, and that this work has not been submitted for any other degree or professional qualification except as specified.

Parts of this work have been published in

D. Piatti, **T. Chillery**, *et al.*, PRL, in prep. (2020)

T. Chillery for the LUNA Collaboration, JPCS, submitted

T. Chillery for the LUNA Collaboration, Il Nuevo Cimento C **42** (2019) 116

R. Depalo for the LUNA Collaboration, Proc. 5^{th} Int. SN Conf. (2019) 233-237

D. Piatti for the LUNA Collaboration, Nuclei in the Cosmos XV (2019) 71-76

T. Chillery for the LUNA Collaboration, EPJ Web of Conf. **184** (2018) 02001

D. Piatti, Ph.D. Thesis, University of Padua (2018) .

(*Thomas William Chillery, July 2020*)

Acknowledgements

First and foremost I thank my supervisors Marialuisa Aliotta and Carlo Bruno, whom I am extremely grateful towards for their supervision and guidance during my studies.

I also extend my gratitude to the wonderful members of the LUNA collaboration, in particular I thank Rosanna Depalo and Denise Piatti for being superb researchers and entertaining co-shifters. I also thank Pietro Corvisiero for his valuable input on the Geant simulations used in the data analysis. I thank the excellent researchers in the CIRCE research group, especially Lucio Gialanella and Raffaele Buompane for their invaluable support during shifts. You all made Italy feel much closer than the early morning flights ever did.

Thanks go out to all the students and staff of the University of Edinburgh Nuclear Physics group and all of the support they provided me. I'm also thankful to all of the flatmates and friends I've made in Edinburgh. You all made the cold Scottish climate one of the warmest places I have ever called home.

Finally my thanks would not be complete without including my loving parents, Jenny and Trevor, my younger brother Logan, and all the rest of my friends and family. Thank you.

Contents

List of Figures

List of Tables

Chapter 1

Astrophysical Motivation

> In the beginning the Universe was created.
> This has made a lot of people very angry and been widely regarded as a bad move.
>
> Douglas Adams

1.1 Hot Big Bang Cosmology

1.1.1 Evidence for the Big Bang

Big Bang theory is framed around the idea that the Universe began with a rapid expansion under extreme conditions $\sim$ 13.9 billion years ago [1], to date the most commonly accepted paradigm of the Universe's origin. This theory has remained successful in part by the strong evidence gathered together over the past century by a wide range of fields, including nuclear astrophysics, cosmology, and particle physics. There are three main sources of experimental evidence supporting the Big Bang: the first is the general agreement between predicted primordial abundances of light elements (D, ^{4}He) and observed abundances in stellar environments. These abundances are governed by the nuclear reactions forming these isotopes, and thus particular focus is placed on this evidence and the motivation behind this thesis work.

The second observation in favour of the Big Bang is the present-day expansion of

the Universe. First discovered by Edwin Hubble, and indeed regarded by many as the birth of Modern Cosmology, the expansion of the Universe suggests that it was smaller in the past. If the rate of expansion is known, then it is simple to extrapolate backwards in time to determine the start and thereby the age of the Universe. This expansion rate is proportional to Hubble's Constant, which has been measured with ever increasing precision since its introduction in 1929 [2]. In fact, evidence [3] now suggests that the Universe is not only expanding, but that its *rate* of expansion is also steadily increasing. The proposed mechanism behind this observation, dark energy, is beyond the scope of this thesis.

The third piece of strong evidence for the Big Bang is the measurement of the Cosmic Microwave Background (CMB) [4]. First observed by Penzias and Wilson, the CMB has recently been measured to exceptional precision by space-based probes, first by the WMAP (Wilkinson Microwave Anisotropy Probe) probe [5] and more recently the Planck experiment [6]. These measurements have ushered in a new age of high-precision cosmology, with cosmological parameters now known to the percent level. As a result, it is now possible to constrain cosmological parameters as inputs to Big Bang models, and extract primordial abundances for comparison with modern-day observations.

1.1.2 Big Bang Model Inputs

Models of the time evolution of the Big Bang require inputs from standard cosmology and the standard model of particle physics. The former describes the early expansion of the Universe with "gravity governed by General Relativity and a homogeneous and isotropic universe" [7] (cosmological principle). The latter includes the "microphysics of the Standard Model of particle physics and the particle content of the Standard Model, supplemented by dark matter and dark energy" [7]. These fields of physics are beyond the scope of this work and in-depth accounts may be found in [1, 7–9] and references therein.

Another input required for Big Bang models is provided by nuclear physics, specifically the reaction rates of relevant nuclear reactions which contribute to the evolution of isotopic abundances during Standard Big Bang Nucleosynthesis (hereinafter referred to as SBBN). These rate inputs are directly relevant to this work, specifically for reactions describing the destruction of ^{6}Li. A nuclear reaction network showing the most important reactions in SBBN up to ^{9}Be is provided in figure 1.1, with the two proton-induced reactions on ^{6}Li relevant to

this study highlighted in red.

1.1.3 Standard Big Bang Nucleosynthesis

Standard Big Bang Nucleosynthesis is presently the best model describing the production of light elements during the early stages of the Universe. SBBN brings together the standard model of particle physics with standard cosmology; light element production is explained by both weak interactions and nuclear reactions occurring during an expanding, cooling Universe.

SBBN proceeds as follows. At time t $\sim$ 1 s the early Universe was exceptionally hot ($T \sim 11.6$ GK), and as a result the density was dominated by radiation (photons, neutrinos, anti-neutrinos, electrons, and positrons) whilst protons and neutrons (the only baryons present) existed in a state of thermal equilibrium through weak interactions described by the following processes:

$$\begin{aligned} n + \nu_{\mathrm{e}} &\leftrightarrow p + e^- \\ n &\leftrightarrow p + e^- + \bar{\nu}_{\mathrm{e}} \\ n + e^+ &\leftrightarrow p + \bar{\nu}_{\mathrm{e}} \end{aligned}$$

As the Universe continued to expand the temperature dropped and at $T \sim 3.3$ GK the n $\leftrightarrow$ p rate became slower than the expansion rate, thus leading to freeze-out with a neutron-to-proton ratio $N_{\mathrm{n}}/N_{\mathrm{p}} \sim 1/6$. Further expansion cooled the temperature down to $T \sim 0.9$ GK, during which the free neutrons beta-decayed such that $N_{\mathrm{n}}/N_{\mathrm{p}} \sim 1/8$. Now the first nuclear reaction, p(n,γ)d, could happen faster than its reverse reaction, and through available nuclear reaction pathways (figure 1.1) the light elements D, ^{3}He, ^{4}He, and ^{7}Li were produced, with traces of other elements heavier than ^{4}He (*e.g.* ^{6}Li). SBBN stopped when the Universe cooled to $T < 0.1$ GK. A diagram of the neutron-to-proton density as a function of time and temperature, taken from [1], is provided in figure 1.2.

The primordial light element abundances predicted from SBBN as a function of baryon-to-photon density η are shown (blue lines) in figure 1.3 (from [1]). The green regions indicate the uncertainty on abundance from the nuclear reaction rates and neutron life time, and the grey line represents the latest observation of the baryon-to-photon density performed by the Planck collaboration [6]. Currently the predicted and observed primordial abundances for D, ^{3}He, and

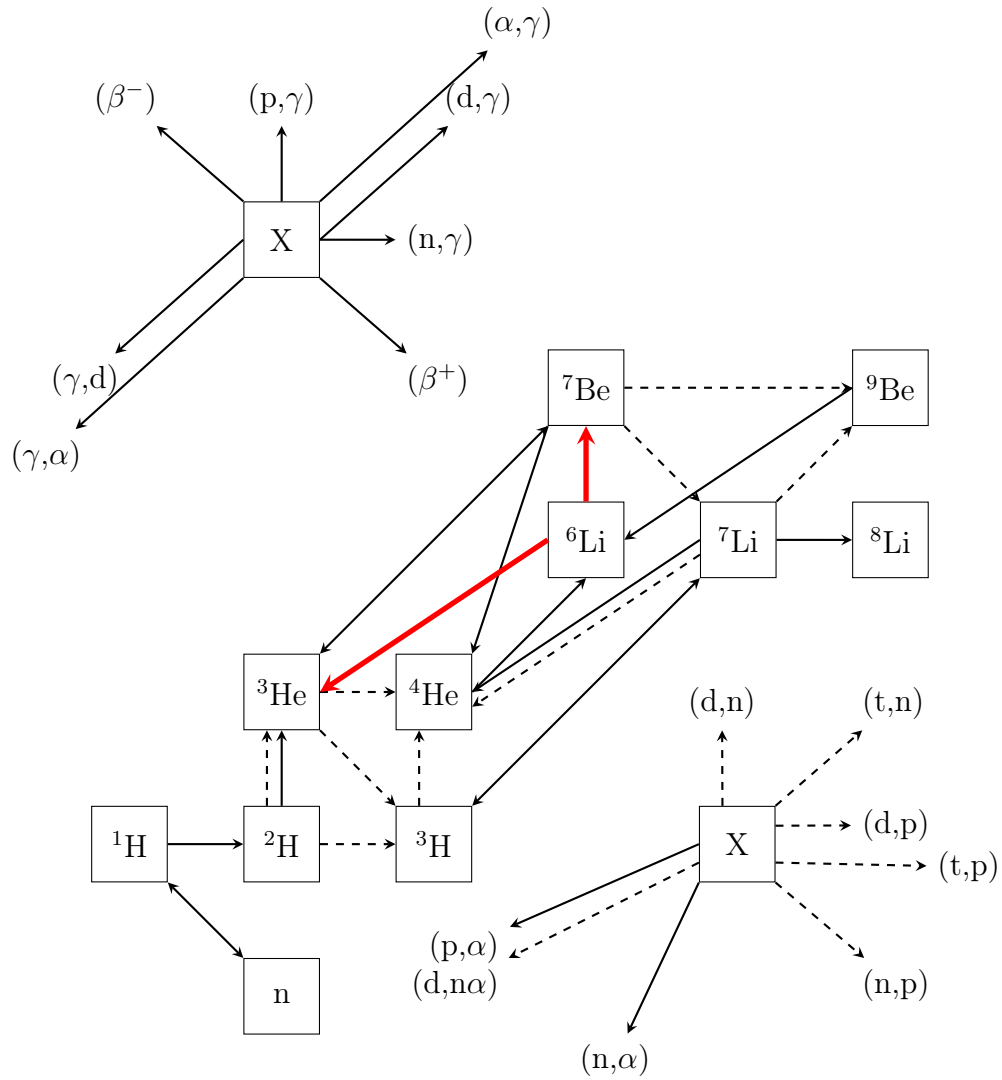

Figure 1.1 *SBBN nuclear network. The* ^{6}*Li(p,α)*^{3}*He and* ^{6}*Li(p,γ)*^{7}*Be reactions relevant to this work have been highlighted in red. Other reactions considered to be the most important in SBBN are also shown up to* ^{9}*Be.*

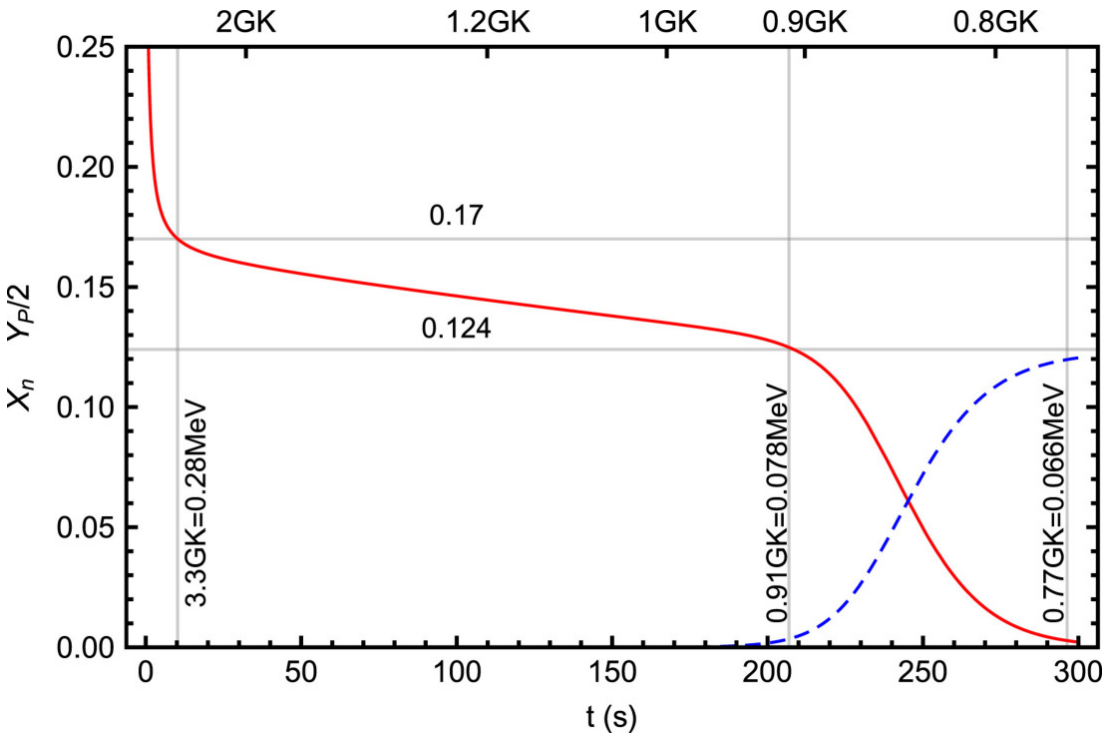

Figure 1.2 *Evolution of neutron-to-proton ratio X_n (Red) and ^{4}He abundance Y_P (blue) during SBBN as a function of temperature and time, taken from [1].*

^{4}He are in excellent agreement (within 1 sigma). However, large discrepancies are found between the predicted ^{6}Li and ^{7}Li abundances compared to those observed. The predicted ^{7}Li abundances are $2.5 - 3.6$ times higher than those measured, and inversely the predicted ^{6}Li abundances are a factor 1000 times lower than measured. These are referred to as the first and second Lithium problems respectively.

The problems may be solved by performing high accuracy measurements of the nuclear reactions responsible for creating and destroying ^{6}Li at SBBN-relevant temperatures. In SBBN ^{6}Li is predominantly produced via the ^{2}H(α,γ)^{6}Li reaction, which was recently measured for the first time at SBBN relevant energies at the Laboratory for Underground Nuclear Astrophysics (LUNA). Results from this measurement, reported by Anders *et al.* in 2014 [10], actually worsen the second Lithium problem by predicting a lower ^{6}Li/^{7}Li ratio of 1.5×10^{-5} compared to the earlier literature value of $\sim 2 \times 10^{-5}$ [7].

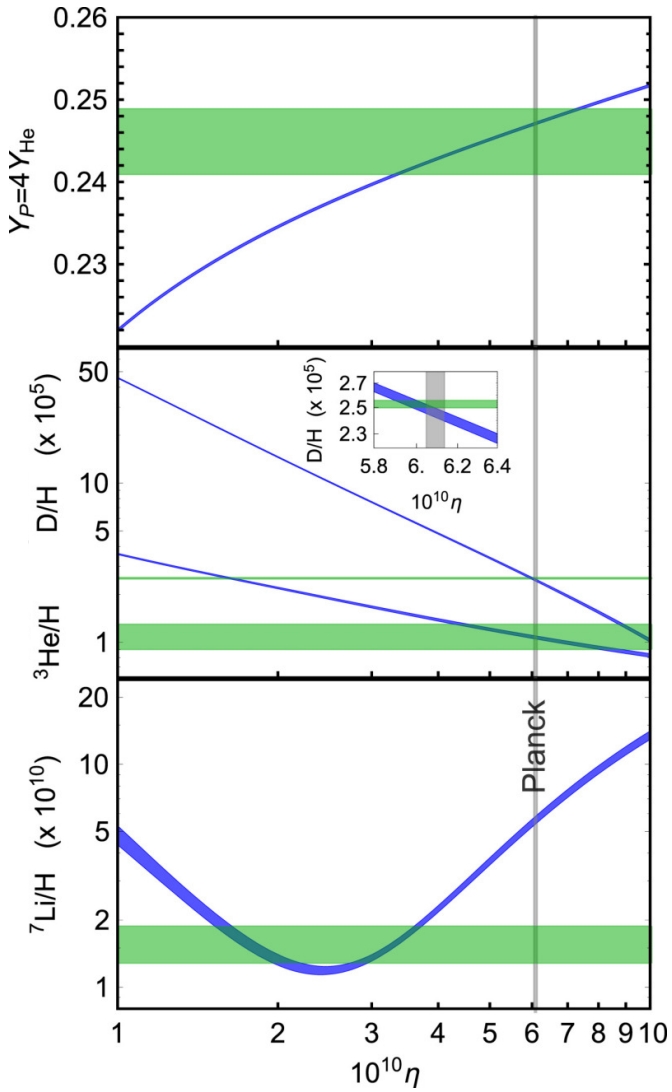

Figure 1.3 *SBBN light element abundances of D, ^{3}He, ^{4}He, and ^{7}Li (from [1]). Abundances from a SBBN model are shown in blue, and abundances from observations are shown in green. The recent measurement of the baryon-to-photon ratio η, performed by the Planck collaboration, is represented by the grey region. A $2.5-3.6$ discrepancy between predicted and observed ^{7}Li abundances is shown.*

1.2 Lithium in Stellar Environments

Lithium has been observed in low mass Pre-Main Sequence (PMS) phase (Population II) stars. The link between observed and SBBN-modelled ^{7}Li abundances was first made by Spite & Spite in 1982 [11, 12] through the observation of the ^{7}Li (absorption) spectral lines from low-metallicity Population II stars in the outer Halo of our Galaxy. By fitting these spectral lines they extracted ^{7}Li abundances for the 13 Population II stars, and discovered that for halo stars within an effective surface temperature range $T_{\text{eff}} = 5700 - 6250$ K the ^{7}Li abundances followed a flat distribution (within uncertainties). This has since been called the "Spite plateau". These stars were formed in the very early stages of the Universe and during their protostellar phase (occurring prior to pre-main sequence phase) no nucleosynthesis of ^{7}Li is expected, thus Spite & Spite concluded that "the ^{7}Li abundance of the old halo stars must be representative of the abundance in the primordial matter" [11]. They thereby proposed a primordial ^{7}Li abundance of $^{7\text{Li}}/_{\text{H}} = (11.2 \pm 3.8) \times 10^{-11}$. Spite & Spite used this abundance to determine a SBBN baryon-to-photon ratio which agreed with ratios predicted from the D and ^{4}He abundances known at the time. This agreement provided strong evidence that we live in a a Universe which is ever-expanding, *i.e.* an Open Universe. It is emphasised that these conclusions were drawn 22 years prior to the WMAP mission, which first determined cosmological constants to a high precision for Big Bang model inputs, notably the baryon-to-photon ratio.

Since the observations performed by Spite & Spite, further studies have been performed to measure the ^{7}Li and, more recently, ^{6}Li abundances from metal-poor halo (PMS) stars (see [13–17] and references therein). Asplund *et al.* [13] reported in 2006 one of the earliest measurements of ^{6}Li in metal-poor stars, whereby they performed fits of the lithium 6707 Å spectral line and explained its anti-symmetry by the presence of ^{6}Li in the stars stellar atmospheres. Over the past decade, observations of the line anti-symmetry in low mass stars were extended to lower metallicity, where it was discovered the observed ^{7}Li abundance decreases with decreasing metallicity [14], thus deviating from the Spite plateau. Accurate knowledge of the $^{6\text{Li}}/_{7\text{Li}}$ isotopic ratio provides a useful tool to constrain atmospheric convection models of PMS stars [18].

Since Asplund 2006 the models used to fit these spectral lines have been updated from 1D local thermodynamic equilibrium (LTE) to more sophisticated 3D non-local thermodynamic equilibrium (NLTE) models [15–17], made possible by

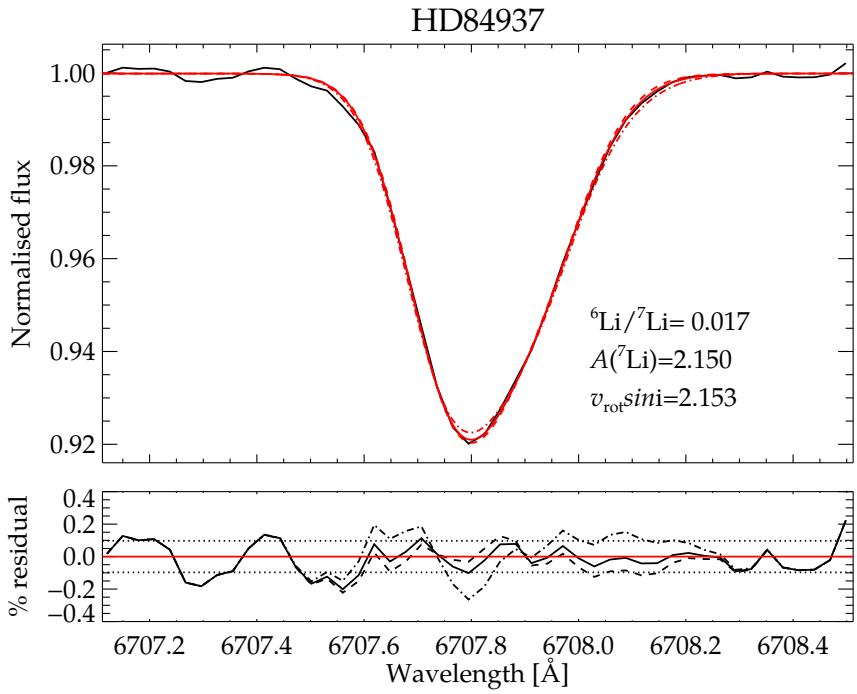

Figure 1.4 *Lithium absorption line profile from [15]. The solid black line is the observed line profile, solid red line represents their best fit (^{6}Li/^{7}Li = 0.017), the dashed line represents ^{6}Li/^{7}Li = 0, and the dotted-dashed line represents ^{6}Li/^{7}Li = 0.05.*

additional computing power in available processors. These models improve our understanding of the physics behind the lithium line spectra and sometimes explain the anti-symmetry without the need for ^{6}Li to be present in the star at all. However, despite these improvements there are still multiple low-mass stars which exhibit ^{6}Li abundances in their outer atmosphere. For example figure 1.4, taken from the 2013 publication of Lind *et al.* [15], shows a sample lithium line absorption spectrum for star HD 84937. The solid black line is the observed line profile and the solid red line represents their best fit using the new 3D NLTE models ^{6}Li/^{7}Li = 0.017 (the dashed line represents ^{6}Li/^{7}Li = 0, and the dotted-dashed line represents ^{6}Li/^{7}Li = 0.05.). For comparison the same star was studied by Smith *et. al.* who reported in 1993 [19], from a 1D LTE model, ^{6}Li/^{7}Li = 0.06. Whilst the new ^{6}Li/^{7}Li from Lind *et al.* is lower, it is still three orders of magnitude larger than the SBBN predicted ratio ^{6}Li/^{7}Li = 2×10^{-5} [20, 21].

1.3 The Lithium Problems

Whilst deuterium and ^{4}He abundances show excellent agreement between those predicted by SBBN and those measured in galaxies [8], large discrepancies are found for ^{6}Li and ^{7}Li between SBBN predictions and measurements of low-metallicity stars. In a review by BD Fields [7] and supported by recent Planck measurements [1] the current literature suggests the predicted ^{7}Li abundances are $2.5 - 3.6$ times higher than those measured, this is referred to as the First Lithium problem. Inversely the predicted ^{6}Li abundances are a factor 1000 times lower than measured, and this is referred to as the Second Lithium problem.

By current SBBN models the abundance ratio $^6\mathrm{Li}/^7\mathrm{Li}$ is $\simeq 2 \times 10^{-5}$; however, the measured ratio has an upper limit of $\simeq 0.5$ [7] — a factor 25000 times larger. Whilst this large discrepancy is currently attributed to ^{6}Li production in PMS stars via proton induced spallation and fusion reactions, the environments encountered in PMS stars are expected to destroy more ^{6}Li than ^{7}Li [7, 15]. To further constrain the predicted abundances of ^{6}Li from SBBN, high accuracy measurements of the destruction processes of ^{6}Li are required. This motivated the present study of the ^{6}Li(p,α)^{3}He and ^{6}Li(p,γ)^{7}Be reactions at LUNA, the same laboratory used for the Anders 2014 measurement. Before covering the current (literature) status of these two reactions the next chapter will explain the general formalism for reaction rate calculations.

Chapter 2

Thermonuclear Reactions in Stars

Thermonuclear reactions play a key role in the energy production and nucleosynthesis processes occurring during the Big Bang and within stellar environments. Consider a nuclear reaction following: $a + b \rightarrow c + d$, formally written as $a(b, c)d$. The left hand side $a+b$ is called the *entrance* channel, and the right hand side $c+d$ is called the *exit* channel. The energy released during this reaction is defined as the mass-energy difference between the entrance and exit channels of the reaction, called the Q-value:

$$Q = (M_a + M_b - M_c - M_d)\,\mathrm{c}^2 \tag{2.1}$$

where M is the atomic mass[1] of each respective particle in atomic mass units[2] (a.m.u) and c is the speed of light (in a vacuum).

The Q-value is a measure of the energy liberated for each interaction, and can be easily calculated for a given nuclear reaction using mass tables [22]. A more challenging quantity to evaluate is the probability of two nuclei interacting and undergoing a nuclear reaction (for example a change in momentum, energy, or the nucleonic structure of the interacting particles), known as the reaction cross section, σ. This provides a measure of how often a reaction takes place in, for instance, the Big Bang or stellar environments, and thus a measure of the Q-value and cross section provides information on the energy production in primordial and stellar nucleosynthesis.

The general empirical definition of the cross section for a nuclear reaction is given

[1]Equation 2.1 ignores the electron binding energy B_e, which typically $B_\mathrm{e} << Q$.

[2]The atomic mass unit is defined as $1/12$ the mass of a neutral ^{12}C atom. $1\,\mathrm{a.m.u} = 931.5\,\mathrm{MeV/c^2} = 1.661 \times 10^{-27}$ kg.

by:

$$\sigma = \frac{N_{\rm r}}{N_{\rm tar} N_{\rm proj}} \tag{2.2}$$

where $N_{\rm r}$ is the number of reactions during a given time period, $N_{\rm tar}$ the number of target atoms per unit area, and $N_{\rm proj}$ the number of projectiles incident on the target during the given time period. The cross section has units of area squared, and is typically quoted in orders of barn[3]. In some cases the cross section is affected by Coulomb and centrifugal barriers from nuclear charge and angular momentum effects, respectively. These effects enhance the energy dependence of the cross section, as does the nature of the force (strong, electromagnetic, weak) governing the nuclear reaction.

Standard Big Bang (and stellar) nucleosynthesis codes require reaction rates as inputs to their calculations of isotopic abundances in primordial (stellar) environments. The derivation of such rate calculations is covered in great detail, for example in [23–25]. Consider two particles, a and b, moving with a relative velocity, v, to each other. If the particles collide there is a probability (cross section) they will undergo a nuclear reaction. Extending this idea to a dense plasma environment (*i.e.* in the Big Bang or a stellar interior) there are large densities of these particles and we require a macroscopic definition for the rate at which interactions occur, called the reaction rate. The reaction rate between interacting pairs is the product of each particle's number density, the cross section of the reaction, and the relative velocity between the nuclei:

$$r_{ab} = N_a N_b \sigma(v) v \tag{2.3}$$

where N_a and N_b are the number densities of the interacting particles, v is the centre-of-mass (c.m) velocity, and $\sigma(v)$ is the cross section at this c.m velocity.

In a plasma environment the interacting nuclei have a range of energies (at the same temperature), modelled as a Maxwell-Boltzmann distribution. Since the energy available to the nuclei arises from the heat of the plasma, the rates are also known as thermonuclear reaction rates. The rate may therefore be generalised for a velocity-dependent distribution:

$$r_{ab} = N_a N_b < \sigma v >_{ab} = N_a N_b \int_0^\infty v P(v) \sigma(v) {\rm d}v \tag{2.4}$$

where $P(v){\rm d}v$ describes the probability for the interacting particles to have a

[3] 1 barn is equal to 10^{-28} m^2.

c.m velocity between v and $v + \mathrm{d}v$. The velocity distribution, $P(v)$, is usually converted to an energy distribution, $P(E)$ [23]:

$$P(v)\mathrm{d}v = P(E)\mathrm{d}E = \frac{2}{\sqrt{\pi}\,(\mathrm{k}T)^{\frac{3}{2}}}\sqrt{E}\ \exp\left(-\frac{E}{\mathrm{k}T}\right)\mathrm{d}E \tag{2.5}$$

where k is Boltzmann's constant, E is the c.m energy, and T is the temperature of the plasma environment. The Maxwellian averaged cross section may then be calculated using the integral [23]:

$$< \sigma v >_{ab} = \int_0^\infty v\ P(v)\ \sigma(v)\mathrm{d}v = \int_0^\infty v\ P(E)\ \sigma(E)\mathrm{d}E \tag{2.6}$$

$$= \sqrt{\frac{8}{\pi}}\frac{1}{(\mathrm{k}T)^{\frac{3}{2}}}\frac{1}{\sqrt{\mu}}\int_0^\infty E\ \sigma(E)\ \exp\left(-\frac{E}{\mathrm{k}T}\right)\mathrm{d}E \tag{2.7}$$

where μ is the reduced mass, defined as $\mu = (m_\mathrm{a}m_\mathrm{b})/(m_\mathrm{a} + m_\mathrm{b})$.

For future use in stellar codes the published thermonuclear reaction rates are already multiplied by Avogadro's number, N_A, and numerically the reaction rate at a temperature T is evaluated by [23]:

$$N_\mathrm{A} < \sigma v >_{ab} = \frac{3.7318 \times 10^{10}}{T_9^{3/2}}\sqrt{\frac{m_a + m_b}{m_a m_b}} \int_0^\infty E\ \sigma(E)\ \exp\left(-11.605\,\frac{E}{T_9}\right)\mathrm{d}E \quad [\mathrm{cm^3 mol^{-1} s^{-1}}] \tag{2.8}$$

where T_9 is the temperature in GK, E is the energy in MeV, $\sigma(E)$ is the cross section in barn, and the masses m_a and m_b are in a.m.u. To calculate the reaction rate requires an accurate knowledge of the cross section across astrophysically relevant energies. The case of charged-particle-induced non-resonant reaction rates, important in the evaluation of this study's ^{6}Li + p rates, is now discussed.

2.1 Charged-Particle-Induced Non-Resonant Reaction Rates

For charged-particle-induced non-resonant reactions the cross section varies smoothly at high energies (E greater than 500 keV), but at low energies it drops across many orders of magnitude as a result of the decreasing transmission probability through the Coulomb barrier. To parametrise the energy dependence

of nuclear cross sections and the s-wave Coulomb barrier transmission probability the astrophysical S-factor is defined:

$$S(E) = E\ \sigma(E)\ \exp(2\pi\eta) \tag{2.9}$$

where $2\pi\eta$ is the Sommerfield parameter given by [23]:

$$2\pi\eta = 0.989534\ Z_a Z_b \sqrt{\frac{\mu}{E}} \tag{2.10}$$

where E is in MeV, and Z_a and Z_b are the atomic numbers of the two interacting particles. $S(E)$ smoothly varies as a function of energy and is thereby easier to handle numerically compared to σ.

The thermonuclear reaction rates for non-resonant reactions are calculated for a given astrophysical temperature by substituting the S-factor (equation 2.9) into equation 2.8:

$$N_{\mathrm{A}} < \sigma v >_{ab} = \frac{3.7318 \times 10^{10}}{T_9^{3/2}} \sqrt{\frac{m_a + m_b}{m_a m_b}} \int_0^\infty S(E)\ \exp(-2\pi\eta)\ \exp\left(-11.605 \frac{E}{T_9}\right) \mathrm{d}E \quad [\mathrm{cm^3 mol^{-1} s^{-1}}] \tag{2.11}$$

where $S(E)$ is the S-factor in MeV b.

Equations 2.10 and 2.11 highlight two significant energy-dependent contributions to the thermonuclear reaction rate. The first is related to the thermal energy available to the nuclei, described by the exponent of the Maxwell-Boltzmann distribution: $\exp(-E/kT)$. The second is the probability of penetrating the Coulomb barrier imposed by the positively charged nuclei, which varies as the Gamow factor: $\exp\left(-\sqrt{1/E}\right)$. By convoluting these two functions a range of energies is obtained which represents the energy region where the reaction rate is maximised. This convoluted function is known as the Gamow peak, and an example is shown by the solid line in figure 2.1 for the ^{6}Li + p reaction occurring at $T = 0.8$ GK, a typical temperature encountered during SBBN nucleosynthesis. Arbitrarily scaled contributions from the Maxwell-Boltzmann and Gamow factors are shown as short-dashed and long-dashed curves, respectively. The Gamow peak shown is centred at $E \sim 0.21$ MeV, well within the energy range accessible with the LUNA-400 accelerator (chapter 5).

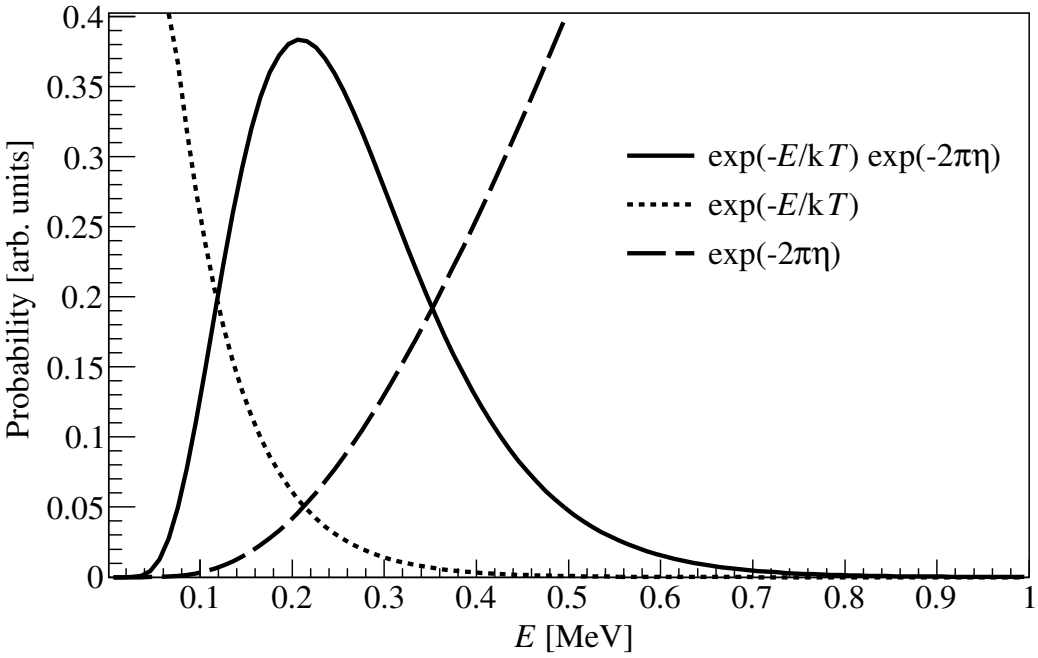

Figure 2.1 *Gamow peak (solid line) for the ^6Li + p reaction at SBBN relevant temperature $T = 0.8$ GK. The Maxwell-Boltzmann (short-dashed) and Coulomb repulsion (long-dashed) components are also shown.*

2.1.1 Electron Screening Effects

The S-factor in equation 2.9 is defined for bare nuclei: both nuclei are assumed to be fully stripped of their electrons. In typical laboratory measurements, the target nuclei are surrounded by electrons which have the effect of screening the positive nuclear charge from the incoming positively-charged ion beam. A diagram of the electron screening effect on the target atom's Coulomb barrier is shown in figure 2.2. For low bombarding energies, these electron screening effects significantly enhance the cross section and must be corrected before calculating reaction rates.

A widely-used approach, reported in [26] and expanded upon in [27], applies the Born-Oppenheimer approximation within a simplified (adiabatic) model. The model assumes the motion of the interacting nuclei is much slower than that of the atomic electrons, such that during the collision the electrons have sufficient time to readjust themselves. The model also assumes that the electron-shielding effect on the Coulomb barrier height is proportional to the ratio of nuclear-to-atomic radii ($R_{\rm nucl}/R_{\rm atom} \sim 10^{-5}$), such that the enhancement ratio $f_{\rm atom}$ is given by:

$$f_{\rm atom} = \frac{\sigma(E+U_e)}{\sigma(E)} = \frac{E}{E+U_e}\frac{\exp\left[2\pi\eta(E)\right]}{\exp\left[2\pi\eta(E+U_e)\right]} \tag{2.12}$$

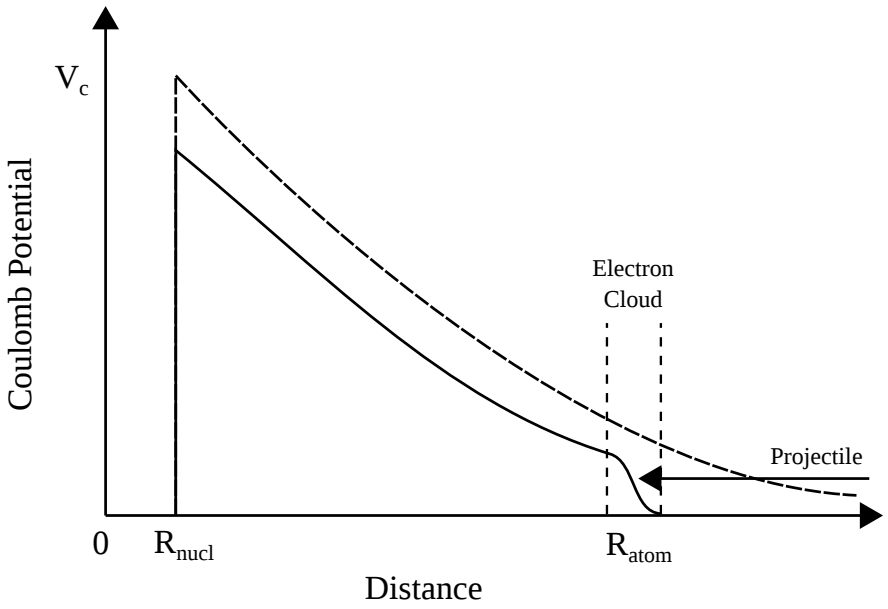

Figure 2.2 *A diagram showing the effect on the Coulomb barrier from atomic electrons screening the nuclear charge from incoming ions, reproduced from [24]. At low projectile energies the Coulomb barrier is reduced by the electron cloud, thereby enhancing the reaction cross section.*

where U_e is the screening potential, $2\pi\eta(E)$ is the Sommerfield parameter, defined in equation 2.10, at energy E. The enhancement ratio becomes significant for energies approaching the screening potential, typically $E/U_e \leq 100$. For ^{6}Li + p this corresponds to $E = 20$ keV.

2.2 Direct Capture and Resonant Reaction Mechanisms

The non-resonant component of the ^{6}Li(p,γ)^{7}Be reaction takes place through the direct capture (DC) reaction mechanism. A formalism of the DC mechanism is provided in reference [28]. An energy level diagram showing the DC reaction mechanism alongside the equivalent diagram for a resonant reaction is shown in figure 2.3. The DC process involves prompt emission of a gamma ray from the formation of C through the a + b entrance channel. The energy of these gamma rays is equal to the energy difference between the entrance channel and the state populated in C.

The level scheme of ^{7}Be is shown in figure 2.4. The energies, spin-parities, and relative transition probabilities are quoted from reference [30]. Gamma rays

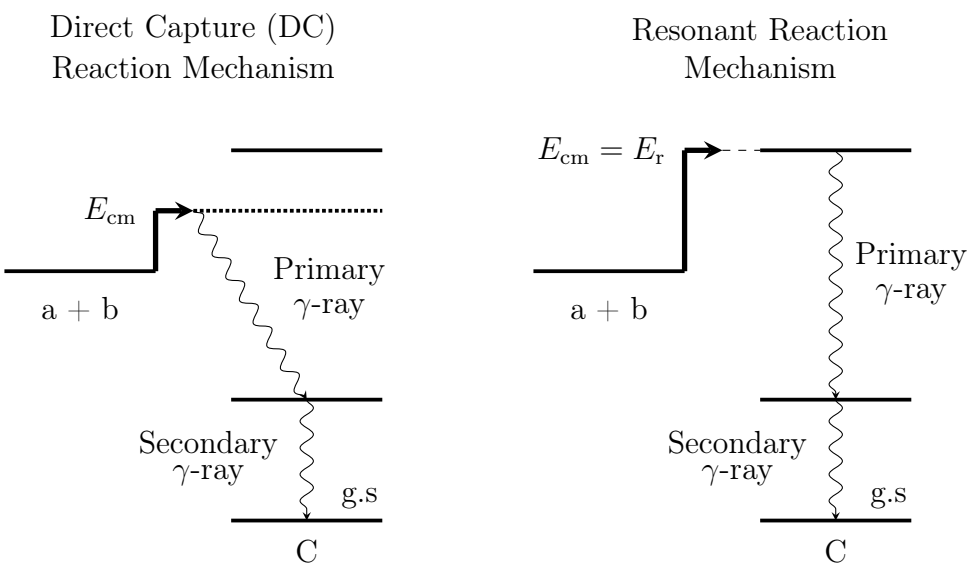

Figure 2.3 *Energy levels showing (left) direct capture (DC) and (right) resonance reaction mechanisms (from [29]).*

associated with the formation of ^{7}Be are referred to as *primary* gamma rays, and those emitted from the subsequent decay of excited states are referred to as *secondary* gamma rays. This distinction is used in the discussion of the ^{6}Li(p,γ)^{7}Be reaction data analysis (chapter 8). The primary and secondary gamma-ray transitions are marked by the red arrows. The next chapter will cover the current status of the ^{6}Li(p,α)^{3}He and ^{6}Li(p,γ)^{7}Be reaction cross sections reported in the literature.

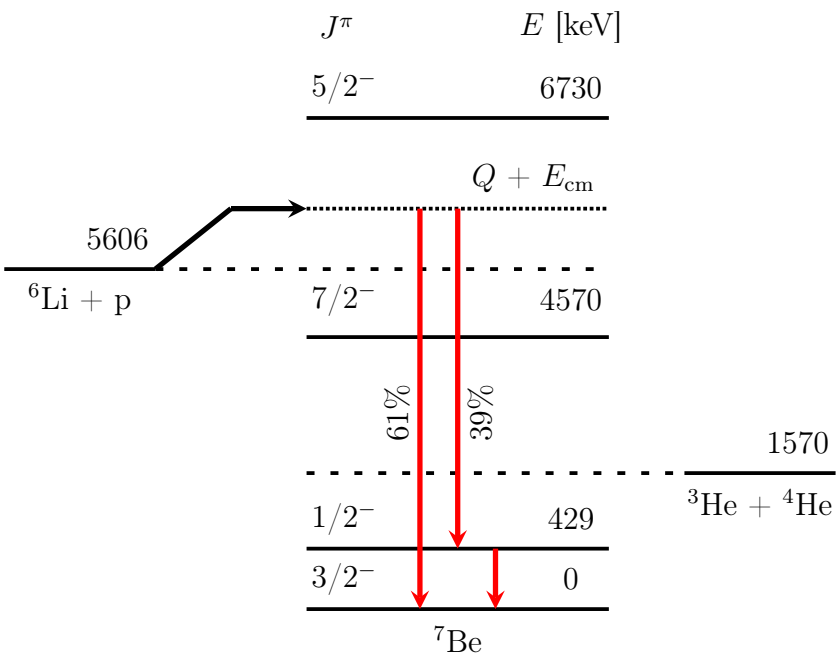

Figure 2.4 *The ^{7}Be level scheme with the ^{6}Li + p entry channel and ^{3}He + ^{4}He exit channel adapted from [30]. The ^{6}Li(p,γ)^{7}Be reaction proceeds via direct capture either directly to the ground state (61%) or through the 1^{st} excited state (39%).*

Chapter 3

Current Status on the ^{6}Li(p,α)^{3}He and ^{6}Li(p,γ)^{7}Be Reactions

This chapter summarises the key results available in the literature for the ^{6}Li(p,α)^{3}He and ^{6}Li(p,γ)^{7}Be reactions.

3.1 The ^{6}Li(p,α)^{3}He Reaction

The earliest published work on the ^{6}Li(p,α)^{3}He reaction cross section was reported by Bowersox in 1939 [31]. Since this measurement the ^{6}Li(p,α)^{3}He reaction S-factor has been extensively studied [32–42]. A summary of selected literature on experimental and theoretical ^{6}Li(p,α)^{3}He reaction S-factors is provided in table 3.1.

Figure 3.1 shows a plot of selected literature S-factors vs $E_{\rm cm}$ for energies at astrophysical interest. A direct measurement performed by Engstler *et al.* and reported in 1992 [37] measured the ^{6}Li(p,α)^{3}He reaction cross section down to the lowest $E_{\rm cm}$ (10 keV) to date. Engstler *et al.* report an extrapolated $S(0) = 3.09(23)$ MeV b, within 1σ of previous values reported in [33–36].

The ^{6}Li(p,α)^{3}He reaction cross section has also been calculated using a four-cluster microscopic model, the results of which were published by Arai *et al.* in 2002 [38]. The theoretical cross sections are in good agreement with those reported in the literature for the energy range $E_{\rm cm} = 30 - 1000$ keV. At lower energies disagreement arises due to the theory's omission of electron screening

Table 3.1 *Summary of previous work on the $^6Li(p,\alpha)^3He$ reaction.*

Reference	E_{cm} Range [keV]	Astrophysical S-factor $S(0)$ [MeV b]	Approach
Bowersox 1939 [31]	171 – 343		Direct
Gemeinhardt 1966 [32]	43 – 163	3.2 in [34]	Direct
Spinka 1971 [33]	129 – 272	3.0 (2.85 in [34])	Direct
Shinozuka 1979 [34]	107 – 600	3.0	Direct
Elwyn 1979 [35]	116 – 2546	3.145	Direct
Kwon 1989 [36]	103 – 433	2.97(3)	Direct
Engstler 1992 [37]	Gas Target: 11 – 500 Solid Target: 10 – 155	3.09(23)	Direct
Arai 2002 [38]	10 – 3000		Theoretical[1]
Cruz 2005 [39]	28 – 73	3.00(8)	Direct
Cruz 2008 [40]	90 – 580	3.52(8)	Direct
Lamia 2013 [41]	10 – 400	3.44(35)	Indirect[2]
He 2013 [42]	87 – 207		Direct[3]

[1] Four-Cluster Microscopic Model
[2] Trojan Horse ^{2}H(^{6}Li,$\alpha\,^3$He)n
[3] Scaled to Cruz 2008

effects (discussed in chapter 2) at low energies ($E_{cm} < 30$ keV). The experimental studies reported by Engstler *et al* in 1992 [37] and Cruz *et al.* in 2005 [39] confirmed the low-energy experimental (screened) S-factor trend significantly deviates from the bare S-factor for $E_{cm} < 45$ keV.

A later study by Cruz *et al.* reported in 2008 [40] extended the energy range studied by Cruz 2005 up to $E_{cm} = 580$ keV. The Cruz 2005+2008 ^{6}Li(p,α)^{3}He reaction S-factors are in strong agreement with those reported by previous measurements and also reduce the experimental S-factor uncertainties by a factor ~ 2 across $E_{cm} = 28 - 580$ keV.

A recent paper published in 2013 by Lamia *et al.* [41] reports the results of the indirect Trojan-Horse method for $E_{cm} = 10 - 400$ keV, with a quoted bare S-factor $S(0) = 3.44$ MeV b. This S-factor is in agreement with the direct results reported in Elwyn *et al.* [35], Engstler *et al.* [37], and Cruz *et al.* 2008 [40], and

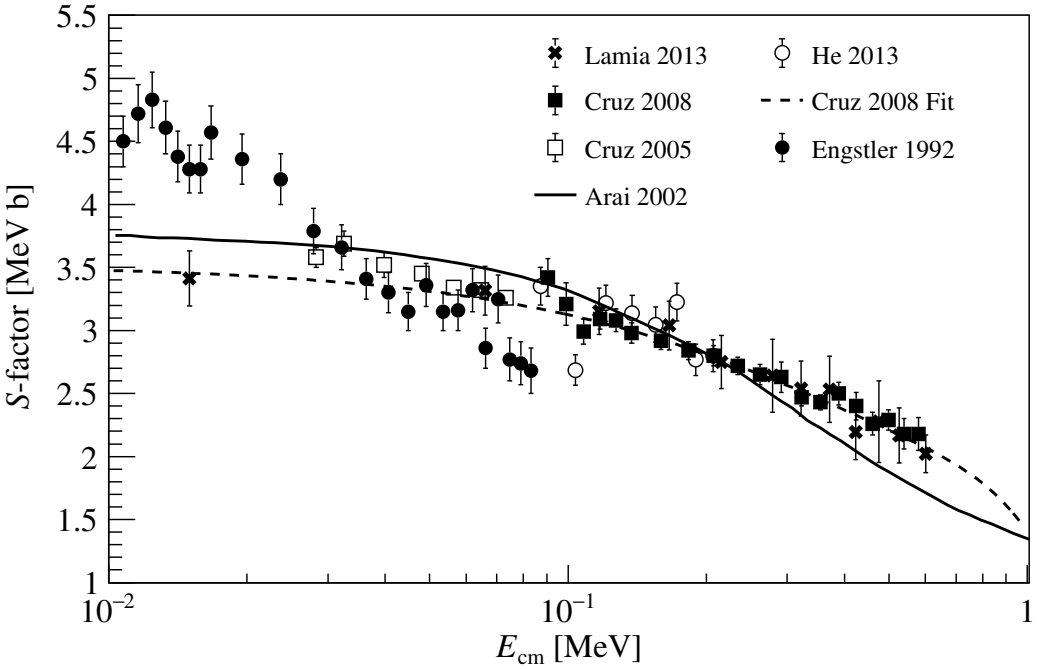

Figure 3.1 *Summary of ^{6}Li(p,α)^{3}He reaction S-factors vs E_{cm} reported in the literature. Experimental data across $E_{cm} = 30 - 600$ keV are in good agreement with each other and the theory by Arai et al. [38]. As a result of non-negligible electron screening effects for $E_{cm} < 30$ keV the measured data deviates from the theory, fit of Cruz et al. [40] data, and Trojan horse measurement (Lamia et al. [41]).*

also the theoretical (bare) model reported in Arai *et al.* [38]. The most recent direct measurement of the ^{6}Li(p,α)^{3}He astrophysical S-factor was published by He *et al.* in 2013 [42], which reports S-factors scaled to those of Cruz *et al.* 2008 at $E_{\rm cm} = 206$ keV. The current status of the literature presents a consistent and well-understood S-factor for the ^{6}Li(p,α)^{3}He reaction at energies of astrophysical interest.

3.2 The ^{6}Li(p,γ)^{7}Be Reaction

Unlike the ^{6}Li(p,α)^{3}He reaction, the situation for the ^{6}Li(p,γ)^{7}Be reaction is rather more controversial. The earliest published measurement of the ^{6}Li(p,γ)^{7}Be reaction cross section was reported by Bashkin and Carlson in 1955 [43]. They measured the DC (direct capture) transitions to the ground state (DC $\rightarrow$ 0 keV) and to the first excited state (DC $\rightarrow$ 429 keV) of ^{7}Be, reporting branching ratios of 65(5)% and 35(5)%, respectively. Table 3.2 summarises the key findings of the

Table 3.2 *Summary of previous work on the $^6Li(p,\gamma)^7Be$ reaction.*

Reference	E_{cm} Range [keV]	$\sigma_{tot}(800)$ [µb]	Astrophysical S-factor $S(0)$ [eV b]	Approach
Bashkin 1955 [43]	154 – 356			Direct
Switkowski 1979 [30]	134 – 1006	2.9(3)		Direct
Barker 1980 [44]	9 – 1713	2.95	$S(10\,\text{keV}) = 106$	Theoretical[1]
Cecil 1992 [45]	34 – 154		g.s: 39(8) 429 keV: 26(6)	Direct
Arai 2002 [38]	25 – 1200		105	Theoretical[2]
Prior 2004 [46]	69 – 111		79(18)	Direct
Huang 2010 [47]	0 – 1200		g.s: 66.8 429 keV: 32.7	Theoretical[3]
He 2013 [42]	47 – 250		Not Reported	Direct
Igamov 2016 [48]	10 – 1100		70(12)	R-matrix fits
Dong 2017 [49]	0 – 1800		88.34	Theoretical[4]
Gnech 2019 [50]	0 – 1000		103.5(4.5)	Theoretical[5]

[1] Direct Capture Potential Model
[2] Four-Cluster Microscopic Model
[3] Single-particle Model
[4] Gamow Shell Model with Coupled-Channel
[5] Cluster Model

^{6}Li(p,γ)^{7}Be reaction in the literature, and figure 3.2 shows a plot of literature S-factors across the astrophysically relevant E_{cm} range.

The work by Bashkin and Carlson was improved upon by Switkowski *et al.* in 1979 [30], who report a weighted average of the ^{6}Li(p,γ)^{7}Be branching ratio of 61(2)% for the DC $\rightarrow$ 0 keV and 39(2)% for the DC $\rightarrow$ 429 keV transitions. Switkowski *et al.* also report direct measurements of the cross section across $E_{cm} = 134 - 1006$ keV. These measurements were later compared with a direct capture potential model, the results of which were published by Barker in 1980 [44]. This model predicts a total cross section at $E_{cm} = 800$ keV of $\sigma_{tot} = 2.95$ µb, in excellent agreement with the measured 2.9(3) µb from Switkowski *et al.* [30].

A direct measurement performed by Cecil *et al.* in 1992 [45] aimed to extend the S-factor measurements to lower energies than those covered by Switkowski

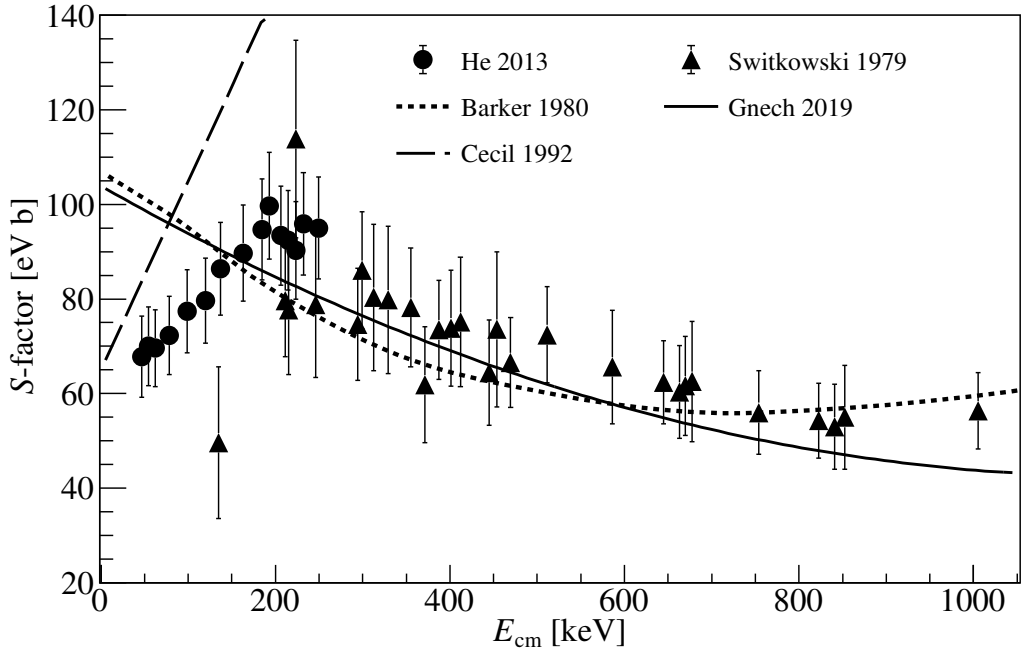

Figure 3.2 *Summary of $^6Li(p,\gamma)^7Be$ reaction S-factors vs E_{cm}. Experimental data from Switkowski et al. [30] are in agreement with theory from Barker [44] and Gnech and Marcucci [50]. However the measured values from He et al. [42] display a downwards trend in S-factor at lower energies, which is supported by Cecil et al. [45] and denied by Barker [44] and Gnech and Marcucci [50].*

et al., specifically $E_{\mathrm{cm}} = 34 - 154$ keV. Cecil *et al.* report a concurrent measurement of the ^{6}Li(p,α)^{3}He and ^{6}Li(p,γ)^{7}Be reactions. Specifically, they measured the gamma-ray-to-charged-particle branching ratios and gamma-ray angular distributions. They then deduced S-factors for the ^{6}Li(p,γ)^{7}Be reaction represented in figure 3.2 by the long-dashed line, in disagreement with the Switkowski *et al.* measurement and Barker theory (dotted line in figure 3.2).

The most recent measurement of the ^{6}Li(p,γ)^{7}Be reaction cross section was reported by He *et al.* in 2013 [42]. The experiment was performed at the Institute of Modern Physics at Lanzhou (China) using an electron cyclotron resonance (ECR) ion source at the 320 kV high voltage platform. Proton beams ($E_{\mathrm{p}} = 70 - 300$ keV) of currents up to 30 µA were impinged onto Li_2O (lithium oxide) solid targets (^{6}Li-enrichment of 95% and thickness 35 µg/cm^2). Charged particles (^{3}He and ^{4}He) and gamma rays from the ^{6}Li(p,α)^{3}He and ^{6}Li(p,γ)^{7}Be reactions were measured concurrently using an Ortec ion-implanted silicon detector and a HPGe (High Purity Germanium) clover detector, respectively. The ^{6}Li(p,γ)^{7}Be

reaction S-factor is reported for $E_{\rm cm} = 47 - 250$ keV, and whilst at ~ 200 keV it agrees with previous values reported by Switkowski *et al.*, the S-factor observed by He *et al.* displays a positive slope at lower energies, reminiscent of the trend reported by Cecil *et al.* but about 23% (43%) lower at $E_{\rm cm} = 47$ keV (193 keV).

The trend in S-factor reported by He *et al.* is puzzling because the reaction at these low energies is expected to occur only via the direct capture mechanism - no excited state has been observed in ^{7}Be at $E_{\rm x} \sim 5800$ keV (figure 2.4). The S-factors at low energies would be expected to follow the trend calculated by Barker [44] and experimentally verified by Switkowski *et al.* [30]. He *et al.* suggest their S-factor trend is reproduced by a resonance at $E_{\rm r} = 195$ keV with either $J^{\pi} = {}^{1}/_{2}^{+}$ or ${}^{3}/_{2}^{+}$ (as deduced from an R-matrix fit). A later paper by Igamov *et al.* published in 2016 [48] reports an improved R-matrix fit of the He *et al.* data, which supports the J^{π} assignment of either ${}^{1}/_{2}^{+}$ or ${}^{3}/_{2}^{+}$.

Dong *et al.* reported in 2017 [49] Gamow Shell Model calculations (with Coupled Channel) of the S-factor across $E_{\rm cm} = 0 - 1800$ keV. The model does not reproduce the resonance-like structure of the low energy S-factor observed by He *et al.*, and the theoretical zero-energy S-factor $S(0) = 88.34$ eV b calculated by Dong *et al.* is more than 1σ larger than the value of 70.2(12.0) eV b reported by Igamov *et al.*. The most recent theory by Gnech and Marcucci published in 2019 [50] uses the cluster model to describe the ^{6}Li + p interaction. They calculated angular distributions for the DC $\rightarrow$ 0 keV and DC $\rightarrow$ 429 keV transitions across proton $E_{\rm lab} = 0 - 1000$ keV. In addition Gnech and Marcucci quote $S(0) = 103.5(4.5)$ eV b, in excellent agreement with earlier theoretical values reported by Barker [44] and Arai *et al.* [38].

In the current literature there is a disagreement over the S-factor low energy trends determined from experiment and theory (figure 3.2), with different theoretical models either supporting or denying the existence of the $E_{\rm r} = 195$ keV resonance. Recall the Gamow peak relevant to SBBN is centred on $E_{\rm cm} \simeq 210$ keV (figure 2.1): close in energy to the resonance proposed by He *et al.*. The existence of this resonance requires independent experimental validation, and was the motivation of the present study which measured the ^{6}Li(p,γ)^{7}Be reaction cross section across the astrophysically relevant energies $E_{\rm cm} = 60 - 320$ keV. The experimental approach applied to calculate reaction cross sections from empirical yields is covered in the next chapter.

Chapter 4

Experimental Approach

This chapter provides the formalism required for extracting cross sections from measurements performed during a nuclear physics experiment.

4.1 Yields and Non-Resonant Cross Sections from Charged-Particle Reactions

To calculate a reaction rate, the cross section is required. The ^{6}Li(p,α)^{3}He and ^{6}Li(p,γ)^{7}Be reaction cross sections can be determined from experimentally measured yields. Experiments are performed by bombarding a target with a charged-particle beam, identifying the reaction products, and extracting a number of observed products. For this study charged particles (^{3}He and ^{4}He) and gamma rays were detected from the ^{6}Li(p,α)^{3}He and ^{6}Li(p,γ)^{7}Be reactions, respectively. For the energy range of interest ($E_{\mathrm{cm}} = 60-320$ keV) there are no well-established resonances reported for either reaction and so only the formalism for non-resonant cross sections will be described here.

The general empirical definition of the cross section for a nuclear reaction is repeated (from chapter 2) here:

$$\sigma = \frac{N_{\mathrm{r}}}{N_{\mathrm{t}} N_{\mathrm{b}}} \tag{4.1}$$

where N_{r} is the number of reactions over a time range, N_{t} the number of target atoms per unit area, and N_{b} the number of projectiles incident on the target over

the time range. The experimental yield, valid for all types of nuclear reactions, is defined as:

$$Y = \frac{N_{\mathrm{r}}}{N_{\mathrm{b}}} = \frac{N_{\mathrm{peak}}}{\eta\, b\, W\, N_{\mathrm{b}}} \tag{4.2}$$

where N_{peak} is the net counts from the detected radiation, η is the detector efficiency, b is the branching ratio, and W is the angular distribution.

Ultimately we want to convert the experimental yield to a cross section. The conversion should consider effects such as target properties (thickness, stoichiometry, and composition), beam fluctuations, and variations in the cross section itself. Two approaches relevant to this study, thin target and median energy, will now be presented. In our study the median energy approach was used to determine the present cross sections, however this method required cross sections calculated using the thin target case as an input.

The choice of approach depends on the physics of the beam interacting with the target. As the beam traverses the target it will deposit energy in a given "slice" of the target, and a certain number of ejectiles may be emitted as a consequence of the interaction between projectile and target nuclei. This interaction is dependent on two factors: the reaction cross section and the energy loss of the beam through the target thickness. The cross section may not be well-understood prior to the measurement. On the other hand the energy loss can be calculated using empirical stopping power tables, for example provided by SRIM-2013 [51]. As charged particles travel through matter they lose energy from inelastic scattering with electrons of the absorber atoms. Whilst the energy loss of individual ions has a statistical nature, the total energy loss does not fluctuate significantly for a given material [52]. It is therefore possible to quote an average stopping power, ϵ, for a given projectile ion incident on a material, which describes the energy loss $\mathrm{d}E$ of the ion as it travels through a thin slice of the target material $\mathrm{d}x$ [23]:

$$\epsilon = -\frac{1}{N}\frac{\mathrm{d}E}{\mathrm{d}x} \tag{4.3}$$

where N is the number of absorber atoms in the material. The stopping power typically has units of eV cm^2/atom.

For targets containing different isotopes, the definition of the stopping power is approximated by taking a weighted average of the individual stopping powers scaled to the fraction of electrons belonging to each isotope. This approximation is called Bragg's rule [53]. This total stopping power is calculated using knowledge

of the isotopic composition and individual stopping powers of each isotope [24]:

$$\epsilon_{\text{tot}} = \frac{1}{N_{\text{C}}} \left(\frac{\mathrm{d}E}{\mathrm{d}x} \right)_{\text{C}} = \sum_i n_i \frac{1}{N_i} \left(\frac{\mathrm{d}E}{\mathrm{d}x} \right)_i \tag{4.4}$$

where N_{C} is the number density of the compound, n_i is the number of a given target isotope per molecule and N_i the number density of that isotope. This stopping power will herein be referred to as the total stopping power and is used to determine the energy lost by the beam ΔE as it traverses the target.

4.1.1 Thin Target Case

The thin target case assumes the energy loss ΔE of the beam through the target is negligible and the reaction cross section σ is constant, thus the experimental yield is directly proportional to the cross section [23]:

$$Y(E_{\text{lab}}) = \sigma(E_{\text{lab}}) \, \frac{\Delta E(E_{\text{lab}})}{\epsilon_{\text{eff}}(E_{\text{lab}})} \tag{4.5}$$

where $Y(E_{\text{lab}})$ is the experimental thin-target yield at a given beam energy (laboratory frame), $\sigma(E_{\text{lab}})$ is the reaction cross section, ΔE is the energy loss of the beam as it traverses the target, and ϵ_{eff} is the effective stopping power introduced here to describe the slowing down of the beam as it interacts with the nuclei directly involved in the reaction contributing to the yield, *i.e.* the active nuclei. The effective stopping power is calculated as [24]:

$$\epsilon_{\text{eff}} = \epsilon_X + \sum_i \frac{N_i}{N_X} \epsilon_i \tag{4.6}$$

where ϵ_X is the stopping power of the active nuclei. For example a Li_2WO_4 compound with a lithium to tungsten to oxygen ratio 2:1:4 has an effective stopping power (with lithium the active nuclei):

$$\epsilon_{\text{eff}} = \epsilon_{\text{Li}} + \frac{1}{2}\epsilon_{\text{W}} + \frac{4}{2}\epsilon_{\text{O}} \tag{4.7}$$

Observe that since the stopping power is dependent on the electrons surrounding the nuclei we neglect the isotopic ratio of a given element, *e.g.* this calculation uses naturally occurring lithium composed of $\sim 92\%$ ^{7}Li and $\sim 8\%$ ^{6}Li [54].

The assumption of a constant cross section through the target thickness means the

reactions are occurring with equal "probability" across the entire target thickness. Therefore the energy assigned to the measured cross section is most accurately represented by the energy of the beam in the centre of the target: $E_{\text{ass}} = E_{\text{lab}} - \Delta E/2$. For calculations of the reaction rate (and comparisons with literature) the energy assigned to the cross section is typically converted to the centre-of-mass frame:

$$E = \left(E_{\text{lab}} - \frac{\Delta E}{2}\right) \frac{m_{\text{tar}}}{m_{\text{tar}} + m_{\text{proj}}} \tag{4.8}$$

where m_{tar} is the target's mass and m_{proj} is the projectile's mass.

4.1.2 Median Energy Approach

In the case of a thick target it is no longer valid to assume a constant cross section and stopping power through the target thickness. Instead of equation 4.5 the experimental yield is now related to the cross section by:

$$Y(E) = \int_{E_{\text{lab}}-\Delta E}^{E_{\text{lab}}} \frac{\sigma(E)P(E)}{\epsilon_{\text{eff}}(E)} \mathrm{d}E \tag{4.9}$$

where $P(E)$ is the target profile, which describes the distribution of the target nuclei of interest through the target thickness. The target profile is normalised such that $P(E)$ takes values between $0-1$, where a perfectly homogeneous target has $P(E) = 1$ at all energies. Empirical profiles specific to this study are presented later in chapter 6.

The cross section may no longer be solved analytically; however, the energy dependence may be deconvolved using a numerical approach. Various deconvolution procedures are available in the literature, for example in the Brune and Sayre paper published in 2013 [55] or the Ph.D. thesis of C.G. Bruno [56], and the most common practices are referred to as *effective*, *mean*, and *median* energy approaches. These different approaches are all specific solutions to the general treatment of the cross-section deconvolution. The aim of this general approach is to rewrite equation 4.9 as:

$$Y(E) = \int_{E_{\text{lab}}-\Delta E}^{E_{\text{lab}}} \frac{\sigma_{\text{ex}}(E)P(E)}{\epsilon_{\text{eff}}(E)} \mathrm{d}E = \sigma_{\text{ex}}(\tilde{E}) f \int_{E_{\text{lab}}-\Delta E}^{E_{\text{lab}}} \frac{P(E)}{\epsilon_{\text{eff}}(E)} \mathrm{d}E \tag{4.10}$$

where $\tilde{E}$ is the deconvolved energy, σ_{ex} is the experimental cross section, and we

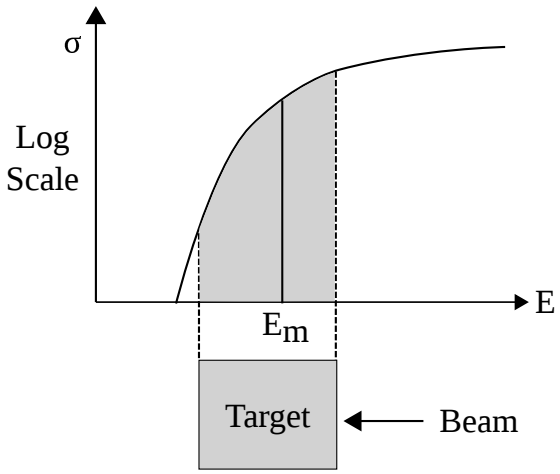

Figure 4.1 *Diagram depicting the median energy, E_m, in the context of cross section deconvolution. By definition an energy E_m splits the yield (integral of the cross section over energy) into two equal parts.*

introduce the correction factor f [55]:

$$f = \frac{\int_{E_{\mathrm{lab}}-\Delta E}^{E_{\mathrm{lab}}} \sigma_{\mathrm{pr}}(E) P(E) \left[\epsilon_{\mathrm{eff}}(E)\right]^{-1} \mathrm{d}E}{\sigma_{\mathrm{pr}}(E) \int_{E_{\mathrm{lab}}-\Delta E}^{E_{\mathrm{lab}}} P(E) \left[\epsilon_{\mathrm{eff}}(E)\right]^{-1} \mathrm{d}E} \tag{4.11}$$

where a prior cross section, σ_{pr}, is defined. The mean and median deconvolution procedures require the correction factor f to be evaluated and applied, whereas the effective energy approach is defined for $f = 1$.

For the present study it was decided to use the median energy approach as it is not prone to ambiguities in energy assignment close to resonances, unlike the effective energy [55]. The median energy approach requires the prior cross section, σ_{pr}, as a starting point, for which the thin-target cross section, equation 4.5, is typically used. The median energy is defined as the energy, E_{m}, at which half of the experimental yield (integral of the cross section over energy) is split into two equal parts:

$$\int_{E_{\mathrm{lab}}-\Delta E}^{E_{\mathrm{lab}}} \frac{\sigma_{\mathrm{pr}}(E) P(E)}{\epsilon_{\mathrm{eff}}(E)} \mathrm{d}E = 2 \int_{E_{\mathrm{m}}}^{E_{\mathrm{lab}}} \frac{\sigma_{\mathrm{pr}}(E) P(E)}{\epsilon_{\mathrm{eff}}(E)} \mathrm{d}E \tag{4.12}$$

A diagram depicting this definition is shown in figure 4.1.

The experimental cross section, $\sigma_{\mathrm{ex}}(E_{\mathrm{m}})$, is then calculated as [56]:

$$\sigma_{\mathrm{ex}}(E_{\mathrm{m}}) = \frac{Y(E)}{\int_{E_{\mathrm{lab}}-\Delta E}^{E_{\mathrm{lab}}} \frac{\sigma_{\mathrm{pr}}(E) P(E)}{\epsilon_{\mathrm{eff}}(E)} \mathrm{d}E} \sigma_{\mathrm{pr}}(E_{\mathrm{m}}) \tag{4.13}$$

The reliability of the deconvolution procedure is checked using the convergence test, expressed as:

$$M = \frac{\sigma_{\mathrm{ex}}(\bar{E}) \int \frac{\sigma_{\mathrm{pr}}(E)P(E)}{\epsilon_{\mathrm{eff}}(E)} \mathrm{d}E}{\sigma_{\mathrm{pr}}(\bar{E}) \int \frac{\sigma_{\mathrm{ex}}(E)P(E)}{\epsilon_{\mathrm{eff}}(E)} \mathrm{d}E} \sim 1 \tag{4.14}$$

where the number of iterations required for convergence is not quantitatively defined by the authors of [55], but typically should be quite low assuming a reasonable prior cross section is provided.

The median energy is evaluated as follows:

1. Use the prior cross section (σ_{pr}, corrected for electron screening) to determine E_{m} via equation 4.12.
2. Calculate the experimental cross section (σ_{ex}, corrected for electron screening) using equation 4.13 with the prior cross section and median energy as inputs.
3. Determine if convergence is reached, that is $M \sim 1$ is met for equation 4.14.
4. If convergence is not reached continue to repeat steps $1 - 3$ taking the experimental cross section as the new prior cross section until $M \sim 1$.

Once the cross section is determined, the S-factor can be calculated as previously defined in equation 2.9. The next chapter will now present the different components of the experimental setup at the Laboratory for Underground Nuclear Astrophysics (Gran Sasso, Italy) used in this study.

Chapter 5

Experimental Setup

A recent experimental campaign was performed at the Laboratory for Underground Nuclear Astrophysics (LUNA) to measure the ^{6}Li(p,α)^{3}He and ^{6}Li(p,γ)^{7}Be reactions at astrophysically relevant centre-of-mass (c.m) energies, $E_{\mathrm{cm}} = 60 - 320$ keV. This chapter presents the Laboratori Nazionali del Gran Sasso (LNGS) halls and the different components of the ^{6}Li experimental setup at LUNA, including the target chamber, detectors, and electronic chain.

5.1 LUNA-400 Accelerator and Beamline

The LNGS experimental halls are located under the Gran Sasso mountain (Italy). The overburden of rock (1400 m thick), equivalent to 3800 m of water, provides underground setups with natural shielding from cosmic-ray events: cosmic-ray muons are attenuated by six orders of magnitude, and cosmic-ray fluxes are reduced by over three orders of magnitude [57] with respect to the Earth's surface. The 400-kV accelerator (hereinafter LUNA-400) is located in a side tunnel as shown in figure 5.1.

The 400 kV electrostatic accelerator (from High Voltage Engineering Europe) is imbedded in a tank. To prevent sparking during operation the tank is filled with a gas mixture of N_2/CO_2 pressurised at 20 bar. The high voltage (HV) is generated by an Inline-Cockcroft-Walton power supply (located inside the tank), which is stabilised at the terminal (ion source) by both an RC-filter and an active feedback loop based on a chain of resistors [59]. This voltage (ion energy) stabilisation is

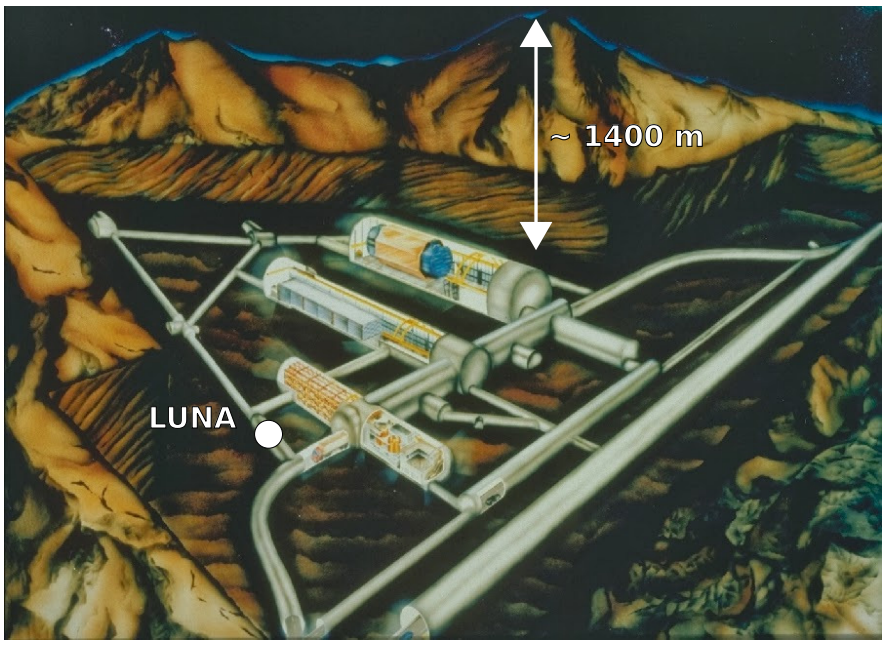

Figure 5.1 *Diagram of the LNGS experimental halls reproduced from [58]. The current location of the LUNA-400 accelerator is marked in white. The LNGS halls are naturally shielded from cosmic-ray events by the overburden of 1400 m thick rock.*

a key feature since the reaction cross sections vary more than exponentially with the beam energy. The LUNA-400 energy calibration of the accelerator follows to a ±0.3 keV accuracy:

$$E_{\text{lab}} = 0.9933(2) \left[\frac{\text{keV}}{\text{kV}}\right] (\text{TV} + \text{PV}) \text{ [kV]} - 0.41(5) \text{ [keV]} \tag{5.1}$$

where TV is the accelerating voltage applied to the high voltage terminal, and PV is the bias voltage applied to the anode (probe) of the ion source.

The radio-frequency ion source is mounted directly on the accelerator tube, where the gas inside the source (pressure $\sim 10^{-7}$ mbar) is excited to form an ion plasma confined by an axial magnetic field. The ions are extracted by an electrode mounted directly in the accelerator tube. The radio-frequency ion source provides ion beams of hydrogen (75% H^+) and He^+ with currents up to 1 mA and 500 µA, respectively. A photograph of the LUNA-400 accelerator with its tank opened and source switched on is shown in figure 5.2. The ions are accelerated into one of two beamlines: the first is used for gas-target experiments [10, 60, 61], and the second is used for solid-target experiments [62–64]. The ^{6}Li campaign used the second beamline for the duration of its measurements, and therefore the first beamline is not discussed further in this work.

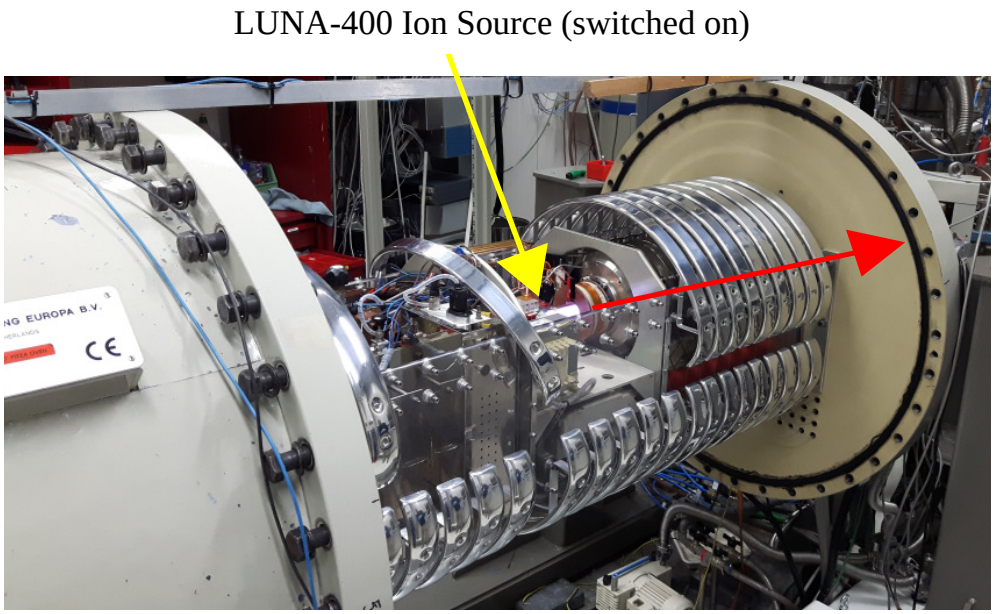

Figure 5.2 *Photograph of the ion source (switched on) located within the tank of the LUNA-400 accelerator. The red arrow indicates the beam direction.*

A simplified diagram of the LUNA-400 beamline used during the ^{6}Li campaign is shown in figure 5.3. Proton beams were used with energies $E_\mathrm{p} = 76 - 393$ keV ($E_\mathrm{cm} = 65 - 337$ keV). After extraction, the steerer magnet aligned the proton beam along its vertical axis and the quadrupole magnet focused the beam by adjusting its shape in the horizontal and vertical planes. A 45° bending magnet, mounted between the steerer and quadrupole, was switched off to ensure the proton beam continued towards the second beamline. A Faraday cup[1] (FC0) was used to monitor the beam current. The steerer and quadrupole settings were adjusted to optimise current on FC0, ensuring the beam was aligned prior to entering the second beamline.

A second 45° magnet was used to direct the beam into the second (solid-target) beamline. A wobbler magnet was used to make the beam oscillate in the horizontal and vertical direction for uniform irradiation of the target. The beam was collimated using two circular apertures: one upstream ($\Phi = 6$ mm) and the other downstream ($\Phi = 3$ mm) of the Faraday cup FC45. These apertures ensured the beamspot size was smaller than the target ($\Phi = 23$ mm) and no beam was being deposited on the target's frame. Care was taken to set the magnet parameters and aperture positions to maximise the beam current at FC45, thus

[1] A Faraday cup is a metal plate (usually cylindrical) used to collect ions in a vacuum. The ions excite electrons in the metal, which are subsequently collected allowing integration of the collected current.

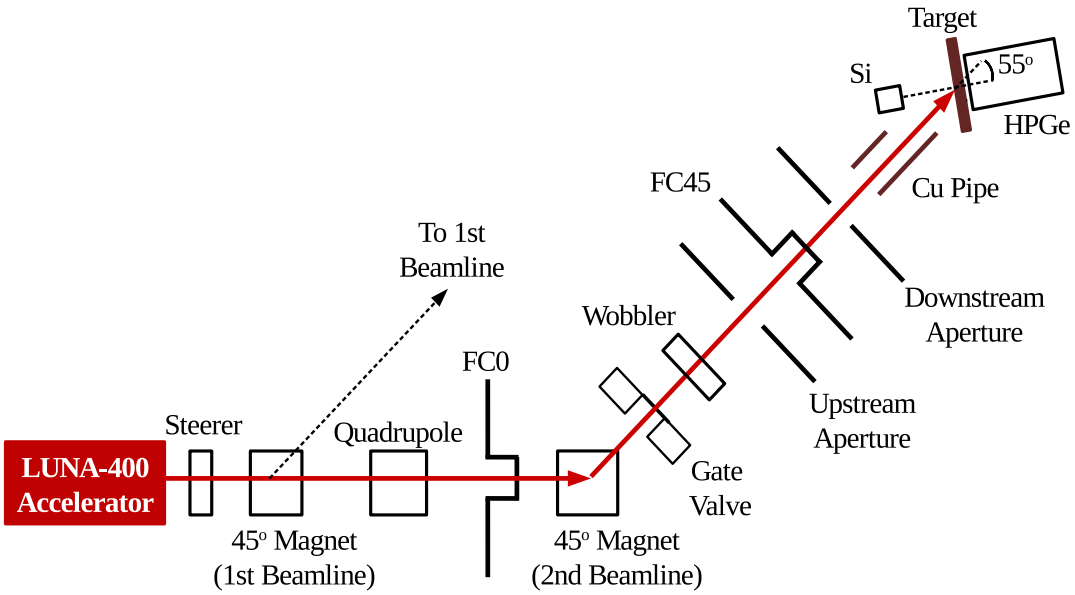

Figure 5.3 *Diagram of the LUNA-400 solid-target beamline used in the ^6Li campaign. The beam direction is marked by the red arrow. The beam travels through the second beamline to the solid-target chamber.*

ensuring the beam was constrained by the downstream aperture. During target changes the target chamber was vented to atmospheric pressure. The gate valve, interlocked for safety reasons, is open when making beam.

5.2 Target Chamber

A schematic diagram of the target chamber with relevant components is shown in figure 5.4. The focused proton beam entered the solid-target chamber through the 3 mm downstream aperture. The beam passed inside a hollow copper pipe before bombarding the target mounted at $\theta_{\text{lab}} = 55°$ to the beam axis. The vacuum pumps along the beamline were able to efficiently pump out light elements (hydrogen, helium), but not heavier contaminants (carbon dioxide, water) which could deposit themselves on the front layers of the target. To avoid deposition the copper pipe was cooled using liquid nitrogen (LN_2) and thus functioned as a cold trap for removal of heavy contaminants from the beamline. With this precaution the solid-target chamber was kept at a pressure of order 10^{-6} mbar.

A copper cable, placed in mechanical contact with the target chamber, collected the beam charge deposited on target. Prior to data collection checks were made to ensure the target chamber was insulated from the beamline and copper tube.

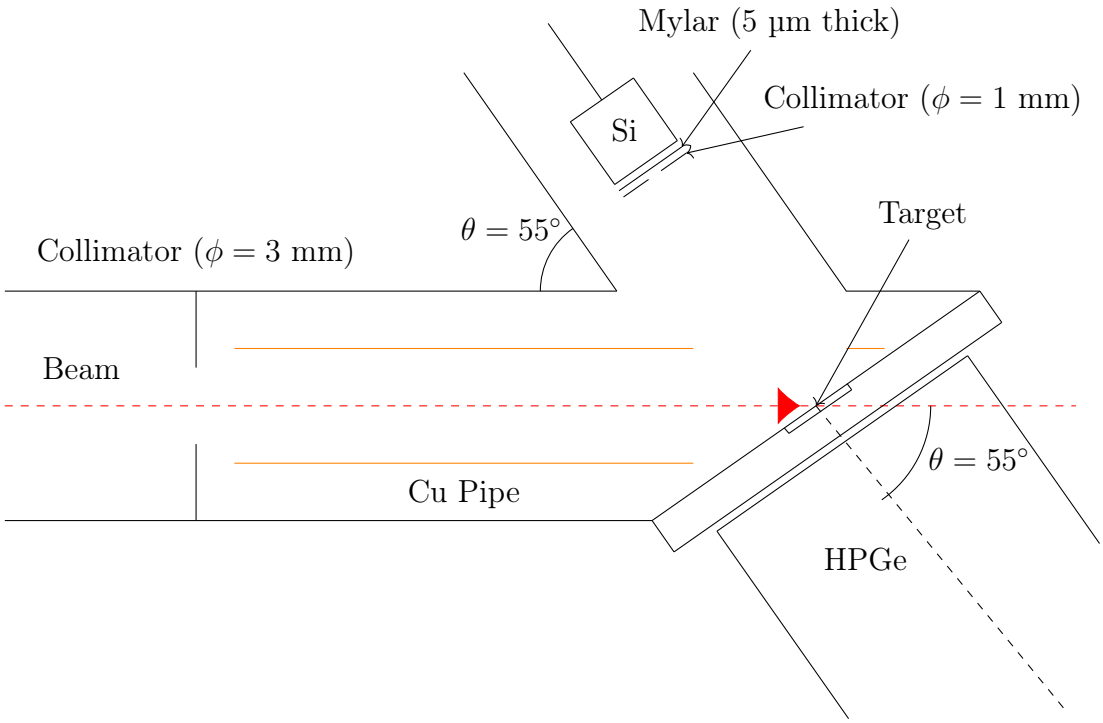

Figure 5.4 *Diagram of the ^{6}Li solid target chamber. The beam direction is indicated by the red arrow. The beam travels through a Cu pipe (biased for electron suppression and LN_2 cooled to remove contaminants) before impinging on the target mounted at 55°. Si and HPGe detectors are placed to measure the charged particles and gamma rays, respectively.*

During bombardment the target emits secondary electrons, causing a higher measured current compared to the actual rate of impinging ions. The copper pipe was biased to −300 V with respect to the beamline to suppress the secondary electrons, allowing an accurate current to be measured. Typical beam currents on target were $I = 40 - 140\,\mu A$.

5.3 Targets

The ^{6}Li-enriched (^{6}Li/^{nat}Li $\sim 95\%$) targets used in this study consisted of Li_2O, Li_2WO_4, or LiCl and are listed in table 5.1. Powder provided by the chemistry laboratory at LNL (Laboratori Nazionali di Legnaro) was used to make the Li_2O targets, while powder supplied by Sigma Aldrich [65] was used to make the Li_2WO_4 targets. Using a Leybold UNIVEX 350 evaporator at Atomki laboratories (Hungary), the Li_2O or Li_2WO_4 powder was evaporated onto a disc-

Table 5.1 *Targets used for the present study, sorted by ^6Li powder supplier. The number following the compound is an identification number. Nominal thicknesses, proton beam energy range covered, and total charge deposited are also listed.*

Powder Supplier	Nominal Composition	Nominal Thickness [µg/cm^2]	E_p Range [keV]	Total Charge [C]
LNL	Li_2O-7	40	$120 - 390$	7.7
	Li_2O-9	20	$120 - 390$	6.4
Sigma Aldrich	Li_2WO_4-1	130	$121 - 389$	6.5
	Li_2WO_4-3	100	$102 - 393$	9.1
	Li_2WO_4-4	100	$81 - 379$	12.4
Univ. Naples	LiCl	Infinite	$76 - 379$	8.7

shaped tantalum backing ($\Phi = 42$ mm, 0.25 mm thick). The powder was placed in a tantalum holder resistively heated by a direct current ($\sim$ 60 A), with the tantalum backing placed 10 cm above the holder to obtain a uniformly deposited layer. Care was taken to avoid contamination of the targets by performing the evaporation under vacuum (10^{-5} mbar). The process was controlled online by measuring the target thickness with a quartz thickness monitor.

The LiCl target was produced at the University of Naples Federico II by heating the compound powder directly onto a copper backing, and then leaving the target to cool and solidify into a thick film. After irradiation at LUNA all the targets were transported to HZDR, Dresden for target characterisation measurements, which are discussed in chapter 6.

During the LUNA beamtime the tantalum backings (containing the evaporated targets) were bolted onto one of two available brass target holders, shown in figure 5.5. Whilst these holders were measured to have the same physical dimensions, their downstream flanges were constructed of either stainless steel or aluminium, hereinafter referred to as target holders 1 and 2, respectively. This difference in material had a significant impact on gamma-ray detection efficiencies, as will be discussed in chapter 8.

Beam bombardment will naturally heat up the targets causing irreversible damage *i.e* altering target composition, stoichiometry, and/or reducing target thickness. To mitigate these unwanted effects the targets were cooled by pumping water through a cavity between the back of the target and the target holder's flange.

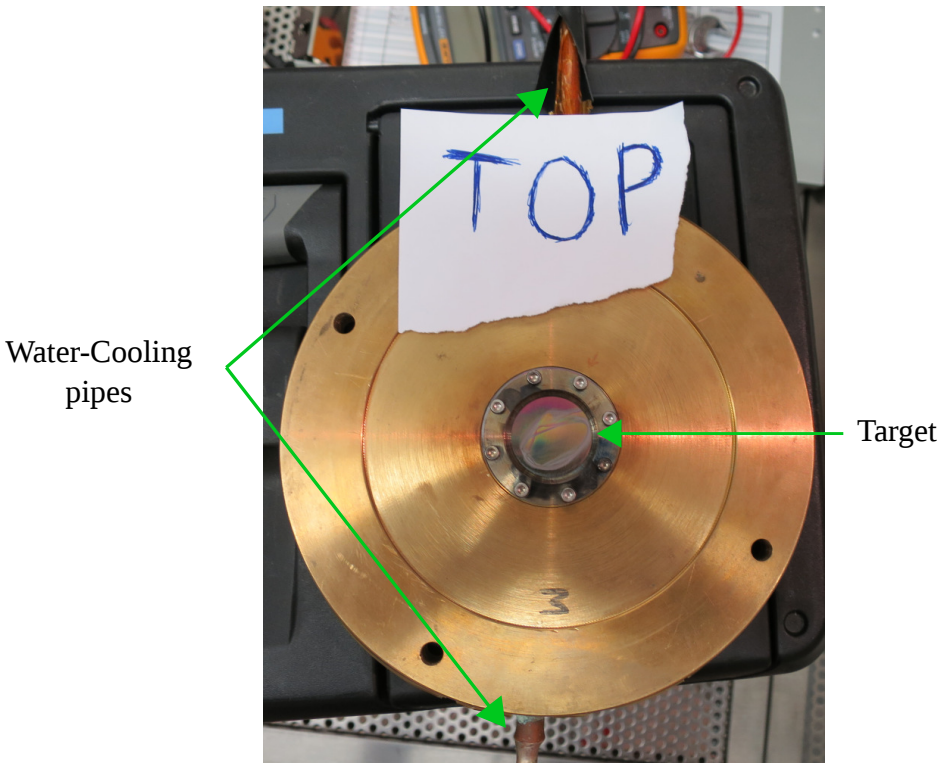

Figure 5.5 *One of the two target holders used in the LUNA ^{6}Li beam runs. The holder was water cooled during beam bombardment to minimise target degradation effects (see text for details). Water pipes are visible at the top and bottom of the holder.*

To facilitate water flow, pipes with Swagelock connectors were mounted on the top and bottom of the target holders.

5.4 Detectors

Silicon (Si) semiconductor detectors have excellent resolution and intrinsic efficiencies of 100%, and thus a small Si detector (Ortec model BU-014-025-100) was selected for measuring the ^{3}He and ^{4}He particles. A photograph of the Si detector setup is shown in figure 5.6. The active area of the Si detector was 25 mm^{2} with a depletion depth of 100 µm, sufficient to stop ^{3}He and ^{4}He particles at laboratory energies up to 11.2 and 12.5 MeV, respectively. To limit the intensity of the scattered proton beam impinging on the Si surface both a copper collimator with a central circular hole ($\phi = 1$ mm) and a 5 µm thick Mylar foil were positioned in front of the detector. The silicon detector was mounted

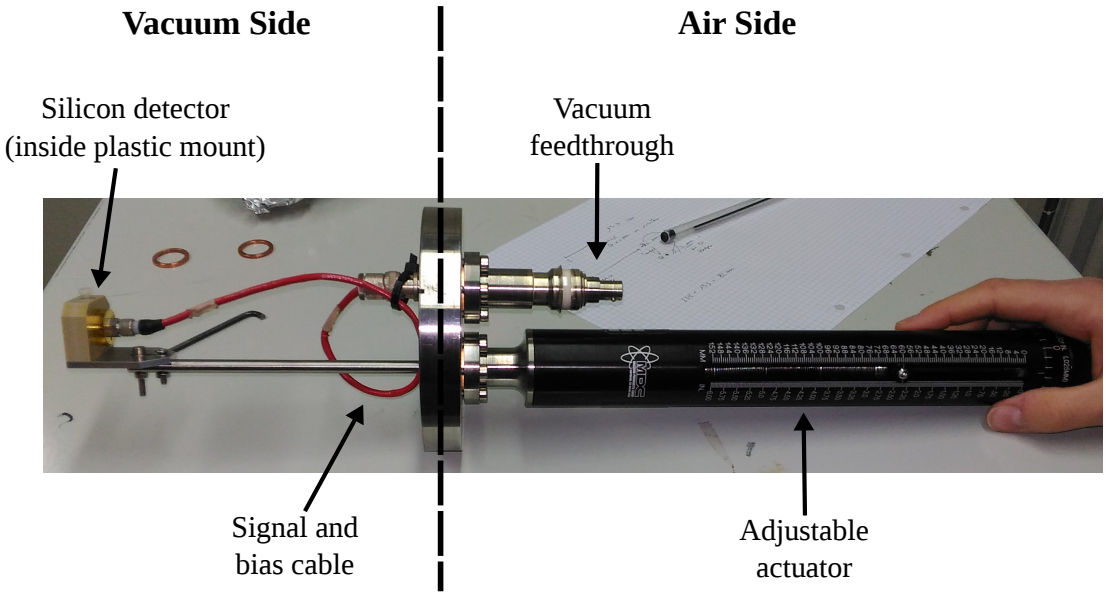

Figure 5.6 *Silicon detector setup for charged-particle detection. The detector is mounted on the arm of an actuator allowing adjustment of the target-to-silicon distance under vacuum. The detector is connected to the vacuum feedthrough by a single cable for both bias input and signal output.*

on an actuator[2] for linear movement and operated outside the target chamber. During the measurement the Si was positioned at a target-to-detector distance of either 9.3 or 10.3 cm.

A High Purity Germanium (HPGe) semiconductor detector (Ortec model GEM-120225-P-ST) was used to measure the gamma rays (E_γ ranging $429 - 6000$ keV) from the ^{6}Li(p,γ)^{7}Be reaction. A photograph of the HPGe detector setup is shown in figure 5.7. The detector had a resolution of $\simeq 0.2\%$ FWHM (Full-Width at Half-Maximum) for a ^{60}Co 1173 keV gamma ray, allowing the distinction of the ^{6}Li(p,γ)^{7}Be 429 keV gamma ray from background lines (*i.e* 511 keV from positron annihilation and 609 keV from ^{214}Bi). A cold finger inside the detector's neck kept the crystal in thermal contact with the LN_2 dewar. During operation the crystal was maintained at a temperature below 120 K by regularly filling the dewar with LN_2 ($\sim$ 77 K). To support the neck of the detector a block of lead surrounded the back of the crystal. To allow maximum counting statistics during beam bombardment, a distance of $\sim$ 1.7 cm was maintained between the target's centre and the end cap of the detector.

[2]An actuator is a device used to move a mechanism or system.

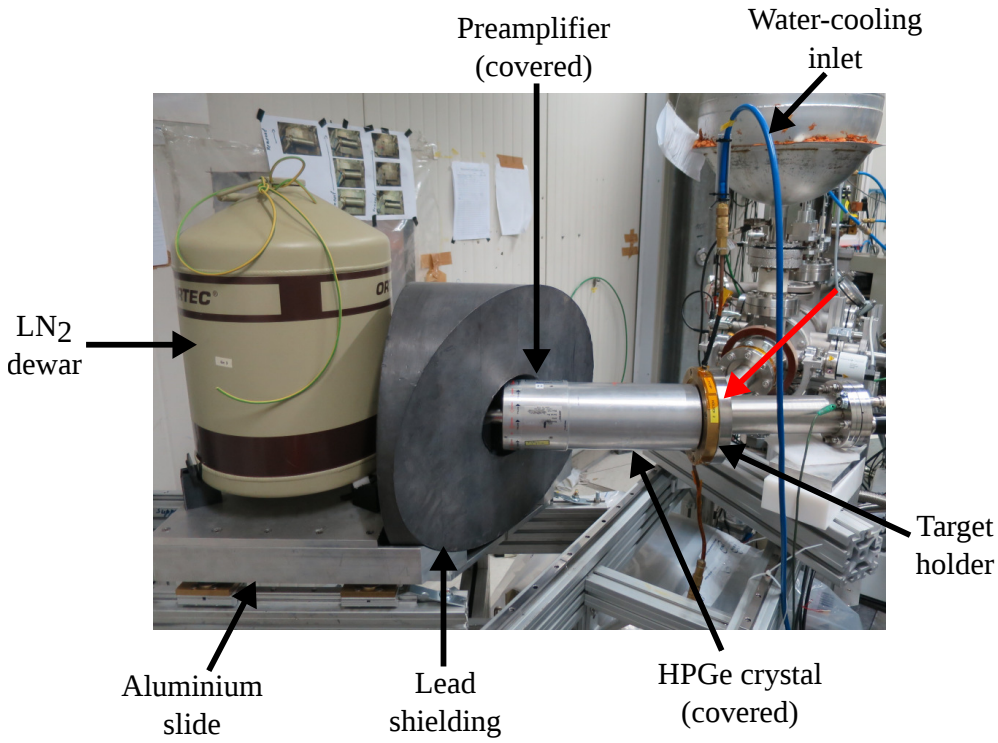

Figure 5.7 *HPGe detector setup used for gamma-ray detection. The dewar holding liquid nitrogen (LN_2) is shown on the left. This is thermally coupled to the HPGe crystal for cooling. The crystal, located at the end of the metal cylinder, is connected to a preamplifier further down the detector's neck. The lead is used to support the neck of the detector. The beam direction is marked by the red arrow.*

5.5 Electronic Chain and Data Acquisition

The signals from the detectors and current integration were processed using the electronic chain shown in figure 5.8. The silicon detector was biased to +50 V (full depletion) using an Ortec 710 bias supply. Signals from charge collected at the Si electrical contact were transferred along a copper cable (shown in figure 5.6) and through the vacuum feedthrough to an Ortec preamplifier (preamp), which shapes and amplifies the signals. The Si-to-preamp cable lengths were kept to a minimum to reduce noise on the front end[3]. The 50 Ω terminated output from a Berkely Nucleonics Corporation (BNC) PB-5 Pulse Generator was provided to the preamp test input with a rate of 10 Hz to check for potential gain shifts in the spectra. The preamp signal output was passed through an Ortec 572a Amplifier (3 µs shaping time, amplification factor 25) which both provided a

[3]The front end is the electronic chain between the detector and preamplifier, which usually provides the most significant contribution to noise.

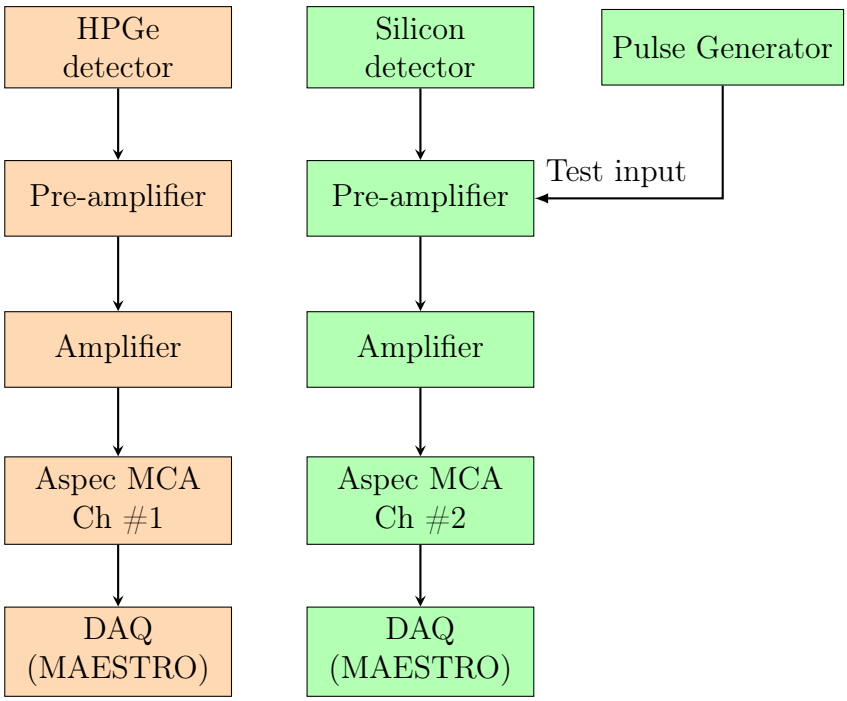

Figure 5.8 *Simplified diagram of the electronic chain used in the ^{6}Li campaign at LUNA. The chain for the HPGe (Si) detector is highlighted in orange (green).*

further amplification and converted the signal into a "Gaussian-like" shape. Once shaped, the signals were then digitised using an Ortec ASPEC 927 Multi Channel Analyser (MCA) for data acquisition (DAQ) and offline analysis.

The signal from the HPGe detector follows a similar chain to that of the Si detector. The HPGe crystal was biased to +4860 V using an Ortec 660 Bias Supply. For signal collection, a cable travelling down the inside of the detector's neck connected the HPGe crystal's electrical contact to an Ortec preamplifier. Next, the output signal from the preamp was sent to an Ortec 672 Spectroscopy Amplifier (shaping time 6 µs, amplification factor 14.2), producing "Gaussian-like" pulses similar to those from the Si amplifier. Finally the amplifier output was connected to a different channel of the same Ortec ASPEC 927 MCA module used for the Si detector.

The beam current signal was connected to an Ortec 439 digital current integrator which integrates the charge deposited on target during a given measurement run. The current integrator output was connected to an Ortec dual counter/timer 994, allowing the integrated beam current to be monitored by the accelerator operator. The counter/timer output was then processed by a CAEN NIM-TTL-

NIM adapter, making it compatible with the gate input on a BNC 8010 Pulse Generator. The pulses from the BNC 8010 were processed by an Ortec EtherNIM 919E MCA.

The ASPEC and EtherNIM modules were connected via USB to a Windows PC running the DAQ software MAESTRO [66] for both online monitoring and preliminary offline data analysis.

5.6 Data Taking Procedure

The ^{6}Li campaign took place over a total of 62 days spread across four measurement periods, including auxiliary measurements both at Naples and Dresden. The first period spanned 44 days at LUNA: 24 for setting up the chamber, calibrating detectors, and optimising beam focusing, followed by 16 days of concurrently measuring the ^{6}Li(p,α)^{3}He and ^{6}Li(p,γ)^{7}Be reactions, before concluding with 4 days of additional post-run detector calibration measurements. The second period spanned 2 days at Naples, where it was first discovered the two target holders used during the measurement had different backing flange materials as mentioned in section 5.3. The third period (5 days in Dresden) was dedicated to target characterisation measurements, the setup and results of which are discussed in chapter 6. The fourth and final period spanned an additional 11 days at LUNA dedicated to further measurements and to understand the impact of the two target holder backing materials on the HPGe gamma-ray detection efficiencies.

The ^{6}Li+p measurements were performed (during the first period) as follows:

- The first run was acquired at $E_{\text{lab}} \simeq 290$ keV, which was used as a reference energy[4] to monitor the ^{6}Li content of the target. Target degradation effects are discussed later in section 8.9. Irradiation at the reference energy was repeated periodically during the measurement.
- Measurements were taken by alternating the beam energies between low ($E_{\text{lab}} \leq 200$ keV), medium ($E_{\text{lab}} = 201-320$ keV), and high ($E_{\text{lab}} > 320$ keV) values.

[4]This lab energy sits approximately in the middle of the energy range studied during the campaign.

- All of the medium and high energy runs were collected until the DC $\rightarrow$ 0 keV peak integral was at least 3000 counts (1.8% statistical uncertainty). Typical count rates were of order $5-10$ counts/s depending on beam energy and thus cross section.

- Longer runs were collected at low energies to achieve good statistics, with $1.0-2.6\%$ statistical uncertainty in the DC $\rightarrow$ 0 keV peak integrals. Count rates of order $0.1-2$ counts/s were observed due to significantly lower cross sections.

- Before and after irradiation targets were kept in a vacuum jar to prevent lithium in the targets from reacting with atmospheric condensation [67].

- Natural background runs (no radioactive sources or beam present) were performed at the start and end of the beamtime.

Figure 5.9 shows sample gamma-ray spectra measured with the HPGe detector for protons ($E_{\mathrm{lab}} = 294.5$ keV) bombarding the Li_2WO_4-1 target (black spectrum) compared to the natural background (red spectrum), both scaled to their respective measurement times. The significantly low background in the energy regions of the primary ($5000-6000$ keV) and secondary (429 keV) peaks highlights the advantage of measuring the reaction underground.

Before covering the data analysis and results from this study of the ^{6}Li(p,α)^{3}He and ^{6}Li(p,γ)^{7}Be reactions, the next chapter is focused on the methods implemented to characterise the target thicknesses, compositions, stoichiometries, and profiles at the Helmholtz-Zentrum Dresden-Rossendorf laboratory in Dresden, Germany.

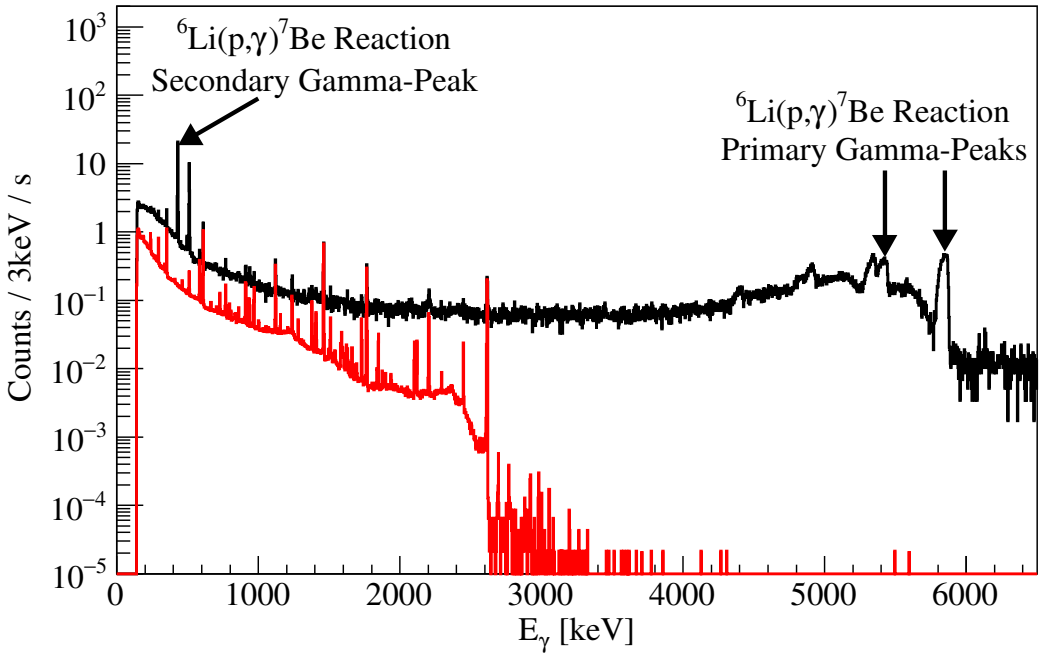

Figure 5.9 *Sample gamma-ray spectra obtained with the HPGe detector for protons bombarding the Li_2WO_4-1 target (black) and from the natural γ-ray background measured at LUNA (red). Spectra are scaled to their respective measurement times.*

Chapter 6

Target Characterisation at Dresden

Extracting cross sections for the ^{6}Li + p reactions required knowledge of the target thicknesses, compositions, stochiometries, and number of ^{6}Li nuclei as a function of the target thickness (target profile). During intense beam irradiation ($I \sim 100$ µA) the targets undergo modification processes (*e.g* by diffusion, sputtering, and/or contamination of target surface layers) which may cause significant changes in the target properties. Ideally during the beamtime at LUNA measurement of the ^{6}Li + p reactions should be stopped at regular intervals, typically every $0.5-1.0$ C of collected charge, and the target properties measured using non-destructive characterisation techniques. This characterisation was not possible to perform at LUNA, as explained in this section.

Two such techniques are relevant to this study: Nuclear Reaction Analysis (NRA) [68] and Elastic Recoil Detection Analysis (ERDA) [69]. Both approaches have been successfully applied to determine properties of targets used in previous studies at LUNA, for example in references [63, 64]. NRA is used to determine the target thicknesses and profiles (and indirectly the effective stopping powers), whereas ERDA is used to determine the target compositions and stochiometries.

A diagram of the NRA approach is shown in figure 6.1. Consider a target composed of multiple isotopes, including the isotope of interest a. The target is bombarded with a particle beam, of known energy E_{lab}, such that the reaction $a(b,c)d$ may occur. If E_{lab} corresponds to the energy, E_{r}, of a narrow resonance the resonance reaction will only take place on the target's surface. At higher bombarding energies the ions must first lose energy (energy loss and stopping powers are discussed in chapter 4) until they reach E_{r} at a given depth within

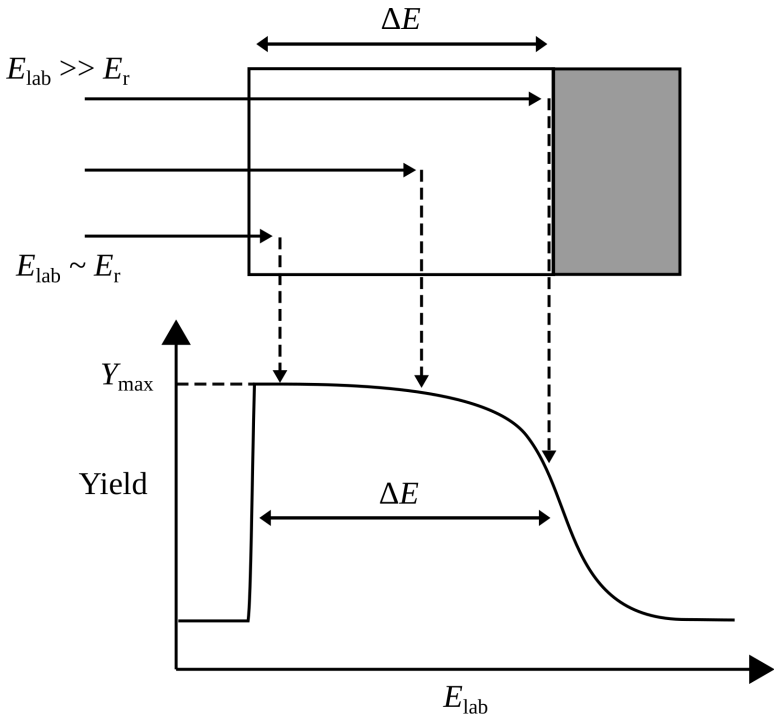

Figure 6.1 *Diagram of the NRA approach with target profile. A beam of energy $E_{lab} \sim E_r$ excites the resonance at the front layers of the target. Increasing the beam energy means the beam must first deposit energy into the target layers before exciting the resonance at a deeper layer. Measuring the yield of gamma rays emitted from this resonance as a function of beam energy produces a characteristic target profile with width equal to the target thickness at the resonance energy.*

the target. The number of gamma rays detected for this bombarding energy is proportional to the isotopic composition of a at that given depth of the target. Hence measuring the yield as a function of bombarding energy, $Y(E_{\mathrm{lab}})$, produces a characteristic yield curve (bottom of figure 6.1).

The width of the yield profile is a measure of the target thickness at the energy $E_{\mathrm{r}} + \Delta E$. The height of the yield profile, Y_{max}, is inversely proportional to the effective stopping power (stochiometry) by the thick-target yield formula [23]:

$$Y_{\mathrm{max}} = \frac{\lambda_{\mathrm{r}}^2}{2} \frac{\omega\gamma}{\epsilon_{\mathrm{eff}}^{\mathrm{r}}} \frac{m_{\mathrm{tar}}}{m_{\mathrm{tar}} + m_{\mathrm{proj}}} \tag{6.1}$$

where m_{tar} and m_{proj} are the respective masses (in a.m.u) of the target and projectile, λ_{r} is the deBroglie wavelength [23], $\omega\gamma$ is the resonance strength, and $\epsilon_{\mathrm{r}}^{\mathrm{eff}}$ is the effective stopping power (equation 4.6) at the resonance energy.

To extract the target thickness from NRA profiles, the target thickness must be

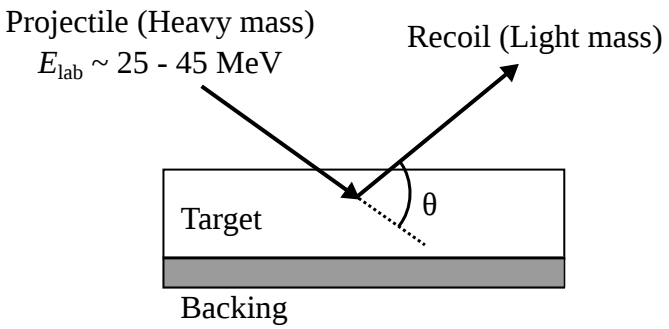

Figure 6.2 *Diagram of the ERDA approach, reproduced from [69]. The target is bombarded with a heavy beam and the recoil particles detected at forward angles. The depth distribution of the light particles can be complemented by computer simulations to extract isotopic compositions of the target.*

larger than the resonance width, $\Delta E > \Gamma_{\text{lab}}$. Otherwise, if $\Gamma_{\text{lab}} \sim \Delta E$ then the rising and falling edges of the target profile will broaden and it will be difficult to measure the target thickness. Alternatively if $\Gamma_{\text{lab}} > \Delta E$ the scan will be dominated by the resonance width and a target thickness cannot be extracted.

A schematic diagram of the ERDA approach, reproduced from [69], is provided in figure 6.2. The ERDA approach is performed by bombarding the target with a high-energy ($\sim 25 - 45$ MeV) beam and detecting the recoils at forward angles ($\theta < 90°$). Ecuyer *et al.* reported using this approach for the first time in 1976 [70], where they bombarded a LiF target with a ^{35}Cl beam ($E_{\text{lab}} = 30$ MeV) and detected recoil ^{7}Li, ^{6}Li, and protons from the target. They were therefore able to determine the depth distribution of these light elements. The ERDA approach has since been improved by using computer programs, *e.g.* SIMNRA [71], to determine the isotopic composition of targets.

Due to the lack of well-understood low-energy resonances in both proton and alpha induced reactions on ^{6}Li, within the beam energies available with the LUNA-400 accelerator ($E_{\text{lab}} \leq 400$ keV), it was not possible to perform NRA measurements at LUNA. In addition the LUNA-400 cannot produce high mass (*e.g.* ^{35}Cl) beams and therefore the ERDA method could not be performed at LUNA either. Instead after the ^{6}Li + p measurements were completed at LUNA the targets were shipped to the Helmholtz-Zentrum Dresden-Rossendorf (HZDR) facility in Dresden (Germany) for characterisation using the NRA and ERDA approaches.

This chapter first reports the NRA experimental procedure with corresponding data analysis and results. It then summarises the ERDA procedure, performed by

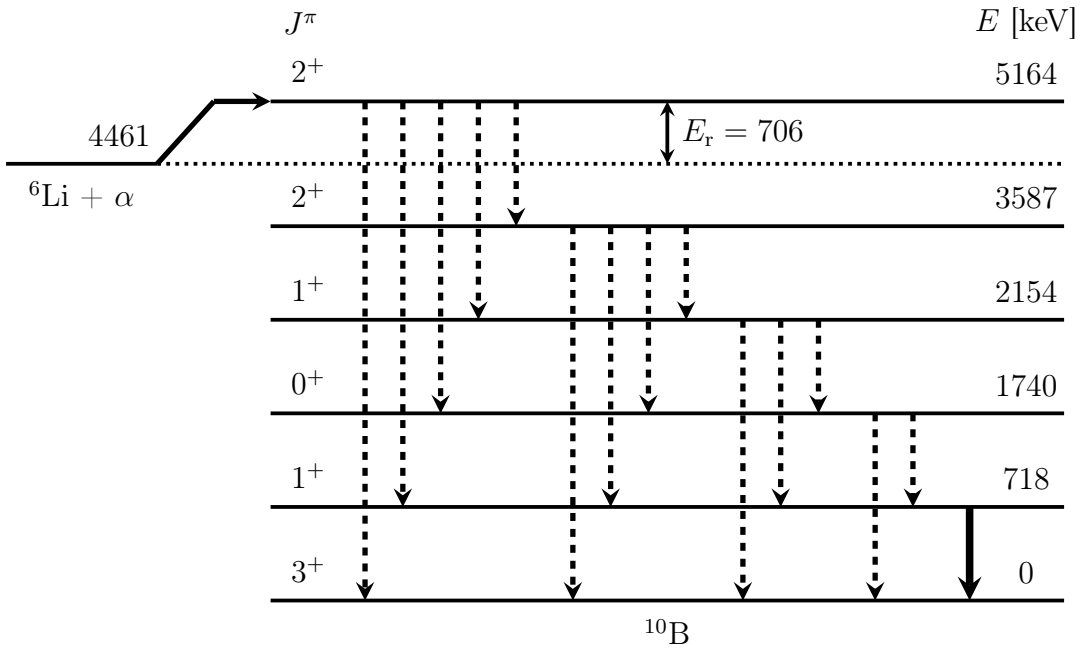

Figure 6.3 *The ^{10}B level scheme. The ^{10}B state (E_x = 5164 keV) populated from ^6Li + α at E_r = 706 keV is shown. The transition in solid black corresponds to emission of the 718 keV gamma rays (80.3% relative intensity) used in this NRA study.*

researchers in-house at HZDR, and results. Finally, a comparison of the effective stopping powers derived from both target characterisation procedures is provided.

6.1 Nuclear Reaction Analysis

6.1.1 Reaction of Study: ^{6}Li(α,γ)^{10}B

The ^{6}Li(α,γ)^{10}B reaction was selected to characterise the ^{6}Li-enriched targets using the NRA approach, specifically the reaction's well-known resonance at E_r = 706 keV (E_{lab} = 1175 keV, $\omega\gamma$ = 387(27) meV) [72], which populates the E_x = 5164 keV excited state in ^{10}B. The alpha beam energies required to populate this resonance are easily accessible by the Tandetron available at HZDR's Ion Beam Centre (IBC). The nominal thickness of each target were all at least ΔE^{α}_{lab} = 59 keV (for alphas incident at 1175 keV), which exceeds the width of the E_x = 5164 keV excited state, Γ_{lab} = 4.1 eV.

Once the E_x = 5164 keV state in ^{10}B has been populated, the ^{10}B* nuclei

subsequently decay via gamma emission in a cascade through the available lower energy states. The ^{6}Li(α,γ)^{10}B level diagram is shown in figure 6.3. It was decided to extract the NRA yields by measuring 718 keV gamma rays emitted from the 718 $\rightarrow$ 0 transition, for two reasons. Firstly of the different transitions the 718 $\rightarrow$ 0 transition has the largest relative intensity, 80.3% [72], and secondly the HPGe detection efficiency (next subsection) was measured between $E_{\gamma} = 662 - 1836$ keV, allowing straightforward interpolation of the efficiency at 718 keV.

6.1.2 Measuring at Dresden

The HZDR facility includes the 3 MV Tandetron accelerator [73] housed in the IBC. The Tandetron was used to accelerate alpha particles (charge state 1^{+}) in the energy range $E_{\mathrm{lab}} = 1145 - 1637$ keV. Typical beam currents of 2 µA were achieved, and the total integrated charge deposited on target varied between $0.02 - 0.06$ C. To reduce target heating effects, targets were water-cooled during beam bombardment. The experimental setup used for the NRA studies is shown in figure 6.4.

To minimise time taken to replace targets, both target holders (using the same aluminium flange) from the LUNA campaign were used in the NRA study. Similar to the LUNA beamtime (see subsection 5.2) a Cu pipe was mounted inside the beamline close to the target. The pipe was cooled using LN_2 to reduce heavy contaminants (carbon dioxide, water) in the beamline, and also biased to -300 V to suppress secondary electrons produced in the interaction of the beam with the target. To obtain an accurate beam current reading on target, the target holder was insulated from the rest of the beamline.

All of the targets (table 5.1) irradiated during the experiment at LUNA were subsequently characterised in this NRA study. For comparison "fresh" targets (not exposed to beam at LUNA) of Li_2O and Li_2WO_4 were also characterised, one of each composition with nominal thicknesses 40 and 200 µg/cm^2, respectively.

A simplified diagram of the electronics chain used at HZDR is shown in figure 6.5, the chain is analogous to the one used in LUNA (chapter 5).

A Canberra HPGe (Model GC6020) detector (biased at +1100 V) positioned at 5.9 cm from the back flange of the target holder, corresponding to a distance of ~ 7.8 cm between the target and detector-end-cap, was used to measure gamma

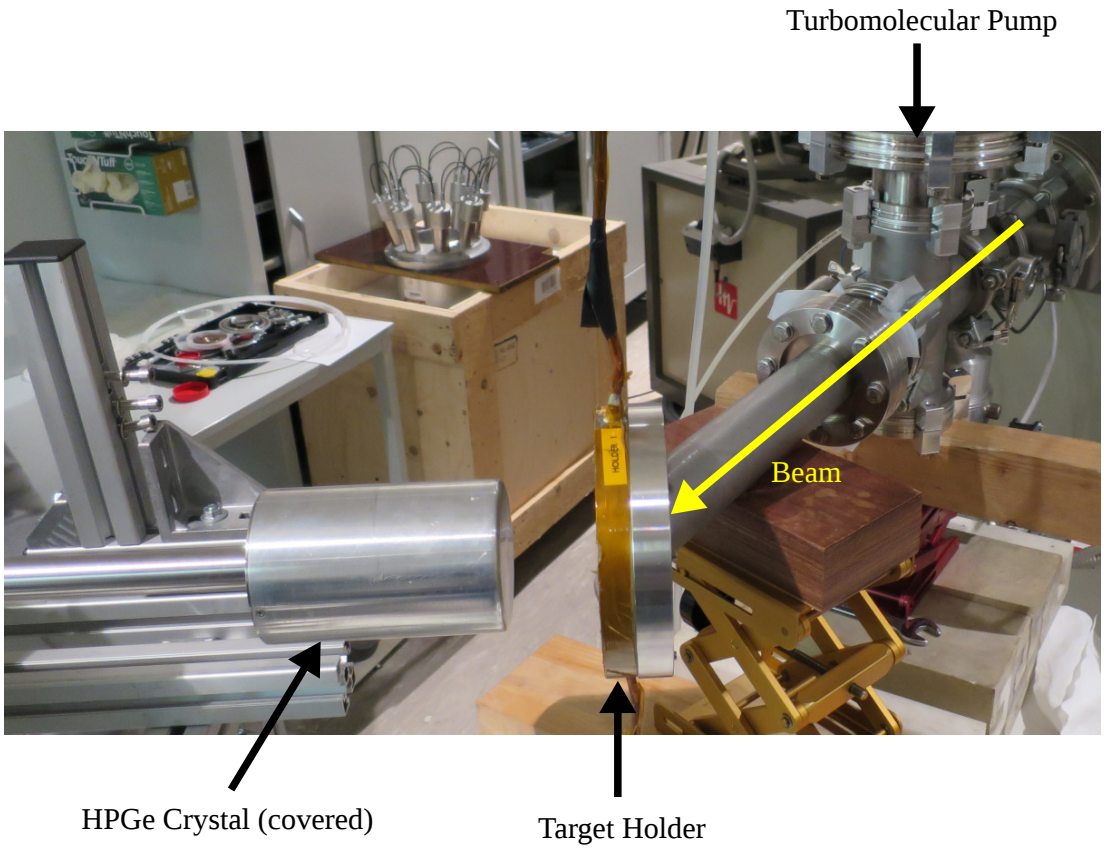

Figure 6.4 *Experimental setup used for NRA target characterisation at HZDR. The beam axis is marked by the yellow arrow. The beam impinges on the target mounted on the target holder (same as used in the LUNA measurement). Gamma rays emitted from the* $^{6}Li(\alpha,\gamma)^{10}B$ $E_r = 706$ *keV resonance are detected by the HPGe crystal.*

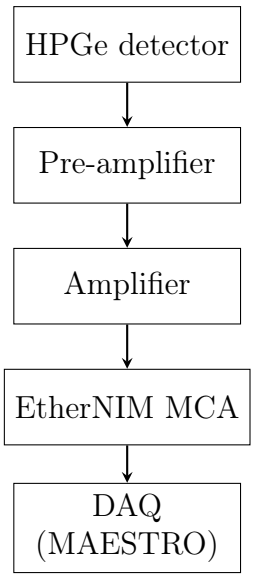

Figure 6.5 *Simplified diagram of the electronic chain used in the NRA study at HZDR.*

rays from both calibration sources and the ^{6}Li(α,γ)^{10}B reaction. To determine the HPGe detector photopeak efficiency at low energies the detector was calibrated using gamma rays emitted from sources (encased in a polyethylene holder) of ^{137}Cs (662 keV), ^{88}Y (898, 1836 keV), and ^{60}Co (1173, 1332 keV).

The photopeak efficiency, η_{ph}, of the HPGe was determined by identifying and integrating the area under the photopeaks using a linear background subtraction approach [74] (photopeak efficiencies discussed further in chapter 8 and appendix B). The net areas were divided by the number of gamma rays emitted by a given source (calculated using the source activity and measurement date). The η_{ph} as a function of gamma-ray energy is plotted with statistical error bars in figure 6.6. The η_{ph} was fitted using a second order polynomial function (black line), which had a reduced *chi*-squared ~ 1.8. The fit was then used to calculate (interpolate) the HPGe efficiency at $E_{\gamma} = 718$ keV, $\eta_{\text{ph}} = 0.71\%$, the energy selected for NRA analysis.

The NRA profiles were measured as follows. The targets were bombarded with alpha particles at the resonance energy $E_{\text{lab}} = 1175$ keV, populating the resonance at the front-most layer of the target and emitting the 718 keV gamma ray from the ^{10}B* cascade. These gamma ray events were detected and used to calculate a reaction yield (equation 4.2). The alpha energies were then increased in steps of $5 - 10$ keV, exciting the resonance deeper and deeper inside the target. The

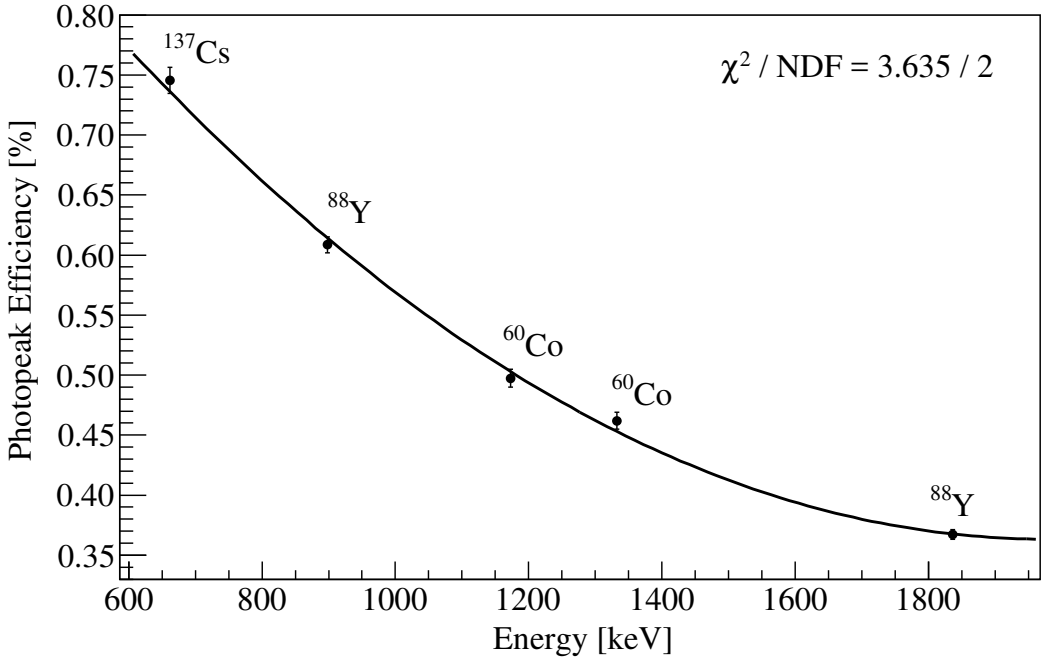

Figure 6.6 *Photopeak efficiency curve of the HPGe detector used at HZDR for NRA data collection. The points represent the measured efficiencies, with statistical error bars, using the radioactive sources. The line represents a second order polynomial fit for interpolation purposes.*

yields were calculated for each beam energy. These yields are proportional to the number of ^{6}Li nuclei present at the slice of the target the resonance is being excited in. The alpha energies were increased until the measured yields decreased back to values similar to the off-resonance offset. This indicated the beam was at a high enough energy such that, even with energy loss effects, the resonance was no longer excited inside the target. The off-resonance offset was measured at alpha energies below the resonance energy. The targets may have contaminants (carbon) present on their outer layers, and so the beam energy was adjusted between $1150 - 1190$ keV to check the rising edge of the target profiles. If the energy of this rising edge did not equal the resonance energy this would indicate deposition on the target's front layers. No signs of deposition were observed for any target. The dead time for all runs, calibration or otherwise, remained below 1%.

6.1.3 Data Analysis and Results

For each target irradiated at HZDR, peaks from the 718 keV gamma ray emitted from an excited state in ^{10}B were identified and integrated run-by-run. A sample

gamma-ray spectrum collected during bombardment of the Li_2WO_4-1 target is shown in figure 6.7. Background contributions to the peak areas were subtracted by assuming a linear background beneath the peak [74]. The net peak areas were then converted to experimental yields using equation 4.2, where the 718 keV gamma emission is isotropic [75]. The yields were then plotted as a function of alpha beam energy, $E^{\alpha}_{\rm lab}$, and fitted with the empirical function:

$$\begin{aligned} P(E^{\alpha}_{\rm lab}) &= Y_{\rm max}\left[1+\exp\left(\frac{E_{\rm r}-E^{\alpha}_{\rm lab}}{\delta_{\rm l}}\right)\right]^{-1}\left[1+\exp\left(\frac{E^{\alpha}_{\rm lab}-E_{\rm r}-\Delta E}{\delta_{\rm r}}\right)\right]^{-1}+C \\ &= Y_{\rm max}\left[1+\exp\left(\frac{E_{\rm r}-E^{\alpha}_{\rm lab}}{\delta_{\rm l}}\right)\right]^{-1}\left[1+\exp\left(\frac{E^{\alpha}_{\rm lab}-E_{\rm r}-\Delta E}{\sqrt{(\Delta_{\rm stragg})^2+(\Delta_{\rm tar})^2}}\right)\right]^{-1}+C \end{aligned} \tag{6.2}$$

where $Y_{\rm max}$ is the maximum yield of the scan, $E_{\rm r}$ is the resonance energy, ΔE is the total beam energy lost inside the target, and C is an offset that accounts for non-resonant contributions. The $\delta_{\rm l}$ and $\delta_{\rm r}$ determine the width of the rising (left) and falling (right) edges of the scan respectively. To account for beam straggling, δ_r is expressed as $\sqrt{(\Delta_{\rm stragg})^2+(\Delta_{\rm tar})^2}$, where $\Delta_{\rm tar}$ is related to the particular depth profile of the target and the beam straggling effect is approximated as [23]:

$$\Delta_{\rm stragg} = 1.20\times10^{-9}\sqrt{\frac{{Z_{\rm tar}Z_{\rm proj}}^2(E^{\alpha}_{\rm lab}-E_{\rm r})}{\epsilon_{\rm tot}}} \quad [\text{keV}] \tag{6.3}$$

where $Z_{\rm tar}$ and $Z_{\rm proj}$ are the atomic numbers of the target and projectile respectively, $(E^{\alpha}_{\rm lab}-E_{\rm r})$ is the beam energy loss inside the target before reaching the resonance energy, and $\epsilon_{\rm tot}$ is the total stopping power defined by equation 4.4. Except for $E^{\alpha}_{\rm lab}$, $Z_{\rm tar}$, $Z_{\rm proj}$, and $\epsilon_{\rm tot}$ all the terms in equations 6.2 and 6.3 are free parameters.

Figures 6.8 and 6.9 show the yield profiles measured on the Li_2WO_4 targets and on the Li_2O and LiCl targets, respectively. The fit parameters are summarised in table 6.1. The reduced *chi*-squared of the fits range between $1.5-4.2$.

Two of the targets previously irradiated at LUNA, Li_2O-7 and LiCl, presented challenging NRA yield profiles. The Li_2O-7 profile, figure 6.9, shows a thin plateau with steadily decreasing yield at higher alpha energies, likely a result of beam-induced damage causing the ^{6}Li to be distributed in the Ta backing. This profile proved difficult to fit with the empirical function used for other similar targets. The LiCl profile shows, as expected, an "infinitely" thick target for the

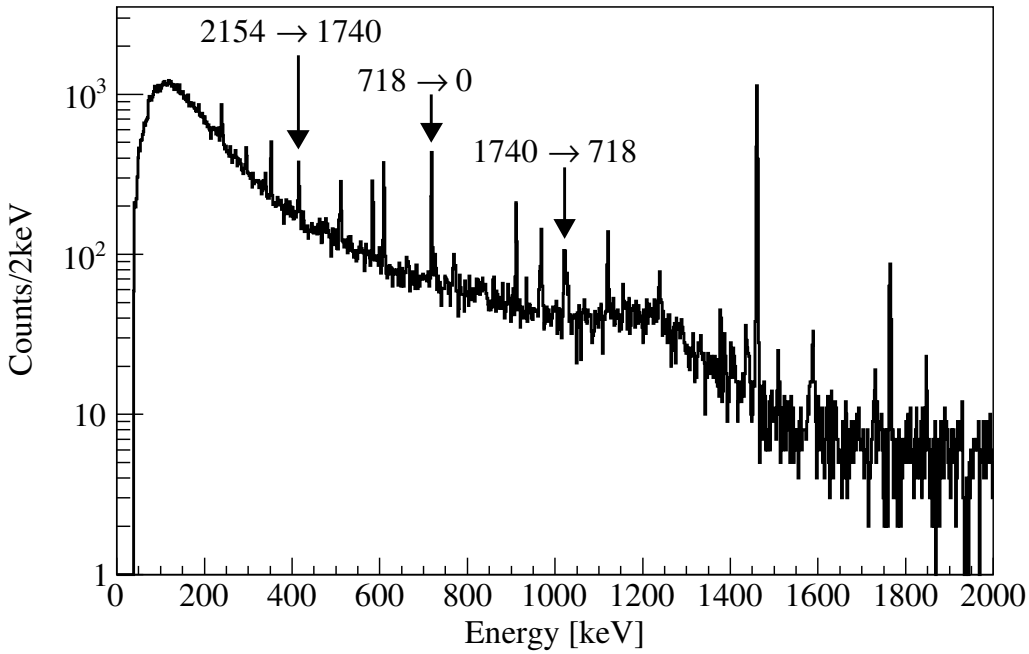

Figure 6.7 *Sample gamma-ray spectrum collected during the alpha bombardment (E^{α}_{lab} = 1237 keV) of the Li_2WO_4-1 target at HZDR. Some peaks corresponding to transitions in $^{10}B^{*}$ have been identified, including the* $718 \rightarrow 0$ *used in this study.*

Table 6.1 *NRA yield fit parameters for all targets irradiated at HZDR, LiCl not listed.*

Target	$Y_{\max}\,10^{-11}$ [1/particle]	δ_{l} [keV]	ΔE [keV]	Δ_{tar} [keV]	E_{r} [keV]	Offset 10^{-11} [1/particle]
Li_2WO_4-1	1.14 (3)	0.07 (17)	226 (4)	41 (4)	1172.8 (5)	0.12 (3)
Li_2WO_4-2	0.94 (3)	0.6 (6)	327 (8)	72 (7)	1173.97 (16)	0.128 (13)
Li_2WO_4-3	0.95 (3)	0 (4)	190 (6)	24 (4)	1174 (5)	0.11 (3)
Li_2WO_4-4	1.02 (3)	0.05 (8)	155 (4)	32 (4)	1173.12 (16)	0.138 (16)
Li_2O-5	1.71 (4)	0.16 (3)	254 (3)	38 (3)	1173.64 (4)	0.21 (3)
Li_2O-7	4.6 (5)	0.23 (7)	36 (24)	109 (7)	1173.97 (5)	2.4 (2)
Li_2O-9	1.45(5)	0 (5)	139 (23)	32 (3)	1173 (24)	0.17 (2)

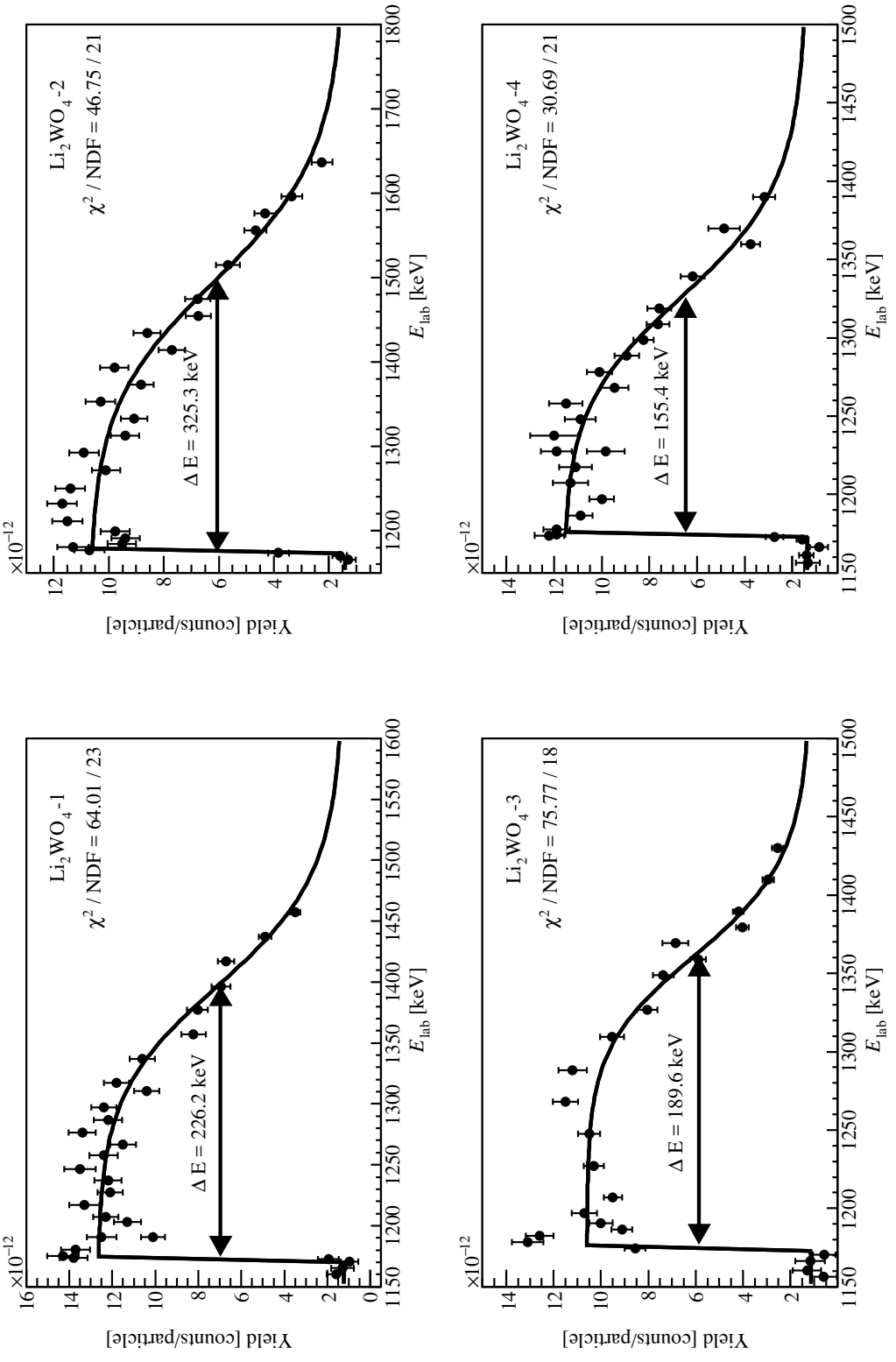

Figure 6.8 *NRA yield curves measured at HZDR for the Li_2WO_4 targets. The profiles have been fitted with equation 6.2.*

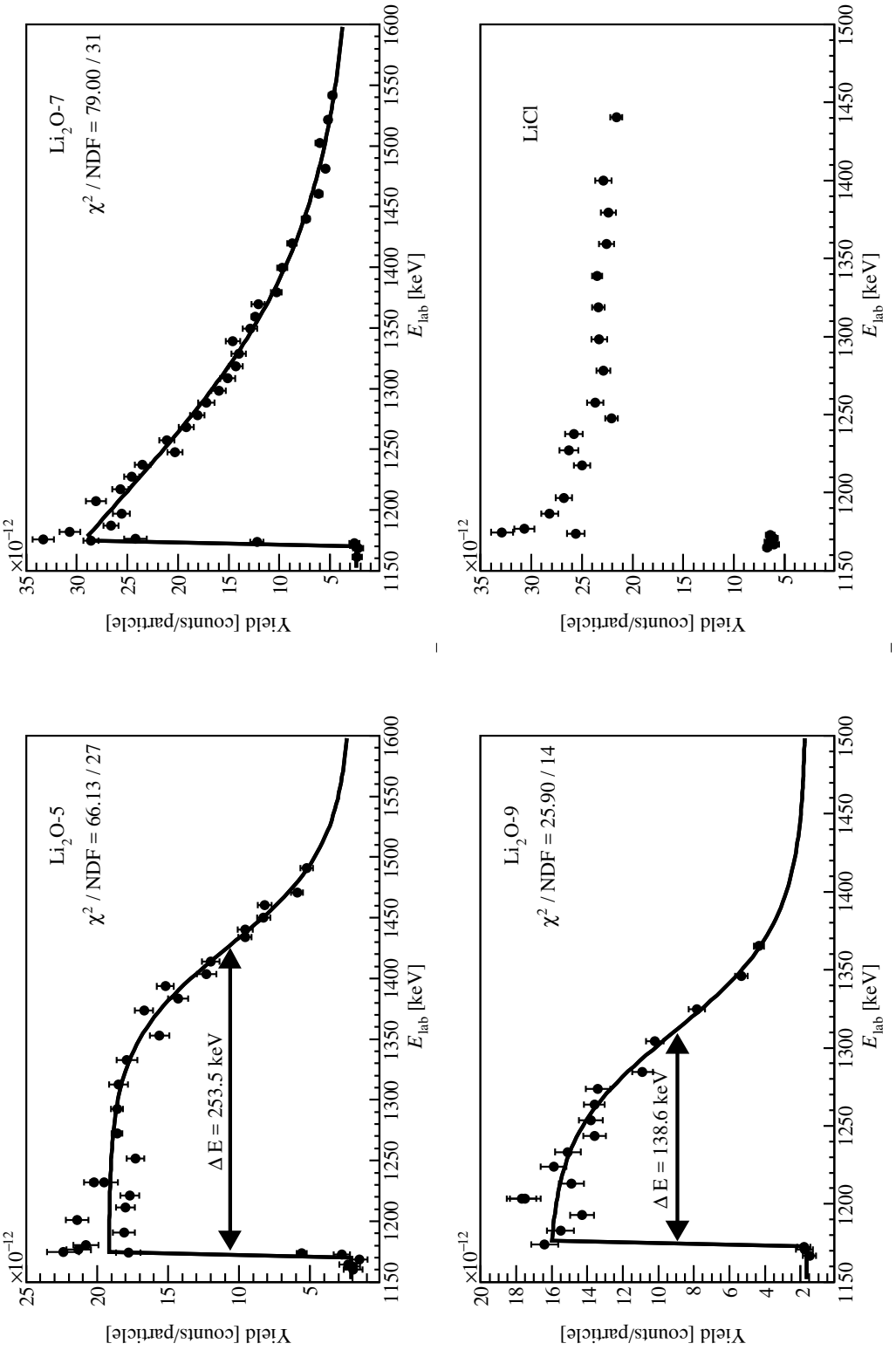

Figure 6.9 *NRA yield curves measured at HZDR for the Li_2O and LiCl targets. The profiles for the Li_2O targets have been fitted with equation 6.2.*

alpha energy range covered. However a significant peak is seen in the profile across $E^{\alpha}_{\rm lab} \sim 1180 - 1270$ keV, which may be caused by surface effects. For the lowest proton beam energy used to irradiate the LiCl at LUNA, $E^{\rm p}_{\rm lab} = 75$ keV, the beam is stopped at an energy corresponding to this peak. As a result of these two target profiles showing unexpected features, it was decided to discard the data collected from these targets in the analysis of the ^{6}Li + p data acquired at LUNA. The other targets irradiated at LUNA (Li_2O-9, Li_2WO_4-1, Li_2WO_4-3, and Li_2WO_4-4) all show expected profiles and were used in the cross section analysis (chapters 7, 8, and 9).

The heights, $Y_{\rm max}$, from the fits of the NRA yield profiles were used in the thick-target yield equation 6.1 to derive the effective stopping power, $\epsilon_{\rm eff}$, (for an alpha particle of incident $E_{\rm lab} = 1175$ keV) for the given target. These were then compared with effective stopping powers calculated from SRIM using either the ERDA or nominal compositions (section 6.3).

The profiles collected at HZDR are a function of alpha beam energy, however the study at LUNA bombarded the targets with a proton beam, and the protons will interact with the targets differently (*e.g.* different straggling effects, stopping power, and energy loss) than alpha particles. To compare target thicknesses extracted from data collected at LUNA (section 8.9) with those measured at Dresden two steps were taken. First the straggling and offset parameters ($\Delta_{\rm stragg}$ and C) were removed from the profiles $P(E^{\alpha}_{\rm lab})$, all other parameters from the fitting procedure were kept the same. A sample modified fit is shown by the dotted line in figure 6.10.

Next the modified profiles were converted from functions of alpha lab energy, $P(E^{\alpha}_{\rm lab})$, to physical thickness (atoms/cm^2), $P(x)$, using total stopping powers calculated (equation 4.4) from SRIM with the ERDA composition (section 6.2):

$$\Delta x = \int_0^{E^{\alpha}_{\rm lab} - E_{\rm r}} \left(\frac{{\rm d}x}{{\rm d}E} \right)_{\rm tot} {\rm d}E = \int_0^{E^{\alpha}_{\rm lab} - E_{\rm r}} (\epsilon_{\rm tot})^{-1} \, {\rm d}E \tag{6.4}$$

where Δx is the target thickness for a given measurement run at $E^{\alpha}_{\rm lab}$ and $\epsilon_{\rm tot}$ is the total stopping power. A sample NRA yield curve converted to physical thickness units is shown in figure 6.11 for the Li_2WO_4-1 target. The profile has been normalised such that $Y_{\rm max} = 1$.

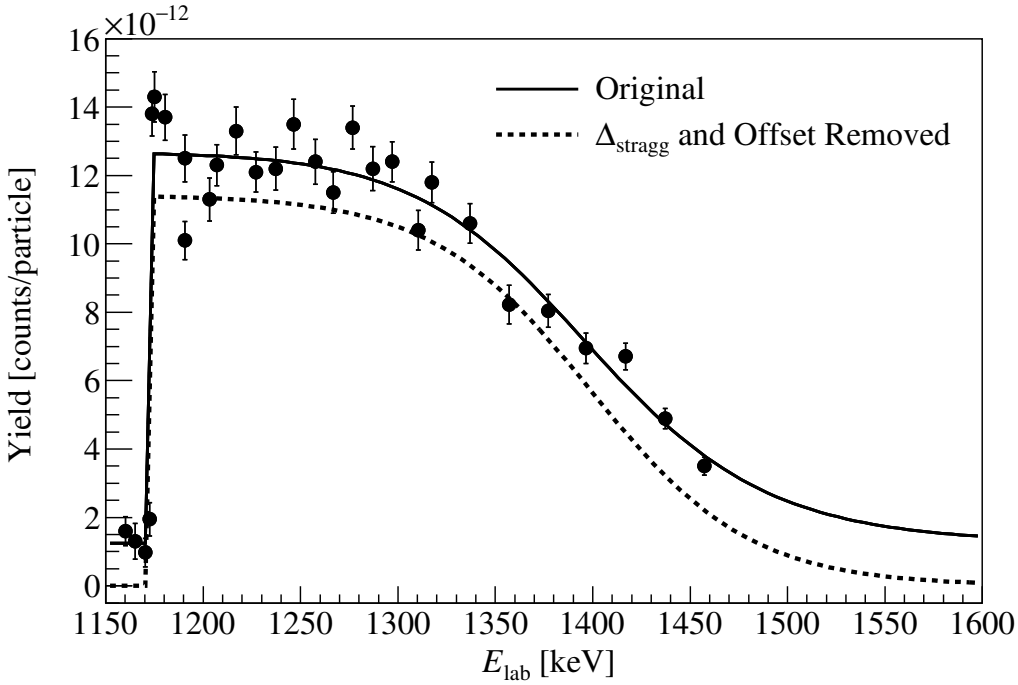

Figure 6.10 *NRA yield curve (solid line) as a function of incident alpha energy collected at HZDR for the Li_2WO_4-1 target. The same curve with the straggling and offset parameters removed (dotted line) is shown for comparison.*

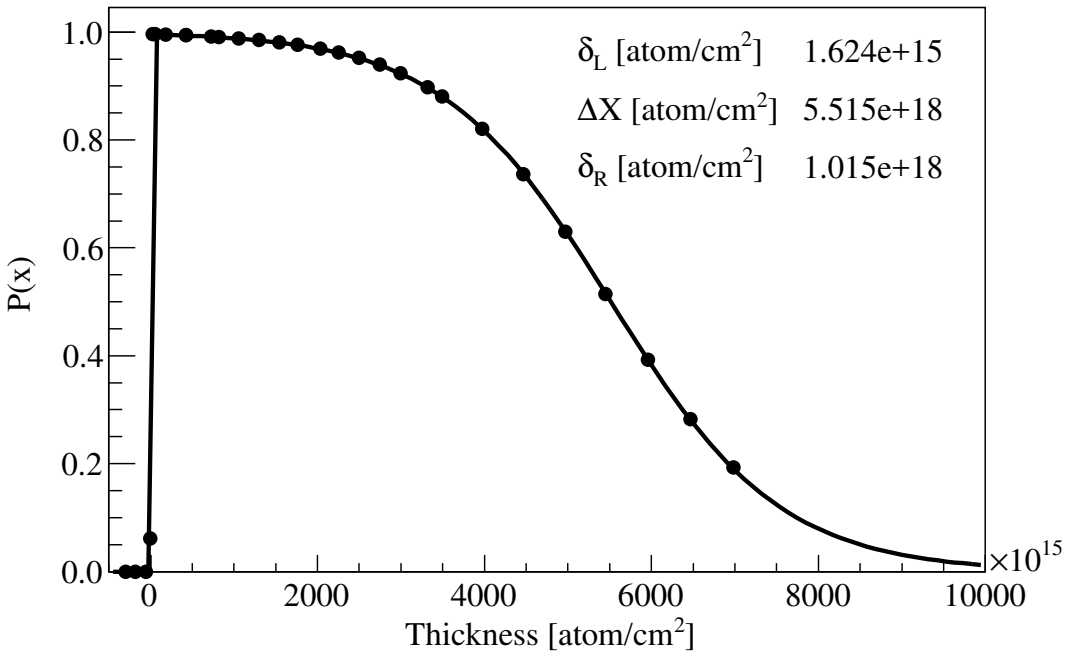

Figure 6.11 *NRA yield curve as a function of target thickness collected at HZDR for the Li_2WO_4-1 target. The thickness Δx is compared later with those measured at LUNA in section 8.9.*

6.2 Elastic Recoil Detection Analysis

Whilst the NRA measurements provide information on the profile, thickness, and effective stopping power of the targets, they do not directly determine the target composition. An alternative target characterisation measurement, known as Elastic Recoil Detection Analysis (ERDA)[69], was therefore used to determine the depth profile of individual atoms in the targets, and thus provide a quantitative description of a target's composition and stoichiometry. The ERDA measurements were performed independently by collaborators at the HZDR laboratories, after the NRA studies.

As stated in the report [76]: "The targets were bombarded by projectiles of 43 MeV $^{35}Cl^{7+}$ incident at an angle 70° to the target normal. The recoil H and Li were detected at 41° using a solid state detector, and other recoils were detected at 31° using a Bragg ionisation chamber." The energy and intensity of the recoils provided respective measures of their emission point and concentration at a particular depth in the target. Depth profiles and isotopic compositions for the targets were extracted and subsequently analysed through comparisons with the outputs from the NDF simulation program [77].

The thicknesses and compositions of the targets studied using ERDA are provided in table 6.2. The target names marked in bold are targets irradiated at LUNA, prior to characterisation, and the rest are "fresh" targets. For some targets, measurements were carried out both inside and outside the beamspot irradiated at LUNA; the offspot is marked with a * next to the name. The LiCl target was not analysed using ERDA. The depth profiles of the Li_2WO_4 targets showed a surface peak of carbon deposition, but the carbon was not distributed through the target thickness [76]. Therefore the carbon stochiometries were neglected from the stopping power calculations of the Li_2WO_4 targets.

6.3 Comparison of Effective Stopping Powers

The effective stopping powers for alpha particles incident at $E^{\alpha}_{\mathrm{lab}} = 1175$ keV on the targets were extracted from both the NRA and ERDA data. The results are shown in table 6.3. The NRA stopping powers were calculated using the fitted Y_{max} parameter of the profiles as an input to the thick-target yield equation 6.1. The ERDA stopping powers were calculated using SRIM with the measured

Table 6.2 *Thicknesses and compositions of targets obtained with the ERDA technique. For some targets measurements were performed both inside and outside the beamspot irradiated at LUNA. The latter measurement is indicated by a * next to the target identification. Targets irradiated at LUNA are marked in bold. The Li_2WO_4-1 and Li_2WO_4-2 target thicknesses are provided as lower limits [76].*

Target	Thickness [10^{15} atom/cm^2]	H [%]	Li [%]	C [%]	O [%]	W [%]
Li_2O-5	4000	7	31	12	50	-
Li_2O-6	2300	5	27	15	53	-
Li_2O-7	6400	3	31	14	53	-
Li_2O-7*	6600	3	29	14	54	-
Li_2O-8	3300	5	27	15	53	-
Li_2O-9	3600	7	26	16	51	-
Li_2O-9*	3600	6	27	13	54	-
Li_2WO_4-1	> 3600?	9	19	< 6	54	9
Li_2WO_4-2	> 4000?	-	-	-	-	-
Li_2WO_4-3	2100	9	17	< 7	56	10
Li_2WO_4-4	2400	11	16	< 5	57	10

compositions in table 6.2. The "fresh" Li_2WO_4-2 target was treated as having nominal composition due to difficulties in the ERDA characterisation for this target. For comparison effective stopping powers from SRIM using nominal compositions are also provided, where the nominal compositions assume targets have isotopic components equivalent to their chemical formula, *e.g* Li_2WO_4 is nominally composed of 2 parts lithium (95% enriched in ^{6}Li), 1 part tungsten, and 4 parts oxygen. The stopping powers from the NRA approach are quoted with uncertainties propagated from the fitted $Y_{\max}$ parameter. Both the ERDA and nominal stopping powers are quoted with 5% uncertainties from the SRIM stopping power tables [51].

The effective stopping powers calculated from NRA and ERDA are in disagreement for all targets, with discrepancies ranging $19-47\%$ for the irradiated targets and $4-20\%$ for the "fresh" targets. This is likely because the strength of the NRA approach lies in its direct measurement of the target profiles and thicknesses, whilst it only provides indirect information on the target compositions (*i.e.* the effective stopping power). By contrast, the ERDA approach directly and reliably measures the target compositions, yet the analysis encountered problems extracting target thicknesses due to inhomogeneities in the target surfaces [76]. For example the Li_2WO_4-1 and Li_2WO_4-2 thicknesses are provided as lower limits

Table 6.3 *Comparison of effective stopping powers calculated from the NRA and ERDA analysis methods, for $E^{\alpha}_{lab} = 1175$ keV. The effective stopping powers from SRIM using the nominal compositions are included. Targets irradiated at LUNA are marked in bold. Uncertainties on values from NRA are propagated from errors on Y_{max}, uncertainties on values from ERDA and nominal are 5%, as quoted for SRIM stopping power tables.*

Target ID	ϵ_{eff} $[10^{-15}\,\text{eVcm}^2/\text{atom}]$		
	NRA	ERDA	Nominal
Li_2O-5	91.8 (1.9)	115 (6)	44 (2)
Li_2O-7	62.3 (1.0)	115 (6)	44 (2)
Li_2O-9	108 (3)	134 (7)	44 (2)
Li_2WO_4-1	137 (4)	212 (11)	173 (9)
Li_2WO_4-2	166	-	173 (9)
Li_2WO_4-3	166 (5)	247 (12)	173 (9)
Li_2WO_4-4	154 (4)	265 (13)	173 (9)

in table 6.2. For the analysis of the data collected at LUNA, the effective and total stopping powers were calculated from SRIM using the ERDA values for the target compositions (table 6.2) and treating the Li to be 95% enriched in ^{6}Li. The use of the NRA and ERDA results in the cross section analysis will be described in the relevant section of chapters 7, 8, and 9. The next chapter focuses on the data analysis and results from the study of the ^{6}Li(p,α)^{3}He reaction at LUNA.

Chapter 7

^{6}Li(p,α)^{3}He Data Analysis and Results

One of the two main objectives of this experimental campaign was the determination of the ^{6}Li(p,α)^{3}He reaction S-factor at energies accessible by the LUNA-400 accelerator ($E_{\rm cm} \sim 65 - 337$ keV). Achieving this goal required knowledge of the experimental yields (chapter 4). This chapter first presents the analysis methods used to determine inputs for the yield calculations: the Si detector efficiency, number of detected events, and angular distributions. Next the yields themselves are presented, and then results from deconvolving the yields into S-factors are shown at the end of the chapter.

Analysis methods used to achieve the second main objective; determining the ^{6}Li(p,γ)^{7}Be reaction S-factor, are covered in the next chapter.

7.1 Data Analysis Procedure

The data analysis proceeded as follows:

1. Si detector efficiencies were determined from measurements of alpha particles emitted by the ^{18}O(p,α)^{15}N reaction.
2. Charged-particle peak areas were calculated from the spectra obtained measuring the ^{6}Li(p,α)^{3}He reaction.

3. Angular distributions of the ^{6}Li(p,α)^{3}He reaction's alpha and ^{3}He particles were extracted from the literature.

4. Experimental yields were calculated using equation 4.2 with inputs from steps $1-3$.

5. Yields were then deconvolved into cross sections (S-factors), using knowledge of the target properties (chapter 6) and target degradation (next chapter).

7.2 Si Detector Efficiency

When discussing detector efficiencies it is necessary to divide them into two categories: *absolute* and *intrinsic* efficiencies [78]. Absolute efficiency, η_{abs}, depends on the detection properties, the target-to-detector geometry, and the energy of the incident radiation; intrinsic efficiency, η_{int}, does not include the solid angle Ω subtended by the detector as a factor.

$$\eta_{\text{abs}} = \frac{\text{number of pulses recorded}}{\text{number of radiation quanta emitted from source}} \tag{7.1}$$

$$\eta_{\text{int}} = \frac{\text{number of pulses recorded}}{\text{number of radiation quanta incident on detector}} \tag{7.2}$$

where for an isotropic source the absolute efficiency is related to the intrinsic efficiency by the solid angle: $\eta_{\text{abs}} = \eta_{\text{int}}(\Omega/4\pi)$.

The Si detector's intrinsic efficiency is 100% ($\eta_{\text{int}} = 1$) for charged-particle detection, therefore the absolute efficiency of the Si detector is described by the solid angle subtended by the detector on the charged-particle emission point in the target (geometrical efficiency). The measurement of the ^{6}Li + p reaction involved a proton beam irradiating an approximate elliptical area of 10 mm by 5 mm on the target face, and therefore the absolute efficiency of the Si detector could not be accurately measured using a point source. Instead this absolute efficiency was measured using a similar beam spot geometry produced by bombarding a proton beam ($E_{\text{p}} = 158$ keV) onto an ^{18}O-enriched ($^{18}\text{O}/^{\text{nat}}\text{O} \sim 99\%$) Ta_2O_5 target. Alpha particles were detected from the well-known ^{18}O(p,α)^{15}N isotropic resonance at $E_{\text{p}} = 151$ keV. This resonance has previously been measured by a recent experiment at LUNA [63] using the same ^{18}O target (manufactured

in the exact same process [79]) and beamline as the current study. The previous LUNA study determined the resonance strength to reasonable precision: $\omega\gamma = 164.2 \pm 0.9_{\text{stat}}\,{}^{+12.1}_{-11.7\,\text{sys}}$ meV, where the 7.4% error on the resonance strength already accounts for uncertainties from target properties and beam focusing. Alpha particles emitted from the reaction, after being slowed down by the 5 µm thick Mylar foil (in front of the Si detector), were detected at typical energies about $E_\alpha = 2.3$ MeV, depending on the proton beam energy.

The absolute efficiencies were determined from the resonance strength:

$$\eta_{\text{abs}} = \frac{1}{\omega\gamma}\,\frac{2}{\lambda_{\text{r}}^2}\,\epsilon_{\text{eff}}\,\frac{N_{\text{peak}}}{N_{\text{b}}\,W}\,\frac{m_{\text{tar}}}{m_{\text{tar}} + m_{\text{proj}}} \tag{7.3}$$

where $\omega\gamma$ is the resonance strength, λ_{r} is the deBroglie wavelength [23], N_{peak} is the integral under the alpha particle peak, N_{b} is the number of beam particles incident on the target during the measurement time, W is the angular distribution ($W = 1$ is assumed), m_{tar} and m_{proj} are the respective masses (in a.m.u) of the target and projectile, and $\epsilon_{\text{r}}^{\text{eff}}$ is the effective stopping power (equation 4.6) at the resonance energy, calculated using SRIM-2013 tables [51] as: $\epsilon_{\text{r}}^{\text{eff}}(E_{\text{p}} = 151\text{ keV}) = 29.3 \times 10^{-15}$ eV cm^2/atom. For this study, the absolute efficiencies for the Si detector were determined for target-to-detector distances ranging $d = 3.9 - 10.3$ cm (target chamber shown in figure 5.4).

To further validate the absolute efficiencies measured using the ^{18}O(p,α)^{15}N reaction a GEANT3 (GEometry ANd Tracking) [80] Monte Carlo simulation, developed inside the LUNA collaboration, was used to model both the Si detector setup and alpha particles emitted from an area on the (Ta_2O_5) target similar to the beamspot area. The simulations used a circular beamspot with radius 5 mm projected onto the target at 55° to the beam axis (forming an ellipse) and horizontally shifted to $x_{\text{c}} = 3$ mm from the target centre, in agreement with similar dimensions and positions of the observed beamspot [81]. The simulated absolute efficiencies are plotted as a long-dashed line in figure 7.1. Results from the simulations accurately reproduced the absolute efficiencies measured from the ^{18}O(p,α)^{15}N alpha particles. The simulations were also used to determine a systematic uncertainty from the effect of the beamspot position on the absolute efficiency. The centre of the simulated 10 mm by 5 mm beamspot was horizontally shifted (the observed beamspot showed no vertical shift) relative to the target centre between $x_{\text{c}} = 0 - 6$ mm, and the absolute efficiencies recalculated for each case. The effect on the simulated absolute efficiencies remained within 5%, and

so a conservative systematic uncertainty of 5% associated to beamspot effects was assigned to the absolute efficiency of the Si detector.

The measured absolute efficiencies were also compared with a calculated solid angle coverage of the Si detector. The common definition for the solid angle coverage, Ω, of a right circular cylindrical detector (like the Si detector used in this study) with active radius r at a distance d from an isotropic point source is defined as [78]:

$$\eta_{\text{abs}} = \frac{\Omega}{4\pi} = \frac{1}{2}\left(1 - \frac{d}{\sqrt{d^2 + r^2}}\right) \tag{7.4}$$

where for this study the active radius is constrained by the circular collimator (radius $r = 0.05$ cm) mounted in front of the Si detector. In the case of $d >> r$ the solid angle is simplified to [78]:

$$\eta_{\text{abs}} = \frac{\Omega}{4\pi} \simeq \frac{\pi r^2}{4\pi d^2} = \frac{A_{\text{active}}}{4\pi d^2} \tag{7.5}$$

where A_{active} is the active exposed area of the collimated Si detector.

Results are shown in figure 7.1, with the two positions used in the ^{6}Li(p,α)^{3}He measurement $d = 9.3$ cm and $d = 10.3$ cm marked by the arrows. For these target-to-detector distances the geometrical efficiencies from the common and simplified solid angle calculations are within 0.018% of each other, so only the common solid angle is plotted in figure 7.1. The absolute efficiencies for the two target-to-detector distances used in the ^{6}Li(p,α)^{3}He measurement, $d = 10.3$ cm and $d = 9.3$ cm, were determined from the ^{18}O(p,α)^{15}N measurements (using a weighted average [82] of repeat measurements at the same distance) as $\eta_{\text{abs}} = (4.44 \pm 0.11_{\text{stat}} \pm 0.39_{\text{sys}})10^{-6}$ and $\eta_{\text{abs}} = (5.42 \pm 0.13_{\text{stat}} \pm 0.48_{\text{sys}})10^{-6}$, respectively. The statistical error of $\sim 2.6\%$ was determined from the uncertainties on the charged-particle peak integration and the random fluctuations in the beam current integration [59]. The systematic error was determined by summing in quadrature the effect of the beamspot on the absolute efficiency, 5%, and the reported error of 7.4% on the resonance strength $\omega\gamma$ [63]. The total estimated uncertainty on the absolute efficiency of the Si detector was 9.3% for both target-to-detector distances.

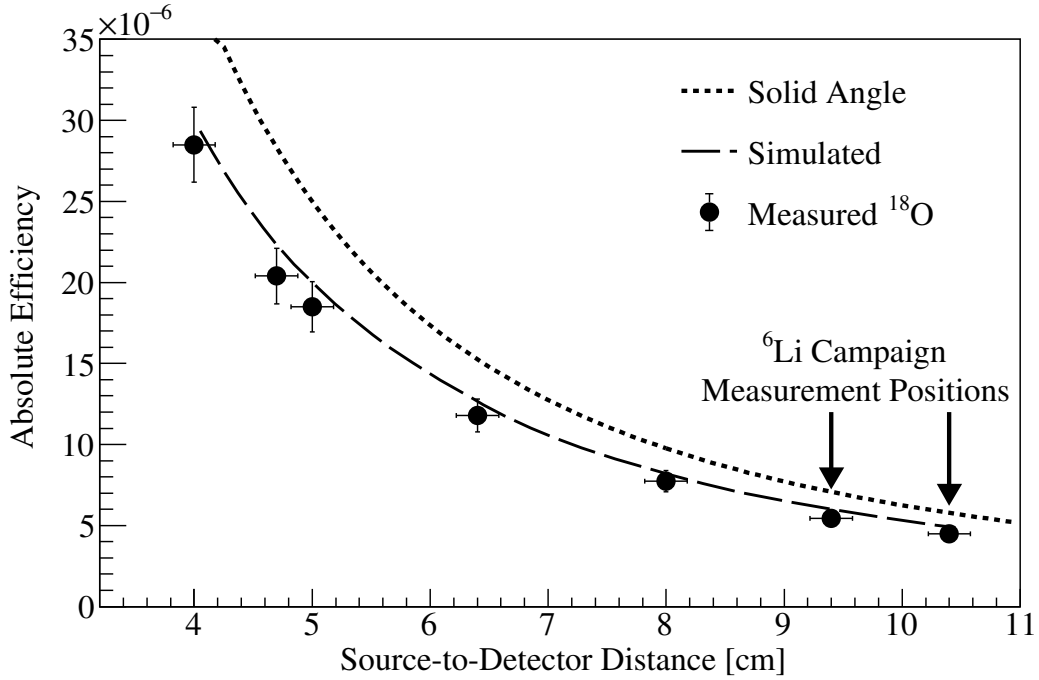

Figure 7.1 *Silicon detector absolute efficiencies vs target-to-detector distance for calculated solid angle (dotted line),* GEANT*3 simulations (long-dashed line), and measured yields of α particles from a known resonance in $^{18}O(p,\alpha)^{15}N$ (filled circles). Total errors shown for measured values.*

7.3 Peak Areas

During beam bombardment of the lithium targets, the Si detector was used to detect charged particles. The low beam energies used in this measurement meant only charged particles from the ^{6}Li(p,α)^{3}He and ^{7}Li(p,^{4}He)^{4}He reactions were emitted from the target and subsequently detected, as shown in figure 7.2. The peaks were easily attributed with either reaction and therefore the charged-particle spectra were not energy calibrated.

The peak areas, N_{peak}, for charged particles produced from the ^{6}Li(p,α)^{3}He reaction may be calculated by integrating either the ^{3}He or ^{4}He peaks in the Si detector spectra. A sample charged-particle spectrum collected from the Si detector at $E_{\mathrm{p}} = 281$ keV bombarding the Li_2O-9 target is shown in figure 7.2. The ^{4}He and ^{3}He peaks from ^{6}Li + p are clearly distinguishable from one another at channels 450 and 2150 respectively, however the ^{4}He peak has a low energy tail extending below the noise threshold. For this reason the ^{3}He peak was integrated by summing the peak contents bin by bin across channels 1300 to

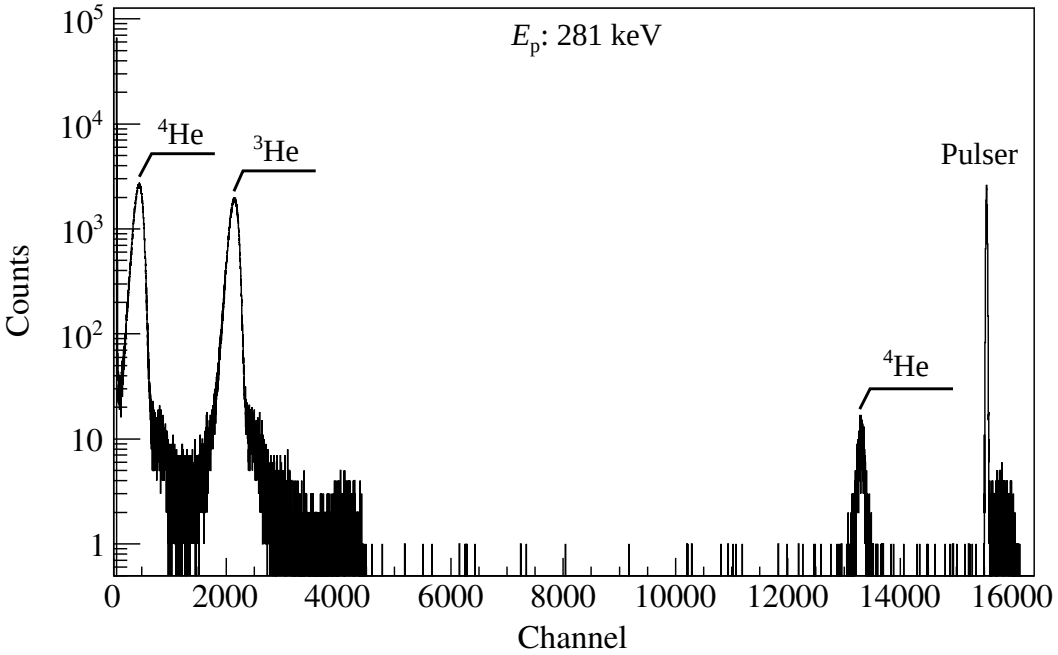

Figure 7.2 *Sample charged particle spectrum collected with the Si detector. The peaks at channels 450 and 2150 are from the ^{6}Li(p,α)^{3}He reactions' ^{4}He and ^{3}He particles respectively. The peak at channel 13300 is from the ^{7}Li(p,^{4}He)^{4}He reactions' alpha particles. The "Pulser" peak is from the PB-5 Pulse Generator (rate 10 Hz).*

3000. The (Poissonian) statistical error on the ^{3}He peak areas was $\sim 0.3\%$ for all measurements.

The ^{4}He peak from the ^{7}Li(p,α)^{4}He reaction is also observed at channel 13300 in the sample spectrum. This peak was integrated using the same approach as the (^{6}Li + p) ^{3}He peak to determine a ^{7}Li(p,α)^{4}He reaction yield. The ratio of ^{6}Li(p,α)^{3}He to ^{7}Li(p,α)^{4}He reaction yields at one set beam energy is directly proportional to the ratio of ^{6}Li/^{7}Li in the target, thus providing a cross check of how much of the target's lithium content is enriched in ^{6}Li. The ^{6}Li enrichment determined for each target was in good agreement with the expected 95%.

7.4 Angular Distributions

The emission of reaction products (ejectiles) from ion beam studies may not obey an isotropic distribution, that is the emission angle of the products may show preference to certain angles. In the centre-of-mass frame the angular distribution

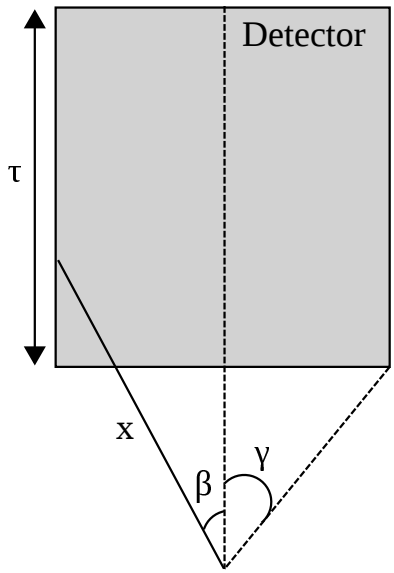

Figure 7.3 *A sketch depicting the simplified case of a rectangular detector covering a range of angles γ as used in the formalism of attenuation coefficients.*

$W(\theta, E)$ is parameterised by:

$$W(\theta, E) = 1 + \sum_{l=1} A_l(E) Q_l P_l(\cos[\theta]) \tag{7.6}$$

where $A_l(E)$ is a coefficient describing the distribution's energy dependence, P_l is a Legendre polynomial of order l as a function of the angle θ in the centre-of-mass frame, and Q_l is the attenuation coefficient defined as [83]:

$$Q_l = \frac{\int_0^\gamma P_l(\cos[\beta])\,(1 - \exp\left[-\tau x(\beta)\right])\,\sin(\beta)\,\mathrm{d}\beta}{\int_0^\gamma P_0(\cos[\beta])\,(1 - \exp\left[-\tau x(\beta)\right])\,\sin(\beta)\,\mathrm{d}\beta} \tag{7.7}$$

where γ is the half-angle subtended on the detector's front face, τ is the detector's thickness, $x(\beta)$ is the distance traversed by the radiation incident on the detector at an angle β with the detector's central axis, and P_l is a Legendre polynomial of order l as a function of the angle β. A sketch of a simplified case with a rectangular detector is shown in figure 7.3. Q_l tends to 1 with increasing source-to-detector distance and decreasing detector thickness. The collimated Si detector covered a small solid angle at $d = 9.3$ cm, $\Omega/4\pi \sim 0.6 \times 10^{-5}$, and therefore its $Q_l = 1$ for all l.

The charged particles from the ^{6}Li(p,α)^{3}He reaction are not emitted isotropically but instead follow an angular distribution which adjusted the measured peak areas depending on both the detection angle and incident beam energy. The angular

Table 7.1 *Uncertainty Budget for the ^{6}Li(p,α)^{3}He experimental yields.*

Source	Uncertainty [%] Statistical	Systematic
$N_{\text{peak}}(^3\text{He})$	~ 0.3	-
Beam Current	3	2
η_{Si}	-	9.3
$\text{W}(\theta, E)_{(\text{p},^3\text{He})}$	-	1.5

distribution of the ^{6}Li(p,α)^{3}He reaction has already been determined by previous experiments [32, 34–37, 84], and the relevant Legendre polynomial coefficients A_1 and A_2 are reported for the energy range $E_\text{p} = 0 - 1000$ keV in [84]:

$$A_1 = -0.363 + 4.02 \times 10^{-2}\ E_\text{p}^{1/2} - 1.13 \times 10^{-5}\ E_\text{p}^{3/2} \tag{7.8}$$

$$A_2 = -0.04 - 1.2 \times 10^{-4}\ E_\text{p} \tag{7.9}$$

An uncertainty of 1.5% is assigned to the angular distribution, determined by propagating 5% uncertainties quoted for the A_1 and A_2 coefficients in [84].

The ^{6}Li(p,α)^{3}He angular distribution determined from these coefficients is plotted in figure 7.4a as a function of incident proton energy for the Si detector positioned at $\theta_\text{lab} = 125°$ and in figure 7.4b as a function of ^{3}He angle in the c.m frame (for $E_\text{p} = 294.5$ keV).

7.5 Experimental Yields

The ^{6}Li(p,α)^{3}He reaction yields were calculated with equation 4.2, using the Si detector efficiency (section 7.2), the peak areas of the ^{3}He peak (section 7.3), the branching ratio $b = 1$, the angular distribution (section 7.4), and the integrated beam current.

Figure 7.5 show a sample plot of the experimental yields for the ^{6}Li(p,α)^{3}He reaction measured using protons impinging onto the Li_2WO_4-1 target. The statistical errors on the total yields were calculated by error propagation of both the Poissonian error on the peak area integration and the error from the random fluctuations in the beam current integration (3% [59]). The uncertainty budget for the experimental yields is shown in table 7.1. Additional plots of the yields measured using the other targets are provided in appendix D.

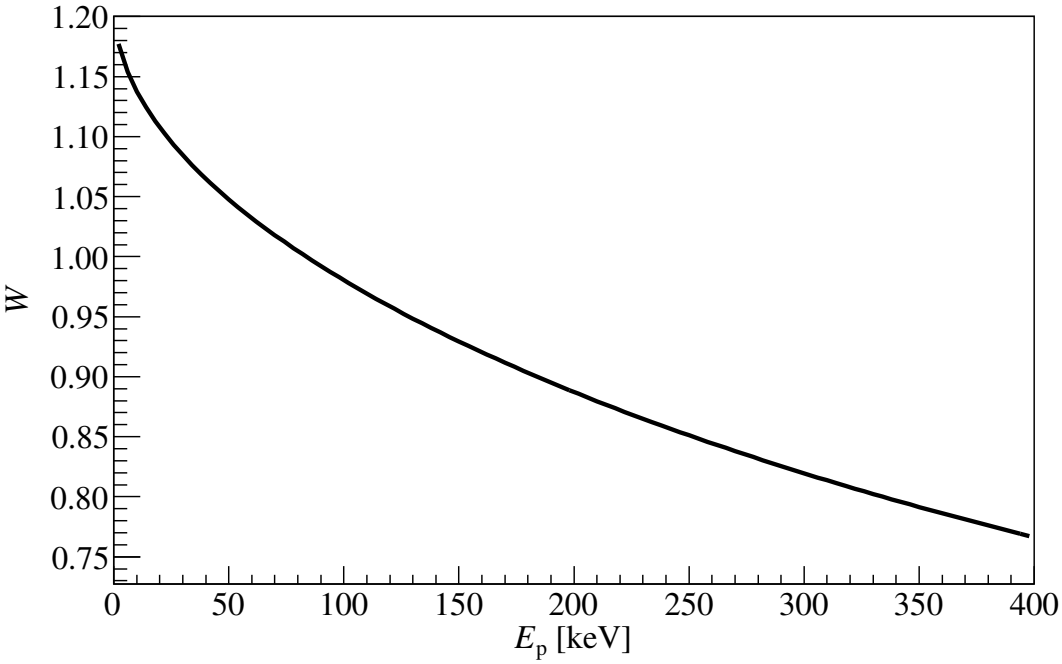

(a)

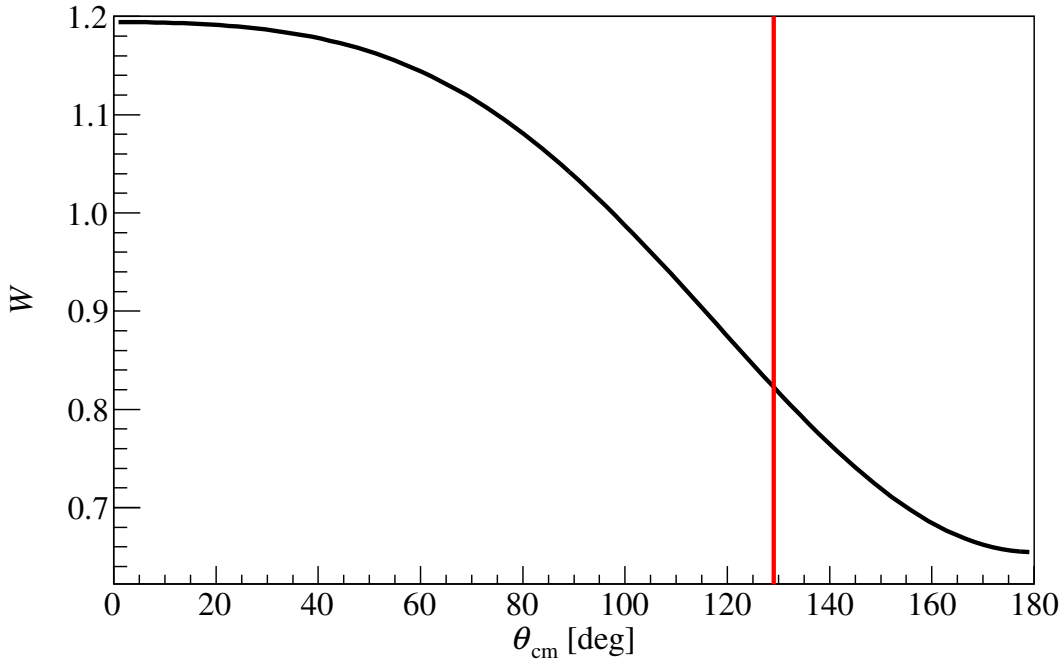

(b)

Figure 7.4 *a)* $^6Li(p,\alpha)^3He$ *angular distribution as a function of incident proton energy for* $\theta_{lab} = 125°$*. b)* $^6Li(p,\alpha)^3He$ *angular distribution for* $E_p = 294.5$ *keV as a function of* ^3He *centre of mass angle. The angle covered by the collimated Si detector is marked by the red line.*

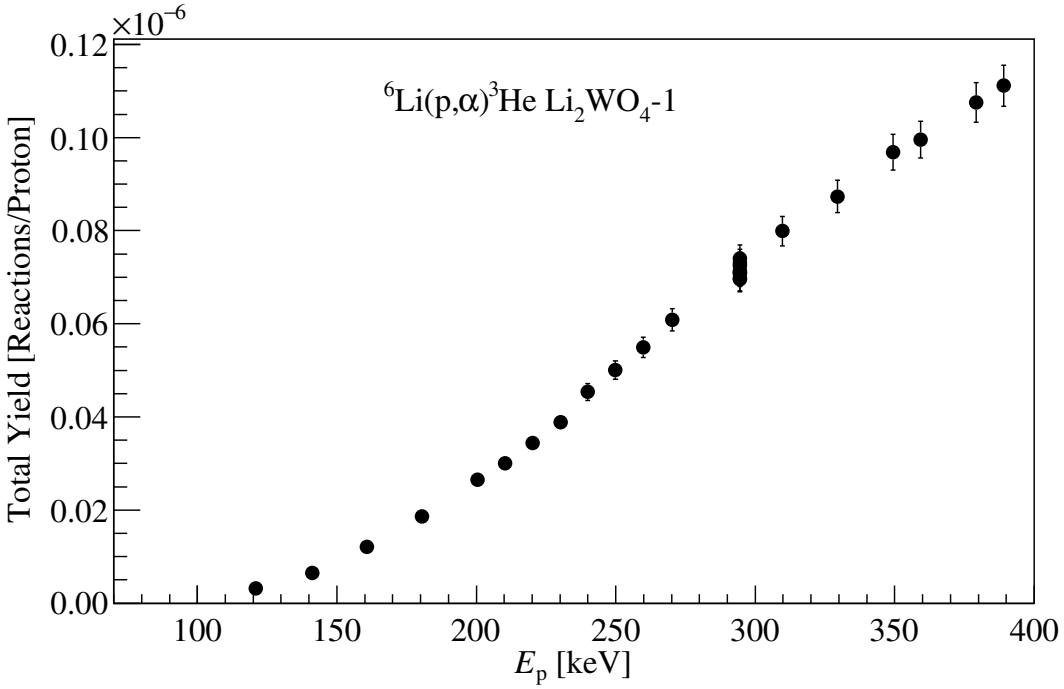

Figure 7.5 *Experimental yields measured using the Li_2WO_4-1 target for the $^6Li(p,\alpha)^3He$ reaction. Error bars are statistical. The vertical increase at $E_p \sim 295$ keV is from repeat measurements performed at the reference beam energy during the target's bombardment.*

7.6 *S*-factors

The experimental yields measured from each target were deconvolved into cross sections, using the median energy approach covered in section 4.1. Data from the Li_2O-7 and LiCl targets were omitted due to difficulties with the target profile collected in HZDR, as discussed in chapter 6. Only data from the Li_2O-9 and Li_2WO_4-1, 3, and 4 targets were used throughout this stage of the analysis. The calculations were performed using the same C++ program described in reference [56]. Specifically, the median energy was implicitly defined using equation 4.12 and a prior cross section was determined from the thin target formalism (equation 4.5). The cross section was then iteratively calculated using equation 4.13 until convergence was reached ($M \sim 1$ in equation 4.14). Cross sections at energies within E_{lab} less than 0.3 keV were re-binned, where 0.3 keV is the beam energy resolution of the LUNA-400 accelerator [59]. The S-factors were calculated directly from the cross sections using equation 2.9. Statistical uncertainties on the S-factors are obtained from the statistical uncertainties on the yields propagated through the deconvolution procedure.

The deconvolution procedure required knowledge of the target thickness, ΔE, for each measured yield. The first measurement run on each target was used to derive each target's thickness using the ΔE parameter of the DC $\rightarrow$ 0 keV peak fits (next chapter, section 8.5). The target thickness degraded (next chapter, section 8.9) during irradiation of a given target, and this degradation was modelled as a function of charge deposited on target. This model was then used to correct the target thickness for each yield in the deconvolution procedure.

The deconvolution procedure also required target profiles, $P(E_{\mathrm{lab}})$ (equation 6.2), as inputs for each target. Since the target profiles were extracted using the NRA approach at HZDR (chapter 6) *after* the ^{6}Li + p measurements at LUNA, these profile shapes were assumed to represent the worst case scenario of how inhomogeneously the ^{6}Li is distributed throughout the targets. The target profile was not known during irradiation at LUNA, therefore the deconvolution assumed the ^{6}Li distribution was uniform throughout the target thicknesses, $P(E_{\mathrm{lab}}) = 1$, for all beam energies. The systematic uncertainty introduced by this assumption was evaluated by repeating the deconvolution procedure with the inhomogeneous $P(E_{\mathrm{lab}})$ included. The effect on the S-factors when including $P(E_{\mathrm{lab}})$ was taken as a conservative systematic error, which varied between $0.7 - 6.1\%$ $(1.0 - 8.5\%)$ for the Li_2WO_4 (Li_2O) targets. The uncertainty budget is summarised later in chapter 9.

During the deconvolution procedure the S-factors were corrected for the adiabatic electron screening effect (subsection 2.1.1) using the screening potential of metallic lithium $U_{\mathrm{e}} = 203.48619$ eV [85]. The electron screening correction adjusted the S-factor by a maximum factor of 1.015 at the lowest measured $E_{\mathrm{cm}} = 61$ keV (corresponding to the measurement using an initial $E_{\mathrm{p}} = 80$ keV incident on the Li_2WO_4-4 target). S-factors corrected for electron screening are herein referred to as "bare".

Figure 7.6 shows a plot of ^{6}Li(p,α)^{3}He reaction S-factors as a function of E_{cm}. The values from this study are represented by the filled triangles for Li_2WO_4 targets and filled squares for the Li_2O-9 target, with statistical uncertainties included. Literature values from [37, 39–42] are plotted in filled and hollow black symbols, with total uncertainties included. The bare S-factor fit reported in [40] is represented by the dashed line. There is a clear offset by a factor $\sim 40 - 50\%$ between the S-factors determined at LUNA and those from the literature. The literature data has been collected by multiple different groups across many decades of study, and they are all consistent with each other (chapter

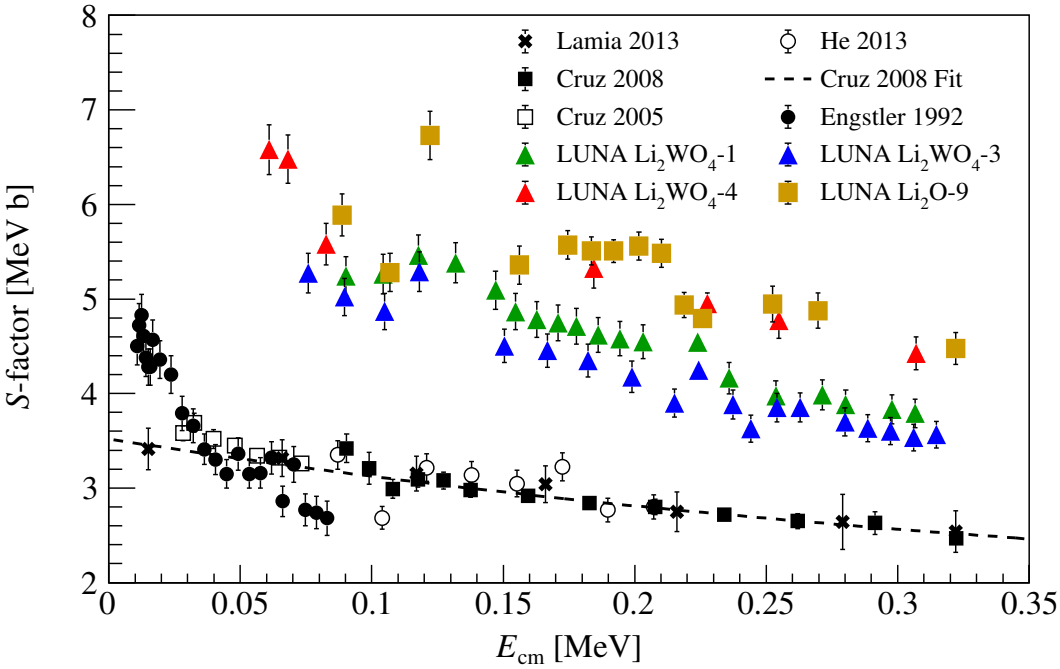

Figure 7.6 *$^{6}Li(p,\alpha)^{3}He$ reaction S-factor vs E_{cm} energy. The bare S-factor data from the current study are plotted as solid triangles and squares with statistical uncertainties. The literature values [37, 39–42] are plotted in a variety of filled and hollow black symbols with total uncertainties. The fit reported in the Cruz et al. 2008 paper for a bare S-factor is shown by the dashed line.*

3). In contrast, the present data determined from different targets are offset by a factor $\sim 5-30\%$ from each other, which indicates inconsistency in the absolute S-factor values of the measurements.

The *trend* of the present data shows a smoothly decreasing S-factor for increasing E_{cm} in agreement with the literature trend. Whilst the present data are offset from literature, the consistent trend suggests the offsets are caused by a systematic effect which was not accounted for in our analysis. In addition, whilst the Li_2WO_4 target data show a smooth trend, the Li_2O-9 data displays more scatter in the S-factors particularly around the $E_{\mathrm{cm}} = 0.122$ MeV data point. The likely explanation for this scatter is the Li_2O target profile is more prone to changes from beam-induced degradation compared to the Li_2WO_4 targets, and thus the assumption of the target profile $P(E_{\mathrm{lab}})$ remaining uniform throughout the measurements is less accurate. Regardless the systematic error assigned to $P(E_{\mathrm{lab}})$ is not sufficient to explain the $\sim 45\%$ offsets between present and literature data.

Data analysis and results for the (p,γ) channel are covered in the next chapter. The present (p,γ) channel S-factors were also systematically higher than those reported in the literature, which prompted the decision to normalise the present data to the ^{6}Li(p,α)^{3}He reaction S-factors reported by Cruz *et al.* in 2008 [40]. The normalisation procedure and final S-factors are presented later in section 9.1.

Chapter 8

^{6}Li(p,γ)^{7}Be Data Analysis and Results

Besides the measurement of the ^{6}Li(p,α)^{3}He reaction S-factor, the other main objective of this experimental campaign was the determination of the ^{6}Li(p,γ)^{7}Be reaction S-factor at energies accessible by the LUNA-400 accelerator ($E_{\rm cm} \sim 65 - 337$ keV). Similar to the (p,α) channel, the calculation of S-factors required experimental yields, which needed multiple inputs. This chapter first presents the analysis methods used to determine inputs for the yield calculations: the HPGe detector efficiency, number of detected events, and angular distributions. Next the branching ratios and experimental yields are presented. Then the target degradation effect is provided, and finally the results from deconvolving the yields into S-factors are shown at the end of the chapter.

8.1 Data Analysis Procedure

The data analysis proceeded as follows:

1. HPGe detector energy calibrations were determined from background sources.
2. The HPGe detector energy resolution was calculated from background and radioactive sources.
3. HPGe detector efficiencies were determined from both measurements

and simulations of gamma rays emitted by radioactive sources and the ^{14}N(p,γ)^{15}O reaction.

4. Gamma-ray peak areas for the primary and secondary peaks were calculated from the spectra obtained measuring the ^{6}Li(p,γ)^{7}Be reaction.

5. Angular distributions of the ^{6}Li(p,γ)^{7}Be reaction's gamma rays were extracted from the literature.

6. Branching ratios were calculated and cross-checked with the literature.

7. Experimental yields were calculated using equation 4.2 with inputs from steps $3-5$.

8. The target degradation was modelled using parameters from fits of the primary gamma-ray peaks.

9. Yields were then deconvolved into cross sections (S-factors), using knowledge of the target properties (chapter 6) and target degradation.

8.2 HPGe Energy Calibration

The HPGe detector was characterised using gamma rays emitted from standard radioactive sources of ^{137}Cs, ^{60}Co, and ^{88}Y (encased in polyethylene holders), the well known $E_{\mathrm{r}} = 259.4$ keV ^{14}N(p,γ)^{15}O resonance [62], natural background sources of ^{214}Bi, ^{40}K, and ^{208}Pb, and beam-induced background from the ^{19}F(p,$\alpha_2\gamma$)^{16}O reaction.

Whilst measurements of gamma rays emitted from the radioactive sources and ^{14}N(p,γ)^{15}O reaction were performed before and after the ^{6}Li + p measurement, gain shifts occurred during the data collection and thus the ^{6}Li(p,γ)^{7}Be spectra could not be energy calibrated using the source data. Instead for each target the energy calibration was performed using the measurements performed whilst targets were under beam, as follows: the natural background and ^{19}F(p,$\alpha_2\gamma$)^{16}O beam induced background peaks were fitted with a Gaussian to determine their peak centroid (in channels). The centroids were checked, run by run, to see if there was any significant shift ($> \pm 5$ channels). For all targets included in the final data analysis, Li_2WO_4-1, 3, 4, and Li_2O-9, the peak centroids did not change between measurements and as a result the gamma-ray spectra collected

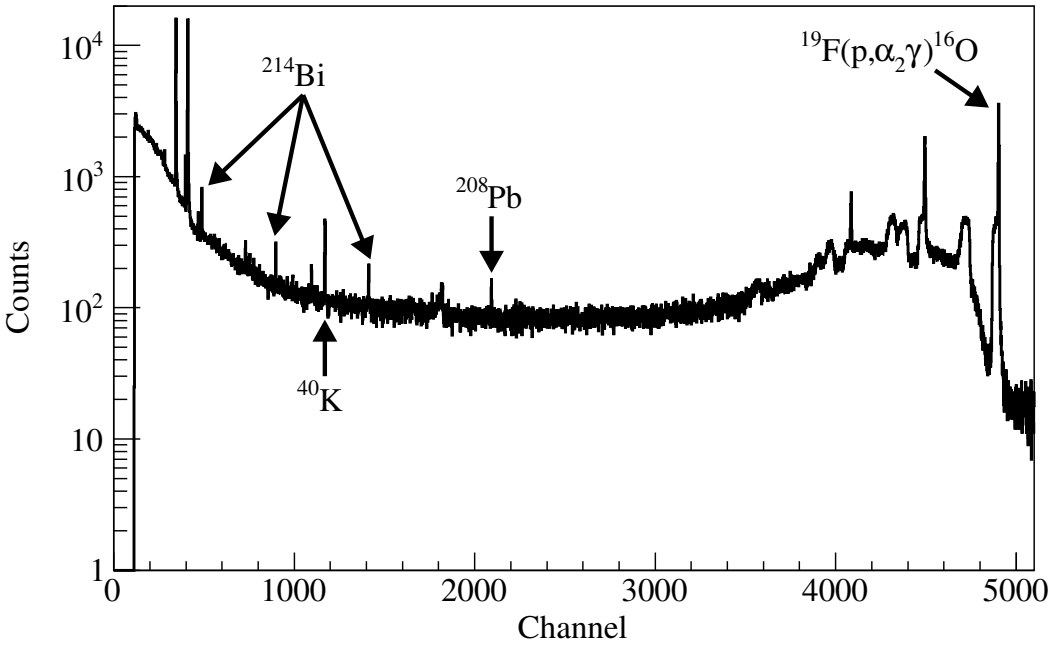

Figure 8.1 *Sample gamma-ray spectrum showing the background peaks used in the HPGe detector's energy calibration. The peaks were fitted with a Gaussian to extract their peak centroids.*

from beam bombardment on these targets required only one energy calibration per target dataset.

One spectrum per target was selected and the energy calibration performed (for low energies) using gamma-ray peaks from natural background sources of ^{214}Bi (609, 1120, and 1764 keV), ^{40}K (1461 keV), and ^{208}Pb (2615 keV), and (for higher energies) the $\sim 6.0 - 6.5$ MeV peak from the ^{19}F(p,$\alpha_2\gamma$)^{16}O beam induced background. A sample spectrum showing the background peaks used in the energy calibration is shown in figure 8.1. The gamma-ray peaks were fitted with a Gaussian to extract their peak centroids. The energies were plotted as a function of peak centroid (channel) and the data fitted with a 2$^{\text{nd}}$ order polynomial[1]. A sample calibration curve, used for the Li_2WO_4-1 target dataset, is provided in figure 8.2a. The reduced *chi*-squared is ~ 0.81. Figure 8.2b shows the residuals between the literature energies and fit, which are small (≤ 0.2 keV) compared to the HPGe energy resolution (see next section). The uncertainties on the residuals are calculated from the propagation of uncertainties in the peak centroid (from Gaussian fits) and the literature energy.

[1]The order was selected to account for non-linearities in the ADC.

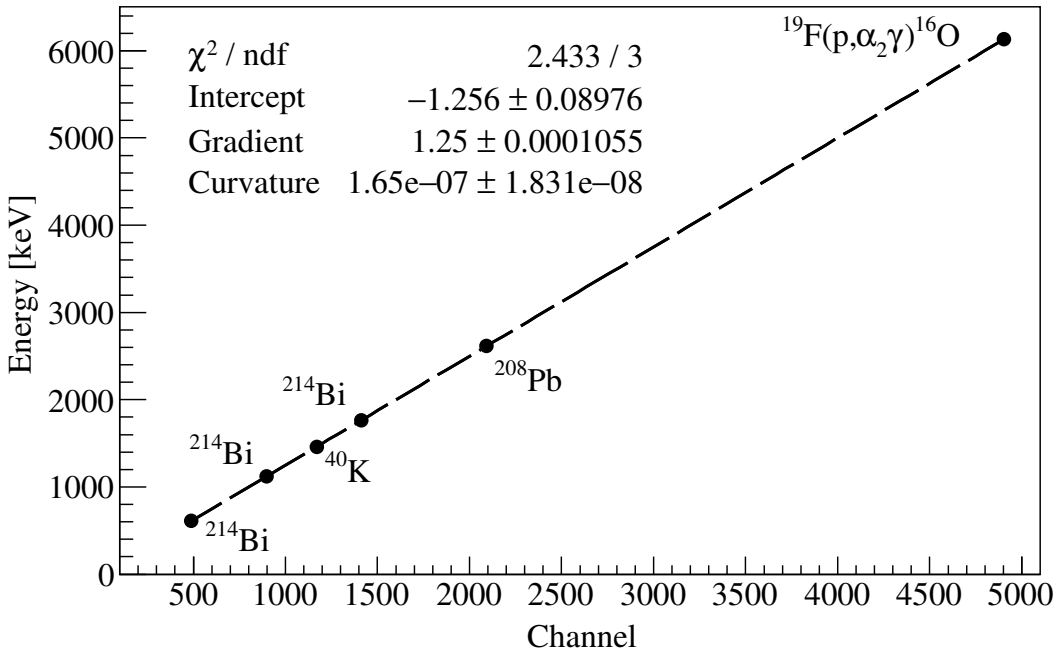

(a) *HPGe energy calibration for Li_2WO_4-1 target dataset. Circles are measured data and the dashed line represents a 2^{nd} order polynomial fit. Statistical errors are smaller than the data point symbols.*

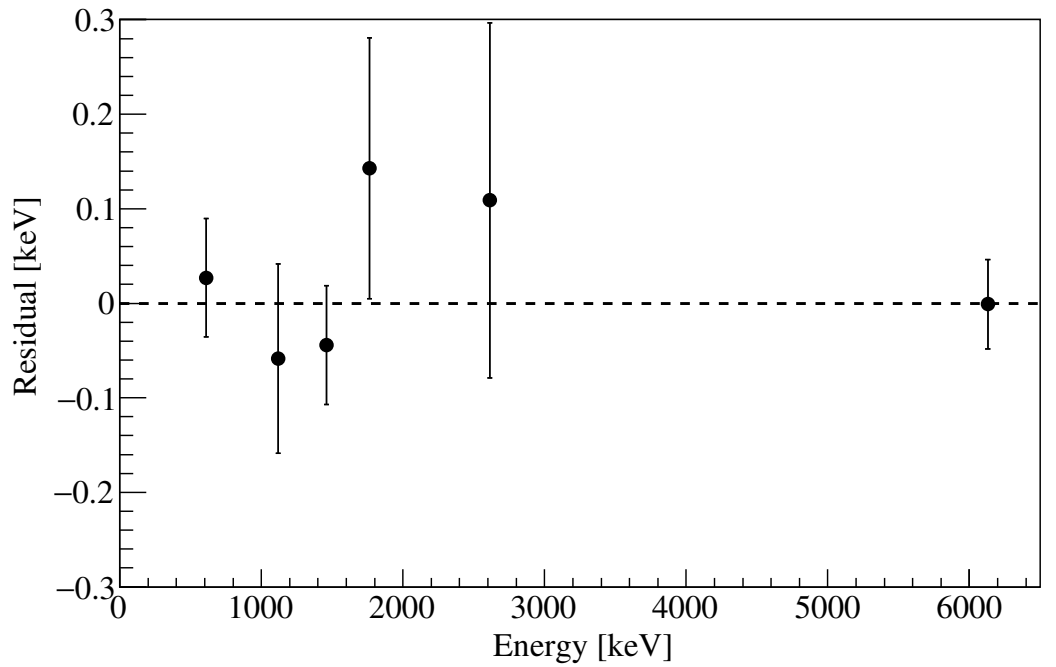

(b) *Residuals from HPGe energy calibration for Li_2WO_4-1 target dataset. Error bars are from the propagation of uncertainties in the peak centroid (from Gaussian fits) and the literature energy.*

Figure 8.2

8.3 HPGe Energy Resolution

The HPGe detector resolution was determined by using a Gaussian function to fit peaks from both the natural background and radioactive sources ^{137}Cs (662 keV), ^{60}Co (1173 and 1332 keV), and ^{88}Y (898 and 1836 keV), the Full-Width at Half-Maximum (FWHM) were extracted from the fits. The gain shift mentioned in the previous section does not affect the detector's resolution. The HPGe detector's FWHM as a function of gamma-ray energy is shown in figure 8.3a, with the data fitted using [86]:

$$\text{FWHM} = f_1 + f_2\sqrt{E_\gamma} + f_3 E_\gamma \tag{8.1}$$

where E_γ is the gamma-ray energy in keV, and the fit parameters are $f_1 = 1.59(9)$ keV, $f_2 = -0.004(6)$ keV$^{-1/2}$, and $f_3 = 7.0(8) \times 10^{-4}$. The plot of residuals is shown in figure 8.3b. The reduced *chi*-squared of the fit is ~ 0.96. The measured HPGe energy resolution of ~ 2.3 keV for a (^{60}Co) 1173 keV gamma ray is expected for this large coaxial HPGe detector [78] and means the detector was functioning correctly.

8.4 HPGe Detector Efficiency

There are two subcategories of the HPGe absolute efficiency: the full-energy photopeak efficiency, ϵ_{ph}, and the total efficiency, ϵ_{tot}. The absolute photopeak efficiency defines the probability of an incoming photon depositing all of its energy into the crystal via a combination of the photoelectric effect, Compton scattering, and (if the gamma-ray energy is greater than 1.022 MeV) pair production processes. The absolute total efficiency defines the probability of a photon depositing *some* but not all of its energy into the crystal, through any process. More information on the interaction of radiation with matter can be found in appendix A. In this work all discussed photopeak and total efficiencies are absolute efficiencies.

One of the inputs in the ^{6}Li(p,γ)^{7}Be reaction yield calculations (refer to equation 4.2) is the HPGe detector photopeak efficiency at the gamma-ray energies relevant to the reaction. For this reaction three gamma-ray transitions were observed (level diagram shown in figure 2.4). Two of these transitions, the direct captures to the ^{7}Be ground state (DC $\rightarrow$ 0 keV) and first excited state (DC $\rightarrow$ 429 keV), produced gamma rays with energies ranging from 5000 to 6000 keV (depending on the beam

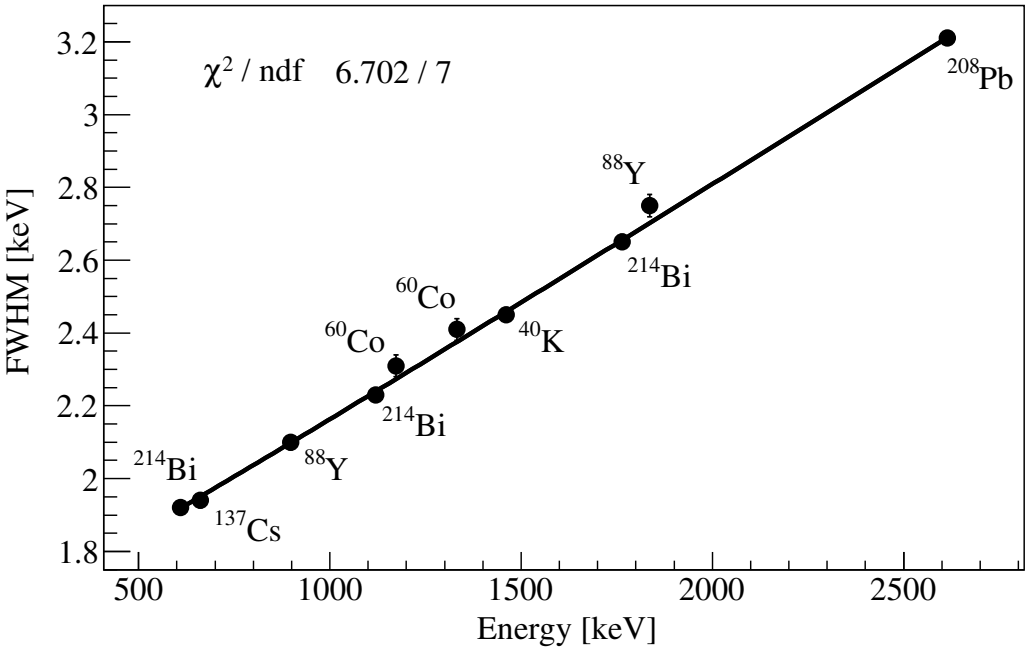

(a) *HPGe FWHM as a function of gamma-ray energy. Uncertainties are statistical only. The line represents the fit using the formalism in [86].*

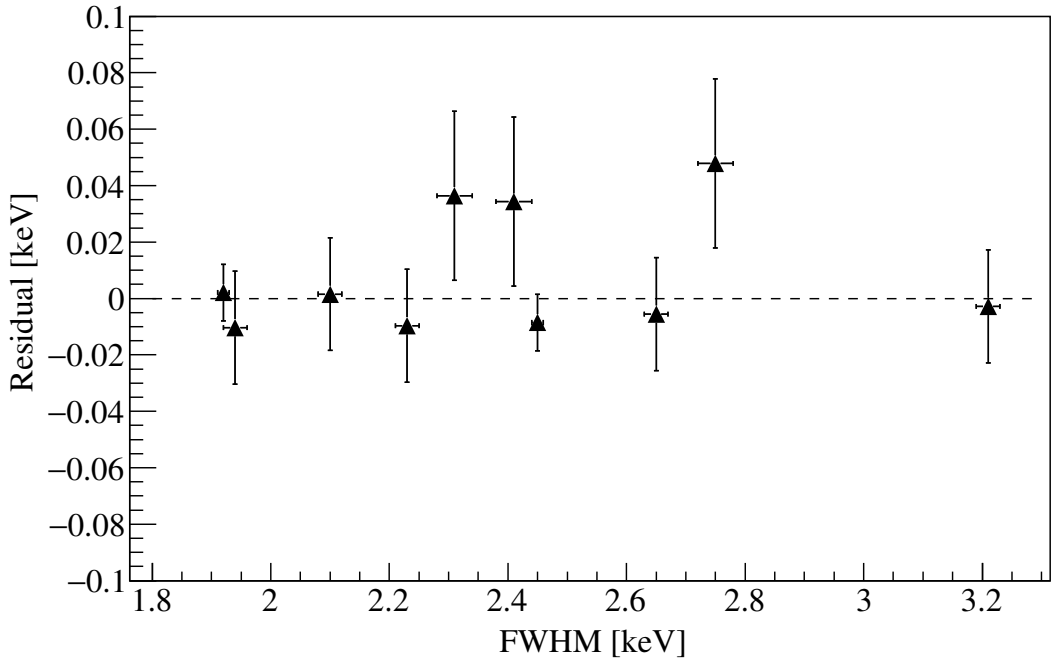

(b) *HPGe FWHM fit residuals. Horizontal error bars are the uncertainties on the FWHM parameter from the Gaussian fits. Vertical error bars are from propagating the uncertainies on the FWHM and Attie fit parameters.*

Figure 8.3

energy). The third transition, 429 → 0 keV, produced gamma rays with energy 429 keV. The HPGe detector efficiency at these energies was determined using a simulation validated by measured efficiencies. The measurements are presented first followed by the simulated efficiencies used in the yield calculations.

8.4.1 Measured Efficiencies

The HPGe efficiencies were measured at low gamma-ray energies (E_γ = 662 − 1836 keV) using gamma rays emitted from radioactive sources of ^{137}Cs, ^{60}Co, and ^{88}Y, and at high gamma-ray energies (up to E_γ = 6792 keV) by detecting gamma rays emitted from the well-known E_r = 259.4 keV ^{14}N(p,γ)^{15}O resonance [62].

The radioactive sources were mounted on a blank tantalum disc connected to the same target holders used for the ^{6}Li targets and, to ensure the same working conditions as the ^{6}Li study were met, the water cooling system was still operating. A sample gamma-ray spectrum collected from the ^{60}Co source is shown in figure 8.4. The ^{60}Co source decays by following a gamma-ray cascade, shown in figure 8.5. The two photopeaks from this cascade are observed at 1173 and 1332 keV. The peak at 2505 keV is caused by the simultaneous detection of both photopeaks, and a formalism of this "summing effect" and its impact on the detector efficiencies is discussed later in this section.

Gamma-ray peaks of characteristic energy from each source were identified and background contributions in the peak areas were removed by applying a linear background subtraction [74]. The HPGe detector photopeak efficiencies from the radioactive sources were calculated as:

$$\eta_{\text{ph}} = \frac{N_{\text{peak}}}{N_{\text{emitted}}} = \frac{N_{\text{peak}}}{A_0 \, \exp\left[-\lambda(t_{\text{meas}} - t_{\text{ref}})\right] \, I \, LT} \tag{8.2}$$

where N_{peak} is the net integrated area under the gamma-ray peak, A_0 is the source activity provided by the source manufacturers at a reference date t_{ref}, t_{meas} is the date the source was used for measurements at LUNA, λ is the decay constant[2] of the source, I is the intensity of the gamma ray under study, and LT is the live time[3], measured by the MAESTRO DAQ, taken to collect the spectrum. At time

[2]The decay constant is defined as the "probability per unit time for the decay of an atom" [87], and is inversely proportional to the radioactive half-life: $\lambda = \ln(2)/t_{1/2}$.

[3]Live time measures the time a detector + DAQ system is able to collect and process charge signals, in contrast to the real time which measures the overall elapsed time over which the measurement is performed.

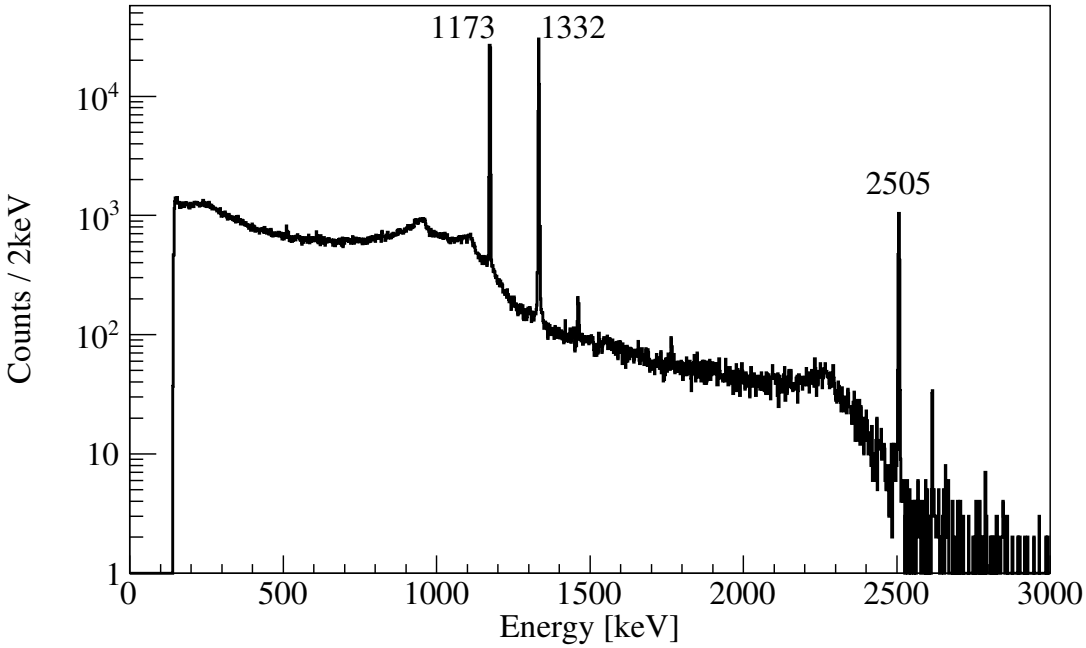

Figure 8.4 *Sample gamma-ray spectrum measured with the HPGe detector positioned at source-to-detector distance $d = 1.7$ cm using gamma rays emitted from the ^{60}Co source. The photopeaks at 1173 and 1332 keV and the sum peak at 2505 keV are labelled.*

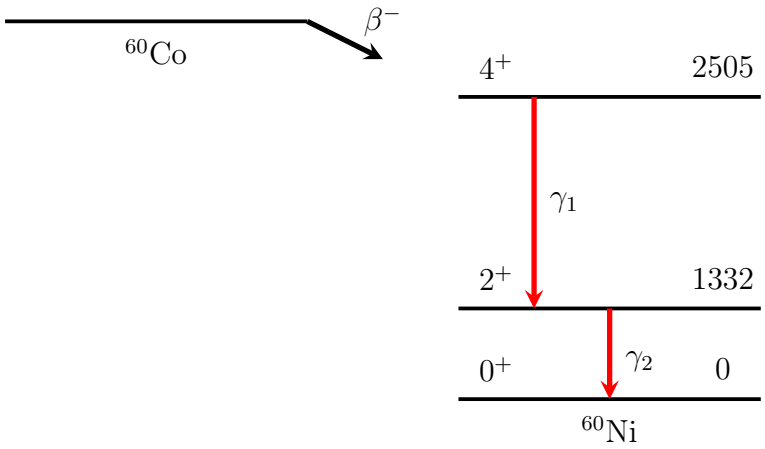

Figure 8.5 *Diagram of the ^{60}Ni level scheme. The transitions corresponding to energies 1173 keV (γ_1) and 1332 keV (γ_2) have been indicated by bold red arrows.*

of measurement the ^{137}Cs, ^{60}Co, and ^{88}Y sources had known activities of 5.41(6), 8.18(6), and 4.27(6) kBq[4], respectively.

To reduce the impact of noise in the electronic chain (section 5.5) contributing to the low channel counts, a soft threshold was set in the MAESTRO DAQ corresponding to $E_\gamma \simeq 150$ keV in the spectra. This is shown by the sharp drop in counts in figure 8.4. A natural background spectrum was scaled to the live time of the source spectrum and subtracted from it, then the measured total efficiencies were calculated as:

$$\eta_{\text{tot}} = \frac{N_{\text{thresh}\rightarrow\text{peak}}}{A_0 \, \exp\left[-\lambda(t_{\text{ref}} - t_{\text{meas}})\right] \; I \; LT} \tag{8.3}$$

where $N_{\text{thresh}\rightarrow\text{peak}}$ is the net integrated area from the threshold energy up to and including the photopeak counts. The full energy range was integrated to account for all gamma-ray interaction processes in the crystal, including the photopeak, Compton continuum, and escape peaks, described in appendix A. The software threshold presented a problem: the measured total efficiency was an underestimate of the actual value. This is addressed later in this section.

Measurements with radioactive sources were performed before and after the irradiation of the ^{6}Li targets. The photopeak efficiencies at $E_\gamma = 662$ keV (from ^{137}Cs) were compared between repeat measurements, where a discrepancy of $\sim 11\%$ was found. Further tests found the two holders (figure 5.5) used during the campaign had backing flanges constructed of one of two materials: stainless steel (target holder 1) or aluminium (target holder 2). Since both holders were used during the ^{6}Li + p measurements, the HPGe efficiencies were determined for both holder setups.

The ^{14}N(p,γ)^{15}O resonance was populated by bombarding TiN targets (deposited on a tantalum backing) with a proton beam ($E_{\text{lab}} = 295$ keV). Two cascades (highlighted in red in figure 8.6) present in the decay of ^{15}O* were studied: the cascade through levels 7556 $\rightarrow$ 6792 $\rightarrow$ 0 which produced gamma rays with energies 765 and 6792 keV, and the cascade through levels 7556 $\rightarrow$ 6172 $\rightarrow$ 0 which produced gamma rays with energies 1384 and 6172 keV.

A sample gamma-ray spectrum measured by the HPGe detector for protons bombarding the TiN target is shown by the black line in figure 8.7, with a

[4]The Becquerel (Bq) is used to quantify the activity of radioactive material. One Becquerel is equal to one disintegration per second.

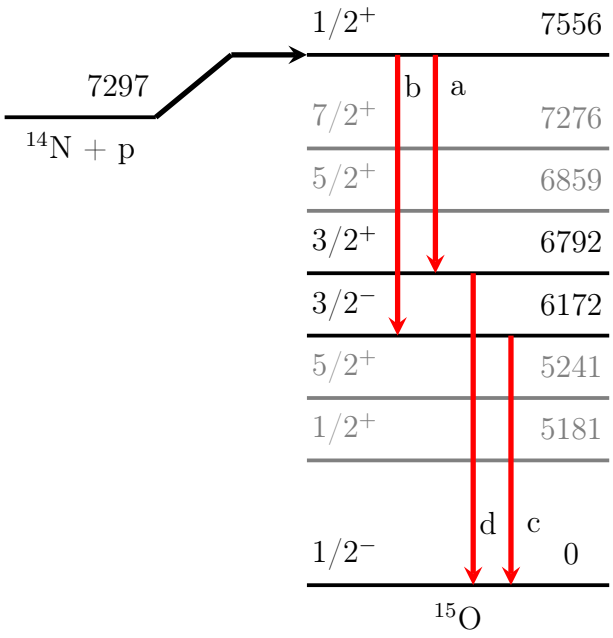

Figure 8.6 *Diagram of the $^{14}N(p,\gamma)^{15}O$ reaction level scheme. The transitions corresponding to energies 765 keV (a), 1384 keV (b), 6172 keV (c), and 6792 keV (d) have been indicated by bold red arrows.*

natural background spectrum measured at LUNA shown by the red line. Peaks corresponding to the four gamma-ray energies under study are marked by the arrows. Ideally to determine the photopeak efficiencies of the HPGe detector at these gamma-ray energies we would have used knowledge of the TiN target stoichiometry to determine the effective stopping power at the resonance energy $E_{\text{lab}} = 295$ keV. Then, similar to the approach used to calculate the Si detector efficiency, the stopping power would be used in equation 7.3. However, the TiN targets did not have well understood stoichiometries and directly measuring the HPGe efficiencies at the ^{14}N(p,γ)^{15}O reaction's gamma-ray energies was not possible. Instead, a relative approach was used. First the measured natural background spectrum, shown in figure 8.7, was scaled to the live time of the ^{14}N(p,γ)^{15}O spectrum and subtracted from it. Then the photopeaks at the studied gamma-ray energies (765, 1384, 6172, and 6792 keV) were integrated. Next, the peak area ratios $N_{\text{peak}}(6792)/N_{\text{peak}}(765)$ and $N_{\text{peak}}(6172)/N_{\text{peak}}(1384)$ were calculated. Finally, the photopeak efficiencies measured at low energies using the radioactive sources were interpolated at 765 keV and 1384 keV, and the

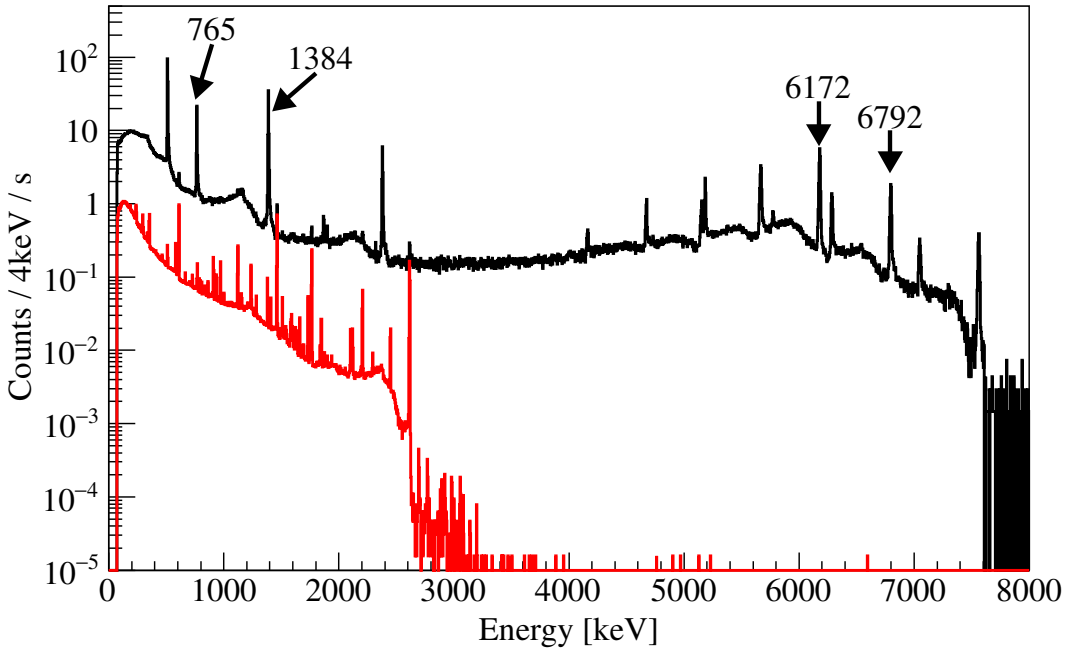

Figure 8.7 *Sample gamma-ray spectra measured by the HPGe detector for both protons bombarding the TiN target (black) and the natural gamma-ray background measured at LUNA (red). Spectra are scaled to their respective measurement times.*

area ratios used to calculate the photopeak efficiencies at 6172 keV and 6792 keV:

$$\eta_{\mathrm{ph}}(6792) = \frac{N_{\mathrm{peak}}(6792)}{N_{\mathrm{peak}}(765)}\eta_{\mathrm{ph}}(765) \tag{8.4}$$

$$\eta_{\mathrm{ph}}(6172) = \frac{N_{\mathrm{peak}}(6172)}{N_{\mathrm{peak}}(1384)}\eta_{\mathrm{ph}}(1384) \tag{8.5}$$

8.4.2 Summing Corrections

Sources typically decay via complex decay patterns and multiple gamma rays may be emitted at similar times. With a combination of close source-to-detector geometry and multiple gamma rays it is possible that two gamma rays are detected within a timescale shorter than the temporal resolution of the HPGe detector. This detection will affect the measured efficiencies of the detector, resulting in a well-documented effect [62, 88, 89] known as True Coincidence Summing (TCS).

Consider the case of a simple energy level scheme representing two excited states

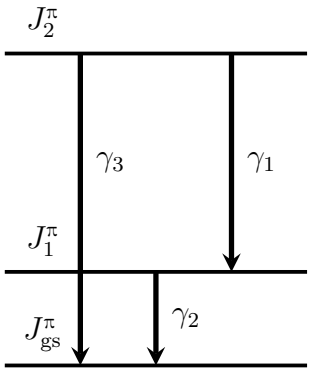

Figure 8.8 *A simple level diagram showing gamma-ray cascades referred to in the explanation of true coincidence summing effects.*

and the ground state within a nucleus, as shown in figure 8.8. There are three available energy levels, and we will assume the three possible cascades, γ_1, γ_2, and γ_3, are allowed. We will also assume the first excited state (J_1) has a very short lifetime (< 1 ns). Starting from the second excited state (J_2), the nucleus may decay via gamma emission to its ground state via two possible paths: either by emitting γ_3, or by emitting γ_1 closely followed by γ_2 in a cascade. One would therefore expect to measure three distinct photopeaks at the corresponding gamma-ray energies with intensities equivalent to the number of gamma rays emitted from each respective energy level.

However, if both gamma rays in the cascade are detected with their full energy, on a timescale shorter than the detector's temporal resolution, this results in a peak in the spectrum at an energy equal to the sum of the two gamma-ray energies. This effect is known as "summing-in" as it will enhance the counts in the peak at energy γ_3. Consequently there will be fewer events recorded at the individual energies of the two cascade gamma rays (γ_1 and γ_2), known as "summing-out". "Summing-out" also occurs if only one of the cascade gamma rays is detected with its full energy whilst the other deposits any amount of energy into the detector, whereby events are lost from the full-energy peak of the first gamma-ray. These "summing-in" and "summing-out" effects, herein referred to collectively as TCS effects, will affect the determined efficiencies of the detector and become more pronounced at larger solid angles.

For a cascade through i excited states, the yields of the measured gamma rays

follow [62]:

$$Y^{\mathrm{gs}} = R\left[b_{\mathrm{gs}}\eta_{\mathrm{ph}}(E_{\mathrm{gs}}) + \sum_i b_i\eta_{\mathrm{ph}}(E_i^{\mathrm{pri}})\eta_{\mathrm{ph}}(E_i^{\mathrm{sec}})\right] \tag{8.6}$$

$$Y_i^{\mathrm{pri}} = Rb_i\eta_{\mathrm{ph}}(E_i^{\mathrm{pri}})\left[1 - \eta_{\mathrm{tot}}(E_i^{\mathrm{sec}})\right] \tag{8.7}$$

$$Y_i^{\mathrm{sec}} = Rb_i\eta_{\mathrm{ph}}(E_i^{\mathrm{sec}})\left[1 - \eta_{\mathrm{tot}}(E_i^{\mathrm{pri}})\right] \tag{8.8}$$

where R is the number of reactions per unit incident beam charge, Y^{gs} is the measured (summing-affected) yield of the transition to the ground state, Y_i^{pri} and Y_i^{sec} are the measured (summing-affected) yields of the transitions through the ith excited state via primary and secondary transitions, respectively, b_{gs} and b_i are the branching ratios for the respective transitions to the ground state and through the ith excited state, η_{ph} and η_{tot} are the respective photopeak and total efficiencies, and E_{gs}, E_i^{pri}, and E_i^{sec} are the gamma-ray energies. It should be noted that equations 8.6, 8.7, and 8.8 only hold for "isotropic angular distributions and in the absence of any angular correlation between γ rays" [29].

For almost all efficiency measurements performed in close geometry ($d \leq 7$ cm) TCS effects had to be taken into account. The exception being measurements of the 662 keV gamma ray emitted from the β^- decay of ^{137}Cs, which is the only possible gamma ray emitted from this decay and therefore its measured efficiency cannot be affected by TCS effects. In this study two approaches for correcting summing effects were investigated: the first by applying an analytical correction (curves in figure 8.9), and the second by using photopeak and total efficiencies deduced from a Monte Carlo simulation of the experimental setup.

The measured HPGe photopeak efficiencies were determined for seven distances across $1.7 - 26.7$ cm between the source and detector-end-cap. Figure 8.9 shows the HPGe photopeak efficiencies as a function of gamma-ray energy for five of the distances and for sources mounted on target holder 1 (stainless steel flange). The curves represent the summing corrected efficiencies calculated by a collaborator at LUNA [90] using an analytical approach [62]. The measured efficiencies at the closest distances ($d \leq 7$ cm) were reduced due to TCS (summing-out) effects such that they were offset lower than the analytical curves. The correction due to summing effects is clearly largest for the distance of 1.7 cm, which was used for the ^{6}Li(p,γ)^{7}Be data collection. Plots of photopeak efficiency for all distances and both target holders are shown in appendix B.

The analytical correction presented two shortcomings in its approach. The first

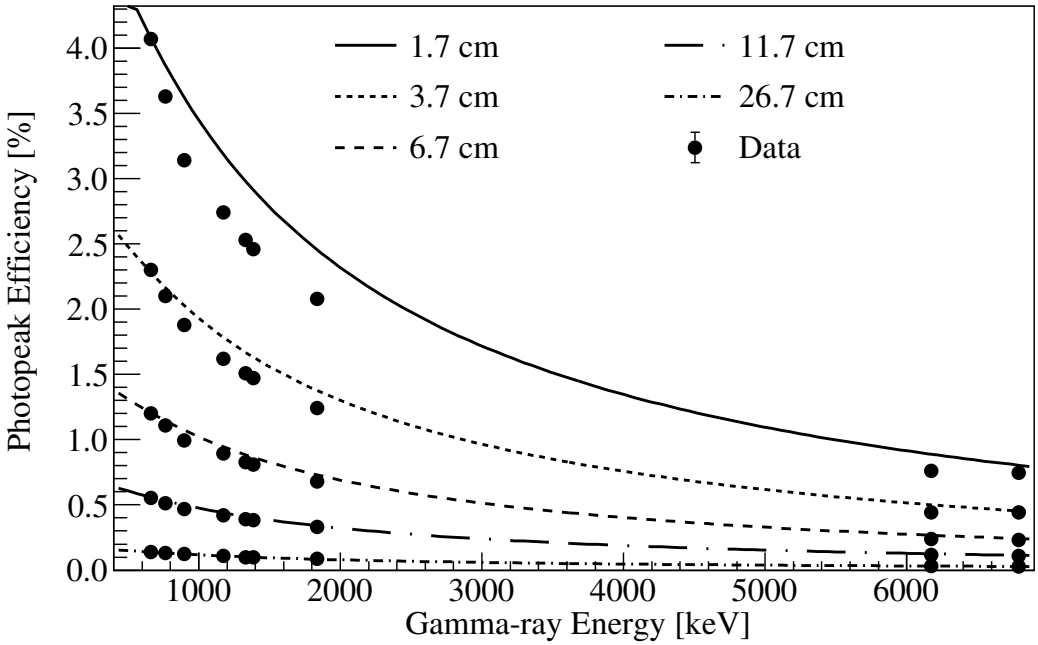

Figure 8.9 *Measured photopeak efficiency vs gamma-ray energy determined for the HPGe detector. The sources were mounted on target holder 1. The circles are measured values, the curves represent the photopeak efficiencies corrected for summing effects using an analytical approach [90]. Such corrections are largest at the shortest distance measured (1.7 cm), as expected.*

was the analytical procedure required accurate knowledge of the HPGe total efficiencies. However we must recall in this study calculations of the total efficiencies (equation 8.3) were affected by the low-energy threshold in the spectra. This threshold effectively "cut off" the low-energy tail of the Compton continuum, thereby removing information needed for the total efficiency calculation. Our analytical procedure therefore lacked accurate inputs from the total efficiencies. The second problem was the analytical approach assumed the emission point of the gamma rays from the radioactive sources to be the same as for the ^{6}Li targets. However the source holder for the radioactive sources is thicker (463 µm) than both the TiN and ^{6}Li-enriched targets (of order 0.45 µm), meaning a different emission point of the gamma-rays and therefore a different solid-angle subtended by the HPGe detector. As a result the photopeak efficiencies measured using gamma rays from the radioactive sources are systematically lower than those expected for gamma rays emitted from the ^{6}Li targets.

The Monte Carlo simulation did not encounter either of these problems. The simulation avoided low energy thresholds in the simulated spectra allowing total

efficiencies to be directly calculated. The simulation also provided the user with full control of the setup geometry thus allowing the target-to-detector geometry to be fine-tuned. For these reasons it was decided to correct the TCS effects on the photopeak and total efficiencies using a Monte Carlo simulation, instead of analytically. These simulated efficiencies were later used in the analysis of the ^{6}Li(p,γ)^{7}Be reaction, and the results from the simulations will now be summarised.

8.4.3 Simulated Efficiencies

The ^{6}Li solid-target setup was simulated using a Monte Carlo simulation written in C++ implementing the GEANT4 [91] version 10.2 source code. The purpose of the simulations was twofold, first to check the Ge crystal geometry was well understood by comparing simulated efficiencies with measurements (thereby validating the simulated HPGe crystal geometry), and the second to determine summing corrected efficiencies for the ^{6}Li(p,γ)^{7}Be data analysis.

The simulation used the GEANT4 standard Livermore (LIV) and Low Background Experiments (LBE) physics lists [92]. The LIV physics describes the photoelectric, Compton scattering, and pair production processes across $E_{\gamma} = 0 - 100$ TeV. The LBE physics is recommended by GEANT4 code developers for simulating measurements performed in low background environments, such as those encountered in LUNA. These two physics lists have been validated in previous experiments at LUNA *e.g.* [56, 93].

The simulated geometry included the target chamber, the target with tantalum backing, the water downstream from the target, and the HPGe detector with relevant casings. A simplified image of the geometry with relevant thicknesses is shown in figure 8.10a, with the geometry (wireframe view) simulated in Geant4 shown in figure 8.10b.

Prior to the ^{6}Li campaign the HPGe was sent to the Ortec manufacturer for maintenance, which involved stripping dead layers away from the outer edges of the crystal, and therefore the original crystal geometry outlined in the detector's original specification was no longer reliable. Starting from the manufacturer specifications, the Ge crystal dead layers were adjusted in the simulation until the simulated efficiencies agreed (within 4%) with measured ones at gamma-ray energies between $662 - 1836$ keV, as shown in figure 8.11. As a further check,

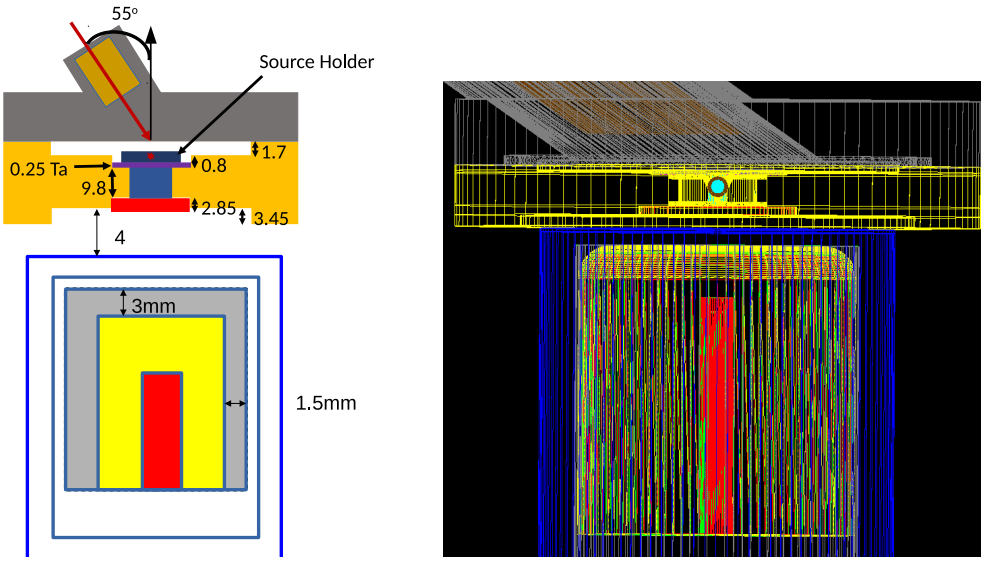

(a) (b)

Figure 8.10 *a) A simplified image of the Geant4 geometry. The dead Ge dead layers are shown in grey, the active Ge is shown in yellow. Units in mm. Not to scale. b) Wireframe view of the geometry simulated in* GEANT4.

Table 8.1 *Total efficiencies above experimental threshold ($E_\gamma^{thresh} \sim 150$ keV) for measured and simulated singles. Statistical errors quoted.*

Source	Gamma Energy [keV]	Holder 1		Holder 2	
		Measured η_{tot} [%]	Simulated η_{tot} [%]	Measured η_{tot} [%]	Simulated η_{tot} [%]
^{137}Cs	662	13.10(5)	12.56(4)	13.75(3)	13.12(4)
^{60}Co	1252.5	12.47(2)	12.78(3)	12.62(3)	13.16(3)

the measured and simulated total efficiencies determined from the ^{137}Cs and ^{60}Co sources were cross-checked and found to be in good agreement, as shown in table 8.1. The ^{60}Co total efficiency was calculated by integrating the counts up to 1173 keV and 1332 keV separately, then taking the average of the two.

Gamma rays characteristic of the radioactive sources and ^{14}N(p,γ)^{15}O reaction measured during the campaign were simulated with branching ratios and angular correlations [83, 94, 95] included. Specifically the ^{60}Co and ^{88}Y cascades used angular correlation Legendre polynomial coefficients from the IAEA (International Atomic Energy Agency) 2007 reference [96] and the ^{15}O* cascades used coefficients measured at LUNA and reported in the Ph.D. thesis of M. Marta [97].

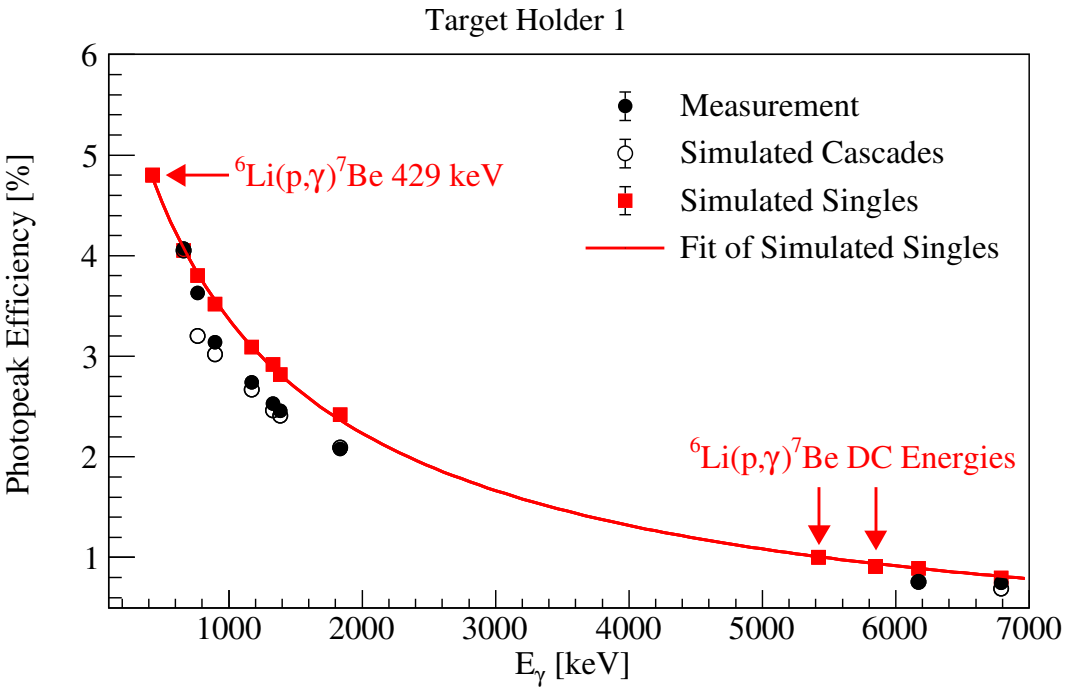

(a)

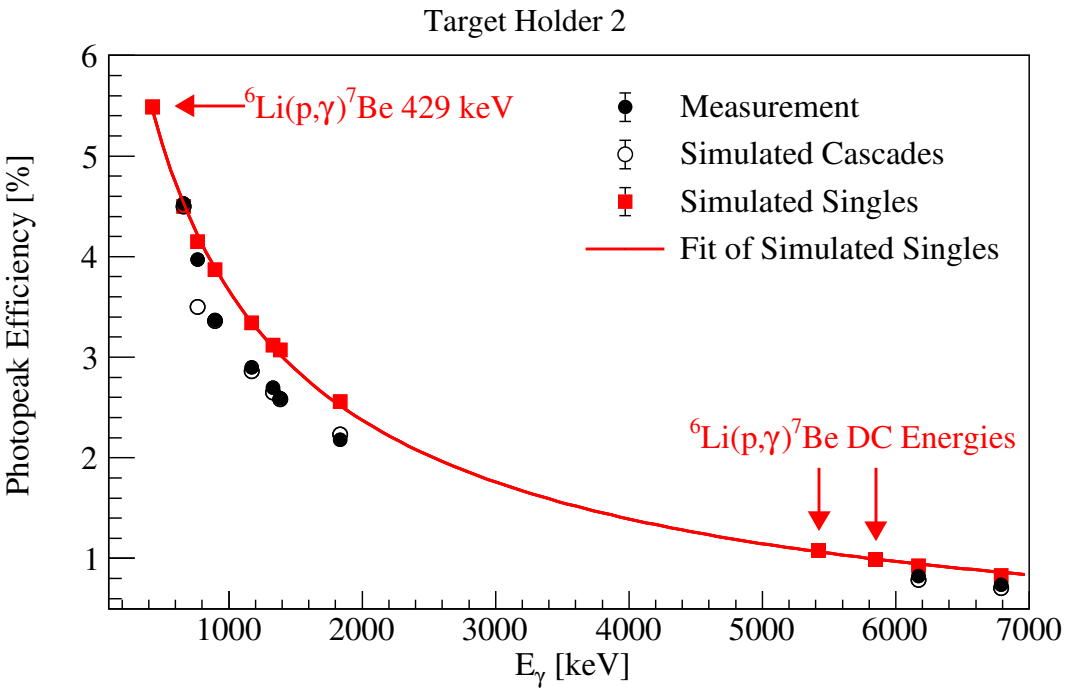

(b)

Figure 8.11 *HPGe photopeak efficiencies for measured (filled black circles), simulated cascades (hollow black circles), and simulated singles (red squares). A fit of the simulated photopeak efficiencies (for singles) is included to guide the eye. Statistical error bars are smaller than the symbols.*

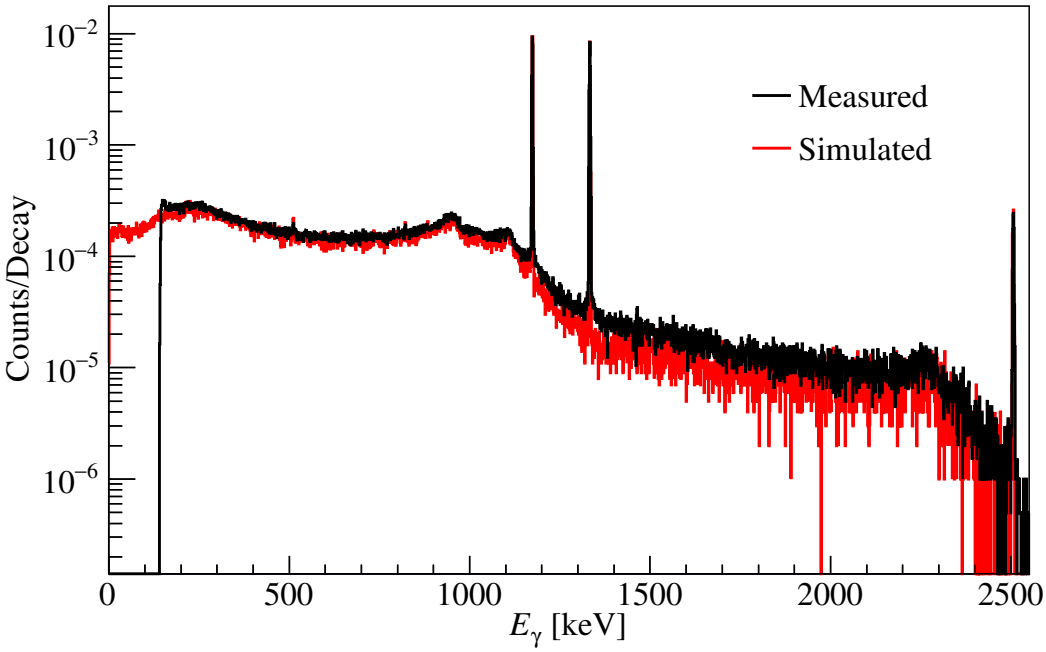

Figure 8.12 *Sample gamma-ray spectra from measurement (black) and simulation (red) of ^{60}Co decay. Both spectra are scaled to the number of 1332 keV gamma rays emitted from the polyethylene source holder. Natural background has been subtracted from the measured spectrum.*

A comparison of the measured (black) and simulated (red) gamma-ray spectra collected for a ^{60}Co source, scaled to the number of 1332 keV gamma rays emitted from the source, is provided in figure 8.12. Natural background (normalised to the spectra live times) has been subtracted from the measured spectrum. The simulated spectrum was smeared by convoluting the bin counts at each gamma-ray energy with a Gaussian of FWHM equal to the measured HPGe energy resolution defined by equation 8.1 (section 8.3).

After the simulated Ge crystal geometry was validated, summing corrections were determined from the simulation at gamma-ray energies ranging $662 - 6792$ keV by simulating gamma rays emitted individually (*i.e.* independently from one another) from the polyethylene source holder. The simulated and analytical summing corrections are in good agreement, as shown in table 8.2.

After cross-checking the summing corrections, the simulated emission point of the gamma-rays was changed from the centre of a polyethylene source holder to that of a ^{6}Li-enriched target (physical thickness $= 0.45\,\mu$m), thereby reproducing the geometry of the ^{6}Li + p measurement. The effect of the beamspot on the

Table 8.2 *Summing corrections from the analytical (analy.) and simulation (sim.) approaches. Differences in percentage points (p.p.) between 0.5 and 6.5 are also quoted.*

Source	Gamma-ray Energy [keV]	Target Holder 1 Analy. [%]	Target Holder 1 Sim. [%]	Target Holder 1 Diff. [p.p.]	Target Holder 2 Analy. [%]	Target Holder 2 Sim. [%]	Target Holder 2 Diff. [p.p.]
^{137}Cs	662	0	0	0	0	0	0
^{15}O*	765	14.3	15.8	< 2.0	16.0	15.6	< 0.5
^{88}Y	898	13.0	14.2	< 1.5	15.1	13.2	< 2.0
^{60}Co	1173	13.8	13.5	< 0.5	16.4	14.5	< 2.0
^{60}Co	1332	15.1	16.0	< 1.0	16.4	15.1	< 1.5
^{15}O*	1384	14.3	14.5	< 0.5	16.2	15.8	< 0.5
^{88}Y	1836	15.2	13.6	< 2.0	17.4	12.9	< 5.0
^{15}O*	6172	15.8	15.0	< 1.0	19.0	14.7	< 4.5
^{15}O*	6792	17.0	12.5	< 5.0	21.0	14.6	< 6.5

HPGe efficiencies was tested by simulating gamma rays emitted with energies corresponding to the ground state (DC $\rightarrow$ 0 keV), primary (DC $\rightarrow$ 429 keV), and secondary (429 keV) peaks, where the DC gamma-ray energies were calculated at $E_{\mathrm{cm}} = 240$ keV:

$$E_{\gamma} = E_{\mathrm{cm}} + Q - E_{\mathrm{x}} + \Delta E_{\mathrm{Dopp}} - \Delta E_{\mathrm{rec}} \tag{8.9}$$

where E_{γ} is the γ-ray energy, Q is the Q-value (5606.85 keV, equation 2.1) of the reaction, E_{x} the excitation energy of the final state being occupied, ΔE_{rec} is the energy of the recoil nucleus, and ΔE_{Dopp} is the Doppler shift of the gamma rays parametrised later in equations 8.13 and 8.14, respectively.

The two geometries, point-like and elliptical beamspot, were simulated with the beamspot in the second geometry conservatively treated as a 20 mm by 10 mm ellipse (figure 8.13) centred on and uniformly distributed throughout the target thickness. The difference between simulated efficiencies determined from both geometries are summarised in table 8.3. Additional tests were performed for a smaller sized beamspot centred on different target positions, and are summarised in appendix C. Adjusting the beamspot position changes the photopeak and total efficiencies within 4% compared to simulating the point-like geometry. For each ^{6}Li + p measurement performed at LUNA the exact geometry of the beamspot was not known, therefore to determine the simulated photopeak and total efficiencies used in the data analysis the point-like geometry was simulated. The effect of the beamspot size and position was treated as an additional systematic uncertainty of 4% on the photopeak and total efficiencies.

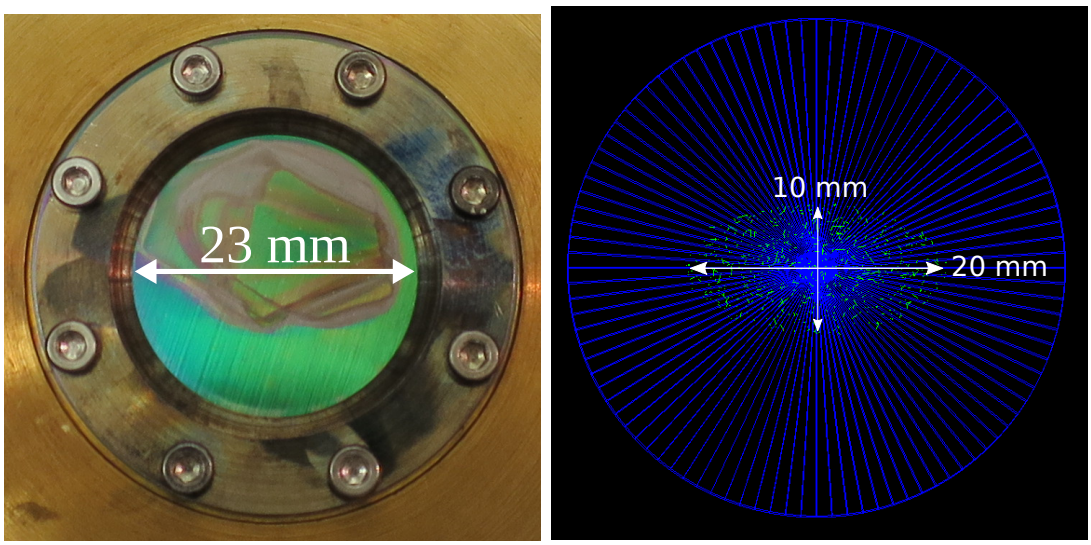

(a) **(b)**

Figure 8.13 *a) Typical beamspot deposited on ^{6}Li-enriched targets during LUNA campaign. b) Simulated conservative (too large and diffuse) beamspot.*

Table 8.3 *Effect of including $20 \times 10 mm^2$ beamspot on efficiencies at gamma-ray energies relevant to ^{6}Li(p,γ)^{7}Be reaction.*

E_γ [keV]	Effect on η_{ph} [%]	Effect on η_{tot} [%]
429	3.8	1.8
5419 (DC $\rightarrow$ 429 keV)	-2.1	0.01
5818 (DC $\rightarrow$ 0 keV)	-0.1	-0.1

8.4.4 Final Efficiencies used in the Data Analysis

After the beamspot tests, the simulation was used to model gamma rays emitted individually from the centre of a ^{6}Li-enriched target. The gamma-rays were simulated with energies calculated from equation 8.9 for $E_{\text{cm}} = 0 - 343$ keV ($E_{\text{lab}} = 0 - 400$ keV), which is the full energy range covered by the LUNA-400 accelerator. The gamma-ray energies ranged across $E_\gamma = 5607 - 5971$ keV (corresponding to DC $\rightarrow$ 0 keV) and $E_\gamma = 5178 - 5522$ keV (corresponding to DC $\rightarrow$ 429 keV). The simulations were performed for both target holders. The simulated spectra were analysed to determine the summing-corrected photopeak and total efficiencies of the HPGe detector. These efficiencies are plotted in figures 8.14 and 8.15 for target holders 1 and 2, respectively. To interpolate these for each *measured* DC gamma-ray energy the efficiencies were fitted with first order polynomials, represented by the lines. The reduced *chi*-squared is ~ 1 for each fit. Notice the change in slope between the photopeak and total efficiencies as a

function of gamma-ray energy. This effect is caused by the physical interactions of the incident gamma rays with the Ge crystal and/or surrounding material, where the probabilities of Compton scattering and pair production are greater than the probability of photoelectric absorption (figure A.1 in appendix A). Simulations were also run for 429 keV gamma rays, which determined the efficiencies for target holder 1 (2): $\eta_{\mathrm{ph}}(429\mathrm{keV}) = 4.8\%$ (5.5%) and $\eta_{\mathrm{tot}}(429\mathrm{keV}) = 14.3\%$ (15.2%).

An additional consideration is that during the ^{6}Li + p measurements the targets were changed in between measurements to ensure "fresh" targets were being irradiated. This involved moving the HPGe detector on its slide away from the holder, removing the target holder from the solid-target chamber and changing the target, remounting the target holder, and moving the detector back to its original position to continue measurements. Whilst care was taken to keep the detector's displacement at a minimum, this re-positioning would have introduced a systematic uncertainty on the detector's photopeak and total efficiencies. To quantify this effect on the detector's efficiencies, repeat measurements were performed of the ^{137}Cs 662 keV gamma ray using the *same* target holder. The re-positioning changed the efficiencies within 3%, and thus a 3% systematic uncertainty is included on the HPGe photopeak and total efficiencies.

The statistical uncertainties on the HPGe photopeak and total efficiencies are negligible (less than 1%). Therefore the total uncertainty on the HPGe photopeak and total efficiencies is dominated by systematic uncertainties from: the 4% discrepancy between measured and simulated cascade efficiencies, the 3% effect of re-positioning the HPGe, and the 4% effect of the beamspot, which summed in quadrature to a total of 6.4%.

8.5 Peak Areas

Figure 8.16 shows a sample gamma-ray spectrum, zoomed on the energy region for the primary transition peaks, collected for $E_{\mathrm{p}} = 294.5$ keV impinging onto the Li_2WO_4-1 target. The DC peaks corresponding to the ^{6}Li(p,γ)^{7}Be reaction's DC $\rightarrow$ 0 keV and DC $\rightarrow$ 429 keV transitions, including the first and second escape peaks, are marked by the green and blue arrows, respectively. The peak associated with beam-induced-background from the ^{19}F(p,$\alpha_2\gamma$)^{16}O reaction [98] is marked by the orange arrow.

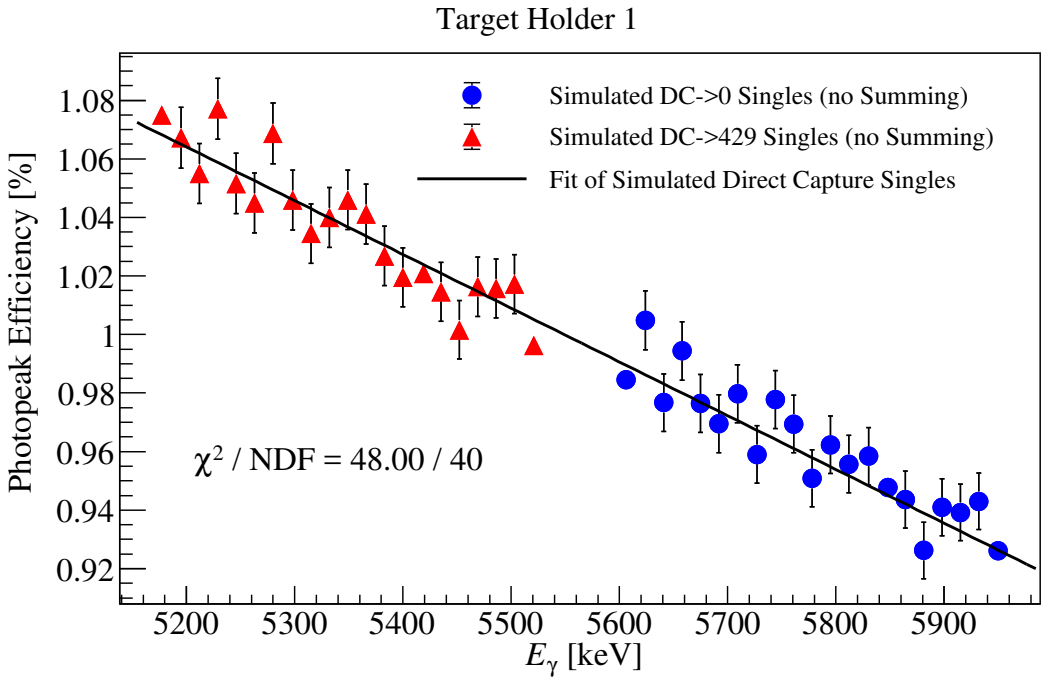

(a) *Simulated HPGe photopeak efficiencies for gamma-ray energies corresponding to transitions DC → 0 keV (blue circles) and DC → 429 keV (red triangles). Statistical errors are shown.*

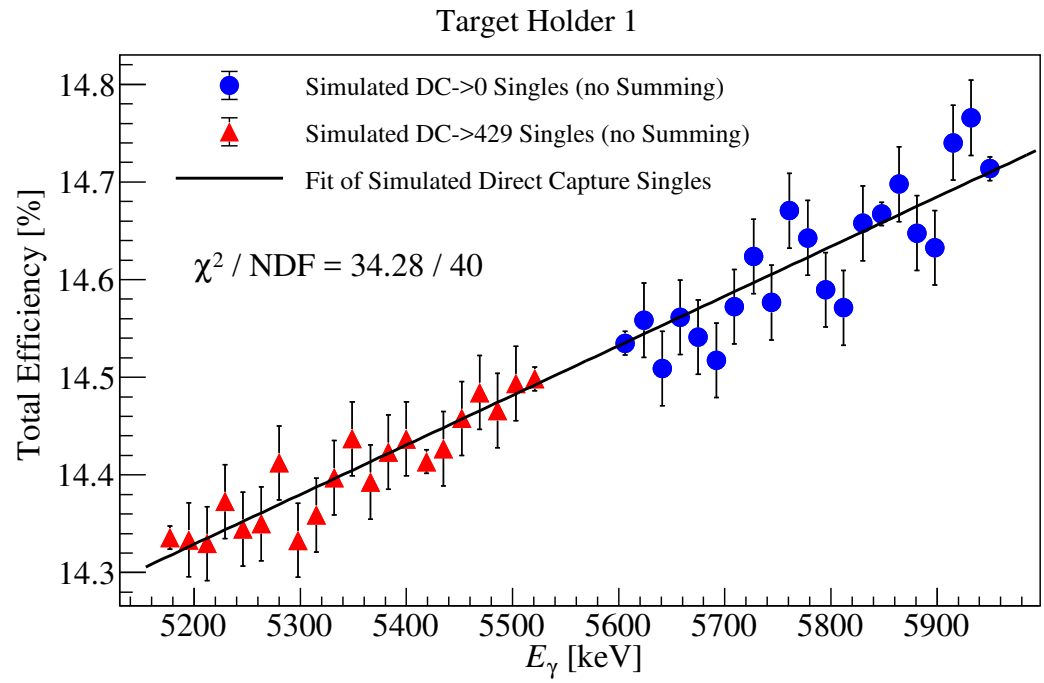

(b) *Simulated HPGe total efficiencies for gamma-ray energies corresponding to transitions DC → 0 keV (blue circles) and DC → 429 keV (red triangles). Statistical errors are shown.*

Figure 8.14

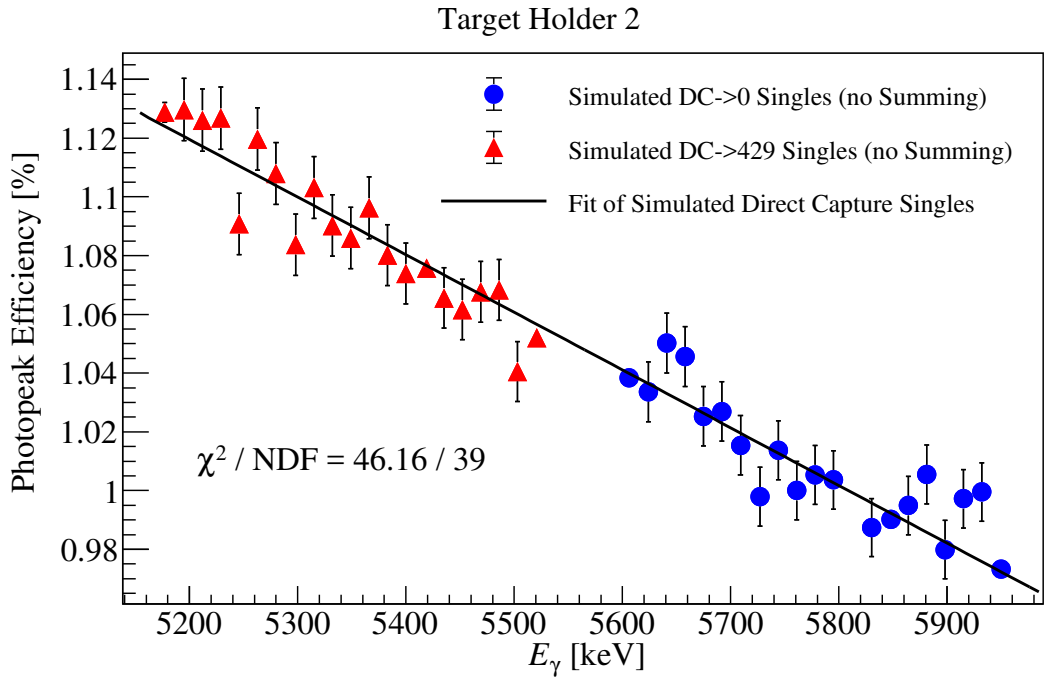

(a) *Simulated HPGe photopeak efficiencies for gamma-ray energies corresponding to transitions DC → 0 keV (blue circles) and DC → 429 keV (red triangles). Statistical errors are shown.*

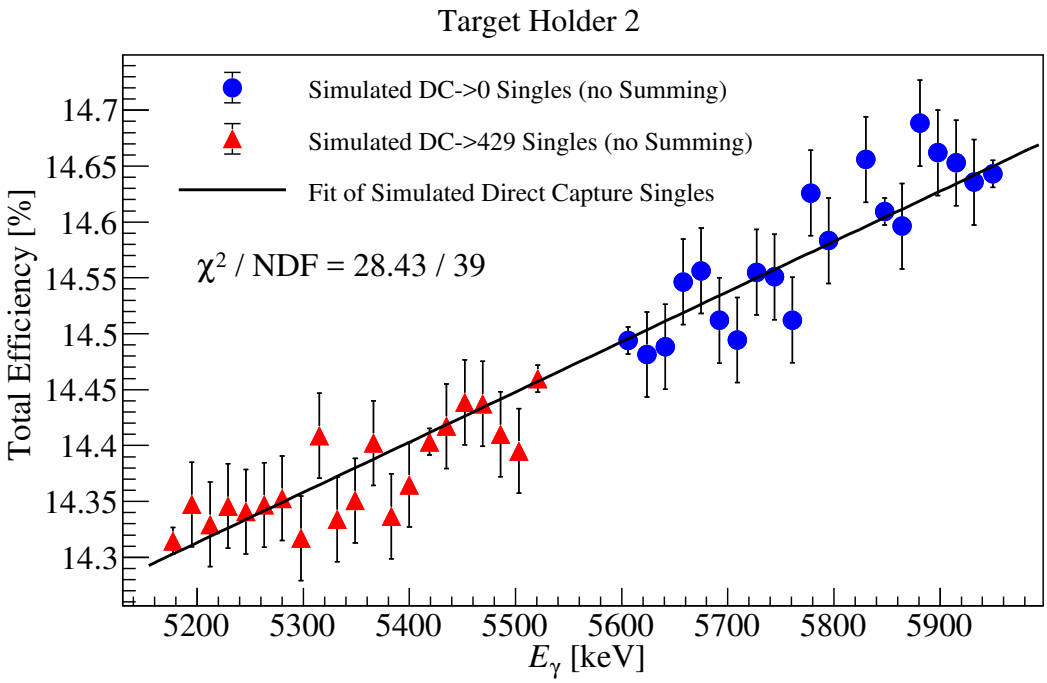

(b) *Simulated HPGe total efficiencies for gamma-ray energies corresponding to transitions DC → 0 keV (blue circles) and DC → 429 keV (red triangles). Statistical errors are shown.*

Figure 8.15

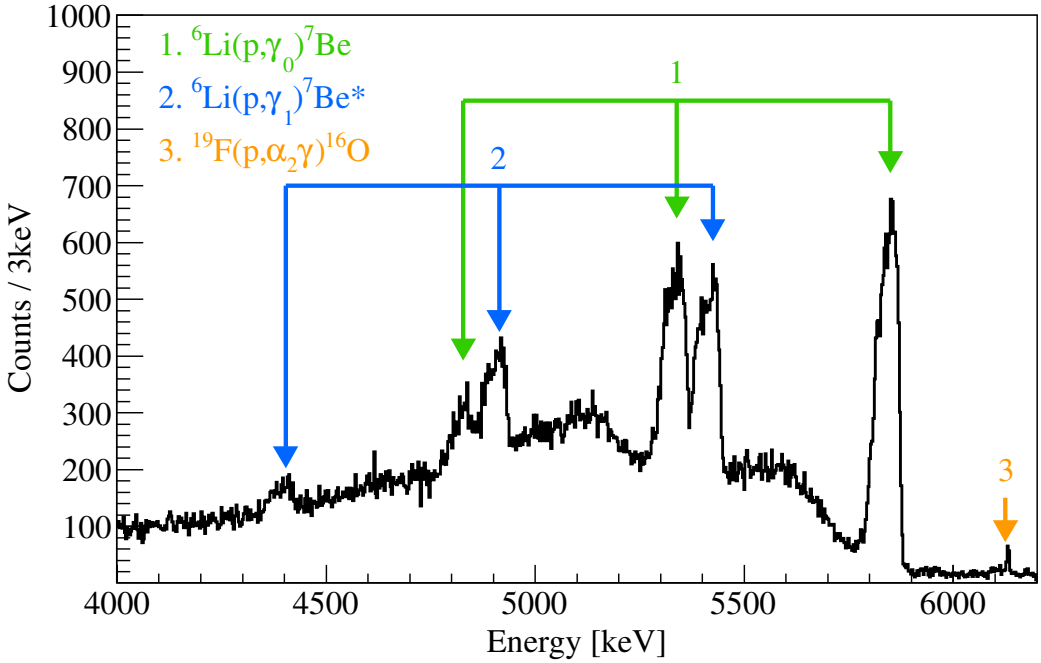

Figure 8.16 *Sample gamma-ray spectrum measured with the HPGe detector for protons (E_p = 294.5 keV) impinging onto the Li_2WO_4-1 target. The spectrum is zoomed into the energy region relevant to the primary γ-ray transitions from the $^{6}Li(p,\gamma)^{7}Be$ reaction. The peak associated with beam-induced-background from the $^{19}F(p,\alpha_2\gamma)^{16}O$ reaction is also visible.*

8.5.1 Primary Peak Analysis

For non-resonant radiative capture reactions A(x,γ)B the gamma-ray peak shape associated with a primary transition is affected by the energy dependence of the cross section as the beam traverses the target (figure 8.17). For this study the primary peaks detected from the ^{6}Li(p,γ)^{7}Be reaction were fitted using a *chi*-squared optimisation approach implemented with the ROOT [84] libraries and the empirical function:

$$f(E_\gamma) = A\frac{1}{E_{\text{cm}}}\exp\left(-2\pi\eta\right)P(E_\gamma) + k_1 + k_2E_\gamma \tag{8.10}$$

where E_{cm} is the beam energy in the c.m frame, $2\pi\eta$ is the sommerfield parameter (equation 2.10), k_1 and k_2 parametrise the background as a straight line beneath the peak, A is a scaling factor which approximates the HPGe photopeak efficiency and the effective stopping power through the target thickness as constant for the energy range spanned by the primary peak. $P(E_\gamma)$ is the profile of the active-nuclei concentration in the target, and typically described by the product of two

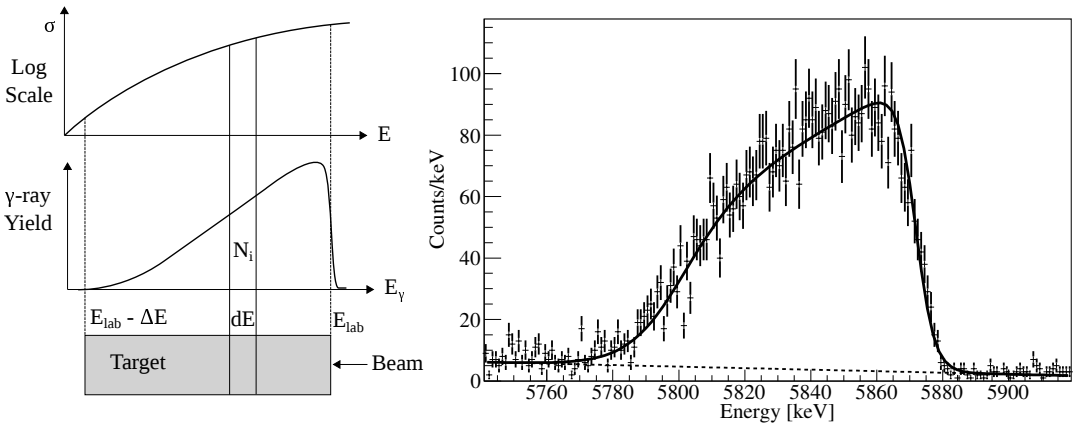

Figure 8.17 *Left: Sketch depicting the relationship between a beam impinging onto a target, the detected gamma ray primary peak, and the reaction cross section. Right: An example of a primary peak measured during the present study.*

Fermi functions:

$$P(E_\gamma) = \left[1 + \exp\left(\frac{-E_{\text{fit}} + E_\gamma}{\delta_{\text{r}}}\right)\right]^{-1} \left[1 + \exp\left(\frac{-E_\gamma + E_{\text{fit}} - \Delta E}{\delta_{\text{l}}}\right)\right]^{-1} \quad (8.11)$$

where δ_{l} and δ_{r} are the left (low energy) and right (high energy) tails of the peak respectively, E_{fit} is the energy at the high-energy edge of the peak, and ΔE is the target thickness (at the beam energy) in c.m frame.

The centre of mass energy is calculated from the gamma-ray (bin) energy as:

$$E_{\text{cm}} = E_\gamma - Q + E_{\text{x}} - \Delta E_{\text{Dopp}} + \Delta E_{\text{rec}} \quad (8.12)$$

where E_γ is the gamma-ray energy, Q is the Q-value (5606.85 keV, equation 2.1) of the reaction, E_{Dopp} is the Doppler shift [23] of the gamma rays, E_{rec} is the energy of the recoil nucleus (^{7}Be), and E_{x} the excitation energy of the final state being occupied: $E_{\text{x}} = 0$ keV when fitting DC $\rightarrow$ 0 keV gamma-ray peaks, $E_{\text{x}} = 429$ keV when fitting DC $\rightarrow$ 429 keV gamma-ray peaks, and $E_{\text{x}} = 511$ keV when fitting DC $\rightarrow$ 0 keV first escape gamma-ray peaks. ΔE_{rec} was calculated via [23]:

$$\Delta E_{\text{rec}} = 5.36772 \times 10^{-4} \, \frac{E_\gamma^2}{m_{\text{rec}}} \, [\text{MeV}] \quad (8.13)$$

where E_γ is the gamma-ray energy in MeV and m_{rec} is the recoil mass in a.m.u

(7.016928717(76)). ΔE_{Dopp} was calculated via [23]:

$$\Delta E_{\mathrm{Dopp}} = 4.63367 \times 10^{-2} \frac{\sqrt{m_{\mathrm{p}} E_{\mathrm{p}}}}{m_{\mathrm{rec}}} E_{\gamma} \cos(\theta) Q_2 \text{ [MeV]} \tag{8.14}$$

where E_{γ} is the gamma-ray energy in MeV, E_{p} is the proton lab energy in MeV, m_{p} is the projectile mass in a.m.u (1.00782503224(9)), and θ is the lab angle (55°) subtended between the beam axis and the detector. Since the HPGe detector had a finite size it subtended a range of angles, and it was necessary to correct for this by including the attenuation coefficient Q_2 [99]. Since the HPGe crystal was coaxial in shape, the integral in equation 7.7 was divided into different angle regions corresponding to the possible gamma-ray path lengths due to the crystal's coaxial hole [100]. For the close distance between target and detector-crystal (d = 2.5 cm) used in the measurement $Q_2 = 0.586$. For the studied energy range $E_{\mathrm{p}} = 80 - 393$ keV the ΔE_{Dopp} spanned the range $3.61 - 8.25$ keV and the ΔE_{rec} spanned the range $2.45 - 2.70$ keV.

Figure 8.18 shows a sample DC $\rightarrow$ 0 keV peak fit, which spans the gamma-ray energy range from 5760 $\rightarrow$ 5900 keV, for gamma-rays emitted from the Li_2WO_4-1 target during irradiation by a proton beam $E_{\mathrm{p}} = 294.5$ keV. The reduced *chi*-squared is ~ 1.1 and representative for all DC peak fits performed on the spectra. Similarly a sample DC $\rightarrow$ 429 keV peak fit for the same measurement is shown in figure 8.19. The DC $\rightarrow$ 429 keV peak is partially overlapped by the 1$^{\mathrm{st}}$ escape peak of the DC $\rightarrow$ 0 keV, and thus both peaks were included in the fit. Whilst the DC $\rightarrow$ 0 keV peak was relatively straightforward to integrate, the DC $\rightarrow$ 429 keV peak integration was complicated by its low energy tail overlapping with the DC $\rightarrow$ 0 keV first escape peak (figure 8.19). The statistical uncertainties on the DC $\rightarrow$ 0 keV peak area integration were of order 2%. The spectra have been calibrated in energy using the procedure in section 8.2. The centroids of the DC peaks were all in agreement with the expected gamma energies calculated from equation 8.12, thus validating the energy calibration procedure discussed in section 8.2.

Both the DC $\rightarrow$ 0 keV and DC $\rightarrow$ 429 keV peaks were affected at high beam energies ($E_{\mathrm{p}} \geq 340$ keV) by beam induced background from the ^{19}F(p,$\alpha_2\gamma$)^{16}O resonance [98], shown in figure 8.20.

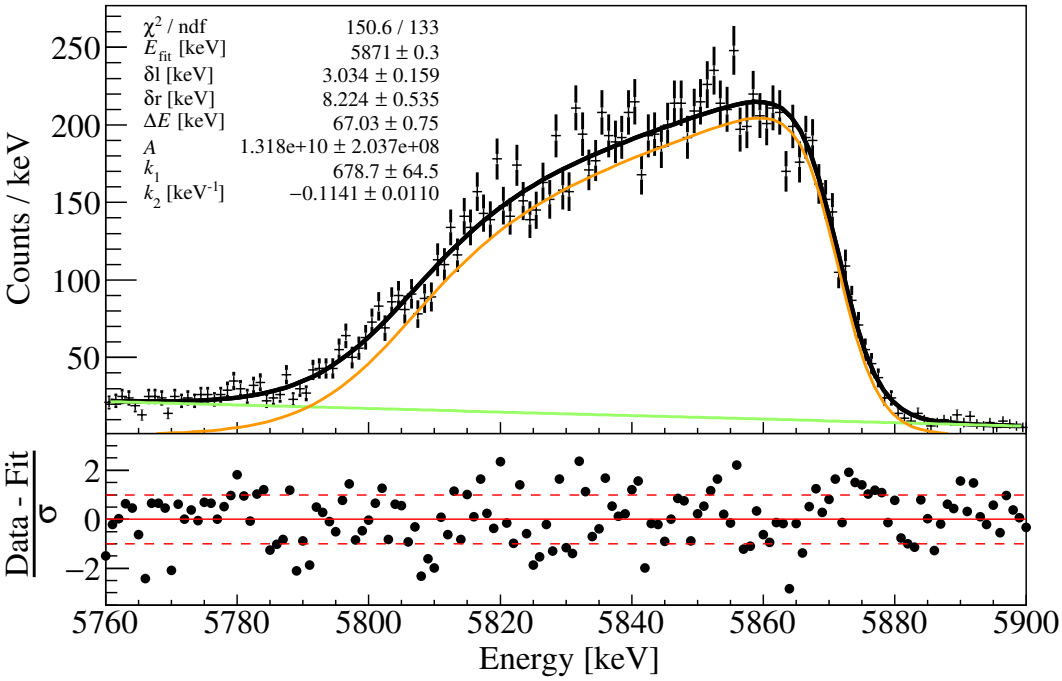

Figure 8.18 *Top: Sample DC → 0 keV peak fit for gamma-rays emitted from the Li_2WO_4-1 target during irradiation by a proton beam E_p = 294.5 keV. The total fit (black), individual peak (orange), and background (green) components of the fit are shown. Bottom: Residuals between the data and total fit with red dashed lines marking 1σ boundary.*

8.5.2 Secondary Peak Analysis

The secondary transition (429 keV) peak did not overlap with peaks from background sources and was thereby simpler to integrate compared to the primary peaks (5100 − 5500 keV). The 429 keV peaks were integrated using the linear background subtraction approach described in [74] to correct for the background Compton continuum. A sample secondary peak from the same spectrum as the primary peaks (figures 8.18 and 8.19) is shown in figure 8.21. The secondary peaks had higher statistics (peak area uncertainties lower by a factor ~ 2) than the primary peaks due to the higher HPGe detector photopeak efficiency. The statistical uncertainties on the 429 → 0 keV peak area integration were of order 1%.

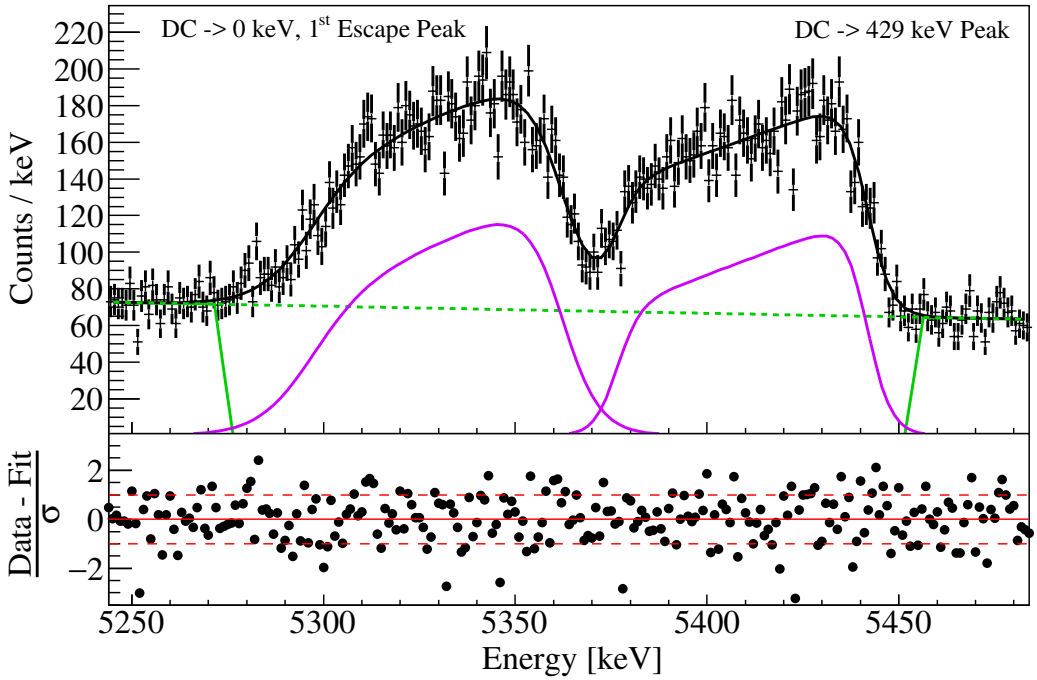

Figure 8.19 *Top: Sample DC → 429 keV and DC → 0 keV 1st escape peak fit for gamma-rays emitted from the Li_2WO_4-1 target during irradiation by a proton beam $E_p = 294.5$ keV. The total fit (black) and individual peak (violet) and background (green) components of the fit are shown. Bottom: Residuals between the data and total fit with red dashed lines marking 1σ boundary.*

8.5.3 Correcting for True Coincidence Summing Effects

The final simulated HPGe detector photopeak and total efficiencies (figures 8.14 and 8.15) were used to correct the measured gamma-ray peak areas for true coincidence summing (TCS) effects, formalised in subsection 8.4.2. Equations 8.7 and 8.8 were rearranged into equations 8.15 and 8.16 for the DC → 429 keV and 429 keV gamma-ray peak areas, respectively.

$$N^{\mathrm{SC}}(\mathrm{DC} \rightarrow 429\ \mathrm{keV}) = \frac{N(\mathrm{DC} \rightarrow 429\ \mathrm{keV})}{1 - \eta_{\mathrm{tot}}(429\ \ \mathrm{keV})} \tag{8.15}$$

$$N^{\mathrm{SC}}(429\ \ \mathrm{keV}) = \frac{N(429\ \ \mathrm{keV})}{1 - \eta_{\mathrm{tot}}(\mathrm{DC} \rightarrow 429\ \mathrm{keV})} \tag{8.16}$$

where N^{SC} is the summing corrected area under the peak, N is the measured area under the peak, and η_{tot} is the HPGe detector total efficiency determined from the GEANT4 simulations. Summing corrections increased the peak areas by about 15%. The total efficiencies were given a 6.4% systematic error (subsection

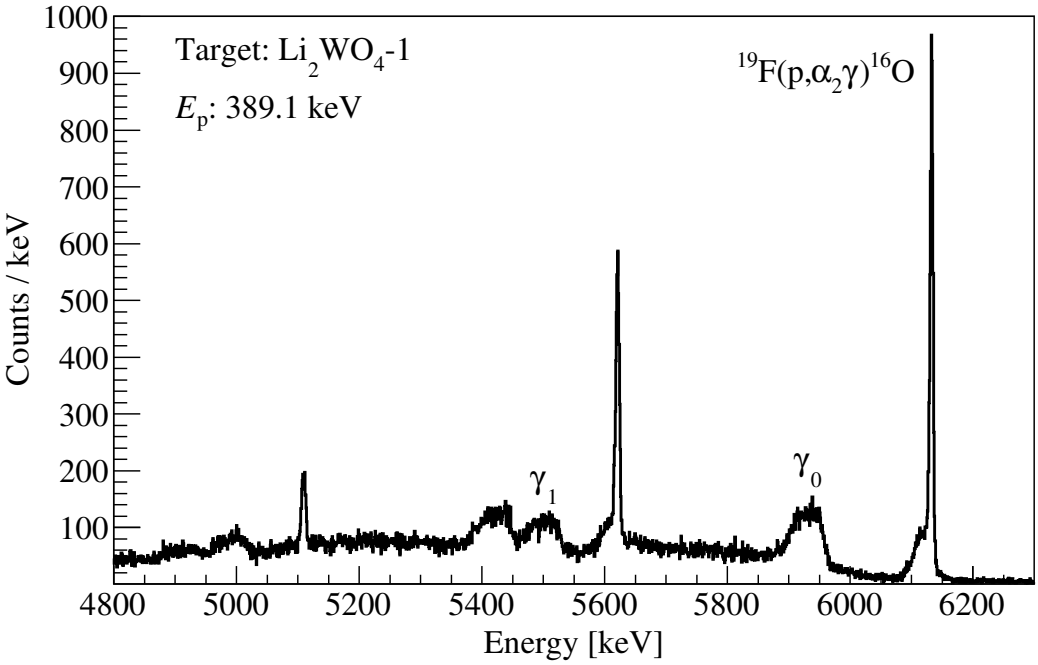

(a)

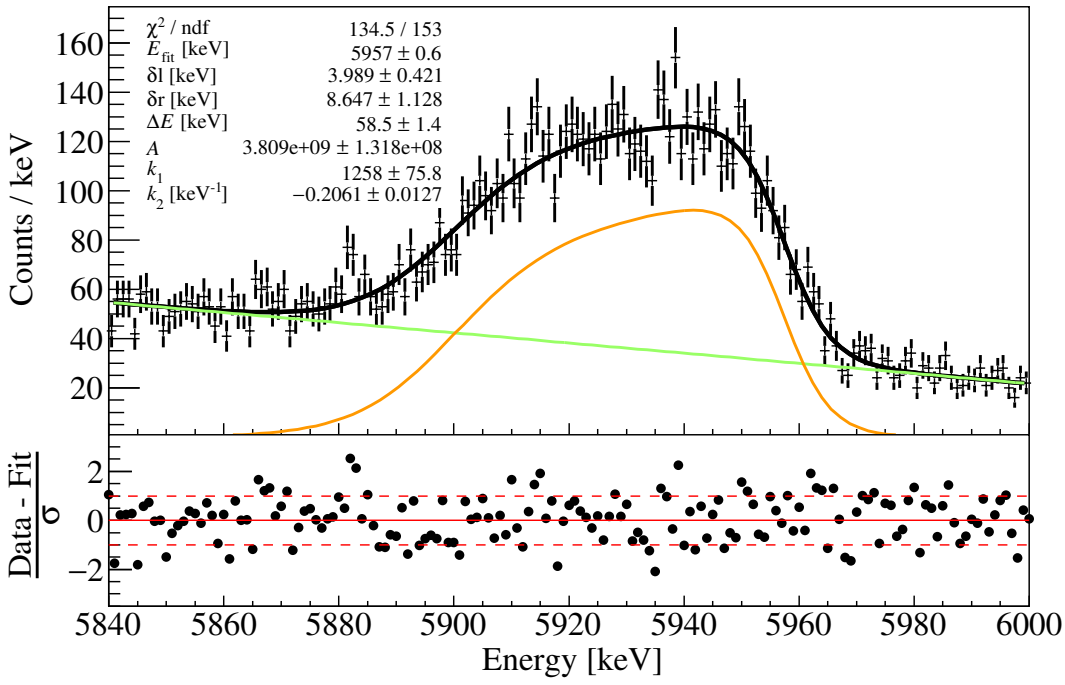

(b)

Figure 8.20 *a) A sample gamma-ray spectrum with the Li_2WO_4-1 target irradiated by a proton beam of 389.1 keV. b) Top: A zoom into the fit of the γ_0 peak (black) with the individual peak (orange) and background (green) components. Bottom: Residuals between the data and total fit with red dashed lines marking 1σ boundary.*

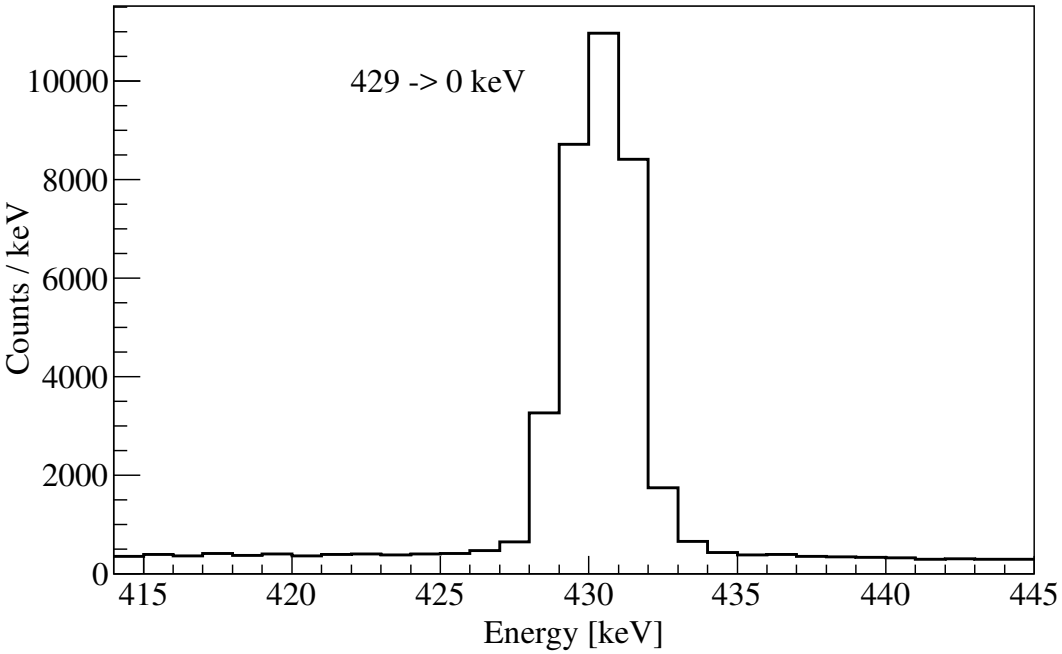

Figure 8.21 *Gamma-ray peak from the secondary transition (429 → 0 keV). The peak was integrated using the linear background subtraction approach described in [74].*

8.4.4). The total efficiency is only used in the primaries (secondaries) summing correction in equation 8.15 (8.16), and since a 6.4% error on the 15% summing correction translates to a ∼ 1% error on the total efficiency, this is neglected from the errors on $N^{\mathrm{SC}}(\mathrm{DC} \rightarrow 429)$ and $N^{\mathrm{SC}}(429)$.

The peak areas from the DC → 0 keV transition were also corrected for the summing, and depending on whether peak areas from the primaries or secondaries were used, the summing correction was applied with a rearrangement of equation 8.6 and using either:

$$N^{\mathrm{SC}}(\mathrm{DC} \rightarrow 0 \text{ keV}) = N(\mathrm{DC} \rightarrow 0 \text{ keV}) - N^{\mathrm{SC}}(\mathrm{DC} \rightarrow 429 \text{ keV})\eta_{\mathrm{ph}}(429\ keV) \tag{8.17}$$

or

$$N^{\mathrm{SC}}(\mathrm{DC} \rightarrow 0 \text{ keV}) = N(\mathrm{DC} \rightarrow 0 \text{ keV}) - N^{\mathrm{SC}}(429\ \text{ keV})\eta_{\mathrm{ph}}(\mathrm{DC} \rightarrow 429 \text{ keV}) \tag{8.18}$$

For either calculation the summing corrections applied to the DC → 0 keV peak areas were of order 5% reduction. The propagated error of ∼ 9% on the summing correction had a less than 0.5% effect on $N^{\mathrm{SC}}(\mathrm{DC} \rightarrow 0)$, and was thus neglected

from the final error for the summing-corrected peak areas.

8.6 Angular Distributions

The ^{6}Li(p,γ)^{7}Be angular distributions for the ground-state transition (DC $\rightarrow$ 0 keV) and secondary transition (429 $\rightarrow$ 0 keV) were determined from equation 7.6, where the A_l coefficients were calculated from a theoretical framework reported by Gnech and Marcucci in 2019 [50]. The angular distributions were corrected for the attenuation factors, Q_l, determined using the formalism in equation 7.7 and the simulated HPGe geometry. The Q_l calculated for angular momenta l = 1, 2, and 3 were 0.843, 0.586, and 0.313 respectively. The angular distribution for the ground-state (secondary) transition as a function of incident proton energy is plotted in figure 8.22a (8.23a), and as a function of centre of mass angle (for fixed E_{p} = 294.5 keV) in figure 8.22b (8.23b).

8.7 Branching Ratios for the ^{6}Li(p,γ)^{7}Be Reaction

For reasons explained in the next section, branching ratios were not required for the experimental yield calculations. However they still provided a useful cross-check with previous values quoted in the literature. The branching ratios were calculated for each measurement on each target using the summing-corrected peak areas $N^{\mathrm{SC}}_{\mathrm{peak}}$ from the ground state (DC $\rightarrow$ 0 keV) and secondary (429 $\rightarrow$ 0 keV) transitions via:

$$b = \frac{Y_{\mathrm{DC}\rightarrow 0\,\mathrm{keV}}}{Y_{429\,\mathrm{keV}}} = \frac{N^{\mathrm{SC}}_{\mathrm{peak}}(\mathrm{DC}\rightarrow 0\,\mathrm{keV})}{\eta_{\mathrm{ph}}(\mathrm{DC}\rightarrow 0\,\mathrm{keV})W(\mathrm{DC}\rightarrow 0\,\mathrm{keV})}\frac{\eta_{\mathrm{ph}}(429\,\mathrm{keV})W(429\,\mathrm{keV})}{N^{\mathrm{SC}}_{\mathrm{peak}}(429\,\mathrm{keV})} \tag{8.19}$$

where $\eta_{\mathrm{ph}}(\mathrm{DC}\rightarrow 0\,\mathrm{keV})$ and $\eta_{\mathrm{ph}}(429\,\mathrm{keV})$ are the absolute photopeak efficiencies of the ground state and secondary transitions, respectively, and $W(\mathrm{DC}\rightarrow 0\,\mathrm{keV})$ and $W(429\,\mathrm{keV})$ are the angular distributions of the ground state and secondary transitions, respectively. The beam current, N_{b} in equation 4.2, cancels out. Including the angular distribution from [50] for the DC $\rightarrow$ 0 keV and the 429 $\rightarrow$ 0 keV enhances the branching ratio by $\sim$ 7% compared to treating DC $\rightarrow$ 0 keV and the 429 $\rightarrow$ 0 keV as isotropic.

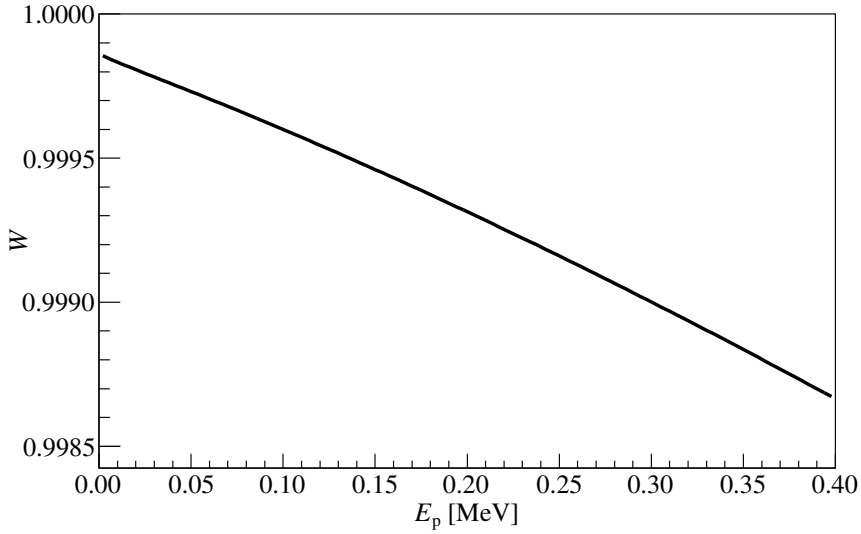

(a)

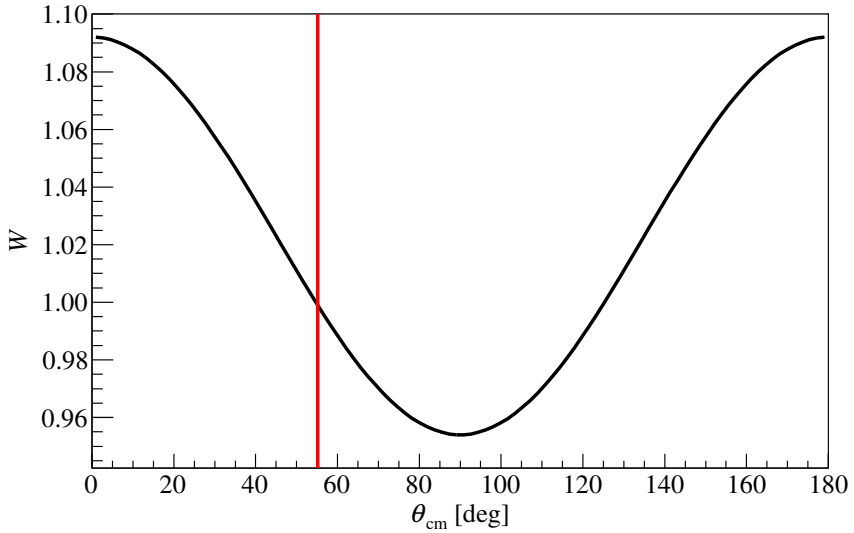

(b)

Figure 8.22 *a) $^6Li(p,\gamma)^7Be$ DC $\rightarrow$ 0 keV angular distribution as a function of incident proton energy. b) $^6Li(p,\gamma)^7Be$ DC $\rightarrow$ 0 keV angular distribution for $E_p = 294.5$ keV as a function of gamma-ray c.m angle. The angle of the HPGe detector is marked as a red line. The distributions have been corrected using the attenuation coefficients, see text.*

Once the branching ratios were calculated from each target they were merged into a global dataset for comparison with the literature. The branching ratios measured at beam energies within $E_p = 4$ keV of each other were merged using the weighted average approach [82]. The merged branching ratios plotted against E_p are shown by the black points in figure 8.24. The branching ratios are constant across the studied energy range, as reported in previous studies [30, 42]. The

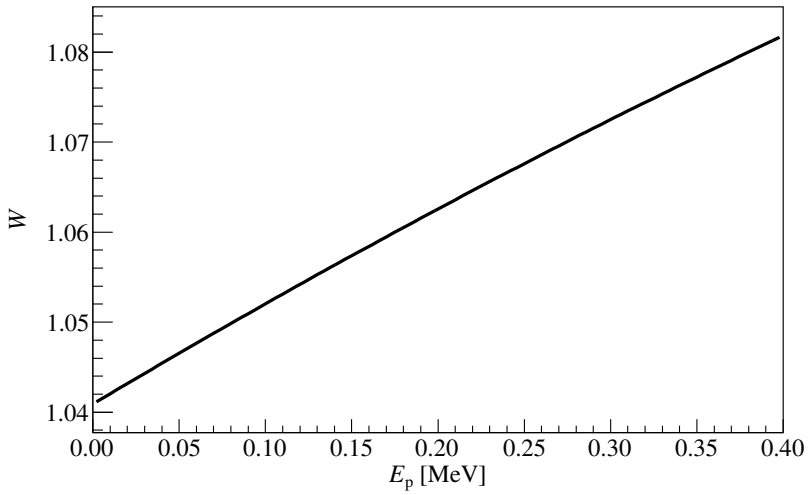

(a)

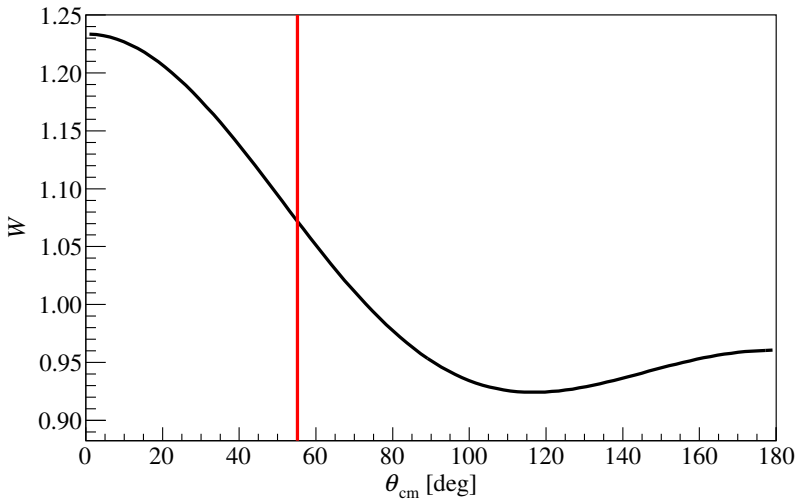

(b)

Figure 8.23 *a)* $^6Li(p,\gamma)^7Be$ 429 $\rightarrow$ 0 *keV angular distribution as a function of incident proton energy. b)* $^6Li(p,\gamma)^7Be$ 429 $\rightarrow$ 0 *keV angular distribution for* $E_p = 294.5$ *keV as a function of gamma-ray c.m angle. The angle of the HPGe detector is marked as a red line. The distributions have been corrected using the attenuation coefficients, see text.*

published branching ratio from He *et al.* (Switkowski *et al.*) is plotted as a solid red (blue) line with quoted errors as dashed red (blue) lines. The weighted average of our measured branching ratio is 1.75 ± 0.07, in agreement with the published branching ratios of 1.57 ± 0.15 from He *et al.* [42] and $1.56^{+0.14}_{-0.26}$ from Switkowski *et al.* [30]. Note branching ratios from both He *et al.* and Switkowski *et al.* were calculated assuming isotropic gamma-ray emission and using the gamma rays from the DC $\rightarrow$ 0 keV and DC $\rightarrow$ 429 keV transitions.

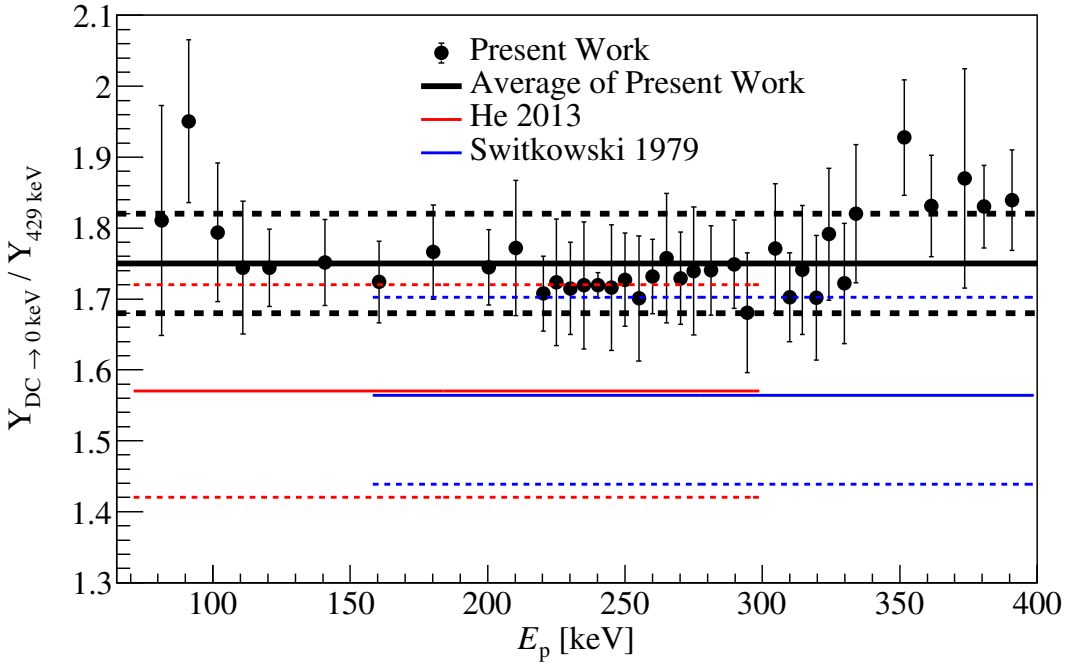

Figure 8.24 *$^6Li(p,\gamma)^7Be$ reaction branching ratios calculated using the DC → 0 keV yields divided by the 429 keV yields, with total error bars shown. The present values are in good agreement with those reported by He et al. [42] (red lines) and Switkowski et al. [30] (blue lines). The dashed lines represent the total errors.*

8.8 Experimental Yields

The ^{6}Li(p,γ)^{7}Be reaction's experimental yields were calculated independently for each transition (ground state, primary, and secondary) in ^{7}Be* using equation 4.2 (treating $b = 1$). Since the branching ratio was constant across the covered energy range (section 8.7) the total yield could be determined using the sum of the ground state yield with either the primary or secondary transition yields. For this study it was decided to use the yields from the secondary transition, because the secondary (429 → 0 keV) peaks did not overlap with background peaks and had larger statistics compared to the primary peaks (DC → 429 keV). The total experimental yields for all measurement (beam) energies and all targets were calculated as:

$$Y_{\text{total}} = Y_{\text{DC}\to 0\,\text{keV}} + Y_{429\to 0\,\text{keV}} \tag{8.20}$$

The total yield is independent of the branching ratios because the cascade in ^{7}Be* could only follow one of two possible paths.

Figure 8.25 shows a sample plot of the total yields for the ^{6}Li(p,γ)^{7}Be reaction

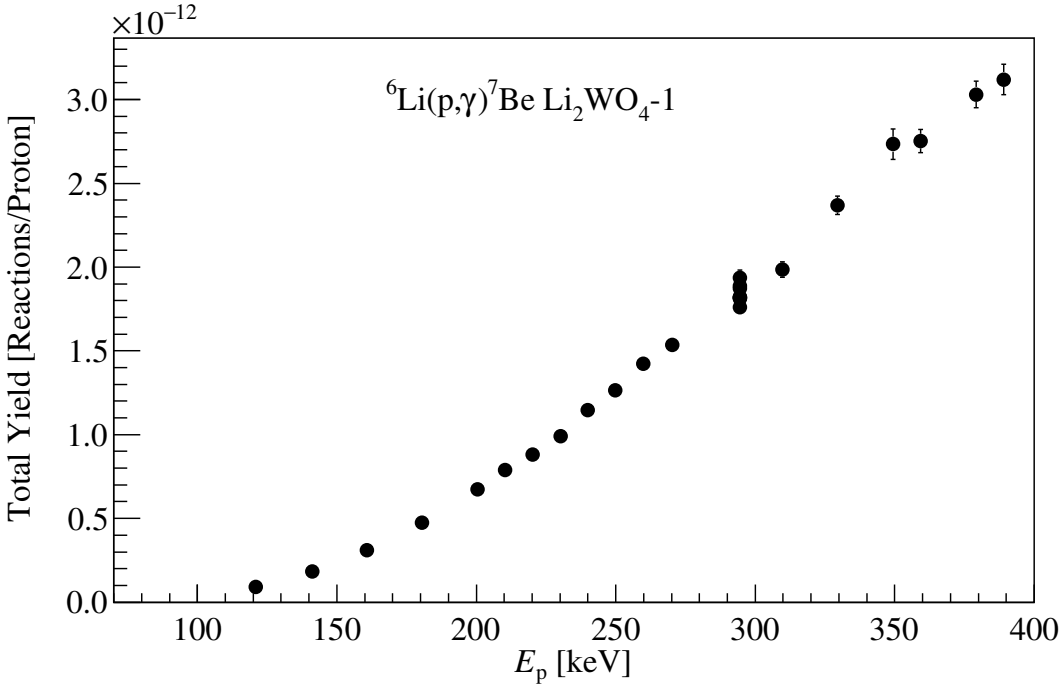

Figure 8.25 *Experimental yields measured using the Li_2WO_4-1 target for the $^6Li(p,\gamma)^7Be$ reaction. Error bars are statistical. The vertical increase at $E_p \sim 295$ keV is from repeat measurements performed at the reference beam energy during the target's bombardment.*

Table 8.4 *Uncertainty Budget for the $^6Li(p,\gamma)^7Be$ experimental yields.*

Source	Uncertainty [%] Statistical	Systematic
$N_{\text{peak}}(\text{DC} \rightarrow 0 \text{ keV})$	~ 2	-
$N_{\text{peak}}(429 \rightarrow 0 \text{ keV})$	~ 1	-
Beam Current	3	2
η_{HPGe}	-	6.4

measured using protons impinging onto the Li_2WO_4-1 target. The statistical errors on the total yields were calculated by error propagation of both the Poissonian error on the peak area integrations and the error from the random fluctuations in the beam current integration (3% [59]). The uncertainty budget for the experimental yields is shown in table 8.4. Additional plots of the total yields measured using the other targets are provided in appendix D.

8.9 Target Degradation Effects

The NRA and ERDA measurements were used to determine target thicknesses, as discussed in chapter 6. These measurements were performed after irradiation at LUNA. Therefore the target thicknesses measured at HZDR (Dresden) will have already been degraded from the irradiation during the LUNA beamtime. To correct for target degradation effects, the ΔE parameter was extracted from each of the DC $\rightarrow$ 0 keV peak fits (equation 8.10). The thickness parameter from the fits is reliable only for runs with E_{p} above 200 keV, because at lower beam energies the cross section decreased steeply with the energy, and as the beam interacted with deeper target layers significantly fewer gamma rays were detected. As a result only a fraction of the target thickness was represented with sufficient statistics by the DC $\rightarrow$ 0 keV peak width and thus the fit became insensitive to the target thickness. Only runs for $E_{\mathrm{p}} > 200$ keV were used in evaluating the target thicknesses.

The target thicknesses from the DC $\rightarrow$ 0 keV peak fits were converted into physical thicknesses, DX, using the compositions (table 6.2) derived from the ERDA approach and SRIM-2013 stopping power tables [51], and then subsequently scaled (normalised) to the thickness from the first measurement, DX_0. The normalised thicknesses provide a direct measure of the target degradation as a function of the accumulated charge deposited onto the targets, and these normalised thicknesses were fitted with a 1^{st} order polynomial (2^{nd} order for the Li_2O-9 target) to describe the degradation during a given target's irradiation.

A sample plot of the degradation as a function of the charge deposited on the Li_2WO_4-1 target is shown by the black points in figure 8.26, the red line represents a linear fit with 68% confidence intervals. For comparison, the target thickness measured using the NRA approach at HZDR (*e.g.* figure 6.11), scaled to the first measured thickness at LUNA, is included as a blue point. The thickness derived at HZDR is $\simeq$ 20% smaller than the thickness derived from the first LUNA measurement run. This indicates the target thickness degraded during the charge deposition at LUNA, likely caused by the target nuclei being sputtered away by the proton beam. The HZDR data point is lower than the last LUNA data point, likely as a result of a different region of the target being irradiated during both measurements. Additional target degradation plots for the other targets analysed (Li_2WO_4-3, 4, and Li_2O-9) are provided in appendix E.

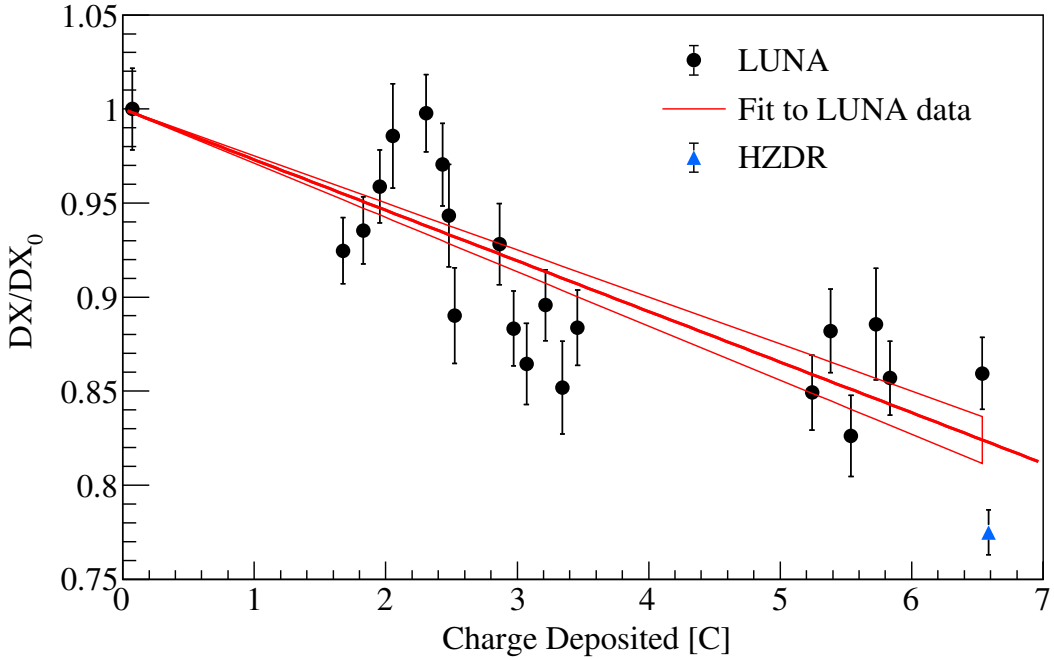

Figure 8.26 *Plot of target degradation vs charge deposited on the Li_2WO_4-1 target. During beam bombardment the measured thickness, DX, decreases from its initial value, DX_0. The ratio of these thicknesses provides a measure of the target degradation.*

8.10 *S*-factors

The experimental yields measured from each target were deconvolved into cross sections using the same procedure as for the (p,α) channel, discussed in section 7.6. Figure 8.27 shows a plot of ^{6}Li(p,γ)^{7}Be reaction S-factors as a function of E_{cm}. The values from this study are plotted using the same data point format as the ^{6}Li(p,α)^{3}He S-factors in figure 7.6, with statistical uncertainties. Literature values from Switkowski *et al.* [30] and He *et al.* [42] are plotted as filled and hollow black circles, respectively, with total uncertainties. The recently calculated S-factor reported by Gnech and Marcucci [50] is included as the black line. The two highest energy points for the Li_2O-9 target show large uncertainties due to difficulties with the DC peak fit integration from the ^{19}F(p,$\alpha_2\gamma$)^{16}O (section 8.5). The present data for different targets are scattered in a similar way as the ^{6}Li(p,α)^{3}He reaction S-factors, whereby the Li_2WO_4-4 and Li_2O-9 data are approximately 25% higher than the Li_2WO_4-1, 3 data. The trend of the present data shows negative slopes for all targets, in qualitative agreement with the previous measurement by Switkowski *et al.* and the recent theoretical calculations by Gnech and Marcucci.

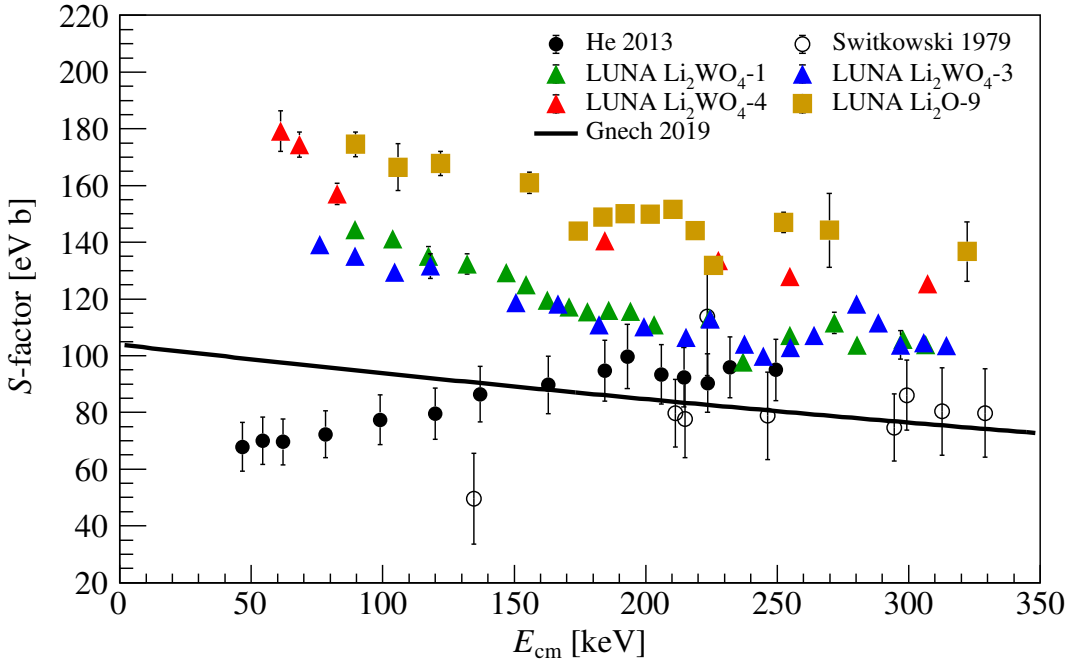

Figure 8.27 *$^{6}Li(p,\gamma)^{7}Be$ reaction S-factor vs E_{cm}. The bare (corrected for electron screening effects) S-factor data from the present study are plotted as solid triangles and squares with statistical uncertainties. The literature values [30, 42] are plotted as black and hollow circles with total uncertainties. The calculated bare S-factor reported in Gnech and Marcucci 2019 [50] is shown by the black line.*

Comparing the LUNA ^{6}Li(p,α)^{3}He and ^{6}Li(p,γ)^{7}Be reaction S-factors with literature, it is clear there is a discrepancy of $\simeq 40-50\%$ for all targets. Since this discrepancy is observed for all targets and both reactions, and the measurements of both reactions were performed *concurrently*, the discrepancy must be from a systematic factor in common for both reactions. One common factor is the beam current integration, which would be incorrectly measured if the beam was poorly focused such that the protons impinged onto the target holder instead of the targets. However, this would mean the beam current is an overestimate, and because the yields are inversely proportional to the beam current the calculated S-factors would *increase* from their present values, increasing the discrepancies with literature.

Another factor in common is the target compositions used in the stopping power calculations. The compositions were measured (by the ERDA approach) after bombardment at LUNA, and so it is reasonable to assume we have an inaccurate understanding of the target compositions during beam bombardment. To solve this issue we decided to scale the LUNA S-factors to the ^{6}Li(p,α)^{3}He data

reported in 2008 by Cruz *et al.* [40], employing a similar method to that used by He *et al.* [42]. This normalisation approach along with final S-factors and calculations of the ^{6}Li(p,γ)^{7}Be reaction rate are detailed in the next chapter.

Chapter 9

Final *S*-factors and Astrophysical Impact

The ^{6}Li(p,α)^{3}He and ^{6}Li(p,γ)^{7}Be reaction S-factors were presented at the end of chapters 7 and 8, respectively. The $40-50\%$ offset between the present and literature data, for both reactions, is explained by an incomplete understanding of our target compositions during beam bombardment. The offset prompted the decision to normalise measured S-factors to the (p,α) channel data in Cruz *et al.* 2008 [40]. This chapter reports the normalisation procedure, followed by the approach used to merge LUNA data into global data sets for both reactions. An updated reaction rate of the ^{6}Li(p,γ)^{7}Be reaction is presented at the end of this chapter, with a complementary discussion of the astrophysical impact.

9.1 Normalisation Procedure

The LUNA ^{6}Li(p,α)^{3}He S-factors were scaled to the Cruz *et al.* 2008 [40] S-factor at a normalisation energy, $E_{\rm n}$, (which varied between targets) using a scaling factor, C:

$$\begin{aligned} S(E_{\rm cm})^{\rm LUNA\text{-}norm}_{\rm (p,\alpha)} &= C \times S(E_{\rm cm})^{\rm LUNA}_{\rm (p,\alpha)} \\ &= \frac{S(E_{\rm n})^{\rm Cruz}_{\rm (p,\alpha)}}{S(E_{\rm n})^{\rm LUNA}_{\rm (p,\alpha)}} S(E_{\rm cm})^{\rm LUNA}_{\rm (p,\alpha)} \end{aligned} \tag{9.1}$$

This method is independent of knowledge of the target composition. LUNA

Table 9.1 *Normalisation energies and corresponding scaling factors, with total uncertainties.*

Target	E_{n} [keV]	Scaling Factor C
Li_2O-9	210.2	0.51(6)
Li_2WO_4-1	203.2	0.62(7)
Li_2WO_4-3	198.9	0.67(7)
Li_2WO_4-4	227.7	0.55(6)

energies closest to $E_{\mathrm{cm}} = 207$ keV (the same energy used by He *et al.* [42]) were selected as the normalisation energy. The normalisation energy for different targets was in the range $198 - 230$ keV (table 9.1).

The Cruz S-factors at each normalisation energy were determined by the fit function reported in the Ph.D. thesis of J. Cruz [101]:

$$S(E_{\mathrm{n}})^{\mathrm{Cruz}}_{(\mathrm{p},\alpha)} = S_0 + S_1 E_{\mathrm{n}} + S_2 E_{\mathrm{n}}^2 + S_3 E_{\mathrm{n}}^3 \tag{9.2}$$

with fit values (quoted in J. Cruz thesis [101]) obtained from a global fit on Cruz data and Elywn *et al.* [35] data: $S_0 = 3.52$ MeV b, $S_1 = -4.42 \times 10^{-3}$ b, $S_2 = 4.9 \times 10^{-6}$ b/MeV, and $S_3 = -2.6 \times 10^{-9}$ b/MeV^2. The scaled ^{6}Li(p,α)^{3}He reaction S-factors are plotted in figure 9.1 with statistical uncertainties.

The $S(E_{\mathrm{cm}})^{\mathrm{LUNA}}_{(\mathrm{p},\gamma)}$ data were scaled using the same scaling factors as the (p,α) channel:

$$S(E_{\mathrm{cm}})^{\mathrm{LUNA\text{-}norm}}_{(\mathrm{p},\gamma)} = C \times S(E_{\mathrm{cm}})^{\mathrm{LUNA}}_{(\mathrm{p},\gamma)} \tag{9.3}$$

where C is the same as in equation 9.1. The scaled ^{6}Li(p,γ)^{7}Be reaction S-factors are plotted in figure 9.2 with statistical uncertainties.

9.2 Uncertainty Budgets for the ^{6}Li(p,α)^{3}He and ^{6}Li(p,γ)^{7}Be Reaction S-factors

The uncertainty budgets of the scaled S-factors are shown in tables 9.2 and 9.3 for the ^{6}Li(p,α)^{3}He and ^{6}Li(p,γ)^{7}Be reactions, respectively. The uncertainties are broken down into statistical, systematics not in common between different target data, and systematics in common between different target data. This separation of uncertainties into distinct categories was required for merging the data into final global LUNA datasets for both reactions, presented in the next section. The

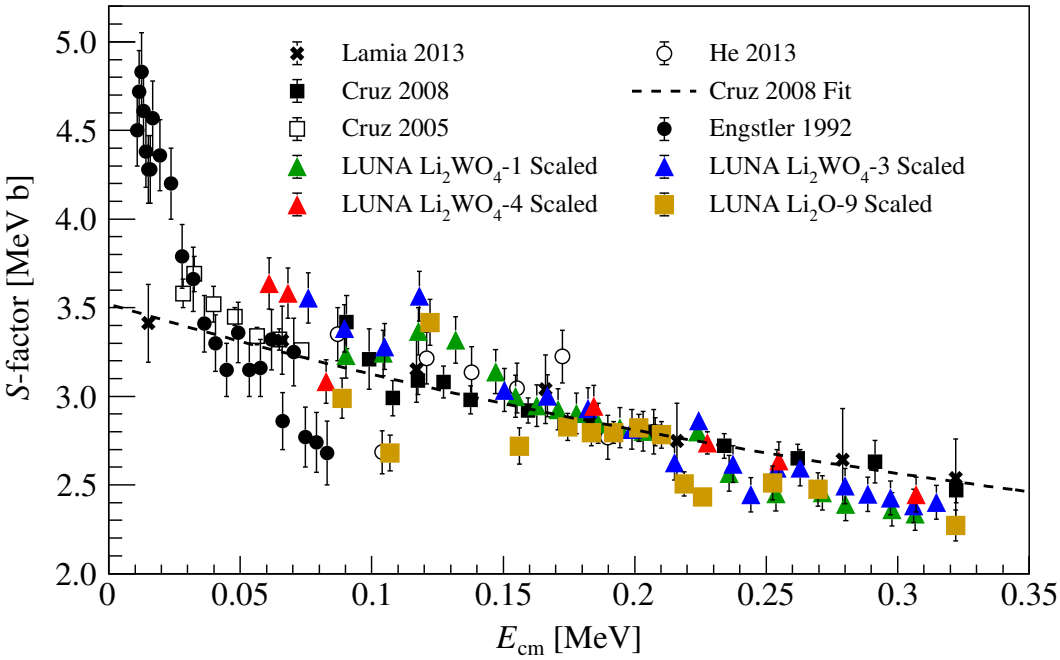

Figure 9.1 *$^{6}Li(p,\alpha)^{3}He$ reaction bare (corrected for electron screening effects) S-factor vs centre of mass energy. LUNA S-factors (scaled to the Cruz et al. 2008 $^{6}Li(p,\alpha)^{3}He$ [40] data) are plotted with statistical uncertainties. Literature values are the same as in figure 7.6.*

systematic uncertainty from the modelled target degradation was negligible (less than 1.3%) compared to other sources of uncertainty, and is thereby omitted from the budget.

For the ^{6}Li(p,α)^{3}He reaction S-factors the statistical uncertainties are from the integration of the ^{3}He peak and the fluctuations in the beam current integration. The systematic uncertainties (not in common between different target data) arise from the effect of the beamspot on the beam current integration, the effect of including the target profile $P(E_{\mathrm{lab}})$ in the cross section deconvolution, and the uncertainty on the scaling factor C. The uncertainty on C for a given target is determined by summing in quadrature the uncertainties on the LUNA S-factor ($2.3 - 4.0\%$), the Cruz 2008 fit ($5.1 - 5.9\%$), and the effect of $P(E)$ on the LUNA S-factor ($1.7 - 3.3\%$), all at the normalisation energy E_{n}. The systematic uncertainties (in common between different target data) are from the total uncertainty on the Si detector efficiency (from statistical, resonance strength, and beamspot effects), the stopping power uncertainty quoted from SRIM [51], and the uncertainty provided in Brune *et al.* [84] for the angular distribution of the ^{3}He particles.

Table 9.2 *Uncertainty Budget for the scaled $^6Li(p,\alpha)^3He$ S-factors. Uncertainties are broken down into statistical, systematic (not in common between different target data), and systematic (in common between different target data). The total uncertainty represents the uncertainty range on the final data.*

Source	Uncertainty [%] Statistical	Systematic (not in common)	Systematic (in common)
$N_{\text{peak}}(^3\text{He})$	~ 0.3	-	-
Beam Current	3	2	-
Target profile	-	$0.7 - 8.5$	-
Scaling Factor	-	$6.6 - 7.3$	-
η_{Si}	-	-	9.3
Stopping Power	-	-	5
$\text{W}(\theta, E)_{(\text{p},\alpha)}$	-	-	1.5

Total 11.3 – 14.8%

Table 9.3 *Uncertainty Budget for the scaled $^6Li(p,\gamma)^7Be$ S-factors. Uncertainties are broken down into statistical, systematic (not in common between different target data), and systematic (in common between different target data). The total uncertainty represents the uncertainty range on the final data.*

Source	Uncertainty [%] Statistical	Systematic (not in common)	Systematic (in common)
$N_{\text{peak}}(\text{DC} \rightarrow 0 \text{ keV})$	~ 2	-	-
$N_{\text{peak}}(429 \rightarrow 0 \text{ keV})$	~ 1	-	-
Beam Current	3	2	-
Target profile	-	$0.5 - 8.0$	-
Scaling Factor	-	$6.6 - 7.3$	-
η_{HPGe}	-	3	5.7
Stopping Power	-	-	5
η_{Si}	-	-	9.3
$\text{W}(\theta, E)_{(\text{p},\alpha)}$	-	-	1.5

Total 12.7 – 16.3%

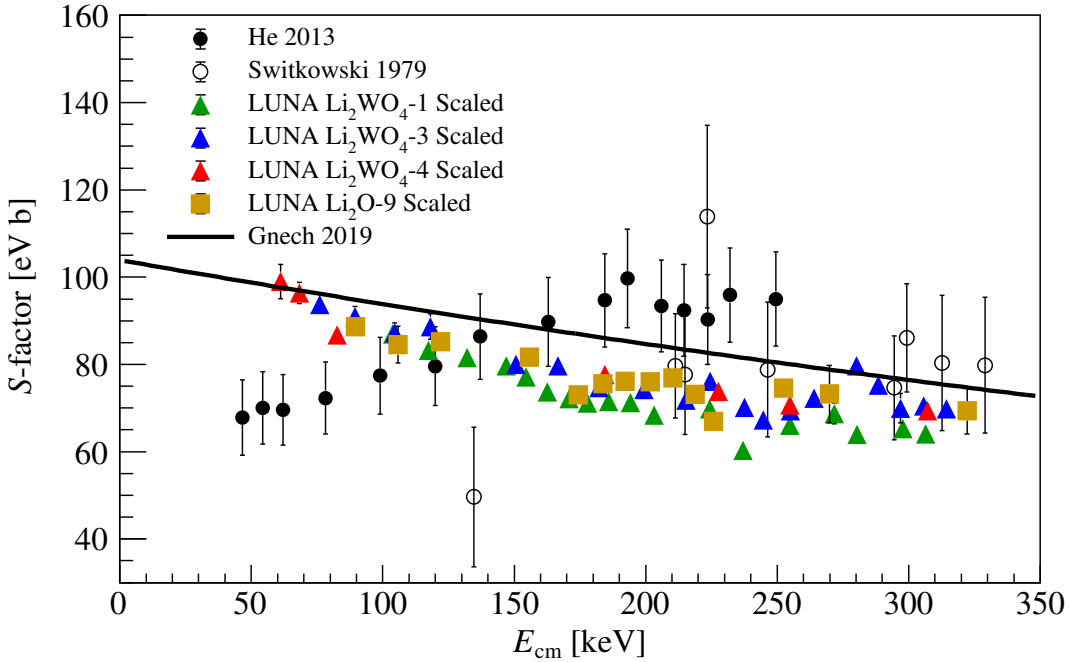

Figure 9.2 *$^{6}Li(p,\gamma)^{7}Be$ reaction bare (corrected for electron screening effects) S-factor vs centre of mass energy. LUNA S-factors (scaled to the Cruz et al. 2008 [40] $^{6}Li(p,\alpha)^{3}He$ data) are plotted with statistical uncertainties. Literature values are the same as in figure 8.27.*

For the ^{6}Li(p,γ)^{7}Be reaction S-factors the statistical uncertainties are from the integration of the DC $\rightarrow$ 0 keV and 429 $\rightarrow$ 0 keV peak areas, and the fluctuations in the beam current integration. The systematic uncertainties (not in common between different target data) are from the effect of the beamspot on the beam current integration, the effect of including the target profile $P(E_{\mathrm{lab}})$ in the cross section deconvolution, the uncertainty on the scaling factor C, and the effect of re-positioning the HPGe detector on its photopeak efficiency. The systematic uncertainties (in common between different target data) are from the discrepancy between simulated and measured HPGe photopeak efficiencies, the stopping power uncertainty quoted from SRIM [51], the total uncertainty on the Si detector efficiency, and the uncertainty provided in Brune *et al.* [84] for the angular distribution of the ^{3}He particles. Notice that since the ^{6}Li(p,γ)^{7}Be reaction S-factors were scaled using the ^{6}Li(p,α)^{3}He reaction data the systematic uncertainties from the silicon efficiency and (p,α) channel's angular distribution had to be included in the total uncertainties on the scaled S-factors.

9.3 Merging *S*-factors (Obtained from Different Targets) into Final *S*-factor Datasets

Once the S-factors were scaled to the literature values they were merged into global datasets, one for the ^{6}Li(p,α)^{3}He reaction and another for the ^{6}Li(p,γ)^{7}Be reaction, using the following procedure (with uncertainties quoted in tables 9.2 and 9.3):

1. Start with scaled S-factors with statistical uncertainties,
2. Combine in quadrature statistical uncertainties with all not-in-common systematic uncertainties,
3. Use the weighted average approach [82] to merge S-factors determined from different targets within $E_{\rm cm} \leq 4$ keV, and assign an interaction energy determined by the average of their $E_{\rm cm}$. The merged data plotted with literature are shown in figures 9.3a and 9.3b for the ^{6}Li(p,α)^{3}He and ^{6}Li(p,γ)^{7}Be reactions, respectively,
4. Combine in quadrature the uncertainties on the merged S-factors with common systematic uncertainties.

The merged S-factor data has total uncertainties ranging $11.3 - 14.8\%$ ($12.7 - 16.3\%$) for the ^{6}Li(p,α)^{3}He (^{6}Li(p,γ)^{7}Be) reaction.

9.4 Comparisons with Literature

As discussed in section 9.1 the ^{6}Li(p,α)^{3}He bare S-factors from this study were scaled to the Cruz 2008 data [40] at the normalisation energies quoted in table 9.1, and for the studied energy range the present data are in complete agreement (less than 1σ) with S-factor values reported by Cruz 2005 [39] and Cruz 2008 [40]. The present data are also in agreement with the (scaled) He *et al.* [42] data, the results from the indirect Trojan Horse study by Lamia *et al.* [41], and several of the data points from Engstler *et al.* [37].

The ^{6}Li(p,γ)^{7}Be bare S-factors from this study are in agreement with the low energy data from Switkowski *et al.* [30]. The trend of our dataset shows an

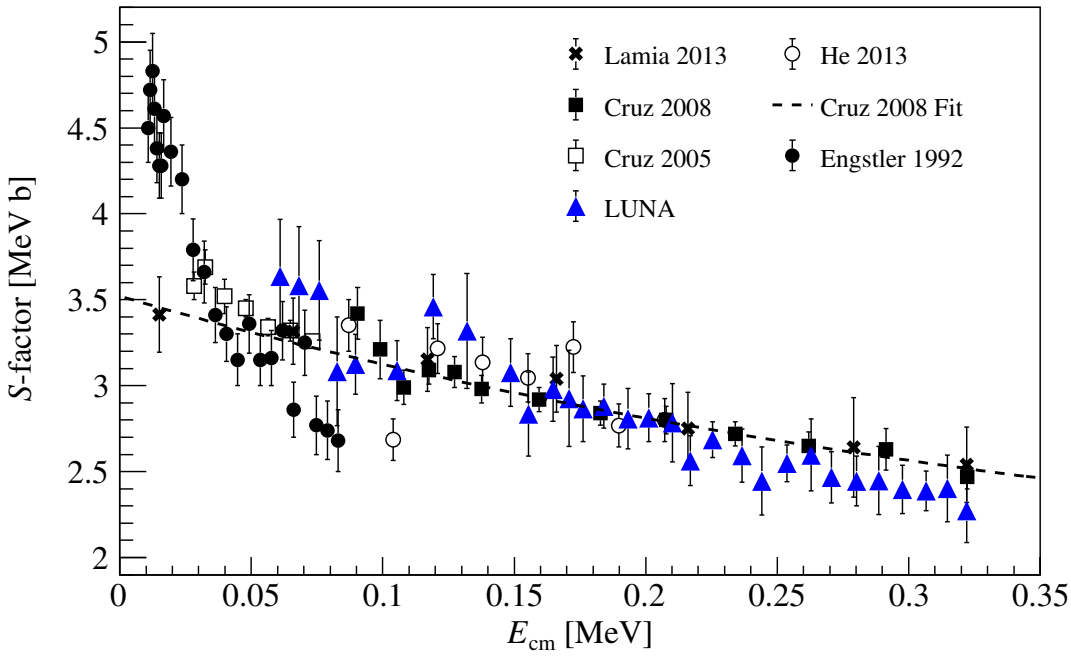

(a) *$^{6}Li(p,\alpha)^{3}He$ reaction S-factors.*

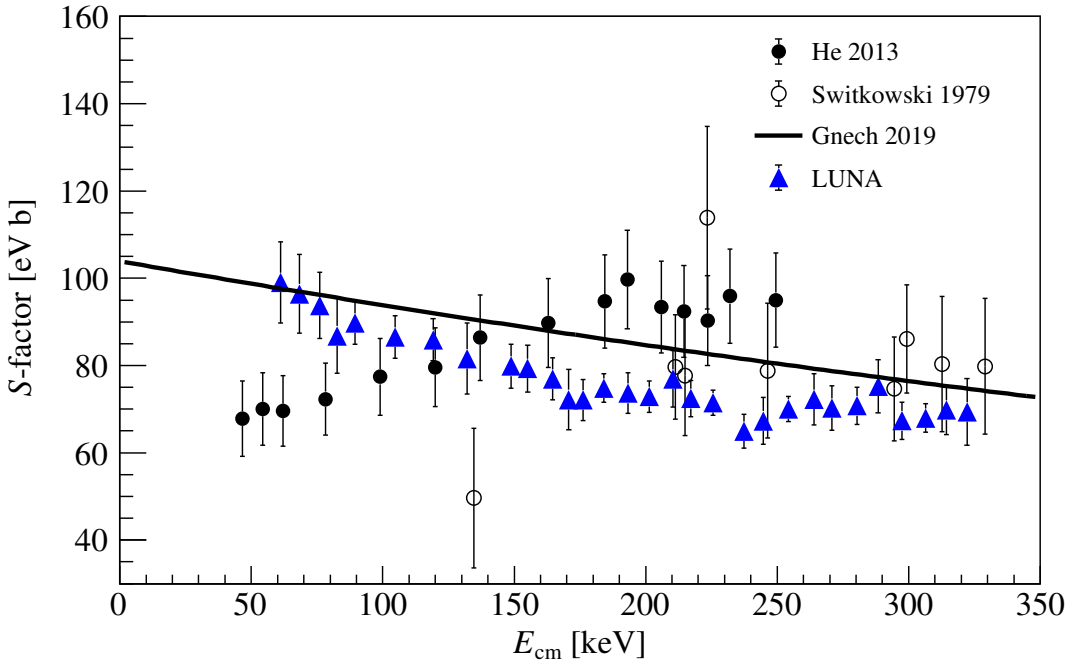

(b) *$^{6}Li(p,\gamma)^{7}Be$ reaction S-factors.*

Figure 9.3 *Present data, corrected for electron screening effects, are scaled to the Cruz et al. 2008 [40] data at E_n using scaling factors shown in table 9.1. The data from different targets have been merged and uncertainties on present data are from statistical and systematic (not in common between target data) uncertainties, see text for details.*

increasing S-factor at decreasing E_{cm}, in agreement with theoretical calculations by Barker [44], Arai *et al.* [38], Dong *et al.* [49], and Gnech and Marcucci [50]. This negative slope in S-factor disagrees with the observation reported by He *et al.*, who attribute their positive slope to a resonance at $E_{\mathrm{r}} = 195$ keV. The S-factors from this study and those reported by Switkowski *et al.* do not support the existence of a resonance in the ^{6}Li(p,γ)^{7}Be reaction across this low energy range, $E_{\mathrm{cm}} = 60 - 350$ keV, confirming multiple theoretical calculations [38, 44, 49, 50].

We propose two reasons for the cause of the disagreement between the He *et al.* 2013 data and our present data. The first is that He *et al.* may not have adequately corrected for target thickness effects in their calculation of the effective energies they assigned to their S-factors. The lowest proton energy reported in their work $E_{\mathrm{lab}} = 70$ keV, impinging on a $35\,\mu\mathrm{g/cm^2}$ Li_2O target, corresponds to an approximate $\Delta E_{\mathrm{lab}} = 27$ keV (using SRIM-2013 tables), or 38% of the incident energy. If we assume thin-target approximations are valid, this corresponds to an interaction energy $E_{\mathrm{cm}} = 48.5$ keV, not too dissimilar to He *et al.* lowest reported energy of 46.6 keV. However, for these low energy measurements it is typical to encounter significant energy loss through the target and, on account of the rapidly decreasing cross section, the front layers of the target contribute more significantly to the measured yield than the back layers of the target. As a result the thin-target energy calculation becomes inappropriate and the energies assigned to the measurement are not representative of the typical interaction energies (see subsection 4.1.2). If the median (or mean) energy approach is applied (instead of the thin-target case) this effect on the data is corrected by using the correction factor f reported in Brune *et al.* [55] and discussed in the cross section deconvolution section of chapter 4. For the effective energy approach used by He *et al.* to be valid, this correction factor must have been equal to one ($f = 1$) in their calculation, otherwise their S-factors and assigned energies would have been incorrectly deconvolved. To demonstrate this the LUNA ^{6}Li(p,α)^{3}He and ^{6}Li(p,γ)^{7}Be reaction S-factors were recalculated for the Li_2O-9 target whilst neglecting the f-correction factor. The scaled S-factors for this case are shown in figure 9.4. There is a clear change in S-factor slope for the ^{6}Li(p,γ)^{7}Be reaction, now in agreement with data from He *et al.*.

A second cause for the disagreement may come from the way in which He *et al.* scaled their ^{6}Li(p,γ)^{7}Be reaction S-factor values to those available in the literature. They report first scaling the (p,α) channel to the Cruz *et al.* 2008 data and then scaling the (p,γ) channel data to their scaled (p,α) data at this

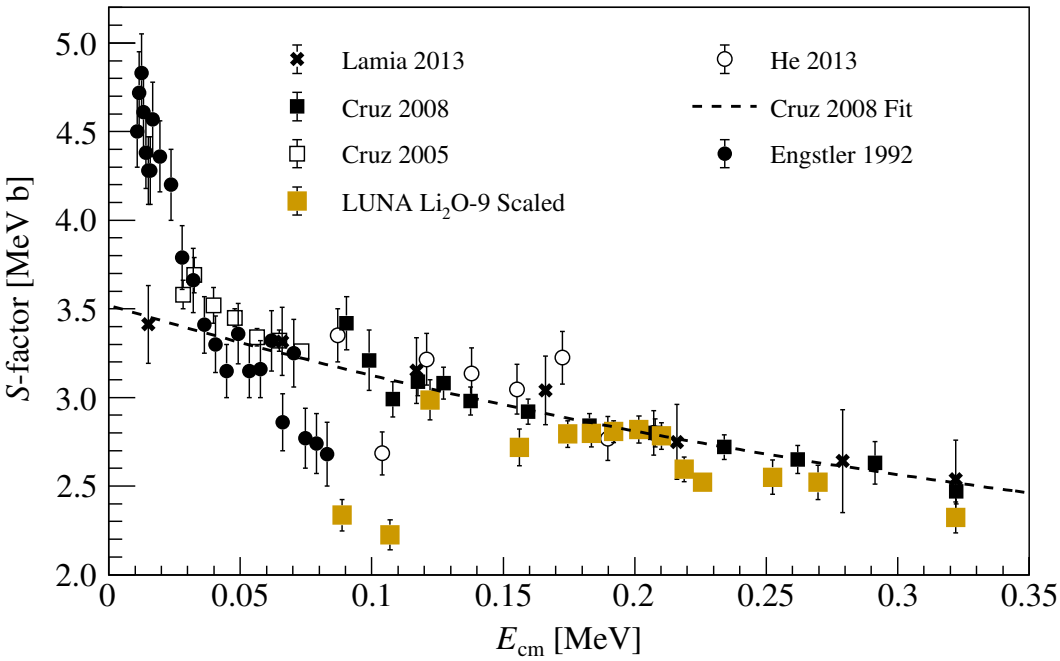

(a) *$^{6}Li(p,\alpha)^{3}He$ reaction S-factors.*

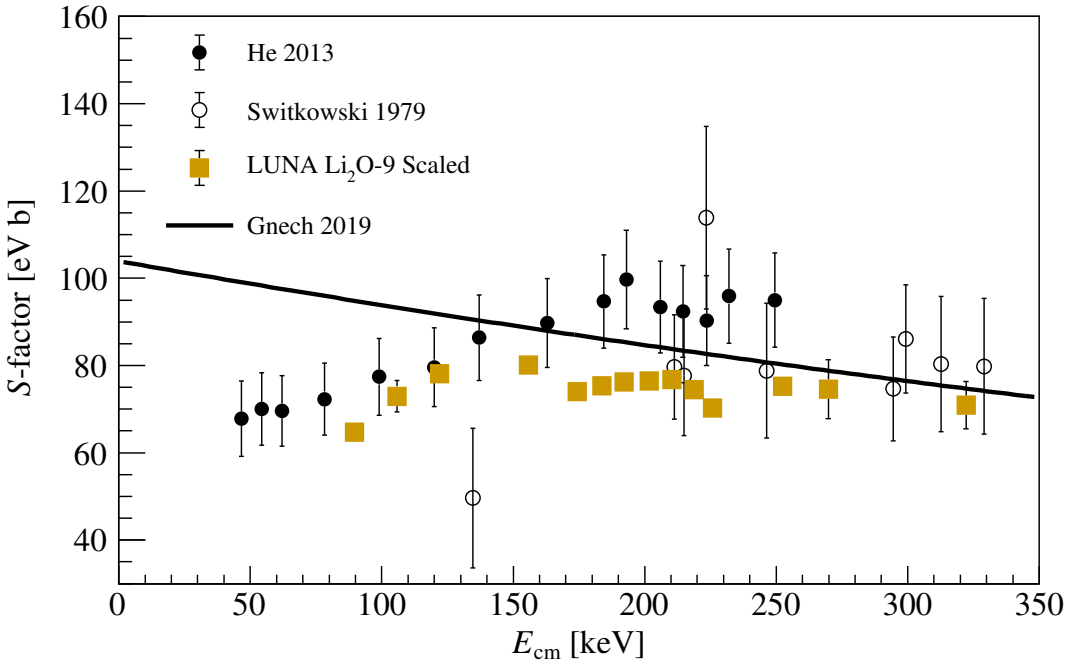

(b) *$^{6}Li(p,\gamma)^{7}Be$ reaction S-factors.*

Figure 9.4 *Bare reaction S-factors determined from the present study using the Li_2O-9 target and neglecting Brune et al. 2013 [55] f-correction factor (yellow squares), statistical error bars included. Literature previously plotted in figures 9.3a and 9.3b are included for comparison.*

same energy. Their scaling approach is consistent with that used in this thesis up to this point, however He *et al.* then report scaling all other (p,γ) channel data to their scaled (p,γ) data point. This may be interpreted as He *et al.* mistakenly scaling their (p,γ) data twice, thereby artificially creating their observed positive slope in S-factor at low energies.

9.5 Thermonuclear Reaction Rates for ^{6}Li(p,γ)^{7}Be Reaction

After scaling and merging, the present ^{6}Li(p,γ)^{7}Be reaction S-factors, complemented by the S-factors reported by Switkowski *et al.*, were used in the calculation of thermonuclear reaction rates (formalised in chapter 2). This required the S-factors to be integrated across the energy range defined by the Gamow window. The LUNA + Switkowski 1979 S-factors were integrated across $E_{\mathrm{cm}} = 0 - 1000$ keV as follows: first the LUNA data were fitted using a second order polynomial shown by the green line in figure 9.5. The fit has a small *chi*-squared as a result of the wide total uncertainty range. This fit was used to extrapolate the S-factor across $E_{\mathrm{cm}} = 61 - 0$ keV, where $S_0^{\mathrm{LUNA}} = 115(14)$ eV b. Next, the LUNA data was linearly interpolated across its E_{cm} range ($61 - 322$ keV). Lastly, the Switkowski 1979 S-factors were linearly interpolated across the higher E_{cm} range outside that covered by the LUNA data ($322 - 1000$ keV).

The He 2013 S-factors were integrated across $E_{\mathrm{cm}} = 0 - 1000$ keV, in a similar manner as the LUNA data. First, a second order polynomial fit was fitted to the He 2013 data, shown by the red line in figure 9.5. Similar to the fit of LUNA data this fit is over constrained (small *chi*-squared) by the total uncertainties. This fit was used to extrapolate the S-factors across $E_{\mathrm{cm}} = 46 - 0$ keV, where $S_0^{\mathrm{He\ 2013}} = 53(13)$ eV b. The He 2013 S-factors were linearly interpolated across their E_{cm} range ($46 - 245$ keV), and the Switkowski 1979 S-factors were linearly interpolated across the higher E_{cm} range outside that covered by the He 2013 data ($245 - 1000$ keV).

The rates were calculated for the temperature range $T = 0.001 - 1.000$ GK and their numerical values are tabulated with 1σ total errors in appendix F. The present reaction rates were fitted using the REACLIB format [102], specifically

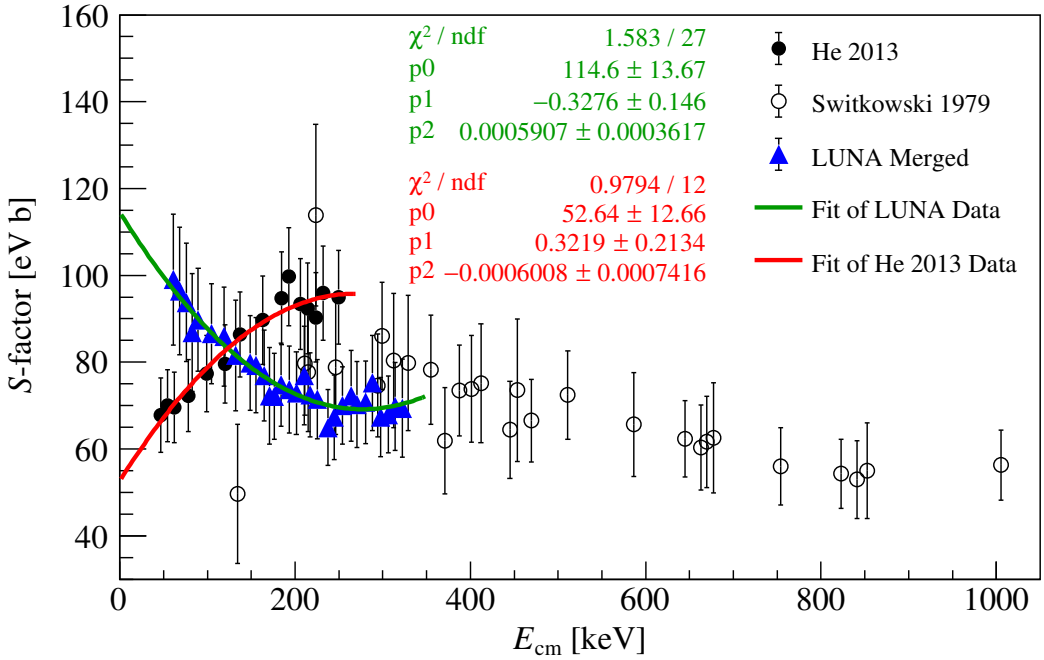

Figure 9.5 *$^{6}Li(p,\gamma)^{7}Be$ reaction S-factor vs E_{cm}. The (bare) LUNA data has been scaled and merged. Second order polynomial fits are shown for this work in green and the He et al. 2013 [42] data in red. All error bars are total. These fits were used as part of the calculation of thermonuclear reaction rates, see text for details.*

the formula:

$$N_{\mathrm{A}} < \sigma v >= \exp\left[a_0 + \sum_{i=1}^{5}\left(a_i T_9^{\frac{2i-5}{3}}\right) + a_6 \ln(T_9)\right] \ [\mathrm{cm^3 mol^{-1} s^{-1}}] \qquad (9.4)$$

using the fitting rules outlined in Cyburt *et al.* [102] for non-resonant charged-particle-induced reactions; $a_0 = \ln\left[B\left(\frac{Z_1 Z_2}{\mu}\right)^{1/3} S_0\right]$, $a_1 = 0$, $a_2 = -4.2486\,(Z_1^2\, Z_2^2\, \mu)^{1/3}$, a_3, a_4, and a_5 are free in the fit, and $a_6 = -2/3$. Where μ is the reduced mass, S_0 is the zero-energy S-factor, Z_1 and Z_2 are the atomic numbers of the target and projectile, respectively, and B is a constant expressed as $B = 7.8318 \times 10^9$ $\mathrm{cm^3 s^{-1} mole^{-1} MeV^{-1} b^{-1}}$. Figure 9.6 shows the present ^{6}Li(p,γ)^{7}Be reaction rates fitted with equation 9.4.

For comparison with previous literature, the rates were subsequently normalised to those in the standard NACRE database [103]. The normalised reaction rates from LUNA + Switkowski 1979 [30] S-factors are shown as the blue solid line in figure 9.7, the normalised reaction rates from He 2013 + Switkowski 1979 S-factors are plotted as a green dot-dashed line, and the normalised reaction

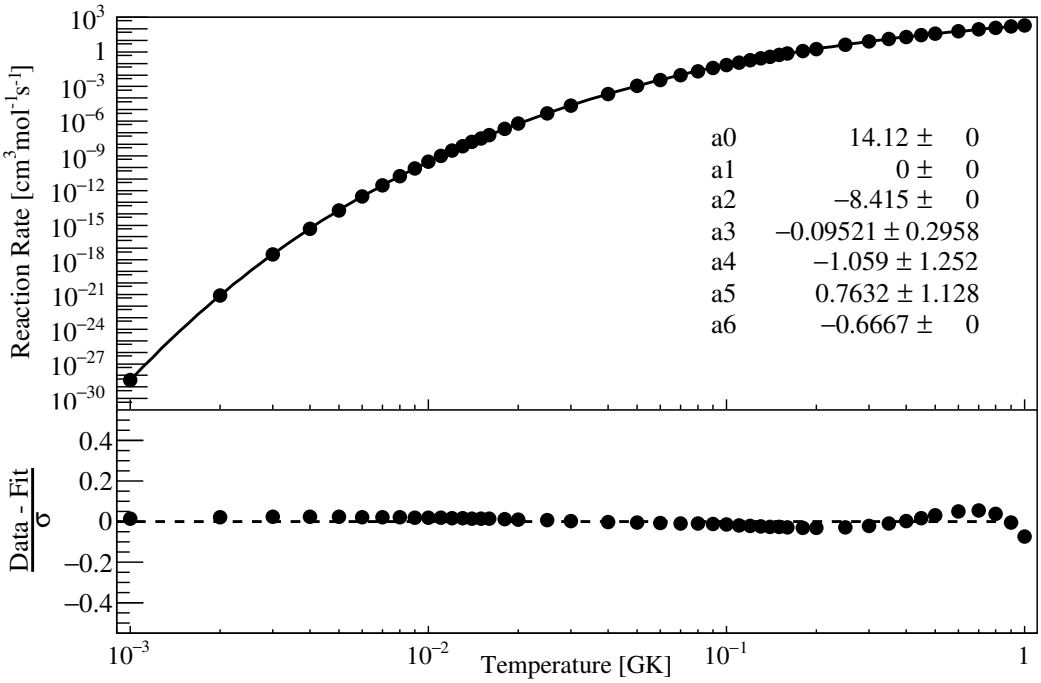

Figure 9.6 *Top: present $^6Li(p,\gamma)^7Be$ reaction rate fitted with the REACLIB formula (equation 9.4), using the fitting rules for a non-resonant charged-particle-induced reaction. Bottom: Residual plot. The fit reproduces the data within 0.2 σ.*

rates from the NACRE2 database [104] are plotted as a purple dashed line. The shaded regions for the LUNA and He 2013 reaction rates represent the total errors propagated from the S-factors. The LUNA rates are in very good agreement with the NACRE database rates. The NACRE2 and presently calculated He 2013 reaction rates show slight disagreement at low temperatures due to the choice of S-factor extrapolation: the NACRE2 database used a potential model to calculate the low energy S-factor instead of a polynomial fit.

In regards to the new reaction rate calculations using the LUNA + Switkowski 1979 data, the additional LUNA data provide additional constraints on the reaction rates. The uncertainties on the reaction rates have thereby been reduced considerably compared to the NACRE compilation [103]. For the temperature range $T = 0.001 - 1.000$ GK the NACRE rate uncertainties cover $1\sigma = 21 - 25\%$, the NACRE2 rate uncertainties cover $1\sigma = 19 - 46\%$, and the present rate uncertainties cover $1\sigma = 12 - 20\%$.

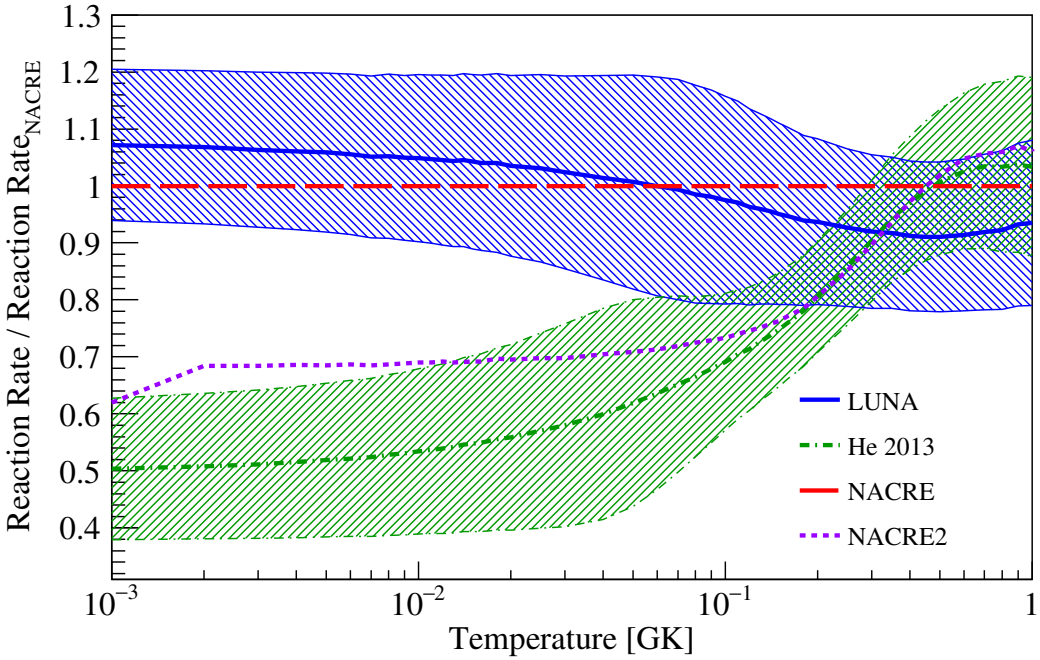

Figure 9.7 *^{6}Li(p,γ)^{7}Be reaction rates vs temperature, scaled to the NACRE database (red long dashed). Reaction rates from LUNA + Switkowski et al. 1979 (blue solid), He et al. 2013 + Switkowski et al. (green dot-dashed), and the NACRE2 database (purple dotted). The shaded regions represent the total errors on reaction rate propagated from the respective S-factor errors from the LUNA, He et al., and Switkowski et al. data.*

9.6 Astrophysical Impact

The puzzle of the lithium problems has motivated nuclear reaction studies of the different production and destruction mechanisms of lithium during Standard Big Bang Nucleosynthesis (SBBN). The ^{6}Li(p,α)^{3}He reaction is the most prominent destructive mechanism of ^{6}Li during SBBN, having a thermonuclear reaction rate a factor 10^4 larger [104] than the ^{6}Li(p,γ)^{7}Be reaction at $T = 0.8$ GK. Despite this, the recent suggestion of a new low energy resonance [42] in the ^{6}Li(p,γ)^{7}Be reaction would likely affect our understanding of the ^{6}Li(p,α)^{3}He reaction. For example the proposed spin-parities of the resonance state in ^{7}Be, J^π assignment of either $1/2^+$ or $3/2^+$, would also explain the dominant A_1 component of the ^{6}Li(p,α)^{3}He angular distribution [105]. As a further example the previously observed drop in the ^{6}Li(p,γ)^{7}Be reaction S-factor at E_{cm} less than 200 keV would mean, by virtue of the reciprocity theorem [23], a drop in the ^{7}Be(γ,p)^{6}Li S-factor. This would result in a lower production yield of ^{6}Li and a larger production of

^{7}Be during SBBN and, since ^{7}Be will naturally decay via electron capture to ^{7}Li ($t_{1/2} \sim 53$ days), the predicted primordial abundances of ^{7}Li and ^{6}Li may significantly increase and decrease, respectively. This would increase tensions between current primordial predictions and modern-day observations of the ^{7}Li abundance, potentially even contributing to the first and second lithium problems. However, results from the present work disprove the existence of a resonance at $E_{\mathrm{r}} = 195$ keV in the ^{6}Li(p,γ)^{7}Be reaction.

The AlterBBN v2.2 [20, 21] code was used to simulate Big Bang nucleosynthesis via a nuclear reaction network, using either the present reaction rate or the one derived from the He *et al.* data. The effect on the primordial abundances is negligible, as expected from the presence of a dominating ^{6}Li(p,α)^{3}He reaction rate, thus confirming the abundance of ^{6}Li predicted by previous reaction rates [103]. The first and second lithium problems are therefore not resolved by this nuclear physics information, and additional studies are required not necessarily in Nuclear Physics but perhaps in the fields of Cosmology and Particle Physics. The reaction rate uncertainty at SBBN relevant temperature $T = 0.8$ GK has been reduced from the NACRE database's $1\sigma = 23\%$ to this thesis work's $1\sigma = 15\%$.

Chapter 10

Summary

The ^{6}Li(p,α)^{3}He and ^{6}Li(p,γ)^{7}Be reactions affect the abundances of ^{6,7}Li in the Big Bang and low-mass Pre-Main Sequence (PMS) stars. Currently, Standard Big Bang Nucleosynthesis (SBBN) models predict a larger ^{7}Li abundance (factors $2.5 - 3.6$) and conversely a smaller ^{6}Li abundance (factor 1000) than those observed in PMS stars. These discrepancies are referred to as the first and second lithium problems, respectively. In addition, the ^{6}Li + p reactions govern the rate of convective mixing between the outer atmosphere and inner cores of PMS stars. It is therefore important to understand these destruction mechanisms of ^{6}Li to improve stellar convection models. The situation for the ^{6}Li(p,γ)^{7}Be reaction is made more complicated by the recent observation of a previously unobserved resonance lying in the energy range relevant to SBBN.

This thesis work describes an experimental campaign designed to measure both reactions concurrently at the underground LUNA laboratory located in Gran Sasso, Italy. The study was performed by accelerating a proton beam onto ^{6}Li-enriched solid targets nominally composed of either Li_2WO_4 or Li_2O. The charged particles from the ^{6}Li(p,α)^{3}He reaction were detected by a Si detector mounted at backward angle $\theta_{\rm lab} = 125°$, and the gamma rays from the ^{6}Li(p,γ)^{7}Be reaction were detected by a High Purity Germanium detector positioned at forward angle $\theta_{\rm lab} = 55°$. The low natural background present underground was essential in detecting these reaction products.

We extracted the ^{6}Li(p,α)^{3}He and ^{6}Li(p,γ)^{7}Be reaction S-factors (cross sections) across $E_{\rm cm} = 61 - 322$ keV, which translates to the corresponding temperature range encountered in SBBN ($T \sim 0.8$ GK). Our results disagree with the

previous claim of a low energy resonance present in the ^{6}Li(p,γ)^{7}Be reaction, and instead show the S-factor as a smoothly varying function in good agreement with other experimental data and theoretical models. We present new ^{6}Li(p,γ)^{7}Be thermonuclear reaction rates calculated by performing a global treatment of literature data and our S-factors. Our rates are in very good agreement with those presented in the NACRE database. In addition, our ^{6}Li(p,γ)^{7}Be reaction rates show reduced uncertainties ($1\sigma \sim 12-20\%$) compared to both the NACRE and NACRE2 compilations.

As a result both reactions were studied successfully and new ^{6}Li(p,γ)^{7}Be reaction rates have been determined at SBBN-relevant temperatures with the best precision to date. These results do not provide a solution for either of the lithium problems, which suggests further studies are required not necessarily in Nuclear Physics but perhaps in the fields of Cosmology or Particle Physics.

Appendix A

Interaction of Gamma rays with Matter

Gamma rays interact with matter in one of three main processes: photoelectric effect, Compton scattering, or pair production, depending on the energy available and the atomic properties of the material. For a material sufficiently thick such that it can completely stop the photons, the photoelectric effect dominates the possible interaction processes at low gamma-ray energies (E_γ less than 0.5 MeV). At higher energies ($E_\gamma = 0.5 - 5.0$ MeV) it becomes more probable for gamma rays to Compton scatter off the atomic electrons in the material, thereby only depositing some of their energy. The energy of the Compton scattered gamma ray, E'_γ, follows the angular dependence parametrised in [106]:

$$E'_\gamma = \frac{E_\gamma^2}{1 + \frac{E_\gamma}{m_e c^2}[1 - \cos(\theta)]} \tag{A.1}$$

where E_γ is the incident gamma ray energy, m_e is the electrons mass, c is the speed of light in a vacuum, and θ is the angle of the scattered gamma ray.

At even higher energies the most likely interaction is that of pair production, where the gamma ray is converted to an electron-positron pair. This occurs as long as the gamma-ray energy is at least the sum of the rest mass energies (1.022 MeV) of the electron-positron pair. The positron will likely interact with a surrounding electron in the material, causing the two to annihilate and be converted into two 511 keV gamma rays, which may interact with the material via the photoelectric or Compton effects. Figure A.1 (taken from [87]) shows which

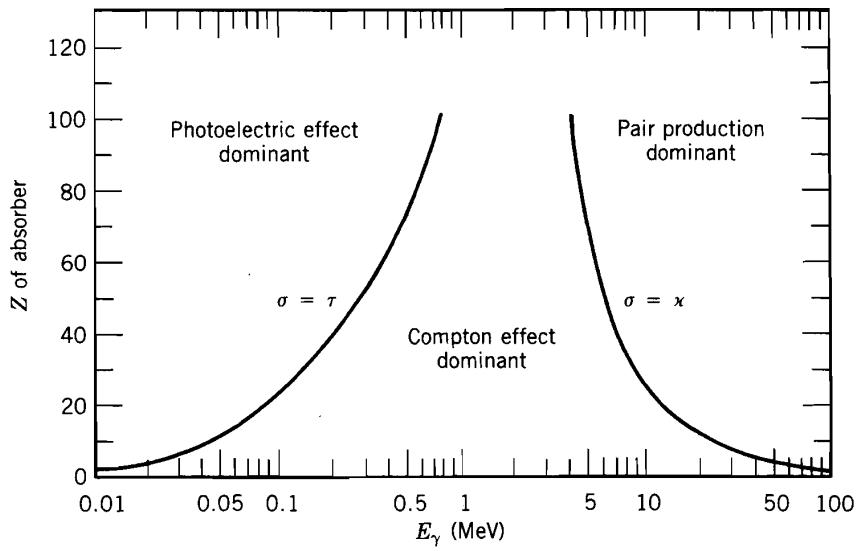

Figure A.1 *Gamma-ray interaction dominance regions as a function of gamma-ray energy and absorber material, Z. Taken from [87].*

of the three interactions has the greatest probability of occurring as a function of gamma-ray energy and absorber material, Z. The three processes all result in the production of free charge which forms the principle behind semiconductor detector operation.

A.1 Semiconductor Detectors

Semiconductor materials have electrical conductivities between those of insulators and metals. At room temperature, $\sim$ 300 K, a HPGe crystal has a band gap 0.67 eV [78], which is not useable for operation due to random thermal fluctuations contributing to large noise ($\sim$ 26 meV). To overcome this during operation the crystals are maintained at 77 K where the band gap is 0.75 eV [78]. In practice only $\sim 1/3$ of the gamma-ray energy is involved in ionisation, with the remainder exciting lattice vibrations, and so an effective band gap of 3 eV is used instead. Radiation incident on a HPGe detector will interact with the material via the photoelectric and Compton processes, producing electron-hole pairs in the Ge crystal. Through application of a high voltage using lithium and boron electrical contacts deposited on the crystal, a strong electric field is applied across the detection volume. This electric field increases the depletion zone between the electrical contacts, which accelerates the electrons (holes) onto the positive lithium (negative boron) contact where they deposit their charge. This charge is passed through a field effect transistor (gated resistor) before being

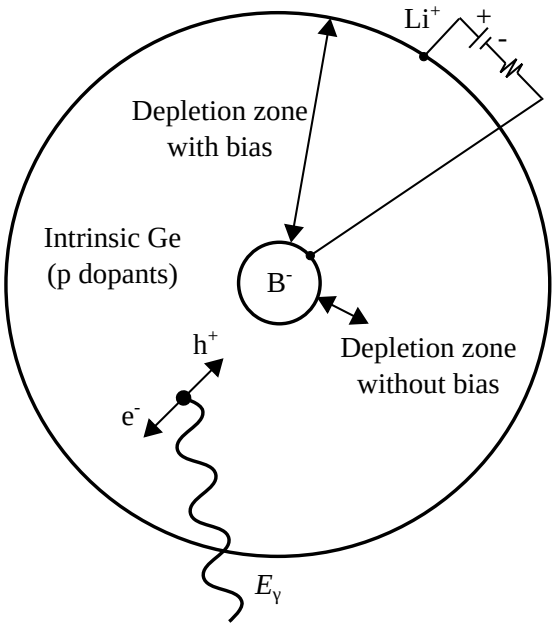

Figure A.2 *Diagram showing charge collection of a p-doped HPGe detector. Incoming photons excite electron-hole pairs in the Ge crystal. Application of a voltage bias at the Li^+ contact increases the depletion zone, setting up an electric field. The field collects the electrons at the Li^+ contact, allowing the charge to be measured.*

sent to a preamplifier for further amplification. Figure A.2 shows a diagram of a p-doped coaxial HPGe detector demonstrating the charge collection effect. At the operating voltage (typically a few thousand volts) the depletion zone is saturated at its maximum size, optimising the charge collection area.

Figure A.3 shows the different gamma-ray interaction processes on a semiconductor detector for a monoenergetic gamma ray, with a corresponding energy spectrum. In the top of the figure the different processes are:

1. Photon Compton scatters through crystal before leaving detector. Part of the gamma-ray's full energy is deposited.

2. Photon Compton scatters through crystal followed by photoelectric absorption. The gamma-ray's full energy is deposited.

3. Photon undergoes pair production followed by positron annihilation, one of the 511 keV photons escapes the detector. The gamma-ray's full energy minus 511 keV is deposited.

4. Same as 3 except both 511 keV photons escape detector. The gamma-ray's full energy minus 1022 keV is deposited.

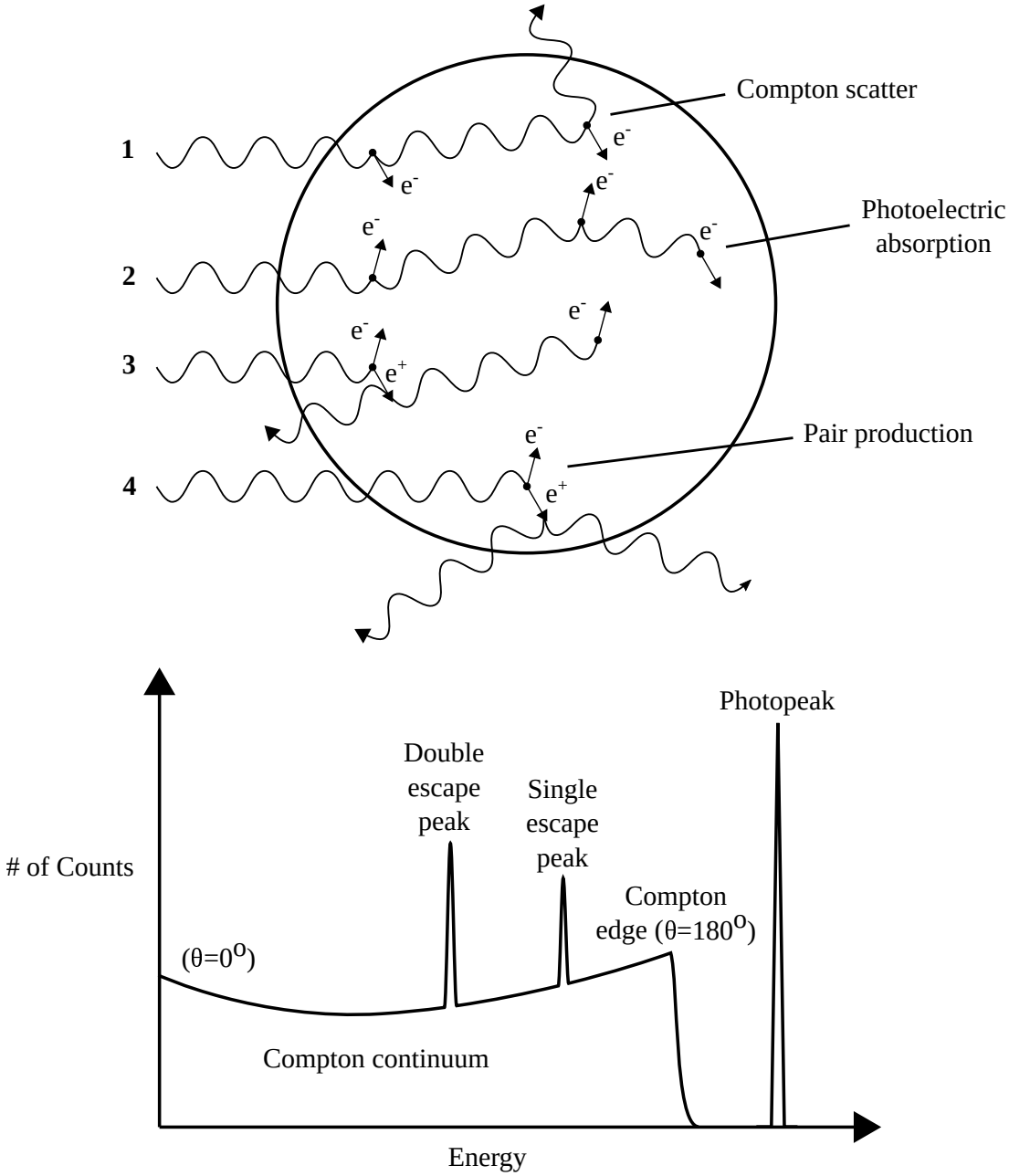

Figure A.3 *Top: Gamma-ray interaction processes on a semiconductor detector for a monoenergetic gamma ray. Bottom: Spectrum with different energy peaks corresponding to interaction of gamma rays with detector crystal.*

Appendix B

Photopeak Efficiencies

Figure B.1 (B.2) shows the absolute photopeak efficiencies measured for the HPGe detector, with the sources mounted on target holder 1 (2) for all seven source to detector-end-cap distances. The distance $d = 1.7$ cm was used when measuring gamma rays from the ^{6}Li(p,γ)^{7}Be reaction. The lines represent analytical summing corrections calculated by a collaborator at LUNA [90].

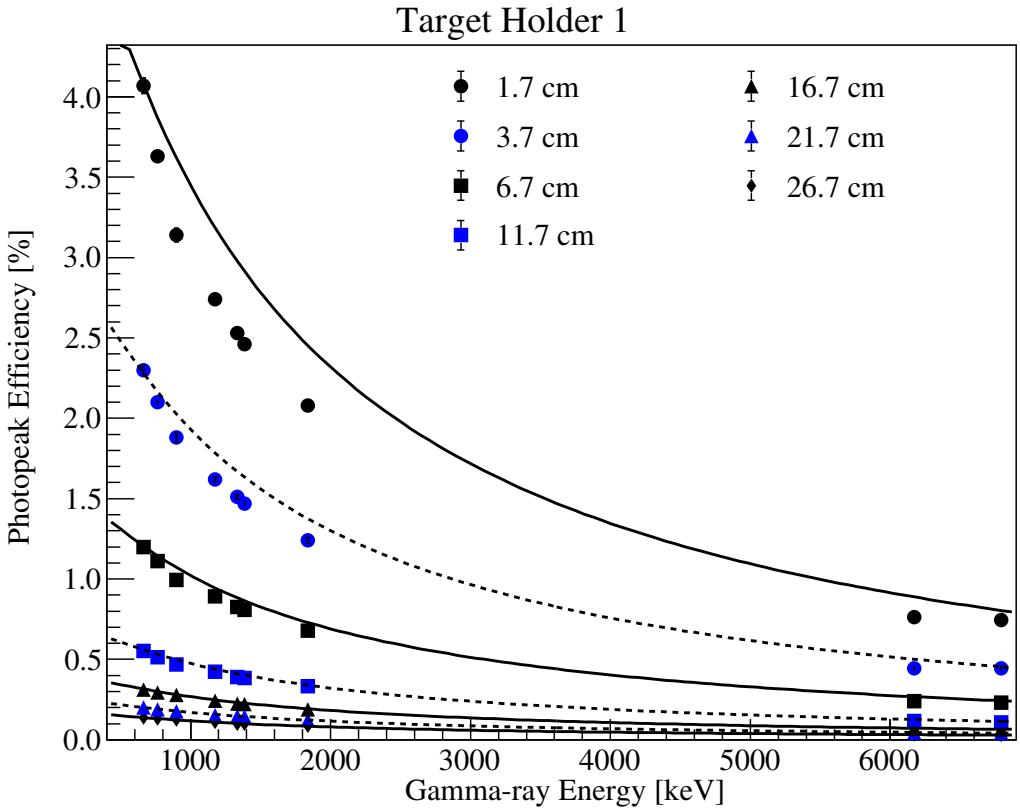

Figure B.1 *Photopeak efficiencies vs gamma-ray energy measured for the HPGe detector. The sources were mounted on target holder 1. Statistical error bars shown. The lines represent the analytical summing corrected photopeak efficiencies (reference [90]) at each distance.*

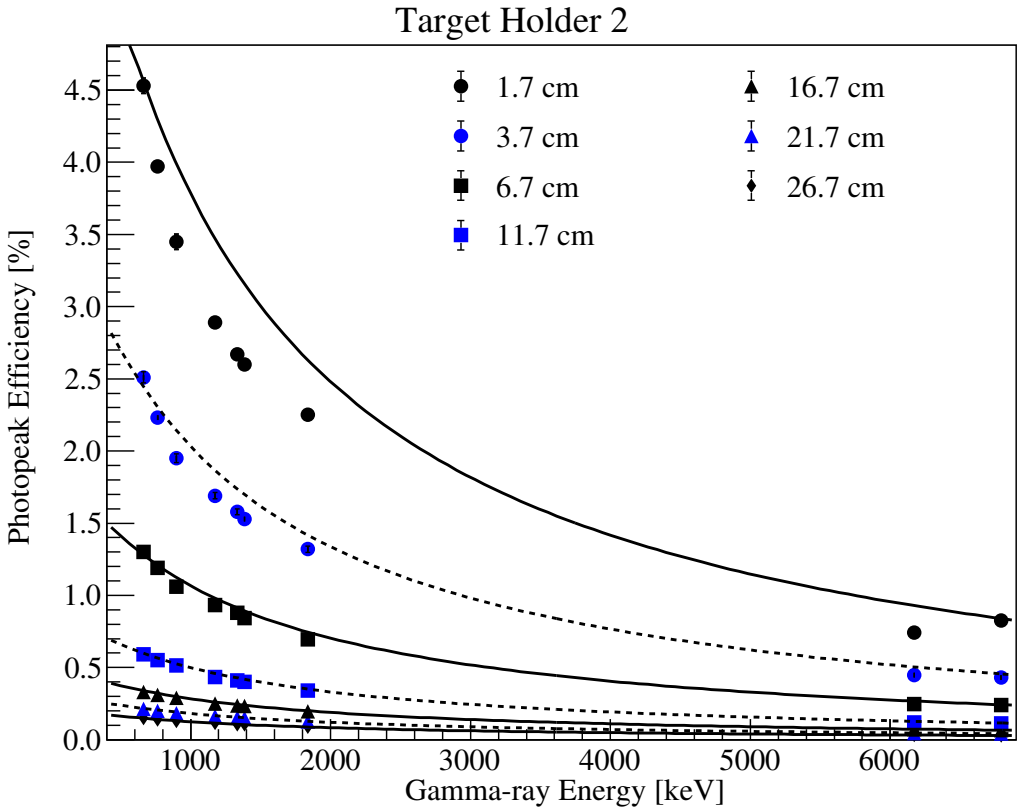

Figure B.2 *Photopeak efficiencies vs gamma-ray energy measured for the HPGe detector. The sources were mounted on target holder 2. Statistical error bars shown. The lines represent the analytical summing corrected photopeak efficiencies (reference [90]) at each distance.*

Appendix C

Effects of Simulated Beamspot Size and Shape on HPGe Efficiency

The following tables C.1, C.2, and C.3 all summarise the effect on the simulated HPGe efficiencies by including beamspots of different shapes and sizes in the GEANT4 simulations. The values provided are calculated as:

$$\text{Effect} = 100\,\frac{\eta(\text{point-like}) - \eta(\text{beamspot})}{\eta(\text{point-like})}\ [\%] \tag{C.1}$$

The columns are labelled with nX nY which define the beamspot semi axis in the X and Y frames, and (x,y) defines the coordinates of the centre of the simulated beamspot. For example the second column, “10X 5Y (0,0)" refers to a 10 mm X by 5 mm Y (radii) beamspot centred on (0,0) - the centre of the target. From the perspective of the beam entering the target, a negative x coordinate corresponds to a beamspot offset to the right of the target and a positive y coordinate corresponds to a beamspot offset to the top of the target.

The simulated cascade photopeak, singles photopeak, and singles total efficiencies are all within 6%, 3%, and 2.5% respectively for all three gamma rays.

Table C.1 *Effect (%) of beamspot on photopeak efficiencies (from simulated cascades) at gamma-ray energies relevant to $^6Li(p,\gamma)^7Be$ reaction. 5419 keV corresponds to the DC → 429 keV transition and 5848 keV corresponds to the DC → 0 keV transition.*

E_γ [keV]	10X 5Y (0,0)	5X 2.5Y (0,0)	5X 2.5Y (0,2)	5X 2.5Y (-2,0)	5X 2.5Y (-2,2)	5X 2.5Y (-5,2)
429	3.8	1.8	0.04	1.2	1.3	3.2
5419	-2.1	-4.1	-1.2	-3.5	-3.7	-5.9
5848	-0.1	0.7	-1.2	0.5	-1.3	-1.0

Table C.2 *Effect (%) of beamspot on photopeak efficiencies (from simulated singles) at gamma-ray energies relevant to $^6Li(p,\gamma)^7Be$ reaction. 5419 keV corresponds to the DC → 429 keV transition and 5848 keV corresponds to the DC → 0 keV transition.*

E_γ [keV]	10X 5Y (0,0)	5X 2.5Y (0,0)	5X 2.5Y (0,2)	5X 2.5Y (-2,0)	5X 2.5Y (-2,2)	5X 2.5Y (-5,2)
429	1.4	0.4	0.00	-0.3	-0.6	1.8
5419	1.2	1.1	0.33	0.3	1.3	2.9
5848	2.4	-0.3	0.36	1.0	2.3	-1.2

Table C.3 *Effect (%) of beamspot on total efficiencies (from simulated singles) at gamma-ray energies relevant to $^6Li(p,\gamma)^7Be$ reaction. 5419 keV corresponds to the DC → 429 keV transition and 5848 keV corresponds to the DC → 0 keV transition.*

E_γ [keV]	10X 5Y (0,0)	5X 2.5Y (0,0)	5X 2.5Y (0,2)	5X 2.5Y (-2,0)	5X 2.5Y (-2,2)	5X 2.5Y (-5,2)
429	1.8	0.3	0.7	0.6	0.6	2.4
5419	0.01	0.2	-0.2	0.3	-0.1	0.5
5848	-0.1	0.1	0.05	0.8	0.8	0.1

Appendix D

Additional Total Yield Plots

Figures D.1, D.3, and D.5 show the ^{6}Li(p,α)^{3}He reaction total yields measured in this work for the Li_2WO_4-3, 4, and Li_2O-9 targets, respectively. Likewise figures D.2, D.4, and D.6 show the ^{6}Li(p,γ)^{7}Be reaction total yields measured in this work for the Li_2WO_4-3, 4, and Li_2O-9 targets, respectively. Error bars are statistical for all plots. The multiple data points at $E_p \sim 290$ keV correspond to the repeat measurements at the reference energy (section 5.6).

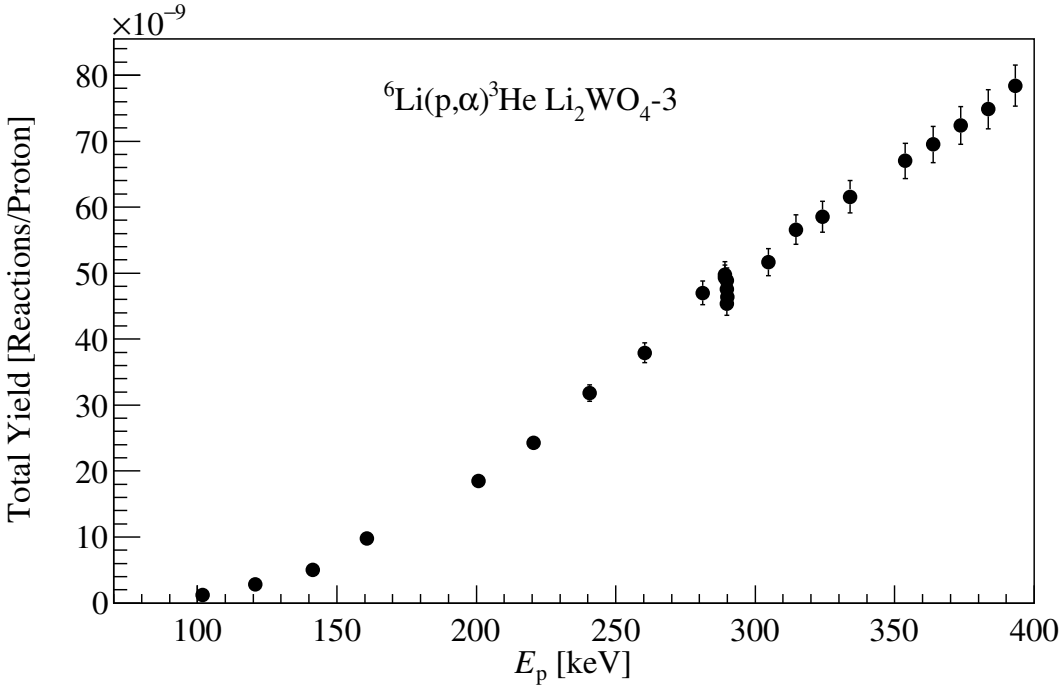

Figure D.1 *$^{6}Li(p,\alpha)^{3}He$ reaction experimental yields measured using the Li_2WO_4-3 target. Error bars are statistical.*

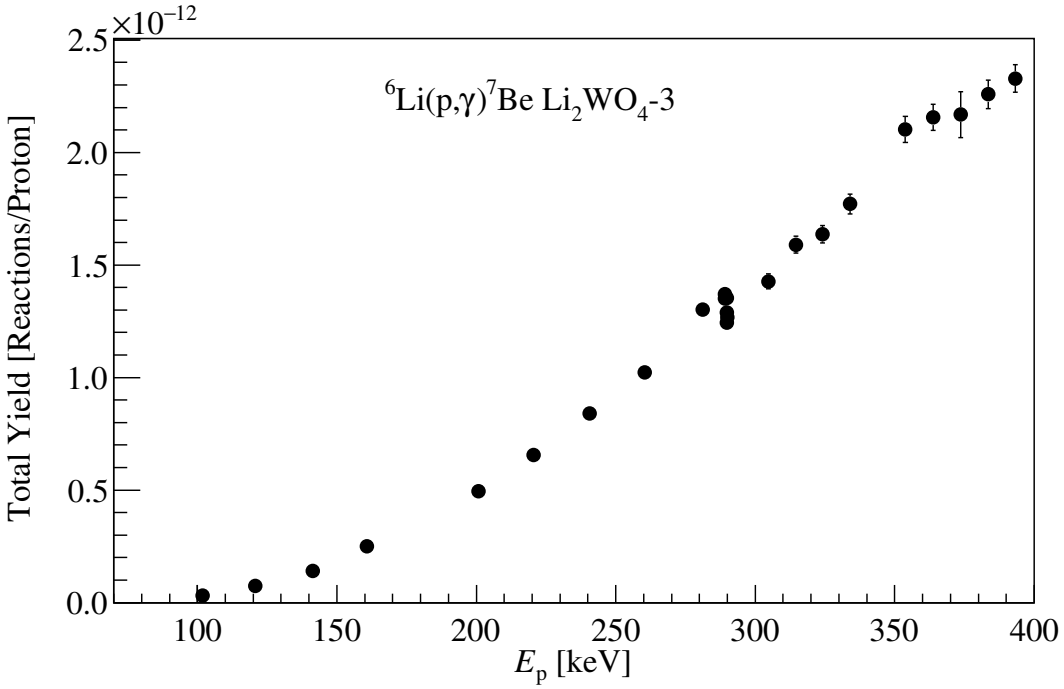

Figure D.2 *$^{6}Li(p,\gamma)^{7}Be$ reaction experimental yields measured using the Li_2WO_4-3 target. Error bars are statistical.*

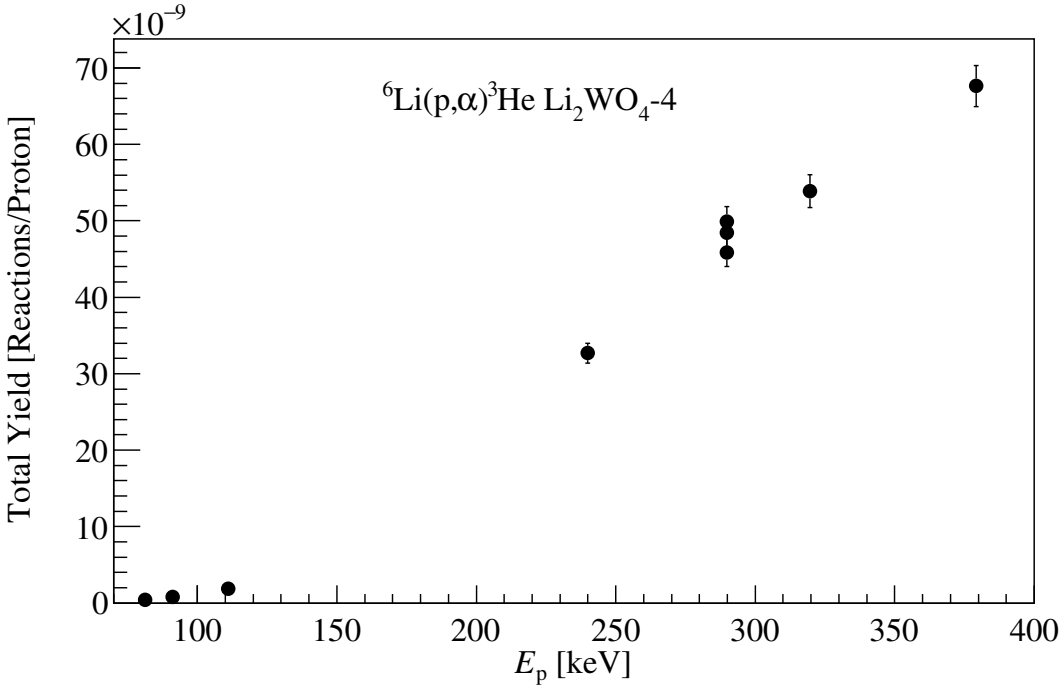

Figure D.3 *$^{6}Li(p,\alpha)^{3}He$ reaction experimental yields measured using the Li_2WO_4-4 target. Error bars are statistical.*

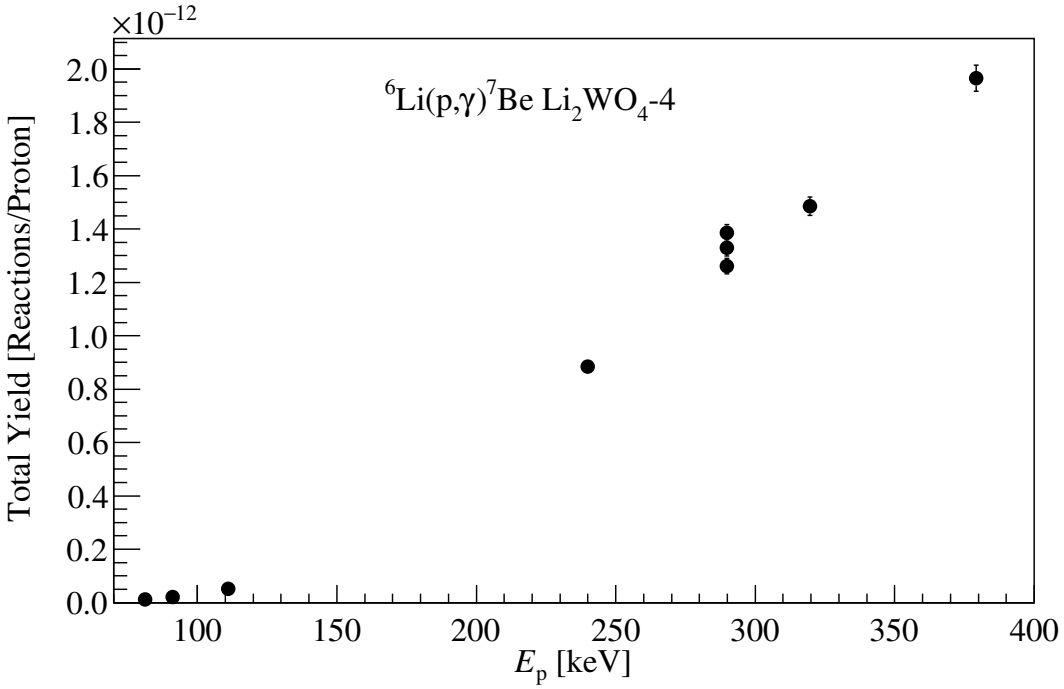

Figure D.4 *$^{6}Li(p,\gamma)^{7}Be$ reaction experimental yields measured using the Li_2WO_4-4 target. Error bars are statistical.*

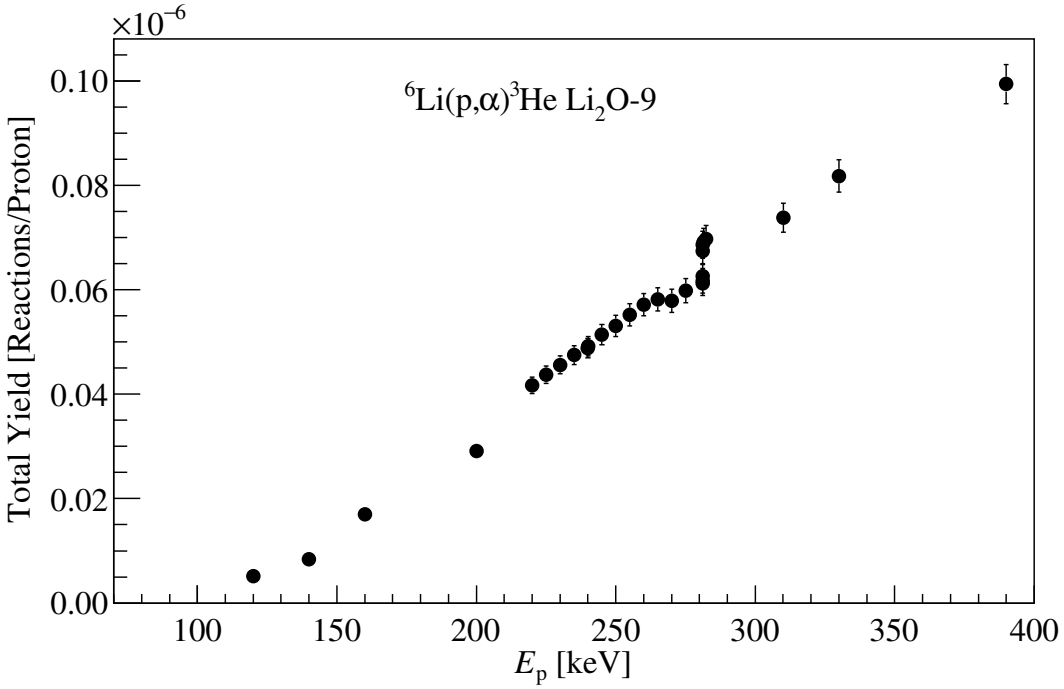

Figure D.5 *$^{6}Li(p,\alpha)^{3}He$ reaction experimental yields measured using the Li_2O-9 target. Error bars are statistical.*

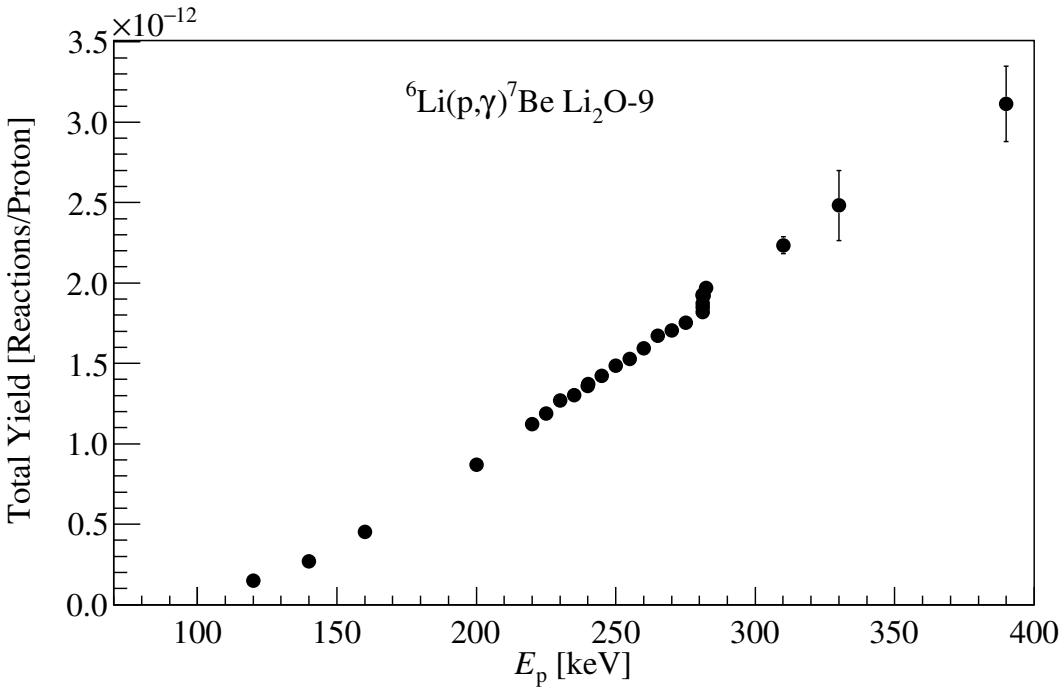

Figure D.6 *$^{6}Li(p,\gamma)^{7}Be$ reaction experimental yields measured using the Li_2O-9 target. Error bars are statistical.*

Appendix E

Additional Target Degradation Plots

Figures E.1, E.2, and E.3 show plots of target degradation against deposited charge for the Li_2WO_4-3, 4, and Li_2O-9 targets, respectively. The data from the DC $\rightarrow$ 0 keV peak fit parameter ΔE (black) are shown with corresponding fit including 68% confidence intervals (red lines) and the measured thickness from NRA performed at HZDR, Dresden (blue).

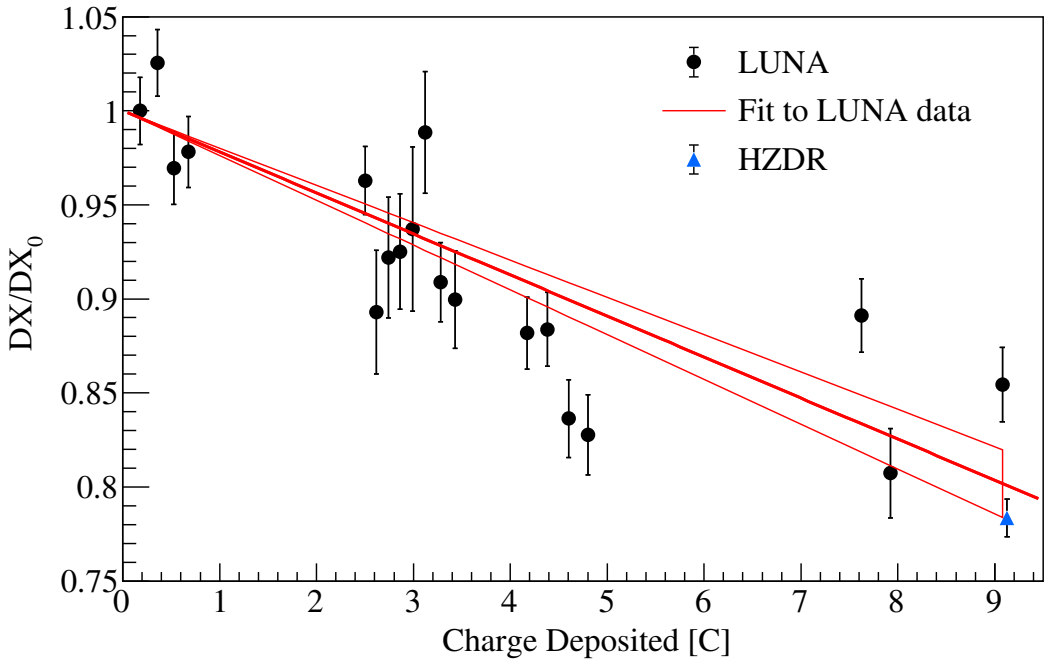

Figure E.1 *Plot of target degradation vs charge deposited on the Li_2WO_4-3 target.*

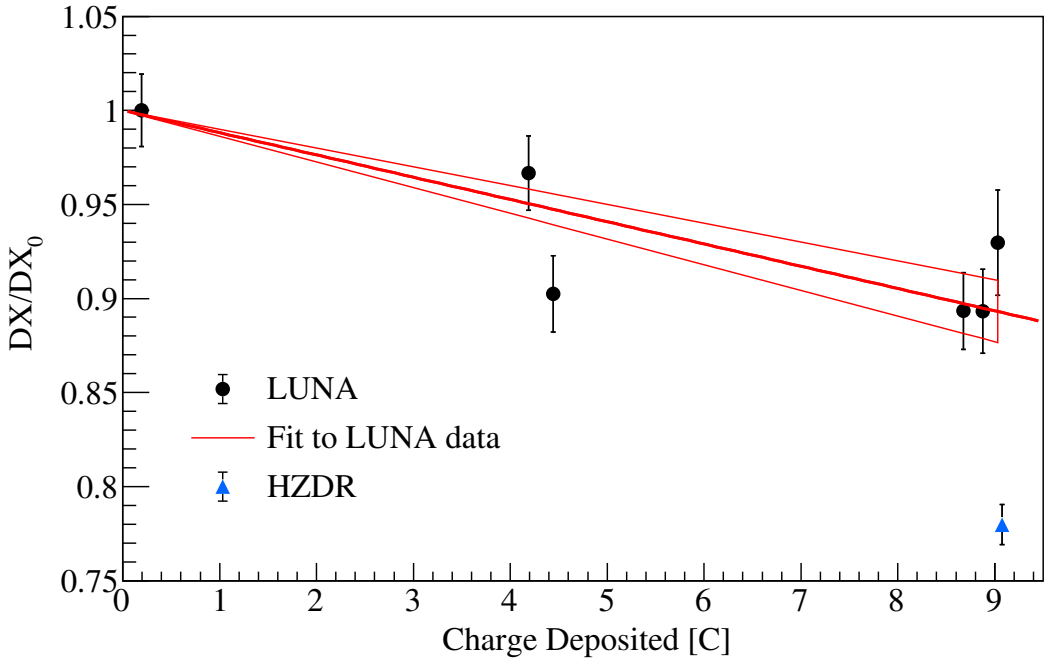

Figure E.2 *Plot of target degradation vs charge deposited on the Li_2WO_4-4 target.*

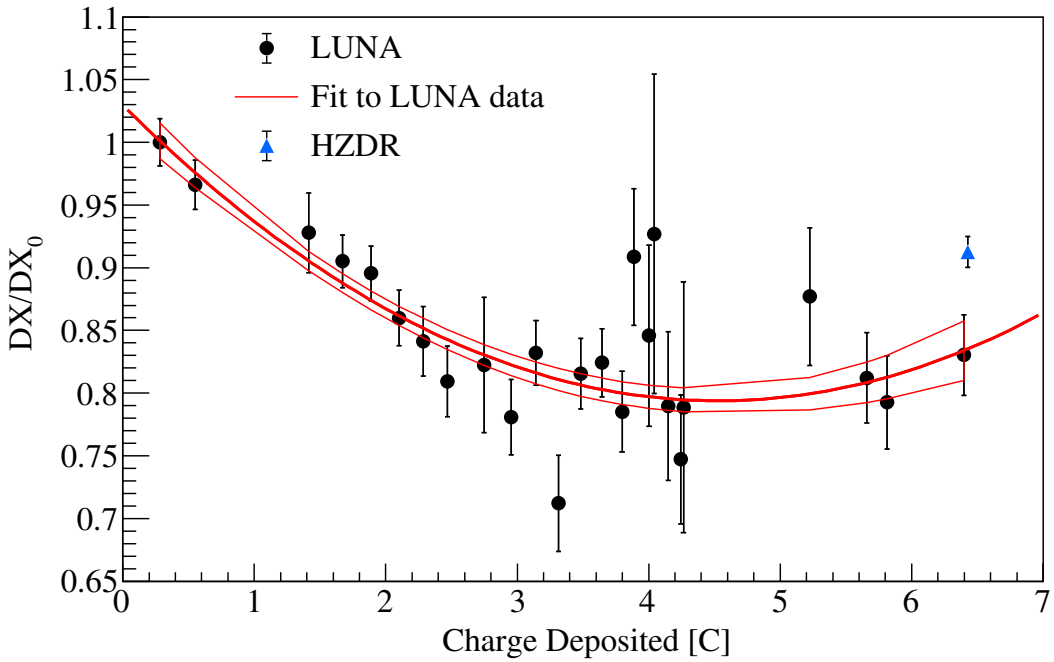

Figure E.3 *Plot of target degradation vs charge deposited on the Li_2O-9 target. Unlike the other targets it was decided to use a second order polynomial for the fit to reproduce the plateau at deposited charges greater than 3 C.*

Appendix F

Tabulated Reaction Rates for the ^{6}Li(p,γ)^{7}Be Reaction

The ^{6}Li(p,γ)^{7}Be reaction rates determined from the present work across $T = 0.001 - 1.000$ GK are provided in table F.1.

Table F.1 *^{6}Li(p,γ)^{7}Be thermonuclear reaction rates from the present study. The upper and lower rates (corresponding to 1σ) are also shown.*

	Reaction Rate [cm^3 mol^{-1} s^{-1}]		
***T* [GK]**	**Lower**	**Central**	**Upper**
0.001	3.38E-29	3.86E-29	4.34E-29
0.002	7.34E-22	8.39E-22	9.45E-22
0.003	2.59E-18	2.97E-18	3.35E-18
0.004	4.41E-16	5.07E-16	5.73E-16
0.005	1.69E-14	1.95E-14	2.20E-14
0.006	2.72E-13	3.13E-13	3.55E-13
0.007	2.48E-12	2.87E-12	3.26E-12
0.008	1.54E-11	1.78E-11	2.02E-11
0.009	7.14E-11	8.29E-11	9.43E-11
0.010	2.68E-10	3.11E-10	3.55E-10
0.011	8.50E-10	9.90E-10	1.13E-09
0.012	2.36E-09	2.75E-09	3.14E-09
0.013	5.86E-09	6.85E-09	7.83E-09
0.014	1.33E-08	1.56E-08	1.78E-08

Continued on next page

Table F.1 – continued from previous page

	Reaction Rate [cm^3 mol^{-1} s^{-1}]		
T [GK]	Lower	Central	Upper
0.015	2.80E-08	3.28E-08	3.77E-08
0.016	5.53E-08	6.49E-08	7.45E-08
0.018	1.84E-07	2.16E-07	2.49E-07
0.020	5.16E-07	6.09E-07	7.02E-07
0.025	4.04E-06	4.80E-06	5.57E-06
0.030	1.92E-05	2.30E-05	2.68E-05
0.040	1.84E-04	2.23E-04	2.63E-04
0.050	9.01E-04	1.11E-03	1.31E-03
0.060	3.01E-03	3.73E-03	4.44E-03
0.070	7.86E-03	9.76E-03	1.17E-02
0.080	1.73E-02	2.15E-02	2.56E-02
0.090	3.37E-02	4.17E-02	4.96E-02
0.100	5.98E-02	7.35E-02	8.73E-02
0.110	9.84E-02	1.20E-01	1.42E-01
0.120	1.53E-01	1.86E-01	2.19E-01
0.130	2.26E-01	2.74E-01	3.21E-01
0.140	3.21E-01	3.87E-01	4.53E-01
0.150	4.41E-01	5.30E-01	6.18E-01
0.160	5.89E-01	7.05E-01	8.20E-01
0.180	9.80E-01	1.16E+00	1.35E+00
0.200	1.51E+00	1.79E+00	2.07E+00
0.250	3.56E+00	4.19E+00	4.81E+00
0.300	6.77E+00	7.93E+00	9.09E+00
0.350	1.12E+01	1.31E+01	1.50E+01
0.400	1.70E+01	1.98E+01	2.26E+01
0.450	2.39E+01	2.80E+01	3.20E+01
0.500	3.22E+01	3.76E+01	4.30E+01
0.600	5.21E+01	6.10E+01	7.00E+01
0.700	7.63E+01	8.96E+01	1.03E+02
0.800	1.04E+02	1.23E+02	1.41E+02
0.900	1.35E+02	1.59E+02	1.84E+02
1.000	1.68E+02	1.99E+02	2.30E+02

Bibliography

[1] C. Pitrou, A. Coc, J.-P. Uzan, and E. Vangioni, Physics Reports **754**, 1 (2018).

[2] E. Hubble, Proceedings of the National Academy of Sciences **15**, 168 (1929).

[3] A. G. Riess *et al.*, The Astronomical Journal **116**, 1009 (1998).

[4] A. A. Penzias and R. W. Wilson, The Astrophysical Journal **142**, 419 (1965).

[5] C. Bennett *et al.*, The Astrophysical Journal Supplement Series **208**, 20 (2013).

[6] P. A. Ade *et al.*, Astronomy & Astrophysics **594**, A13 (2016).

[7] B. Fields, Annual Review of Nuclear and Particle Science **61**, 47 (2011).

[8] B. Fields, P. Molaro, and S. Sarkar, Chinese Physics C **38**, 339 (2014).

[9] A. Coc and E. Vangioni, International Journal of Modern Physics E **26**, 1741002 (2017).

[10] M. Anders *et al.*, Phys. Rev. Lett. **113**, 042501 (2014).

[11] F. Spite and M. Spite, Astronomy and Astrophysics **115**, 357 (1982).

[12] M. Spite and F. Spite, Nature **297**, 483 (1982).

[13] M. Asplund *et al.*, The Astrophysical Journal **644**, 229 (2006).

[14] L. Sbordone *et al.*, Astronomy & astrophysics **522**, A26 (2010).

[15] K. Lind *et al.*, Astronomy & Astrophysics **554**, A96 (2013).

[16] X. Fu *et al.*, Monthly Notices of the Royal Astronomical Society **452**, 3256 (2015).

[17] H. Reggiani *et al.*, Astronomy & Astrophysics **608**, A46 (2017).

[18] G. Harutyunyan *et al.*, Astronomy & Astrophysics **618**, A16 (2018).

[19] V. V. Smith, D. L. Lambert, and P. E. Nissen, The Astrophysical Journal **408**, 262 (1993).

[20] A. Arbey, Computer Physics Communications **183**, 1822 (2012).

[21] A. Arbey, J. Auffinger, K. P. Hickerson, and E. S. Jenssen, AlterBBN v2: A public code for calculating Big-Bang nucleosynthesis constraints in alternative cosmologies, 2018.

[22] M. Wang *et al.*, Chinese Physics C **41**, 030003 (2017).

[23] C. Iliadis, *Nuclear Physics of Stars*, *Physics textbook* (Wiley, Weinheim, Germany, 2007).

[24] C. Rolfs and W. Rodney, *Cauldrons in the Cosmos: Nuclear Astrophysics*, *Theoretical Astrophysics* (University of Chicago Press, Chicago, USA, 1988).

[25] D. D. Clayton, *Principles of Stellar Evolution and Nucleosynthesis*, *Physics textbook* (The University of Chicago Press, Chicago, USA, 1983).

[26] H. J. Assenbaum, K. Langanke, and C. Rolfs, Zeitschrift für Physik A Atomic Nuclei **327**, 461 (1987).

[27] L. Bracci *et al.*, Nuclear Physics A **513**, 316 (1990).

[28] C. Rolfs, Nuclear Physics A **217**, 29 (1973).

[29] D. A. Scott, Ph.D. thesis, University of Edinburgh, 2014.

[30] Z. Switkowski *et al.*, Nuclear Physics A **331**, 50 (1979).

[31] R. B. Bowersox, Phys. Rev. **55**, 323 (1939).

[32] W. Gemeinhardt, D. Kamke, and C. von Rhöneck, Zeitschrift für Physik **197**, 58 (1966).

[33] H. Spinka, T. Tombrello, and H. Winkler, Nuclear Physics A **164**, 1 (1971).

[34] T. Shinozuka, Y. Tanaka, and K. Sugiyama, Nuclear Physics A **326**, 47 (1979).

[35] A. J. Elwyn *et al.*, Physical Review C **20**, 1984 (1979).

[36] J. Kwon, J. Kim, and B. Sung, Nuclear Physics A **493**, 112 (1989).

[37] S. Engstler *et al.*, Zeitschrift für Physik A Hadrons and Nuclei **342**, 471 (1992).

[38] K. Arai, D. Baye, and P. Descouvemont, Nuclear Physics A **699**, 963 (2002).

[39] J. Cruz *et al.*, Physics Letters B **624**, 181 (2005).

[40] J. Cruz *et al.*, Journal of Physics G: Nuclear and Particle Physics **35**, 014004 (2008).

[41] L. Lamia *et al.*, The Astrophysical Journal **768**, 65 (2013).

[42] J. He *et al.*, Physics Letters B **725**, 287 (2013).

[43] S. Bashkin and R. R. Carlson, Phys. Rev. **97**, 1245 (1955).

[44] F. C. Barker, Australian Journal of Physics **33**, 159 (1980).

[45] F. Cecil *et al.*, Nuclear Physics A **539**, 75 (1992).

[46] R. Prior *et al.*, Physical Review C **70**, 055801 (2004).

[47] J. Huang, C. Bertulani, and V. Guimarães, Atomic Data and Nuclear Data Tables **96**, 824 (2010).

[48] S. Igamov *et al.*, Вестник НЯЦ РК **65**, 82 (2016).

[49] G. Dong *et al.*, Journal of Physics G: Nuclear and Particle Physics **44**, 045201 (2017).

[50] A. Gnech and L. Marcucci, Nuc. Phys. A **987**, 1 (2019).

[51] J. F. Ziegler, SRIM - The Stopping and Range of Ions in Matter, `http://www.srim.org/`, accessed: October 2016.

[52] H. H. Andersen and J. F. Ziegler, *The stopping and ranges of ions in matter* (Elsevier, New York, USA, 2013), Vol. 3.

[53] W. H. Bragg and R. Kleeman, The London, Edinburgh, and Dublin Philosophical Magazine and Journal of Science **10**, 318 (1905).

[54] R. H. James and M. R. Palmer, Chemical Geology **166**, 319 (2000).

[55] C. R. Brune and D. B. Sayre, Nuclear Instruments and Methods in Physics Research Section A: Accelerators, Spectrometers, Detectors and Associated Equipment **698**, 49 (2013).

[56] C. G. Bruno, Ph.D. thesis, University of Edinburgh, 2017.

[57] A. Caciolli *et al.*, The European Physical Journal A-Hadrons and Nuclei **39**, 179 (2009).

[58] H. Costantini *et al.*, Reports on Progress in Physics **72**, 086301 (2009).

[59] A. Formicola *et al.*, Nuclear Instruments and Methods in Physics Research A **507**, 609 (2003).

[60] F. Cavanna *et al.*, The European Physical Journal A **50**, 179 (2014).

[61] D. Bemmerer *et al.*, Europhysics Letters **122**, 52001 (2018).

[62] G. Imbriani *et al.*, European Physical Journal A **25**, 455 (2005).

[63] C. G. Bruno *et al.*, European Physical Journal A **51**, 94 (2015).

[64] G. Ciani *et al.*, The European Physical Journal A **56**, 75 (2020).

[65] Sigma Aldrich Catalogue, `https://www.sigmaaldrich.com/catalog/product/aldrich/900545?lang=en&region=GB`, accessed: 14th October 2019.

[66] ORTEC, MAESTRO Multichannel Analyser Emulation Software, `http://www.ortec-online.com/products/application-software/maestro-mca`, accessed: October 2019.

[67] T. Furukawa *et al.*, Fusion Engineering and Design **98**, 2138 (2015).

[68] J. R. Tesmer and M. A. Nastasi, *Handbook of Modern Ion Beam Materials Analysis* (Materials Research Society, Pittsburg, Pennsylvania, USA, 1995).

[69] O. Benka, in *Surface and Thin Film Analysis*, edited by G. Friedbacher and H. Bubert (Wiley-VCH Verlag & Co, Weinheim, Germany, 2011), pp. 217 – 227.

[70] J. L'ecuyer *et al.*, Journal of Applied Physics **47**, 381 (1976).

[71] M. Mayer, AIP Conference Proceedings **475**, 541 (1999).

[72] G. Gyürky *et al.*, The European Physical Journal A-Hadrons and Nuclei **21**, 355 (2004).

[73] M. Friedrich, W. Bürger, D. Henke, and S. Turuc, Nuclear Instruments and Methods in Physics Research Section A: Accelerators, Spectrometers, Detectors and Associated Equipment **382**, 357 (1996), proceedings of the Seventh International Conference on Heavy Ion Accelerator Technology.

[74] J. Parker, in *Passive Nondestructive Assay of Nuclear Materials*, edited by R. Doug, E. Norbert, and H. Smith, Jr. (NUREG/CR-5550, Washington, DC, USA, 1991), p. 95.

[75] L. Meyer-Schützmeister and S. S. Hanna, Phys. Rev. **108**, 1506 (1957).

[76] J. Julin, Private communication, 2017.

[77] N. P. Barradas, C. Jeynes, and R. P. Webb, Applied Physics Letters **71**, 291 (1997).

[78] G. F. Knoll, *Radiation Detection and Measurement*, 3rd ed. (Wiley, New York, USA, 2000).

[79] A. Caciolli *et al.*, European Physical Journal A **48**, 144 (2012).

[80] R. Brun *et al.*, *GEANT 3: user's guide Geant 3.10, Geant 3.11*, 1987.

[81] P. Corvisiero, Private communication, 2019.

[82] J. Taylor, *An Introduction to Error Analysis*, 2nd ed. (University Science Books, California, USA, 1997).

[83] M. E. Rose, Physical Review **91**, 610 (1953).

[84] C. R. Brune, H. J. Karwowski, and E. J. Ludwig, Nuclear Instruments and Methods in Physics Research A **389**, 421 (1997).

[85] D. R. Lide, *CRC Handbook of Chemistry and Physics* (CRC Press, Boca Raton, 2003).

[86] D. Attie *et al.*, Astronomy & Astrophysics **411**, L71 (2003).

[87] K. S. Krane, *Introductory Nuclear Physics* (John Wiley & Sons, USA, 1988).

[88] R. Gehrke, R. Helmer, and R. Greenwood, Nuclear Instruments and Methods **147**, 405 (1977).

[89] H. El-Gharbawy *et al.*, Nuclear Instruments and Methods in Physics Research Section A: Accelerators, Spectrometers, Detectors and Associated Equipment **550**, 201 (2005).

[90] D. Piatti, Private communication, 2019.

[91] Geant4: A Simulation Toolkit, `http://geant4.web.cern.ch/`, accessed: 11th November 2016.

[92] Physics Reference Manual, Version: geant4 10.2 (4 December 2015), `https://geant4.web.cern.ch/support/user_documentation`, accessed: 11th November 2016.

[93] A. Boeltzig, Ph.D. thesis, Gran Sasso Science Institute, 2016.

[94] E. L. Brady and M. Deutsch, Phys. Rev. **78**, 558 (1950).

[95] E. D. Klema and F. K. McGowan, Phys. Rev. **91**, 616 (1953).

[96] O. A. Helene *et al.*, International Atomic Energy Agency: Vienna **210**, 35 (2007).

[97] M. Marta, Ph.D. thesis, Der Technischen Universität Dresden, 2011.

[98] D. Tilley *et al.*, Nuclear Physics A **636**, 249 (1998).

[99] A. Formicola, Ph.D. thesis, Ruhr-University Bochum, 2004.

[100] K. S. Krane, Nuclear Instruments and Methods **98**, 205 (1972).

[101] J. Cruz, Ph.D. thesis, Universidade Nova de Lisboa, 2006.

[102] R. H. Cyburt *et al.*, The Astrophysical Journal Supplement Series **189**, 240 (2010).

[103] C. Angulo *et al.*, Nuclear Physics A **656**, 3 (1999).

[104] Y. Xu *et al.*, Nuclear Physics A **918**, 61 (2013).

[105] F. C. Barker, Nuclear Physics A **707**, 277 (2002).

[106] W. R. Leo, *Techniques for Nuclear and Particle Physics Experiments: A How-to Approach*, 2nd ed. (Springer, Berlin, Heidelberg, 1994).